Applied rheology for production of polypropylene nanofibers

Bc. Jiří Drábek

Master thesis
2013

Tomas Bata University in Zlín
Faculty of Technology

Univerzita Tomáše Bati ve Zlíně
Fakulta technologická
Ústav výrobního inženýrství
akademický rok: 2012/2013

ZADÁNÍ DIPLOMOVÉ PRÁCE

(PROJEKTU, UMĚLECKÉHO DÍLA, UMĚLECKÉHO VÝKONU)

Jméno a příjmení:	**Bc. Jiří Drábek**
Osobní číslo:	**T11159**
Studijní program:	**N3909 Procesní inženýrství**
Studijní obor:	**Konstrukce technologických zařízení**
Forma studia:	**prezenční**
Téma práce:	**Aplikovaná reologie pro výrobu polypropylenových nanovláken**

Zásady pro vypracování:

1. Prepare the literature overview for the given research subject.
2. Utilize novel experimental techniques and tools for rheological characterization of extremely low viscosity polypropylene samples, especially in uniaxial and planar extensional flows.
3. Describe obtained experimental data by an appropriate rheological model.
4. Determine basic morphological characteristics of nanofiber based polypropylene nonwovens produced by the melt blown technology.
5. Evaluate the relationship between the flow behaviour of tested polymer samples, processing conditions and final nanofiber based nonwoven product properties.

Rozsah diplomové práce:

Rozsah příloh:

Forma zpracování diplomové práce: **tištěná/elektronická**

Seznam odborné literatury:

1. Macosko, CH.W.: Rheology: Principles, measurements and applications. New York, 1994.
2. Ugbolue, S.C.O: Polyolefin fibres: Industrial and medical applications. New York, 2009.
3. Chapman, R.A.: Applications of nonwovens in technical textiles. NewYork, 2010
4. Sambaer, W., Zatloukal, M., Kimmer, D.: The use of novel digital image analysis technique and rheological tools to characterize nanofiber nonwovens. Polymer Testing, 29 (1), 82–94 (2010).
5. Zatloukal, M.: Novel non-Newtonian fluid model for polymer melts. Annual Technical Conference – ANTEC, Conference Proceedings, 1, 92–96 (2011).
6. Sambaer, W., Zatloukal, M., Kimmer, D.: 3D air filtration modeling for nanofiber based filters in the ultrafine particle size range. Chemical Engineering Science, 82, 299–311 (2012).
7. Zatloukal, M.: Measurement and modeling of planar and uniaxial extensional viscosities for LDPE polymer melt. Annual Technical Conference – ANTEC, Conference Proceedings, 1, 66–70 (2012).

Vedoucí diplomové práce: **prof. Ing. Martin Zatloukal, Ph.D.**
Centrum polymerních materiálů

Datum zadání diplomové práce: **8. února 2013**

Termín odevzdání diplomové práce: **10. května 2013**

Ve Zlíně dne 11. února 2013

L.S.

doc. Ing. Roman Čermák, Ph.D.
děkan

prof. Ing. Berenika Hausnerová, Ph.D.
ředitel ústavu

Příjmení a jméno: Jiří Drábek Obor: Konstrukce technologických zařízení

PROHLÁŠENÍ

Prohlašuji, že

- beru na vědomí, že odevzdáním diplomové/bakalářské práce souhlasím se zveřejněním své práce podle zákona č. 111/1998 Sb. o vysokých školách a o změně a doplnění dalších zákonů (zákon o vysokých školách), ve znění pozdějších právních předpisů, bez ohledu na výsledek obhajoby [1)];
- beru na vědomí, že diplomová/bakalářská práce bude uložena v elektronické podobě v univerzitním informačním systému dostupná k nahlédnutí, že jeden výtisk diplomové/bakalářské práce bude uložen na příslušném ústavu Fakulty technologické UTB ve Zlíně a jeden výtisk bude uložen u vedoucího práce;
- byl/a jsem seznámen/a s tím, že na moji diplomovou/bakalářskou práci se plně vztahuje zákon č. 121/2000 Sb. o právu autorském, o právech souvisejících s právem autorským a o změně některých zákonů (autorský zákon) ve znění pozdějších právních předpisů, zejm. § 35 odst. 3 [2)];
- beru na vědomí, že podle § 60 [3)] odst. 1 autorského zákona má UTB ve Zlíně právo na uzavření licenční smlouvy o užití školního díla v rozsahu § 12 odst. 4 autorského zákona;
- beru na vědomí, že podle § 60 [3)] odst. 2 a 3 mohu užít své dílo – diplomovou/bakalářskou práci nebo poskytnout licenci k jejímu využití jen s předchozím písemným souhlasem Univerzity Tomáše Bati ve Zlíně, která je oprávněna v takovém případě ode mne požadovat přiměřený příspěvek na úhradu nákladů, které byly Univerzitou Tomáše Bati ve Zlíně na vytvoření díla vynaloženy (až do jejich skutečné výše);
- beru na vědomí, že pokud bylo k vypracování diplomové/bakalářské práce využito softwaru poskytnutého Univerzitou Tomáše Bati ve Zlíně nebo jinými subjekty pouze ke studijním a výzkumným účelům (tedy pouze k nekomerčnímu využití), nelze výsledky diplomové/bakalářské práce využít ke komerčním účelům;
- beru na vědomí, že pokud je výstupem diplomové/bakalářské práce jakýkoliv softwarový produkt, považují se za součást práce rovněž i zdrojové kódy, popř. soubory, ze kterých se projekt skládá. Neodevzdání této součásti může být důvodem k neobhájení práce.

Ve Zlíně 8.5.2013 .....

[1)] *zákon č. 111/1998 Sb. o vysokých školách a o změně a doplnění dalších zákonů (zákon o vysokých školách), ve znění pozdějších právních předpisů, § 47 Zveřejňování závěrečných prací:*
(1) Vysoká škola nevýdělečně zveřejňuje disertační, diplomové, bakalářské a rigorózní práce, u kterých proběhla obhajoba, včetně posudků oponentů a výsledku obhajoby prostřednictvím databáze kvalifikačních prací, kterou spravuje. Způsob zveřejnění stanoví vnitřní předpis vysoké školy.

(2) Disertační, diplomové, bakalářské a rigorózní práce odevzdané uchazečem k obhajobě musí být též nejméně pět pracovních dnů před konáním obhajoby zveřejněny k nahlížení veřejnosti v místě určeném vnitřním předpisem vysoké školy nebo není-li tak určeno, v místě pracoviště vysoké školy, kde se má konat obhajoba práce. Každý si může ze zveřejněné práce pořizovat na své náklady výpisy, opisy nebo rozmnoženiny.

(3) Platí, že odevzdáním práce autor souhlasí se zveřejněním své práce podle tohoto zákona, bez ohledu na výsledek obhajoby.

[2)] zákon č. 121/2000 Sb. o právu autorském, o právech souvisejících s právem autorským a o změně některých zákonů (autorský zákon) ve znění pozdějších právních předpisů, § 35 odst. 3:

(3) Do práva autorského také nezasahuje škola nebo školské či vzdělávací zařízení, užije-li nikoli za účelem přímého nebo nepřímého hospodářského nebo obchodního prospěchu k výuce nebo k vlastní potřebě dílo vytvořené žákem nebo studentem ke splnění školních nebo studijních povinností vyplývajících z jeho právního vztahu ke škole nebo školskému či vzdělávacího zařízení (školní dílo).

[3)] zákon č. 121/2000 Sb. o právu autorském, o právech souvisejících s právem autorským a o změně některých zákonů (autorský zákon) ve znění pozdějších právních předpisů, § 60 Školní dílo:

(1) Škola nebo školské či vzdělávací zařízení mají za obvyklých podmínek právo na uzavření licenční smlouvy o užití školního díla (§ 35 odst. 3). Odpírá-li autor takového díla udělit svolení bez vážného důvodu, mohou se tyto osoby domáhat nahrazení chybějícího projevu jeho vůle u soudu. Ustanovení § 35 odst. 3 zůstává nedotčeno.

(2) Není-li sjednáno jinak, může autor školního díla své dílo užít či poskytnout jinému licenci, není-li to v rozporu s oprávněnými zájmy školy nebo školského či vzdělávacího zařízení.

(3) Škola nebo školské či vzdělávací zařízení jsou oprávněny požadovat, aby jim autor školního díla z výdělku jím dosaženého v souvislosti s užitím díla či poskytnutím licence podle odstavce 2 přiměřeně přispěl na úhradu nákladů, které na vytvoření díla vynaložily, a to podle okolností až do jejich skutečné výše; přitom se přihlédne k výši výdělku dosaženého školou nebo školským či vzdělávacím zařízením z užití školního díla podle odstavce 1.

ABSTRAKT

Optimalizace produkce polymerních nanovláken pomocí technologie meltblown je velmi obtížná díky tomu, že vztah mezi reologickým chováním polymerních tavenin, designem zpracovatelského zařízení, procesními podmínkami a konečnými vlastnostmi finálního produktu není dosud plně pochopen, a to především z důvodu extrémně nízkých viskozit používaných polymerních systémů, které není možné charakterizovat standardními reologickými metodami. Hlavním cílem této práce je provedení reologické charakterizace různých typů nízkoviskózních polymerních systémů ve smykovém a elongačním toku pomocí nových reologických metod za účelem detailního porozumění produkce polymerních nanovláken pomocí technologie melt blown.

Klíčová slova: polymerní nanovlákna, smyková a elongační reologie, polypropylen, meltblown technologie

ABSTRACT

Optimization of polymeric nanofibers production by the meltblown technology is highly complicated task due to the fact that relationship between polymer rheology, equipment design, processing conditions and final product properties is not fully understood yet mainly due to extremely low viscosity of the utilized polymer systems for which the standard rheological methodologies are not applicable. In order to overcome this difficulty, the main aim of this work is utilization of novel rheological techniques and tools for rheological characterization of low viscosity polymer samples in shear and extensional flows to understand polymeric nanofibers production in more detail.

Keywords:

polymeric nanofibers, shear and elongational rheology, polypropylene, meltblown technology

ACKNOWLEDGEMENTS

I would like to express my sincere gratitude to all people who supported me during the work on the thesis.

I am especially grateful to my supervisor, prof. Ing. Martin Zatloukal, Ph.D. for his patience, guidance and support throughout the process of measuring and analyzing data and writing the thesis.

Many thanks go to Joachim Fiebig for his support during measurements on the meltblown pilot plant line during my research visit in BOREALIS company, Linz, Austria.

Finally, I would like to extend my gratitude to my family and all my true friends for their support.

I declare that surrender release Master Thesis and recorded in the electronic version of IS/STAG are identical.

I agree that the results of my Master Thesis can be used by my supervisor's decision. I will be mentioned as a co-author in the case of any publication.

I declare I worked on this Master Thesis by myself and I have mentioned all the used literature.

Zlín, May 8, 2013

_ _ _ _ _ _ _ _ _ _ _ _ _

Jiří Drábek

CONTENTS

INTRODUCTION

Polymeric nanofibers offer a smaller average pore size enhancing their performance in filtration applications, wound dressing, and tissue scaffolding [1]. Additionally, reducing the fiber diameter increases the surface area per unit volume, which can be used in high efficiency filters with super oleophobic/hydrophobic surfaces, immobilized catalysts, and tissue scaffolds and wound dressings in biomedical engineering [2, 3]. Even if the polymeric nanofibers can be manufactured using melt blowing, melt spinning, or electrospinning methods, the melt blowing is of particular interest because it does not require solvent which translates into a more economical process and higher production rate [4]. The key problem in meltblown production is the observation that if the fiber diameter decreases, the production becomes more unstable, which leads to broader fiber diameter distribution, which is unwanted. From the rheological point of view, the extensional viscosity, characterizing the resistance of the fluid against the stretching (i.e. planar extensional flow occurring in the corverging/diverging channels of the flat extrusion die and uniaxial extensional flow occurring between the flat extrusion die and collector unit), should be considered as the key rheological parameter, which play a crucial role in meltblown process and it is very sensitive to the molecular structure of the fluids. However, due to the fact that generation and control of the extensional flow is difficult, experimental determination of the extensional viscosity is a problem.

In order to understand the role of polymer melt rheology on the meltblown polymeric nanofibers production, the work is focused on rheological characterization of carefully selected polypropylene homopolymers and polypropylene blends by advanced experimental techniques in shear and elongational flows. In the second part of this work, selected polypropylene based polymers are used to produce polymeric nanofiber based nonwovens on the meltblown pilot plant line at different processing conditions with the aim to understand the relationship between polymer melt rheology, processing conditions and final characteristics of the produced nonwovens such as air permeability, average fiber diameter and coefficient of variation for average fiber diameter.

I. THEORY

1 SHEAR AND EXTENSIONAL FLOWS

In this chapter, basic flow types occurring during melt-blown process are introduced.

1.1 Simple shear flow

Shear flow is the most common type of flow discussed in rheology. Figure 1. shows a two-dimensional schematic of the velocity profile in simple shear flow. In this flow, layers of fluid slide past each other and do not mix. The flow rectilinear, and the velocity only varies in one direction, the direction x_2 in this diagram. Particle path lines in simple shear flow are straight parallel lines. Simple shear flow can be produced by sandwiching material between two parallel plates and then causing one plate to move at a constant velocity in some unchanging direction. For many practical rheometers, this flow is only achieved approximately in the limit of narrow gaps, small angles, and relatively slow flows. In processing equipment shear flow occurs near walls [5].

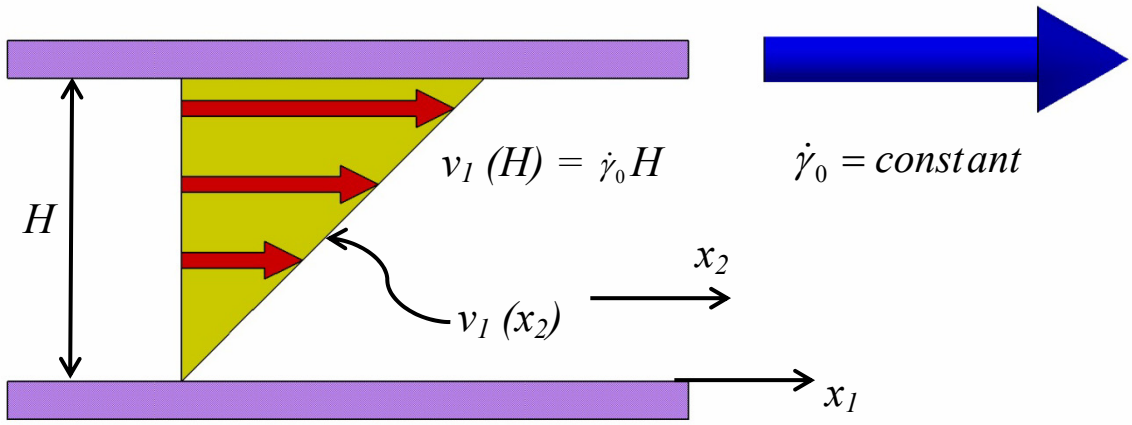

Fig. 1. Flow field in simple shear, velocity profile [5].

Definition of shear flow:

$$\underline{v} = \begin{pmatrix} v_1 \\ v_2 \\ v_3 \end{pmatrix}_{123} = \begin{pmatrix} \dot{\varsigma}(t)x_2 \\ 0 \\ 0 \end{pmatrix}_{123} \tag{1}$$

Shear flow may be produced in many ways, and it is standard practice to call the flow direction of shear flow in Cartesian coordinates the 1-direction, with the 2-direction reserved for the direction in which the velocity changes (the gradient direction), and the 3-direction called the neutral direction, since flow neither occurs in this direction nor changes in this direction. The function $\dot{\varsigma}(t)$, which equals the derivate $\partial v_1 / \partial x_2$, is often denoted by the symbol $\dot{\gamma}_{21}(t)$ because it is equal to the 21-component of the shear-rate tensor $\underline{\underline{\dot{\gamma}}}$ for this flow. The magnitude of $\underline{\underline{\dot{\gamma}}}$ for shear flow is called the shear rate or rate of strain and is denoted by the symbol $\dot{\gamma}(t)$.

1.1.1 Steady shear

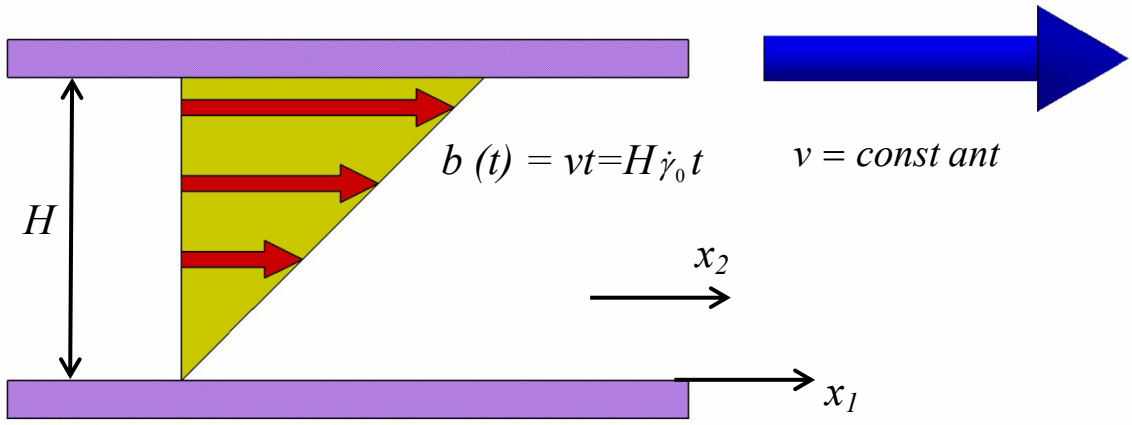

Fig. 2. Flow field in steady shear, velocity profile [5].

For steady shear flow, $\dot{\varsigma}(t) = \dot{\gamma}_0$ is a constant, that is, the flow is at steady state:

Kinematics for steady shear:

$$\dot{\varsigma}(t) = \dot{\gamma}_0 \tag{2}$$

This flow is typically produced in a rheometer where the fluid is forced through a capillary at a constant rate (see Fig. 2), and the steady pressure required to maintain the flow is measured. Another common method is to use a cone-and-plane or parallel-plate geometry an to rotate the cone or plane at a constant angular velocity while measuring the torque generated by the fluid being tested.

For the case of steady–state flow, the stress tensor is constant in time, and three constant stress quantities are measured τ_{21}, N_1, and N_2. There are three material functions that are defined with these three stress quantities:

Viscosity:

$$\eta(\dot{\gamma}) \equiv \frac{\tau_{21}}{\dot{\gamma}_0} \tag{3}$$

First normal-stress coefficient:

$$\Psi_1(\dot{\gamma}) \equiv \frac{N_1}{\dot{\gamma}_0^2} = \frac{\tau_{11} - \tau_{22}}{\dot{\gamma}_0^2} \tag{4}$$

Second normal-stress coefficient:

$$\Psi_2(\dot{\gamma}) \equiv \frac{N_2}{\dot{\gamma}_0^2} = \frac{\tau_{22} - \tau_{33}}{\dot{\gamma}_0^2} \tag{5}$$

The material functions Ψ_1 and Ψ_2 are also functions of $\dot{\gamma}$ in general, both functions are zero for Newtonian fluids. For most polymers Ψ_1 is positive, and Ψ_2 is small and negative ($\Psi_2 \approx -0.1\Psi_1$) [5].

1.1.2 Small-amplitude oscillatory shear

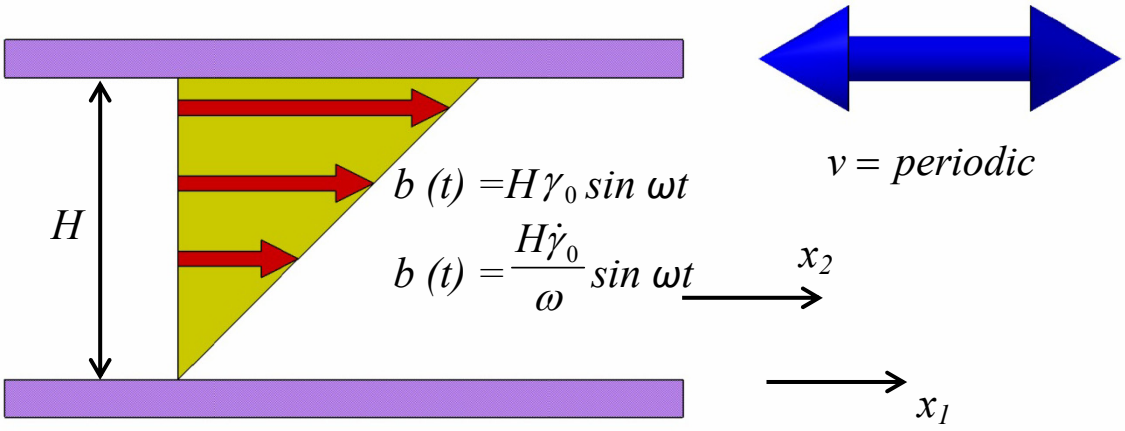

Fig. 3. Schematic of how small-amplitude oscillatory shear is produced [5].

The final set of unsteady shear material functions that I would like to introduce are very widely used to characterize complex fluids by chemists, chemical engineers, and materials

scientists. The flow is again shear flow, and the time-dependent shear-rate function $\dot{\varsigma}(t)$ used for this flow is periodic (a cosine function). This flow is called small-amplitude oscillatory shear (SAOS) (see Figure 3):

Kinematics for SAOS:

$$\dot{\varsigma}(t) = \dot{\gamma}_0 \cos \omega t \tag{6}$$

The frequency of the cosine function is ω (rad/s), and $\dot{\gamma}_0$ is the constant amplitude of the shear-rate function.

It serves as a definition of the elastic modulus *G* and describes the stress of a limited class of solids that are called elastic. For elastic materials the stress generate is directly proportional to the strain, that is, to the deformation. This is similar to the response of mechanical springs, which generate stress that is directly proportional to the change in length (deformation) of the spring. Thus the SAOS experiment is ideal for probing viscoelastic materials, defined as materials that show both viscous and elastic properties.

The material functions for SAOS are the storage modulus $G'(\omega)$ and the loss modulus $G''(\omega)$, and they are defined as follows:

SAOS material functions:

$$\frac{-\tau_{21}}{\gamma_0} = G' \sin \omega t + G'' \cos \omega t \tag{7}$$

Storage modulus:

$$G'(\omega) \equiv \frac{\tau_0}{\gamma_0} \cos \delta \tag{8}$$

Loss modulus:

$$G''(\omega) \equiv \frac{\tau_0}{\gamma_0} \sin \delta \tag{9}$$

Recall that:

$$\gamma_0 = \frac{\dot{\gamma}_0}{\omega} \tag{10}$$

G' is equal to the amplitude of the portion of the stress wave that is in phase with the strain wave divided by the amplitude of the strain wave. G'' is defined analogously as the amplitude of the portion of the stress wave that is out of phase with the strain wave, divided by the amplitude of the strain wave [5].

Tab. 1. Definitions of material functions for small-amplitude oscillatory shear (SAOS) in terms of storage modulus G' and loss modulus G'' [5].

Name	***Equation***
Complex modulus magnitude	$\left\|G^*\right\| = \sqrt{G'^2 + G''^2}$
Loss tangent	$\tan\delta = \frac{G''}{G'}$
Dynamic viscosity	$\eta' = \frac{G''}{\omega}$
Out-of-phase component of η^*	$\eta'' = \frac{G'}{\omega}$
Complex viscosity magnitude	$\left\|\eta^*\right\| = \sqrt{\eta'^2 + \eta''^2}$
Complex compliance magnitude	$\left\|J^*\right\| = \frac{1}{\left\|G^*\right\|}$
Storage compliance	$J' = \frac{1/G'}{1+\tan^2\delta}$
Loss compliance	$J'' = \frac{1/G''}{1+\left(\tan^2\delta\right)^{-1}}$

The meaning of the symbols provided in Table 1) is following: G^* is the complex modulus, G' is the storage modulus, G'' is the loss modulus, $\tan\delta$ is the loss tangent, η' is the real part of complex dynamic viscosity, η'' is the imaginary part of complex dynamic viscosity, ω is the frequency of oscillation, η^* is the complex dynamic viscosity, J^* is the complex compliance, J' is the storage compliance and J'' is the loss compliance.

1.2 Elongation flow

The study of the elongation or extensional flow of polymeric fluids has been the subject of intense research since the early 1960s. This, no doubt, is due to the fact that several industrially important polymer processing operations, such as fibre spinning, blow moulding, flat film extrusion and film blowing, involve a predominantly extensional mode of deformation. This flow field is also highly effective in orienting polymer molecules in flow direction, and the high deformation rates which typically occur in industrial operations, albeit for a short duration, produce unusually large fluid stress, the accurate, theoretical prediction of these stresses is not yet completely resolved, and it remains an intellectual challenge to rheologists [6].

$$\underline{v} = \begin{pmatrix} -\frac{1}{2}\dot{\varepsilon}(t)(1+b)x_1 \\ -\frac{1}{2}\dot{\varepsilon}(t)(1+b)x_2 \\ \dot{\varepsilon}(t)x_3 \end{pmatrix} \tag{11}$$

Differences among the flows are achieved by varying the function $\dot{\varepsilon}(t)$ and the parameter b.

1.2.1 Steady elongation flow

Steady-state elongation flows [uniaxial, biaxial, planar] are produced by choosing the following kinematics:

Kinematics of steady elongation:

$$\dot{\varepsilon}(t) = \dot{\varepsilon}_0 = constant \tag{12}$$

For these flows, constant stress differences are measured. The material functions defined are two elongation viscosities based on the measured normal-stress differences. For both uniaxial and biaxial extension, the elongation viscosity based on $\tau_{22} - \tau_{11}$ is zero for all fluids, planar elongation flow has two nonzero elongation viscosities.

Uniaxial elongation flow:

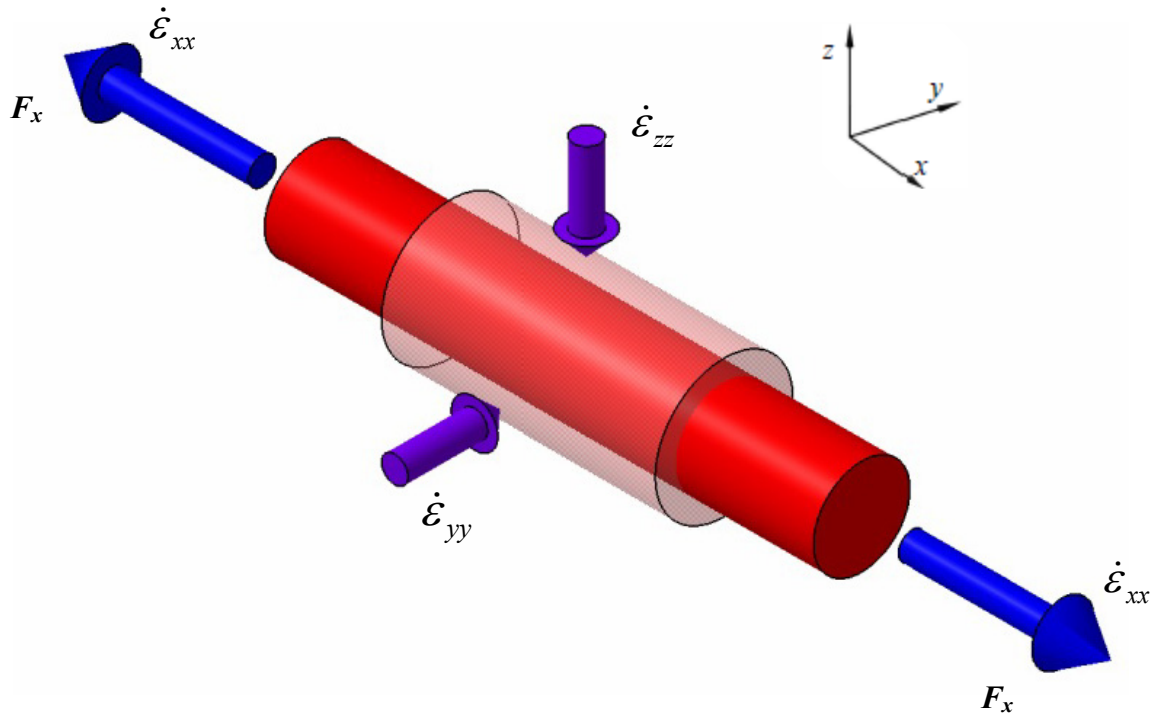

Fig. 4. Uniaxial elongation flow [7].

Near the centerline of the flow in fiber spinning for example, fluid particles are stretched uniformly. The idealized version of this stretching flow is called uniaxial extensional flow or uniaxial elongation flow (see Fig. 4) and is defined by the following equations.

Uniaxial elongation (b=0, $\dot{\varepsilon}_0 > 0$):

$$\underline{v} = \begin{pmatrix} -\frac{1}{2}\dot{\varepsilon}_0 x_1 \\ -\frac{1}{2}\dot{\varepsilon}_0 x_2 \\ \dot{\varepsilon}_0 x_3 \end{pmatrix}_{123} \tag{13}$$

Uniaxial elongation viscosity:

$$\eta_{E,U}(\dot{\varepsilon}_0) \equiv \frac{\tau_{33} - \tau_{11}}{\dot{\varepsilon}_0} \tag{14}$$

Trouton ratio

$$\eta_{E,U} = 3\eta_0 \tag{15}$$

The function $\dot{\varepsilon}_0$ is called the elongation rate, and for uniaxial elongation flow is positive. The flow pattern that this velocity profile describes is three-dimensional, with a strong stretch occurring in the x_3-direction and contraction occurring equally in x_1-and x_2-directions (see Fig. 5).

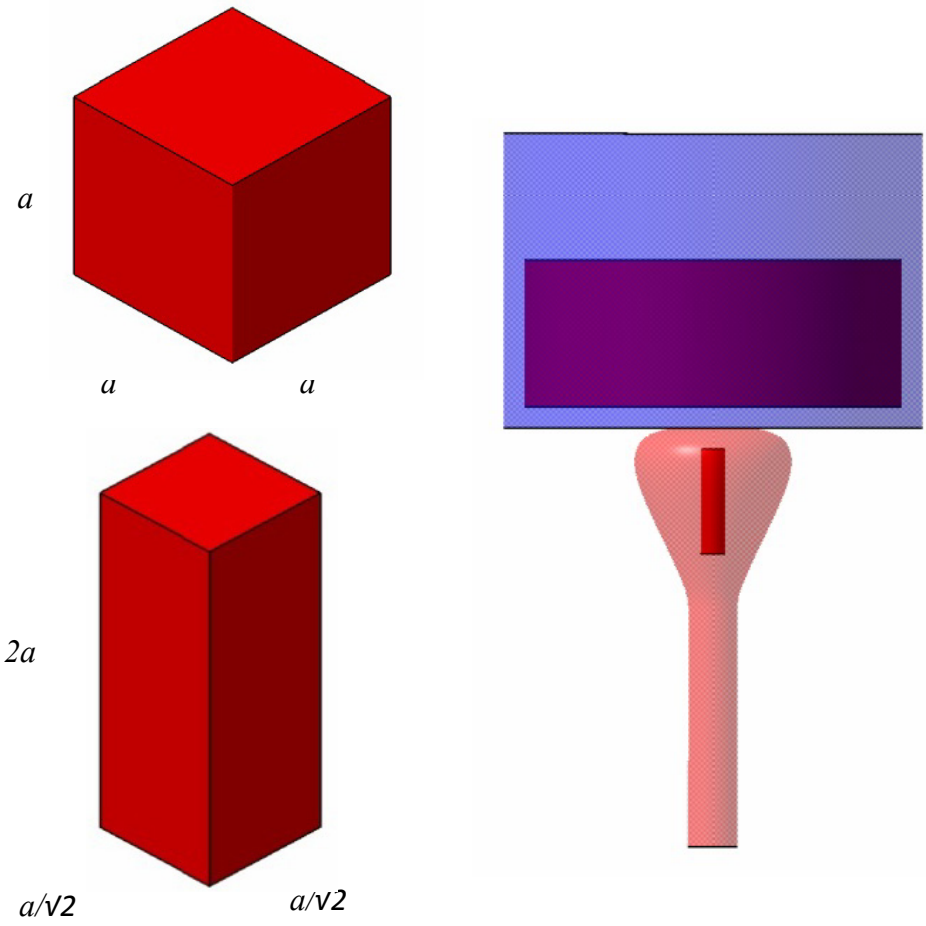

Fig. 5. Schematic of the deformation (shape change) produced by uniaxial elongation flow [5].

Biaxial elongation flow:

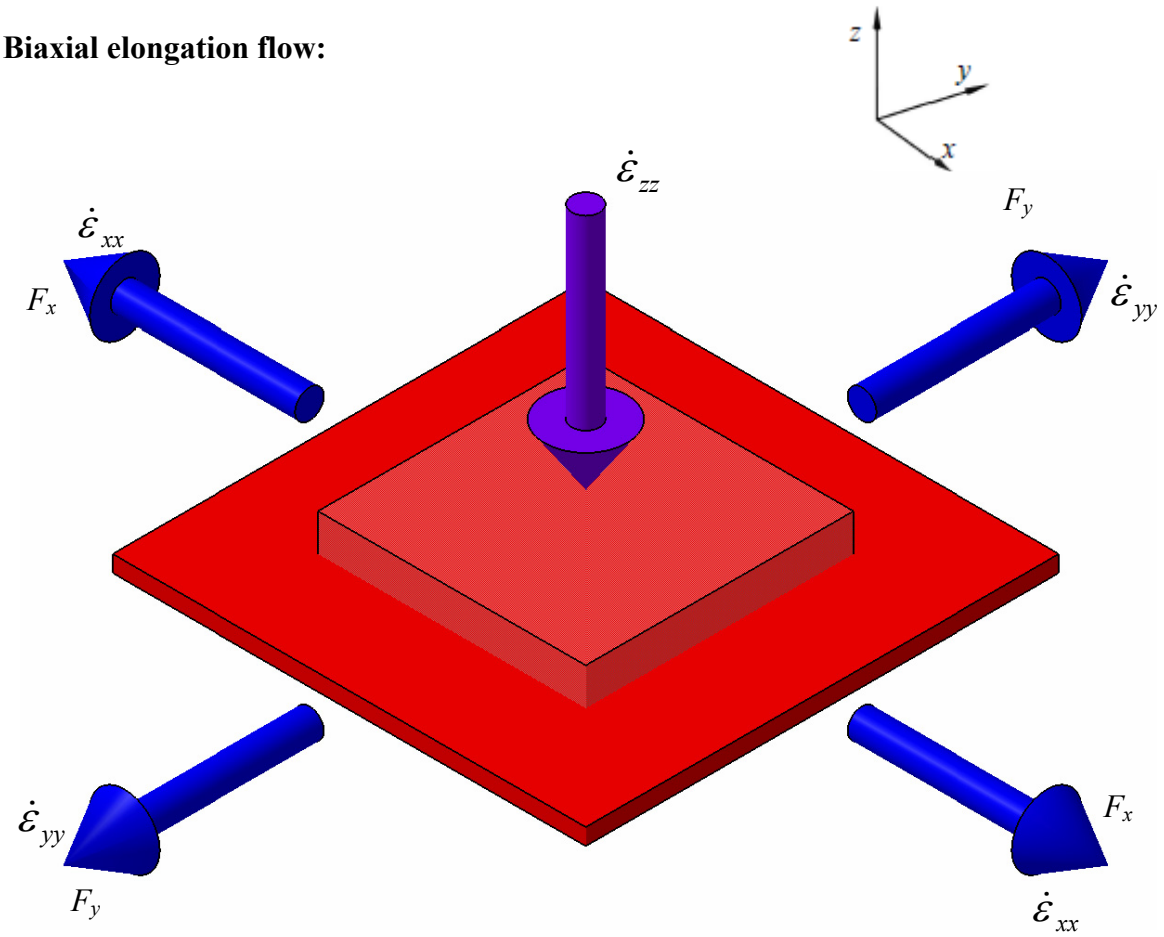

Fig. 6. Biaxial elongation flow[7].

The second type of shear-free flow that we study is biaxial stretching. This flow has the same form of velocity profile as uniaxial elongation flow, but $\dot{\varepsilon}_0$ is always negative for this flow. In biaxial stretching (or biaxial extension) the flow is considered to occur in the 1- and 2-directions at the same rates, while contraction occurs in the 3-direction (see Fig. 6).

Biaxial elongation (b=0, $\dot{\varepsilon}_0 < 0$):

$$\underline{v} = \begin{pmatrix} -\frac{1}{2}\dot{\varepsilon}_0 x_1 \\ -\frac{1}{2}\dot{\varepsilon}_0 x_2 \\ \dot{\varepsilon}_0 x_3 \end{pmatrix}_{123} \tag{16}$$

Biaxial elongation viscosity:

$$\eta_{E,B}\left(\dot{\varepsilon}_0\right) \equiv \frac{\tau_{33} - \tau_{11}}{\dot{\varepsilon}_0} \tag{17}$$

Trouton ratio:

$$\eta_{E,B} = 6\eta_0 \tag{18}$$

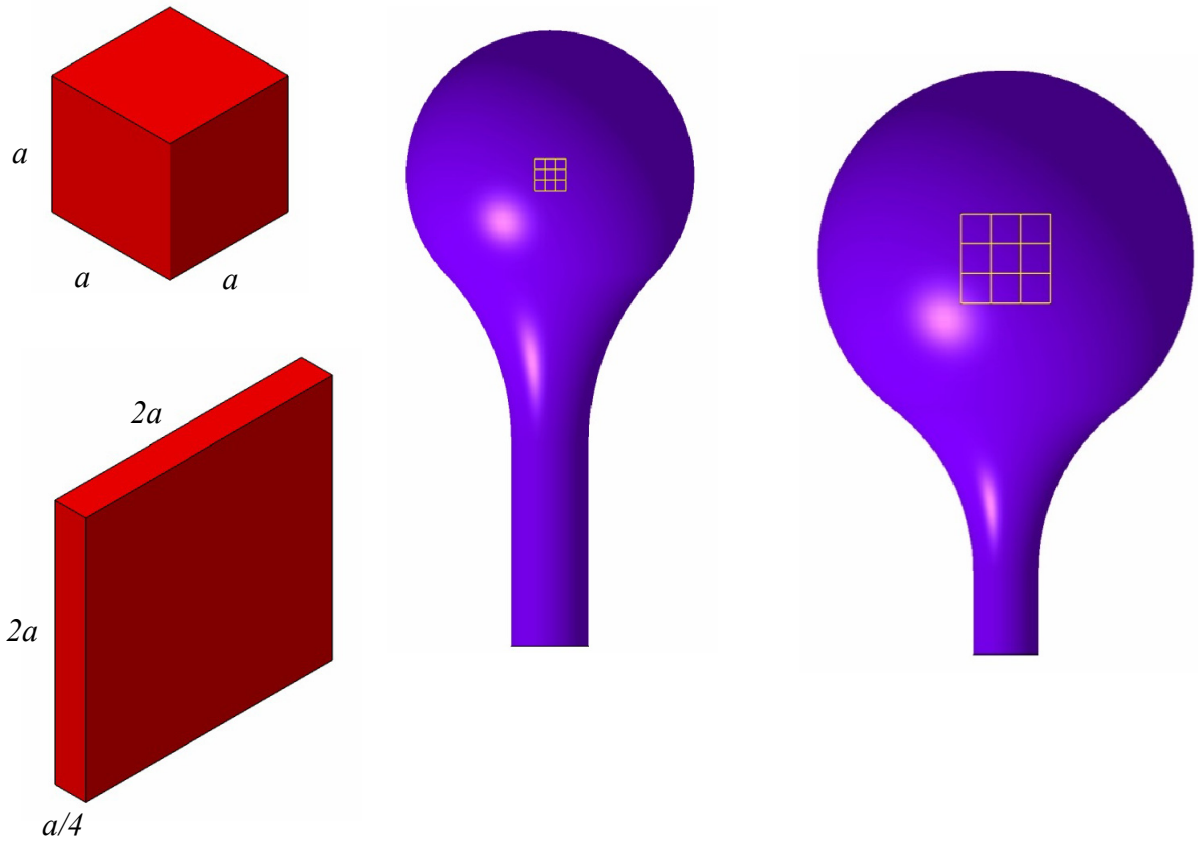

Fig. 7. Schematic of the deformation (shape change) produced by biaxial elongation flow [5].

Planar elongation flow:

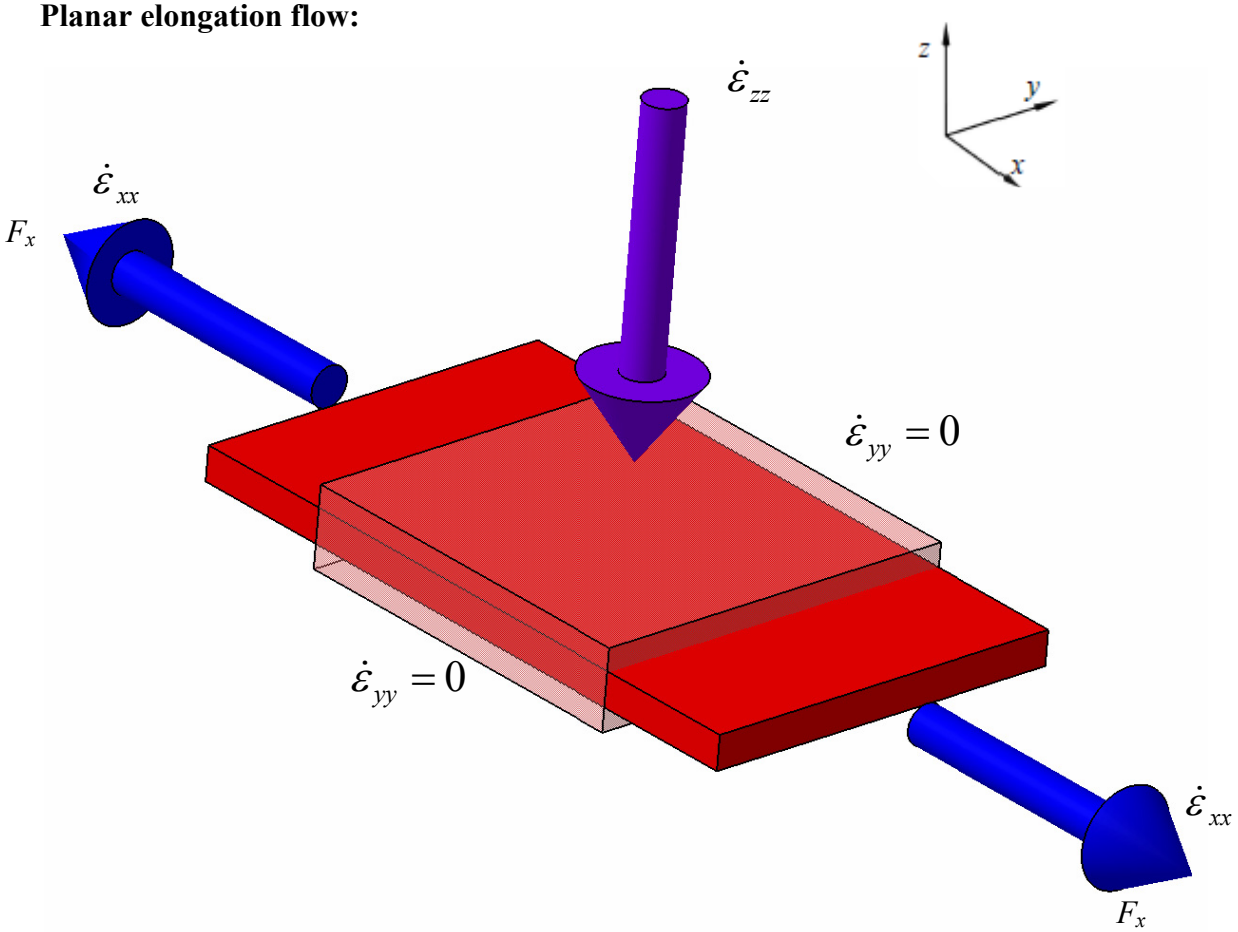

Fig. 8. Planar elongation flow[7].

The final type of shear-free flow discussed here is planar elongation flow (see Fig. 8), defined by following velocity profile:

Planar elongation (b=1, $\dot{\varepsilon}_0 > 0$):

$$\underline{v} = \begin{pmatrix} -\dot{\varepsilon}_0 x_1 \\ 0 \\ \dot{\varepsilon}_0 x_3 \end{pmatrix}_{123} \tag{19}$$

First planar elongation viscosity:

$$\eta_{E,P1}(\dot{\varepsilon}_0) \equiv \frac{\tau_{33} - \tau_{11}}{\dot{\varepsilon}_0} = \eta_{E,P}(\dot{\varepsilon}_0) \tag{20}$$

Second planar elongation viscosity:

$$\eta_{E,P2}(\dot{\varepsilon}_0) \equiv \frac{\tau_{22} - \tau_{11}}{\dot{\varepsilon}_0} \tag{21}$$

Trouton ratio:

$$\eta_{E,P} = 4\eta_0 \tag{22}$$

In planar elongation flow, no deformation is allowed in the 2-direction ($v_2 = 0$). The deformation experienced by a cube of incompressible fluid in planar elongation is shown in Figure 9. If the side of the cube is stretched to twice its length in the flow direction (3-direction), then the cube must contract by a factor of 2 along the 1-direction to satisfy conservation of mass.

All three shear flow mentioned, along with many others, can be described by a single expression for the velocity profile. The different flows are produced by different values for the two parameters $\dot{\varepsilon}_0$ and b.

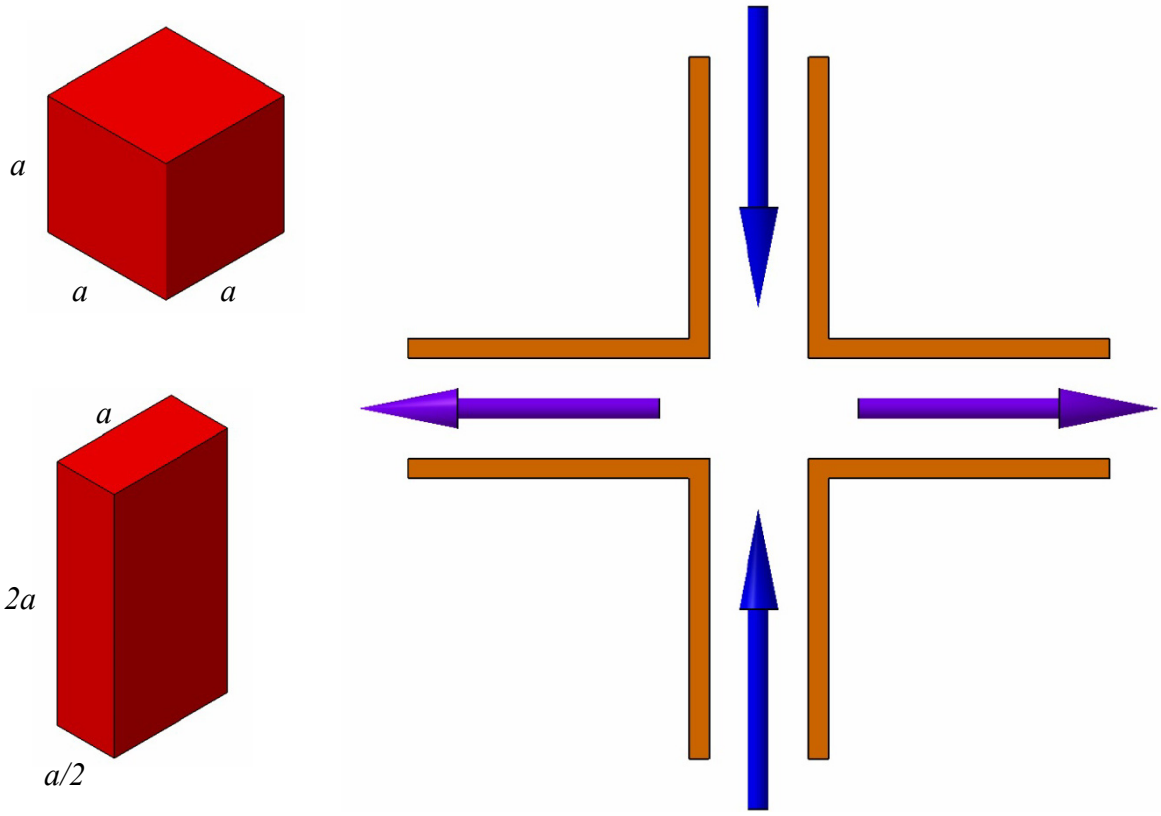

Fig. 9. Schematic of the deformation (shape change) produced by planar elongation flow [5].

In the Cartesian coordinate system these shear-free flows can be written as follows:

Tab. 2. Summary of parameters definition for standard shear-free flows [5].

Type of flow	***Parameters***
Uniaxial elongation flow	$b = 0,\ \dot{\varepsilon}(t) > 0$
Biaxial stretching flow	$b = 0,\ \dot{\varepsilon}(t) < 0$
Planar elongation flow	$b = 1,\ \dot{\varepsilon}(t) > 0$

For the flows we have discussed, the values and ranges of the parameters $\dot{\varepsilon}(t)$ and b are listed in (Tab. 2). The parameter b in velocity profile affects the way that the streamlines of the flow change with rotations around the flow direction. Zero-shear viscosity (Newtonian-shear viscosity) η_0 [5]. Summarization of basic rheological characteristics at yero deformation rates for all considered elongational flows type sis provided in Table 3.

Tab. 3. Summarization of the Viscosity and modulus at zero deformation rate for different elongational flow types[8].

Flow	***Viscosity***	***Modulus***
simple shear	η	G
uniaxial extension	3η	3G
planar extension	4η	4G
Biaxial extension	6η	6G

2 RHEOMETRY

Tab. 4. Classes of rheometer for melts in common use [8].

Classification	*Method*	*Variables*	*Output*	*Limitations*
ROTATIONAL METHODS	Eccentric rotating disc and "balance" rheometer Oscillatory cone and plane	Strain amplitude and frequency	Dynamic shear viscosity and elasticity PRECISE DATA	Near to linear response Strain <1.0
	Steady-flow cone and plane Concentric cylinders	Strain Strain rate Strain recovery Stress Stress growth Stress relaxation Time	Viscosity and elasticity Normal stress PRECISE DATA	Low stress level $<10^4$ Pa
	Torsion	As above	Apparent shear viscosity	High viscosity $>10^8$ Pa.s
SQUEEZING	Penetrometer Parallel plate	Complex history	Apparent shear viscosity	Usually only used for viscosity $>10^5$ Pa.s
EXTRUSION	Melt flow rate		Comparative fluidity (kinematic)	Single point determination
	Capillary flow	Flow rate Pressure	Apparent viscosity and elasticity in shear	Stress level 10^4-10^6 Pa Viscosity $<10^6$ Pa.s
	Converging flow	Swell ratio Extrudate appearance	Apparent extensional rheology COMPARATIVE ENGINEERING DATA	Interpretation APPARENT PROPERTIES
TORQUE	Instrument extruder "Brabender" type	Speed Packing force Charge volume	COMPARATIVE Resistance to flow gelation	Scaling Interpretation
FREE SURFACE FLOWS	Simple elongation	Stress Strain Strain rate Time	Extensional viscosity and elasticity PRECISE DATA	Handling difficulties Viscosity $>10^4$ Pa.s Strain rate <1 s^{-1}
	Extrudate drawing	Speed Tension	Drawing force Drawing stability Rupture COMPARATIVE	Interpretation
	Sheet inflation Bubble inflation		PRECISE DATA Biaxial extension COMPARATIVE	Handling difficulties

Basic rheometer types for polymer melts are provided in Table 4.

2.1 Shear rheometry

The first measurements of viscosity were done using a small straight tube or capillary. Hagen (1839) in Germany and independently Poiseuille (1840) in France used small diameter capillaries to measure the viscosity of water. A key development that made their work possible was the advent of precision diameter, small bore.

A capillary rheometer induces is a pressure-driven flow. As Hagen first observed, when pressure drives a fluid through a channel, velocity is maximum at the center (see Fig. 10). The velocity gradient or shear rate and also the strain will be maximum at the wall and zero in the center of the flow. Thus all pressure-driven flows are nonhomogeneous. This means that they are only used to measure steady shear functions: the viscosity and normal stress coefficients [9].

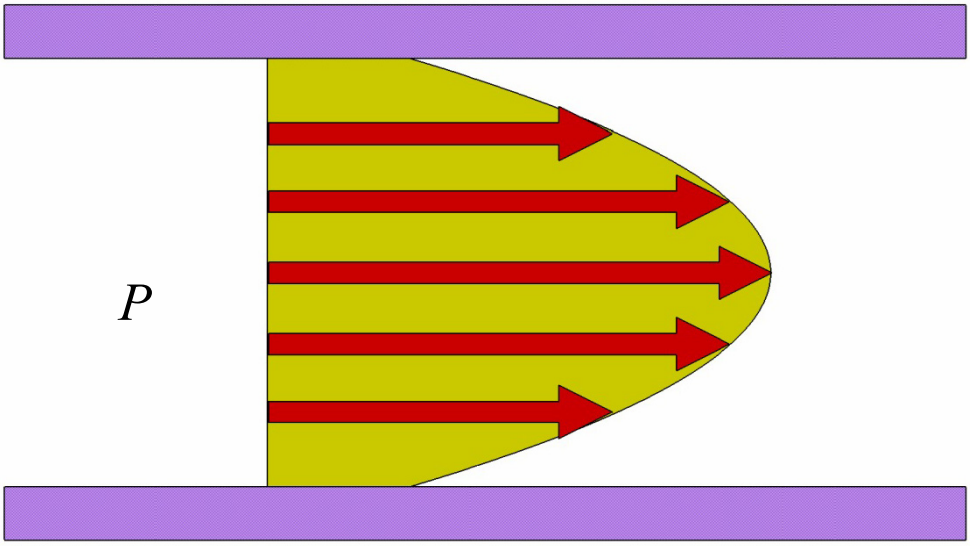

Fig. 10. Pressure driven flow [8].

2.1.1 Capillary rheometer

Capillary rheometry is concerned with the way fluid or ductile material flows into and within a capillary. In most circumstances the pressure difference along the capillary is measured as a function of material flow rate and certain rheological information is inferred from this data. The capillary rheometer can be thought of either as an apparatus for rheological characterization or alternatively as a well-defined processing geometry. Most extrusion processes such as plastic pipe manufacture, injection moulding, film blowing and many other shape-forming processes all incorporate the feature seen in capillary rheometry where the process material is forced into a flow constriction then flows within an essential-

ly uniform cross-section. The way the material emerges from the die can also be of great importance. A good understanding of capillary rheometry not only aids in understanding the problem in term rheometry, it also helps to explain extrusion in general [6].

2.1.1.1 Geometrical constrains and principle

The primary geometric parameters of a capillary rheometer (Fig. 11) are the ratio L_C / D_C of the capillary section, the entrance contraction ratio D_1 / D_C, and the entrance angle ϕ of the capillary. Typically we might expect D_C to vary from say 100 μm to 5 mm and L_C / D_C from 0 to 500. Entrance contractions D_1 / D_C vary from about 2 to 200 and the entrance angle is usually 90° but can vary between say 15° and 90°.

The mode of operation for capillary rheometers is also shown in (Fig. 11). The process fluid is usually forced through the capillary at a constant volumetric flow rate by using a piston that is advanced at a constant crosshead speed, the pressure difference is measured by an upstream pressure transducer. With the ´Rosand´capillary rheometer, two barrels are used so the entry pressure for a zero L_C / D_C die can be readily subtracted from the pressure difference over the second die, which has a finite L_C / D_C ratio, this leads to the extrusion pressure difference within the capillary section alone [6].

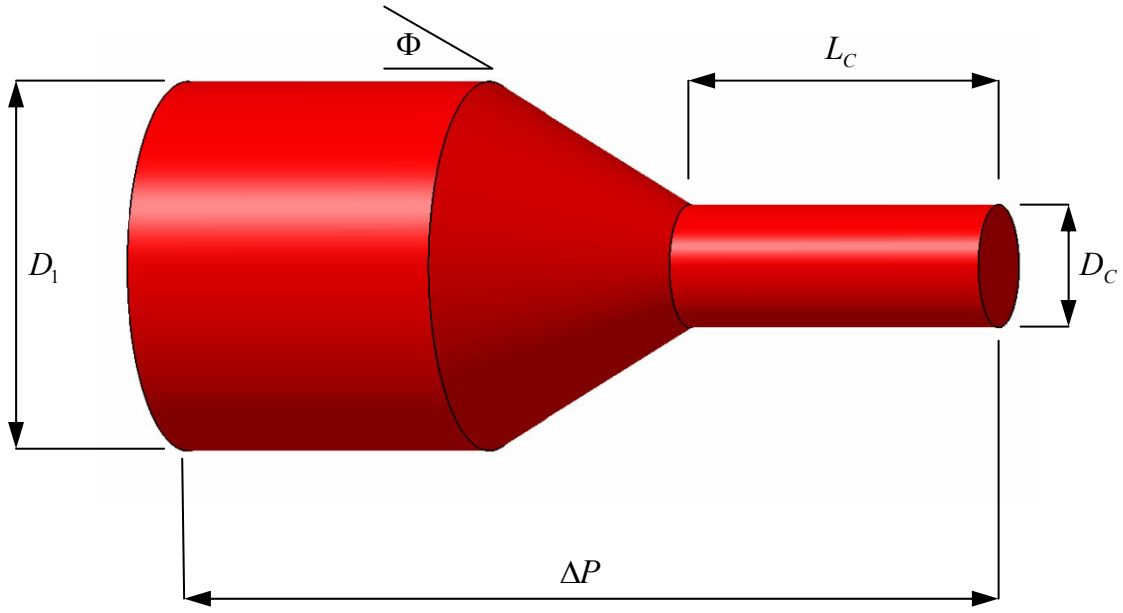

Fig. 11. Schematic diagram of capillary extrusion duct parameters [6].

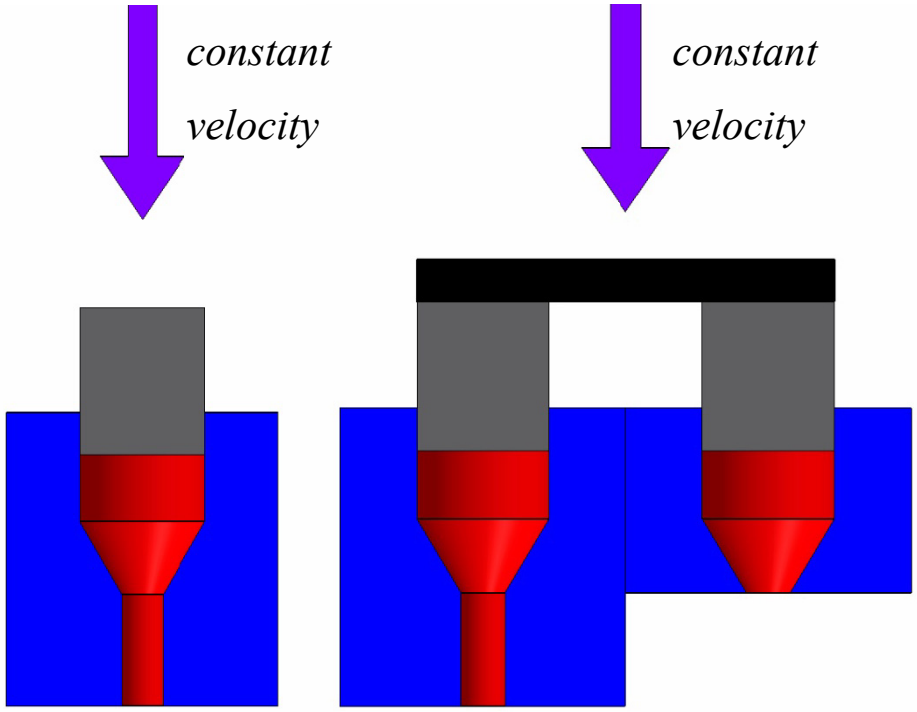

Fig. 12. Schematic diagram of capillary extrusion [6].

Tab. 5. Equations for basic rheological properties [8].

Shear flow	
apparent shear rate	$\dot{\gamma}_{APP} = \frac{4Q}{\pi R_C^3}$
corrected shear stress	$\tau_{xy} = \frac{(P_{LC} - P_{OC})R_C}{2L_{LC}}$
recoverable shear γ_R, from	$B_L^2 = \frac{2}{3}\gamma_R\left[\left(1+\frac{1}{\gamma_R^2}\right)^{3/2} - \frac{1}{\gamma_R^3}\right]$
shear viscosity	$\eta = \frac{\tau_{xy}}{\dot{\gamma}_{APP}}$
shear modulus	$G = \frac{\tau_{xy}}{\gamma_R}$
pseudoplasticity index n from	$\tau_{xy} \propto \dot{\gamma}^n$

Schematic diagram of capillary extrusion is provided in Figure 12 whereas Table 5-6 summarizes basic equations and errors/utility, respectively, utilized in the for capillary rheometry.

Extensional flow by Cogswell	
extensional stress	$\sigma_E = \frac{3}{8}(n+1)P_{OC}$
extensional viscosity	$\eta_E = \frac{9}{32}\frac{(n+1)^2}{\eta}\left(\frac{P_{OC}}{\dot{\gamma}}\right)^2$
recoverable extension	$\varepsilon_R = \ln B_O^2$
modulus in extension	$E = \frac{\sigma_E}{\varepsilon_R}$
rupture stress (at onset of non-laminar flow)	$\sigma_R = \frac{3}{8}(3n+1)P_{OC}$

Tab. 6. Errors and utility in capillary rheometry [9].

Errors	***Utility***
Wall slip with concentrated dispersions	Simples rheometer, yet most accurate for steady viscosity
Melt fracture at $\tau_c \sim 10^5\,Pa$	High $\dot{\gamma}$
Reservoir pressure drop	Sealed system: pressurize, prevent evaporation
Entrance pressure drop	Process simulator
Bagley plot	Quality control: melt index
Single die $L/D \cong 60$	Nonhomogeneous flow, only steady shear material functions
Kinetic energy for low η, high $\dot{\gamma}$	Entrance corrections entail more data collection
Viscous heating $Na \geq 1$	
Material compressibility	
Pressure dependence of viscosity	
Shear history, degradation in reservoir	

2.1.1.2 Correction

In reality, the measurements of viscosity require a number of corrections (see Tab. 7), which are intended to account for deviations of specific conditions of experiment from idealized requirements. Even in measurements of viscosity of Newtonian liquid, deviations from linearity of dependence of volumetric flow rate on imposed pressure can be observed. More detail description of the errors occurring in the capillary rheometry is provided in Table 8. These deviations are caused by factors, which lead to the introduction of corrections. Corrections are of general importance in the practice of capillary viscometry [10].

Tab. 7. Type of corrections [12].

Correction	***Methods***
Entrance and exit effects	The Couette-Hagenbach method [10, 11,12]
	The Bagley method [5-11, 13]
	The use of dies of zero land length [11]
	The end correction and scale-up [11]
Head effects	Metzner and Knox [11]
	Vignale [11]
	Cook [11]
Kinetic Energy effects	Pezzin [10-12]
	Hagenbach [10-12]
Non-parabolic velocity profile	Rabinowitch [8, 11]
Temperature correction	Tabor [8, 10]
Pressure correction	Mackley and Spitteler [8, 10]
Correction for slip near a wall	Mooney [5, 8, 9, 10, 11, 13]
Surface tension correction	Barr [10, 12]
Wall effects	Reiner [12]
Turbulence	Ryan and Johnson [12]

Tab. 8. Errors in capillary rheometry [12].

Factor	***Cause***	***Applicability***
Kinetic-energy losses	Loss effective pressure because of the kinetic energy in issuing stream.	General
End effects	Energy losses due to viscous or elastic behavior when a fluid converges or diverges at the ends of a capillary	General
Elastic energy	Energy loss by elastic deformation of the fluid not recovered during flow in the capillary.	Viscoelastic materials
Turbulence	Departure from laminar flow.	General
Pressure losses prior to the capillary	Sticking of the piston or energy dissipated in flow of the material within the cylinder before entering the capillary.	Cylinder-piston viscometers
Drainage	Liquid adhering to the wall of the viscometer reservoir.	Glass capillary viscometers
Surface-tension effects	Variations of surface tension from one test substance to another.	Glass capillary viscometers
Heat effects	Conversion of pressure energy into heat energy through flow.	High-shear viscometers
Wall effects	Surface phenomena at the fluid-wall interface.	Polyphase fluids (some Bingham bodies and other liquids)
Effect of time-dependent properties	Variations in the residence time in the capillary.	Thixotropic and rheopectic materials

Kinetic (Hagenbach) correction

Liquid being investigated typically enters a capillary from a large reservoir. Then, the flow velocity of the stream substantially accelerates as a result of change in cross-section, kinetic energy of flow increases.

If, the total measured pressure drop is P, then the part of this pressure, P_k, is spent on an increase of the kinetic energy of the stream, and only the remaining part, P_v, is responsible for overcoming resistance of flow through a capillary, for measured viscosity.

$$P_v = P - P_k \tag{23}$$

where the value of P_k is responsible for the kinetic correction.

P_k can be calculated

$$P_k = \frac{\rho Q^2}{\alpha \pi^2 R^4} \tag{24}$$

where ρ is density, Q volumetric flow rate, α coefficient reflecting and R radius.

The correction taking into account a change in the kinetic energy leads to the following expression for Newtonian viscosity.

$$\eta = \frac{\pi P R^4}{8QL} - \frac{\rho Q}{8\pi L \alpha} \tag{25}$$

If we accept the standard value, $\alpha = 1$, then the introduction of kinetic correction leads to the measurement error, which can reach even 10%. For non-Newtonian liquids, it is difficult to determine the value of α a priority, but it is also of the order of 1.

The calculation of kinetic correction is important during measurements of viscosity of low-viscosity liquids, for example, dilute polymer solutions, where a high accuracy of measurements is required [10].

Entrance (Bagley) correction

This correction combines different dynamic phenomena at the entrance to a capillary as a result of rearrangement of the inlet velocity profile.

If we neglect the entrance corrections of different origin, then the results of measurements become dependent on the length of the capillary, due to the fact that the relative contribution of transient phenomena becomes greater when a shorter capillary is utilized for measurements [10]

$$\Delta p_{cap} = \Delta p - \Delta p_{end} \tag{26}$$

The velocity profile in the die (Rabinowitsch) correction

A correction is frequently made to take into account the fact that the pseudoplastic nature of the melt means that the assumed parabolic velocity profile in the die is actually more plug-like. This correction, usually attributed to Rabinowitsch, is simply expressed in the form:

$$\dot{\gamma} = \left(\frac{3n+1}{4n} \right) \frac{4Q}{\pi R_C^3} \tag{27}$$

where n is the power in the relationship shear stress proportional to (shear rate)^n at a given shear rate and n can be obtained from the following expression [8]:

$$n = \frac{d\left(\log \tau_{xy}\right)}{d\left(\log \dot{\gamma}_{APP}\right)} \tag{28}$$

2.1.2 Rotation rheometry

The use of rotation instruments makes it possible to measure various parameters characterizing rheological properties of material. Therefore, in discussion of rotation viscometers, it is more appropriate to use a general term rheometry.

Special features of application of rotation instruments for investigation of rheological properties of liquids are as follows. The use of rotation instruments makes it possible, firstly, to create within the sample the homogenous regime of deformation with strictly controlled kinematic and dynamic characteristics, and, secondly, to maintain the assigned regime of flow for unlimited period of time.

During material testing by rotation rheometry, different regimes of deformation are possible. The most important among them is imposition of a constant rotation speed $\Omega = constant$, or a constant torque, $M = constant$. However, in many modern instruments the method of scanning (or sweep) – imposition of the controlled change of rotation speed or torque with time is realized.

2.1.2.1 Plane-and-plane technique

This method of measuring normal stresses is almost the same as Cone-and-plane technique, but the rotation of two parallel plates around their common axis is used instead of the cone and plane assembly. The main difference is the variation of shear rate along the

radius of the measuring device according to formula $\dot{\gamma} = \frac{\omega R}{H}$, where *R* is the current radius and *H* is the distance between the parallel plates.

Analysis of force balance of liquid element, and assuming that $(\tau_{22} - \tau_{33}) << (\tau_{11} - \tau_{22})$ results in the following relationship directly valid for measuring the first difference of normal stress:

$$N_1 = \frac{d\tau_{22}}{d \ln R} \tag{29}$$

Then, measuring dependence of τ_{22} as a function of *R* at different shear rate, it is possible to find the dependence of N_1 on shear rate.

Simultaneous application of two geometries of flow (plane-plane and cone-plane) permits finding the second normal stress difference.

$$N_2 = \dot{\gamma} \int_0^{\dot{\gamma}} \left[\left(R \frac{\partial \tau_{22}}{\partial R} \right)_{p-p} - \left(r \frac{\partial \tau_{22}}{\partial R} \right)_{c-p} \right] \frac{d\dot{\gamma}}{\dot{\gamma}^2} \tag{30}$$

where subscripts p-p and c-p relate to values measured in plane-plane and cone-plane geometries, respectively.

The alternative form of this equation, which is used in experimental practice, can be written as:

$$N_2(\dot{\gamma}_R) = \frac{F_{c-p}}{\pi R_{c-p}^2} - \frac{F_{p-p}}{\pi R_{p-p}^2} \left(2 + \frac{d \ln F_{p-p}}{d \ln \dot{\gamma}_R} \right) \tag{31}$$

The value $N_2(\dot{\gamma}_R)$ is N_2 as measured at shear rate corresponding to the outer radius of planes.

This is one of the possibilities of measuring N_2, which has very low value (if not zero) in comparison with N_1. The application of Eg. 29 and 30 gives the best way to measure the second normal stress difference [10].

Shear rate:

$$\dot{\gamma}(R) = \frac{R\,\Omega}{H} \tag{32}$$

Shear stress:

$$\tau_{12} = \frac{M}{2\pi R^3}\left[3 + \frac{d\ln M}{d\ln \dot{\gamma}_R}\right] \tag{33}$$

Oscillatory shear measurement

The subjection of a material to a sinusoidal shear history and measurement of the stress response is well established as a useful way of obtaining precise information about the rheology of melts. If the material is entirely viscous the stress response is exactly $\pi/2$ out of phase. No melt is entirely viscous or entirely elastic, so the response involves a phase shift (see Fig. 13.) It is common for the response at low frequencies to approximate to viscous flow, while that at high frequency is usually far more elastic, thus the phase shit and the derived dynamic viscosity and modulus are frequency-dependent [8].

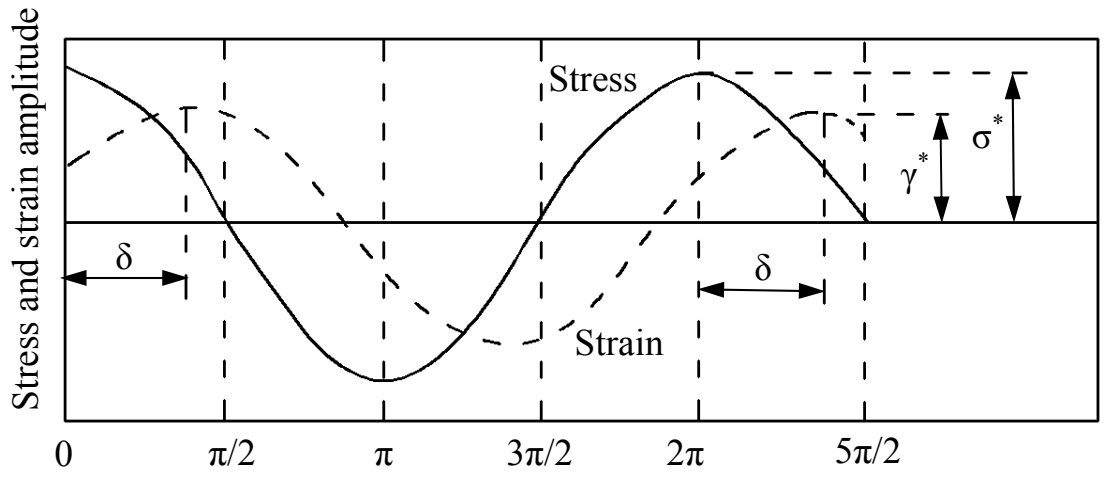

Fig. 13. Measurement of stress response, σ^*, where γ^* is strain amplitude and δ is the phase lag [8].

Most commonly strain is assumed to be the controlling variable, yielding the dynamic viscosity:

$$\eta' = \frac{\sigma^*}{\omega\gamma^*}\sin\delta \tag{34}$$

and the modulus:

$$G' = \frac{\sigma^*}{\gamma^*}\cos\delta \tag{35}$$

where σ^* and γ^* are the stress and strain amplitudes, δ is the phase lag and ω is the angular velocity [8].

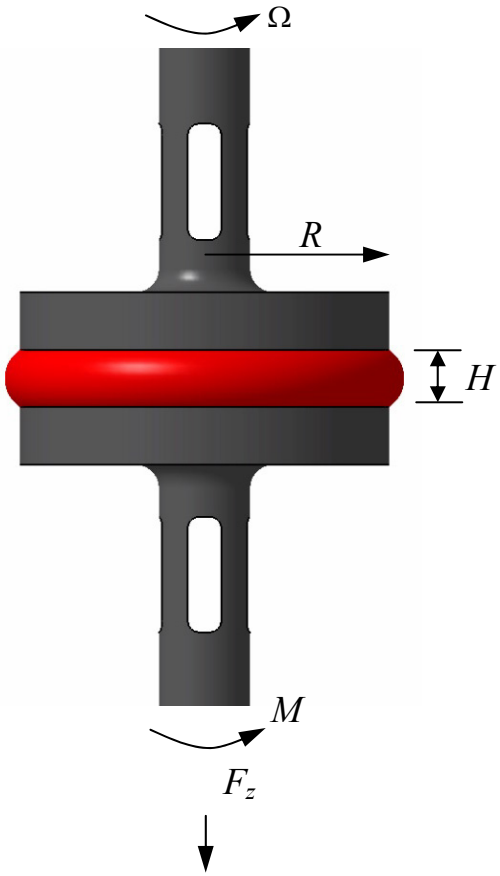

Fig. 14. Scheme of parallel disks rheometer [9] where Ω is the rotation rate, R is the plate radius, h is the gap size, M is the torque and Fz is the normal force.

Errors and utility in rotation rheometry is provided in Table 9.

Tab. 9. Errors and utility in rotation rheometry [9].

Errors	***Utility***
Inertia and secondary flow	Sample preparation and loading is simple for very viscous material and soft solids
Edge failure (same as cone-plane)	Can vary shear rate (and shear strain) independently by rotation rate Ω or by changing the gap h, permits increased range with a given experimental set up
Shear heating	Determine wall slip by taking measurements at two gaps
Nonhomogeneous strain field (correctable)	Delay edge failure to higher shear rate by decreasing gap during an experiment (requires change of cone angle in cone and plane)
	Measure N_2 when used with cone and plane thrust data
	Preferred geometry for viscous melts for small strain material functions

2.2 Elongation rheometry

Tab. 10. Extensional rheometers overview [5, 7].

Feature	*Munstedt tensile rheometer*	*Meissner´s metal belt clamping rheometer*	*Capillary rheometer*	*SER Universal Testing Platform*	*Cross-flow extensional reometry*
Type of elongation	Uniaxial	Planar or equibiaxial	Uniaxial or planar	Uniaxial	Planar
Sample	Polymer film	Polymer film	Granules	Polymer film	Granules
Sample size	10 g, care must be taken to minimalize end effects	< 2 g, requires careful preparation and loading	40 g minimum	5 - 200 mg	10 g minimum
Restriction of gravity force	Silicone oil	Inert gas cushion	None	Geometry of the sample and its clamping	None
Viscosity range	High viscosity	High viscosity	Both low and high viscosities	> 10 000 Pa.s (zero shear viscosity)	Both low and high viscosities
Flow stability	Subject to gravity, tension and air currents	Can be unstable at high rates	Unstable at very high rates	Stable up to 20 s^{-1}	Unstable at very high rates
Homogenous	Not at the ends	Could be, with care	No - mixed shear and elongation flow	Yes - truly uniform extensional deformation	Yes - truly uniform extensional deformation
Pressure effects	None	None	Yes - compressibility of melt in the reservoir could cause difficulties	None	Yes - compressibility of melt in the reservoir could cause difficulties
Elongation rates	Maximum rates depend on clamp speeds	Maximum elongation rate is limited by the ability to maintain the sample in steady flow	High and low rates possible	Maximum recommended elongational strain rate is 20 s-1	High and low rates possible
References	6, 14	5, 6, 9, 10, 14, 15	15	15	16, 17

Basic extensional rheometer types for polymer melts are provided in Table 10.

2.2.1 Münstedt

Constant-stress extensiometer was developed by Münstedt, sketch of his ´creepmeter´is shown in Figures 15-16). The sample is extended vertically in an oil bath providing very good temperature control. A later version uses small samples (3-10 mm in diameter, 10-50 mm long) which can be stretched either at constant stress or at constant stretch rate, one end of the sample is connected to a load cell located in the oil bath itself, and the other end is moved upwards with the help of a DC servomotor [6].

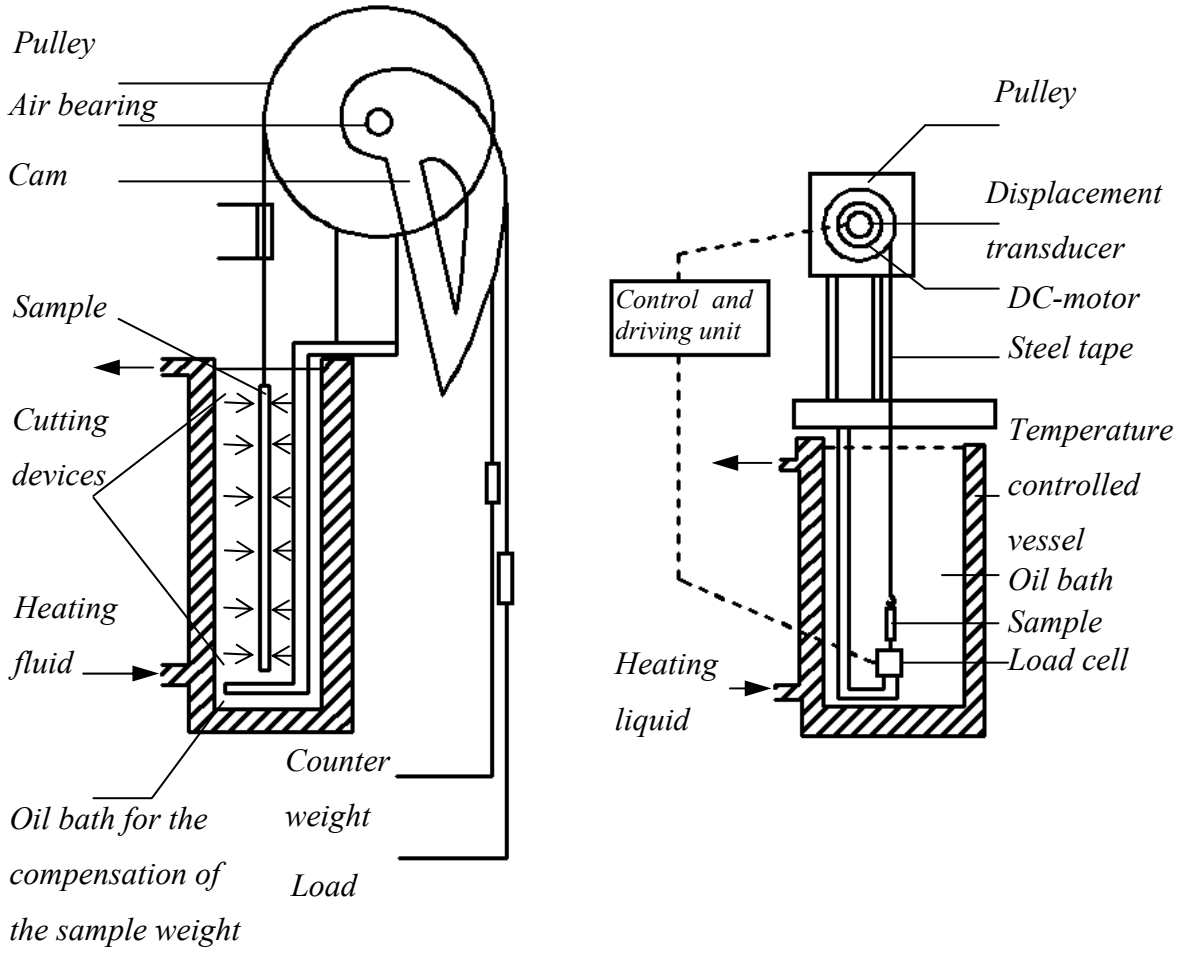

Fig. 15. The Münstedt creepmeter [14].

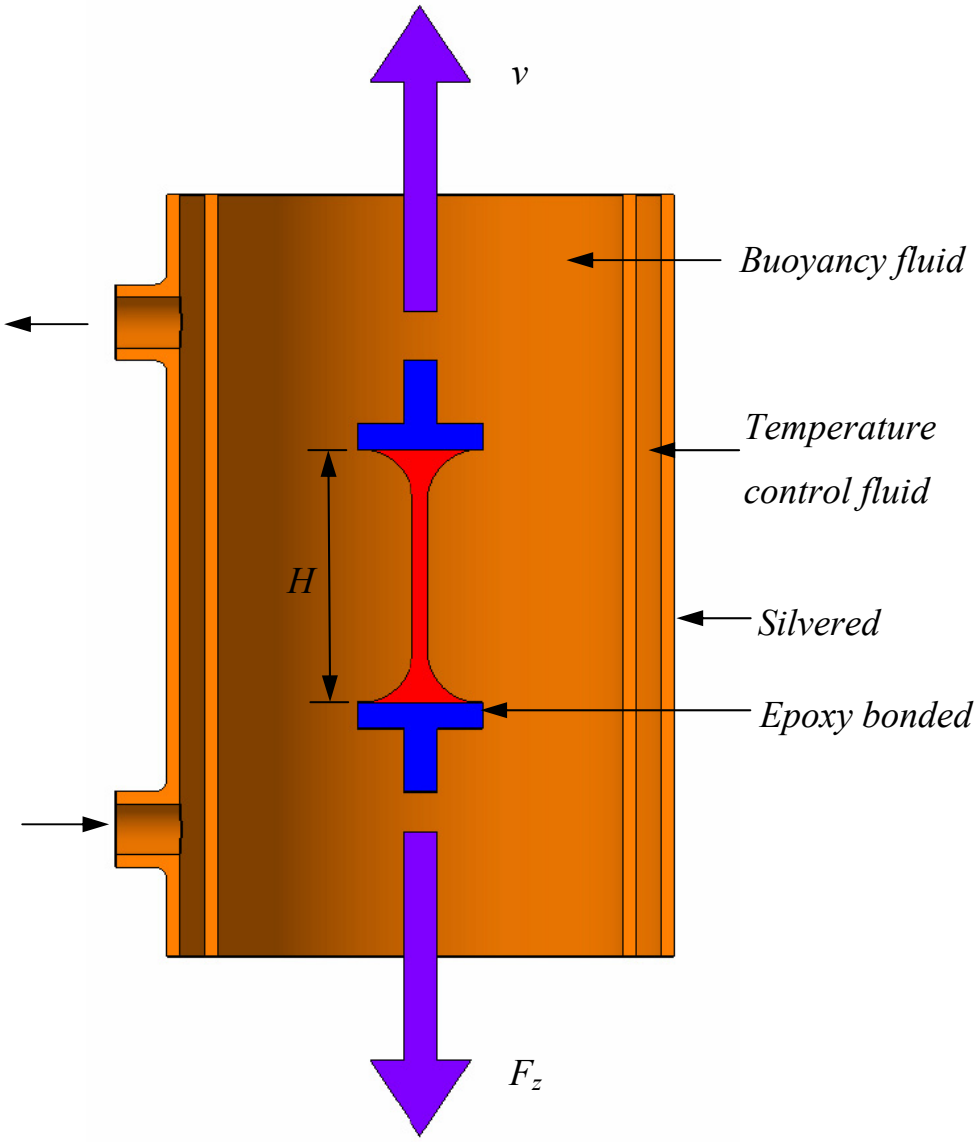

Fig. 16. Schematic of extensional rheometer with a transing clamp and vertical buoyancy control bath [9].

2.2.2 Meissner

In the Meissner instrument, the tensile force is measured by mounting one set clamps or rollers at the lower end of a strain-gauge transducer. The motion of the strain gauge is proportional to the force experienced by the metal-belt clamp or roller. In the commercial version of this instrument the samples are suspended over a porous table on a cushion of inert gas, eliminating chemical interactions present in designs that incorporated a supporting liquid.

The Meissner instrument is also capable of measuring unconstrained recoil after elongation at a constant rate. This is accomplished by cutting the sample at a desired time and then

monitoring the sample shrinkage with the video equipment. It is also possible to measure stress relaxation after the cessation of constant elongational deformation by stopping the flow at a desired time and monitoring the decay in the tensile stress. In all cases the stress is measured through the transducer mounted on the drawing clamp or belt, and the strain is measured by visually observing markers on the sample.

The Meissner rheometer is the best instrument available for measurements on viscous polymer melts (see Fig. 17). Since the sample must float on a bed of air, there is a minimum viscosity that can be measured, however. The maximum strain rate is limited by the speed of the clamps and the stability of the flow. The maximum viscosity is limited by the range of the strain-gauge transducer [5].

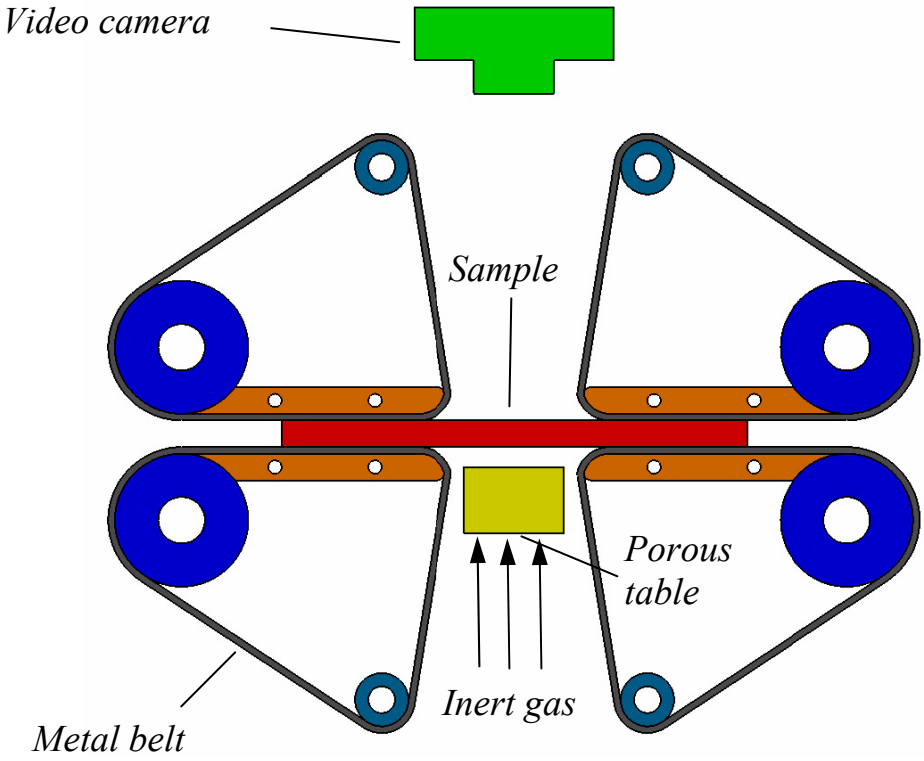

Fig. 17. Sketch showing the principle of operation of the extensional rheometer of Meissner and Hastettler [15].

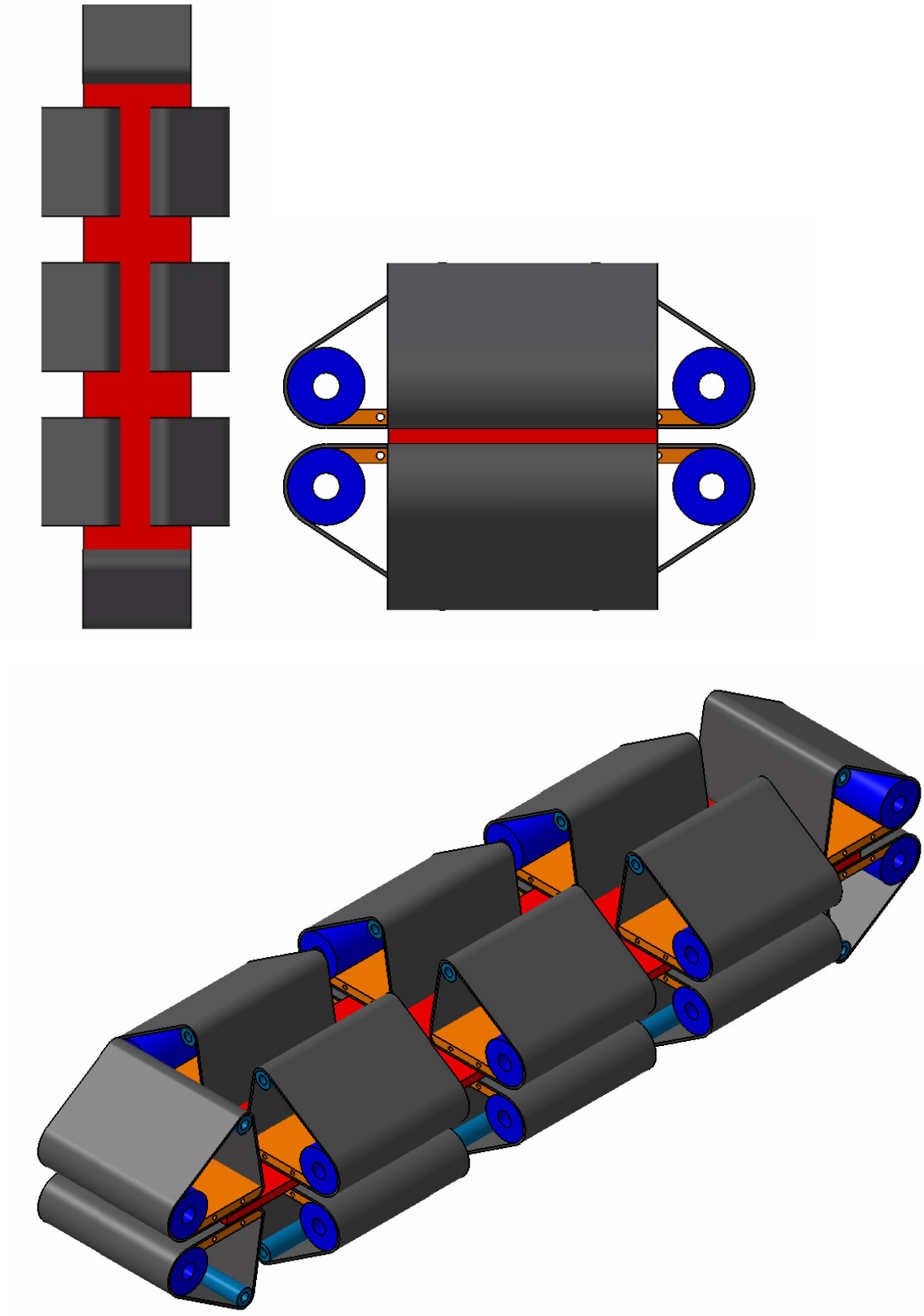

Fig. 18. 3D visualization of the Meissner and Hastettler extensional rheometer [9].

2.2.3 Sentmanat extensional rheometer (SER)

A very simple device for measuring the response of melt and elastomers to uniaxial extension has been reported by Sentmanat. A sketch is shown in Figures 19-20. The sample is a small rectangular plaque that is clamped at each end to a rotating drum. Both drums are rotated by the motor of a rotational rheometer, and the force in the sample is calculated from the torque output of the rheometer. In addition to star-up of steady, simple extension. Creep and stress relaxation experiments can be carried out. The entire device is designed to fit within the thermostatted chamber of a standard rotation rheometer, and the sample can be viewed through a window in the chamber.

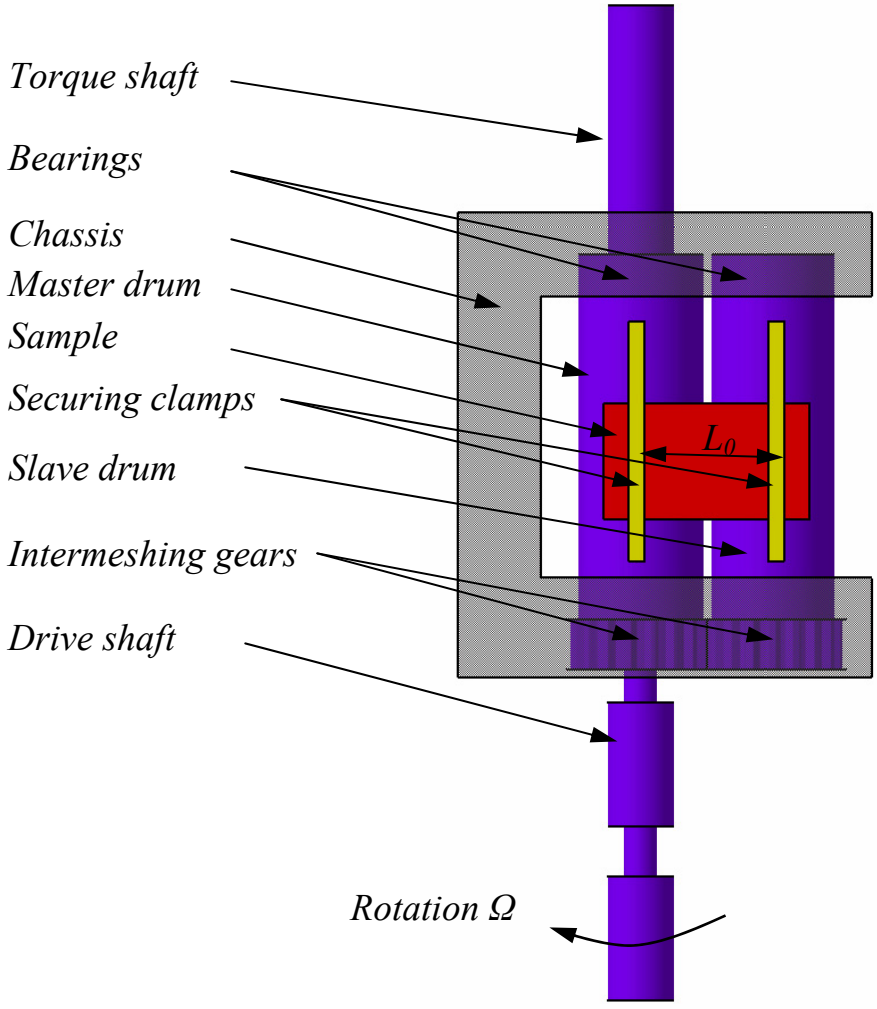

Fig. 19. The principle of operation of the SER [15].

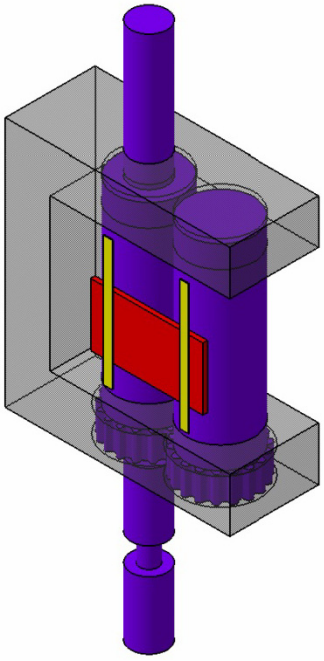

Fig. 20. The 3D view of SER [15].

2.2.4 Cross-flow extensional rheometer

Stress-optical measurements at a flow stagnation point in confined geometries such as the cross-slot provide an elegant way to perform extensional testing for polymer melts. This technique is especially useful for samples which have a steady-state that cannot be reached easily in standard elongational rheometry, for example, highly branched polymers which show a nonhomogeneous deformation that occurs in stretching experiments for Hencky strains above 4. In contrast to filament stretching, the cross-slot provides one point at which steady-state extensional flow may be sustained indefinitely [16].

In order to generate cross-slot flow, the basic action of the hydraulic pistons and barrels was retained and a new test section fabricated to accommodate cross-slot flow (see Fig. 21-24). Cross-slot flow experiments are primarily suited to study through flow birefringence. The key element of the stagnation point flow is that as fluid elements progressively approach the stagnation point, they experience increasing levels of strain. To a first approximation, the level of strain experienced by the fluid is inversely proportional to the distance from the exit symmetry plane and therefore in principle, fluid elements that pass through the stagnation point experience infinite strain. By examining flow birefringence stress fields it is therefore possible to explore a full range of strain histories for a given flow condition. While it is possible to measure pressure difference using the multi-pass rheometer,

the magnitude of pressure difference observed due to the extensional flow at the stagnation point is small when compared with the pressure drop in the inlet and outlet regions of the device. Thus it is difficult to measure the pressure drop that is directly related to localized extensional flow events in the central region of the cross-slot [17].

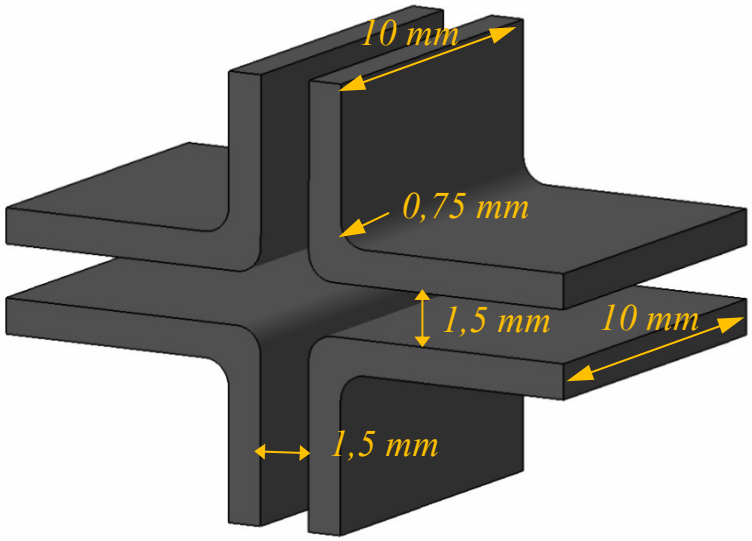

Fig. 21. The 3D view of the cross-slot flow domain [17].

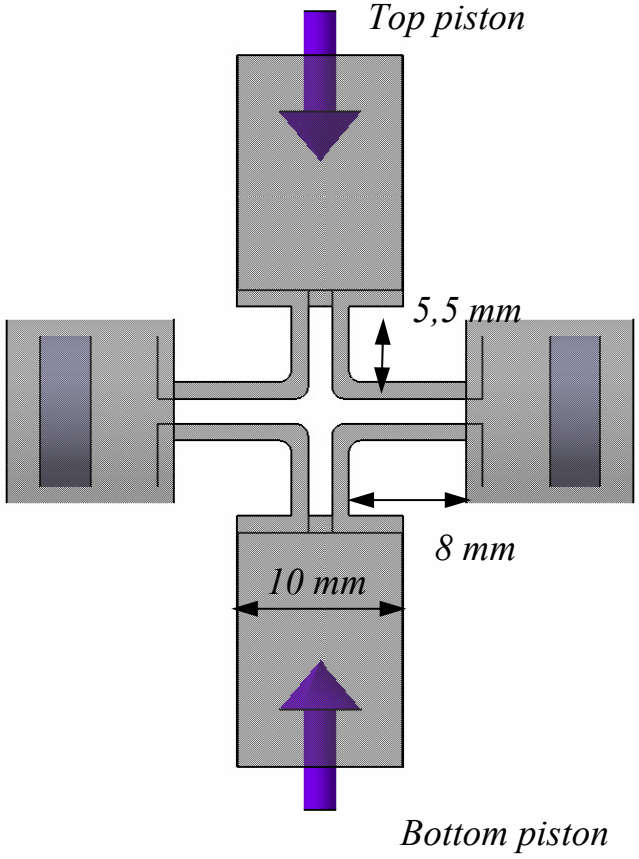

Fig. 22. 2D visualization of the cross-slot section [17].

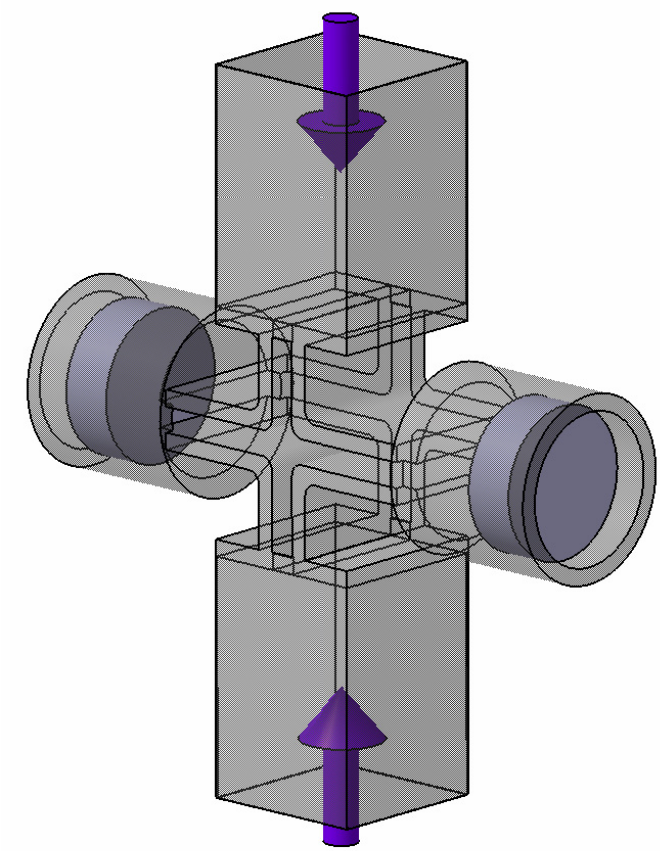

Fig. 23. 3D visualization of the cross-slot section [17]

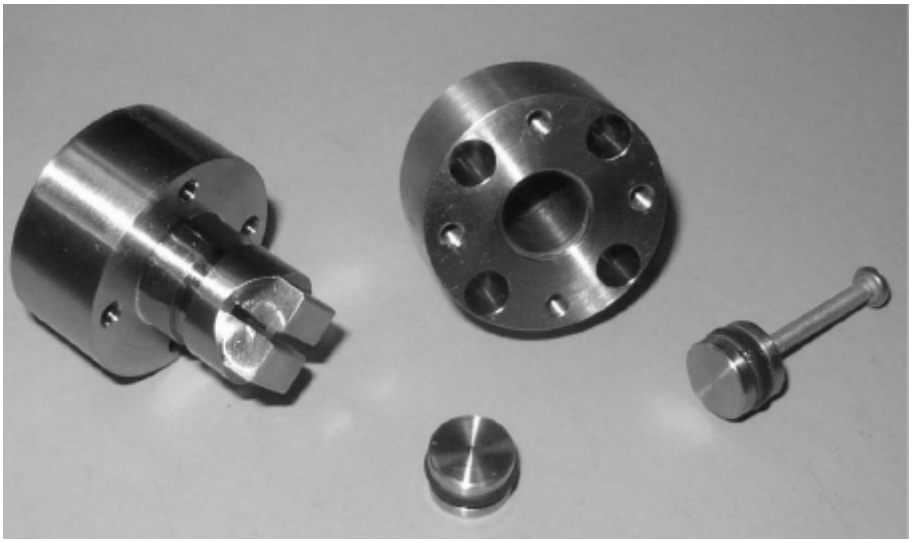

Fig. 24. Real view of the cross-slot inserts [17].

3 MELT BLOWN LINE

In 1951 a project was initiated at the Naval Research Laboratory for the investigation of organic fibers that were less than 1 micron in diameter. Various manufacturing methods were to be considered and, after the feasibility of one became established, an evaluation was to follow of the submicron fibers as a filter media. The "fiber-forming'' thermoplastic materials were of particular interest in this investigation because of their high strength and ability to undergo molecular orientation when stretched. Emphasis was placed on obtaining the extremely small fiber size because such fibers were known to possess aerosol filtration efficiencies far in excess of ordinarily used materials. Furthermore, superfine plastic fibers represented a new area of research where completely altered physical properties might be anticipated as a result of the nearly colloidal state of the substance [18].

Almost all fiber barrier membranes used in the nonwovens industry are based on meltblowing technology, a melt spinning processes used to produce microfibers by injecting molten polymer streams into high velocity gas/air jets that form a self-bonded web when collected on a moving surface. Figure 25 shows a schematic illustration of the process in which high-velocity air jets impinge upon the polymer as it emerges from the spinneret. The drag force cause by the air attenuates the fiber rapidly, and reduces its diameter by as much as hundred times from that of the nozzle diameter. Typical meltblown membranes have fiber sizes ranging from 0,5 to 10 μm with an average fiber diameter of 1-2 μm. Meltblown webs are known for their high surface area per unit weight, high insulation value, and high barrier properties [1].

The common materials used in melt-based polymer industries are polyolefins (especially polypropylene (PP)), because of their commercial importance and versatility to make a wide range of products. These products have been widely used in applications, such as medical, electrical insulation, thermal insulation, optical, protective clothing and filtration, because of their chemical inertness, light weight, lack of heat shrinkage and good mechanical properties. Majority of the products of polyolefins are used as fibrous materials predominantly in the form of microfibers [19].

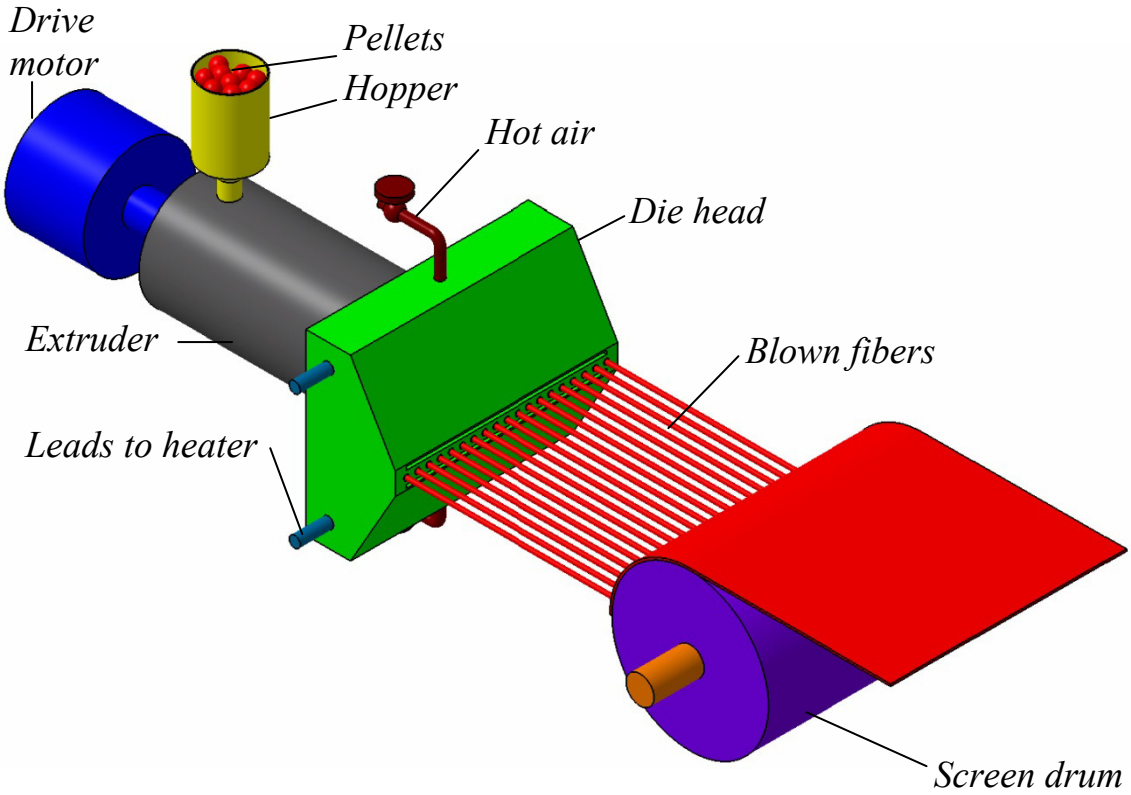

Fig. 25. Melt blown line [20].

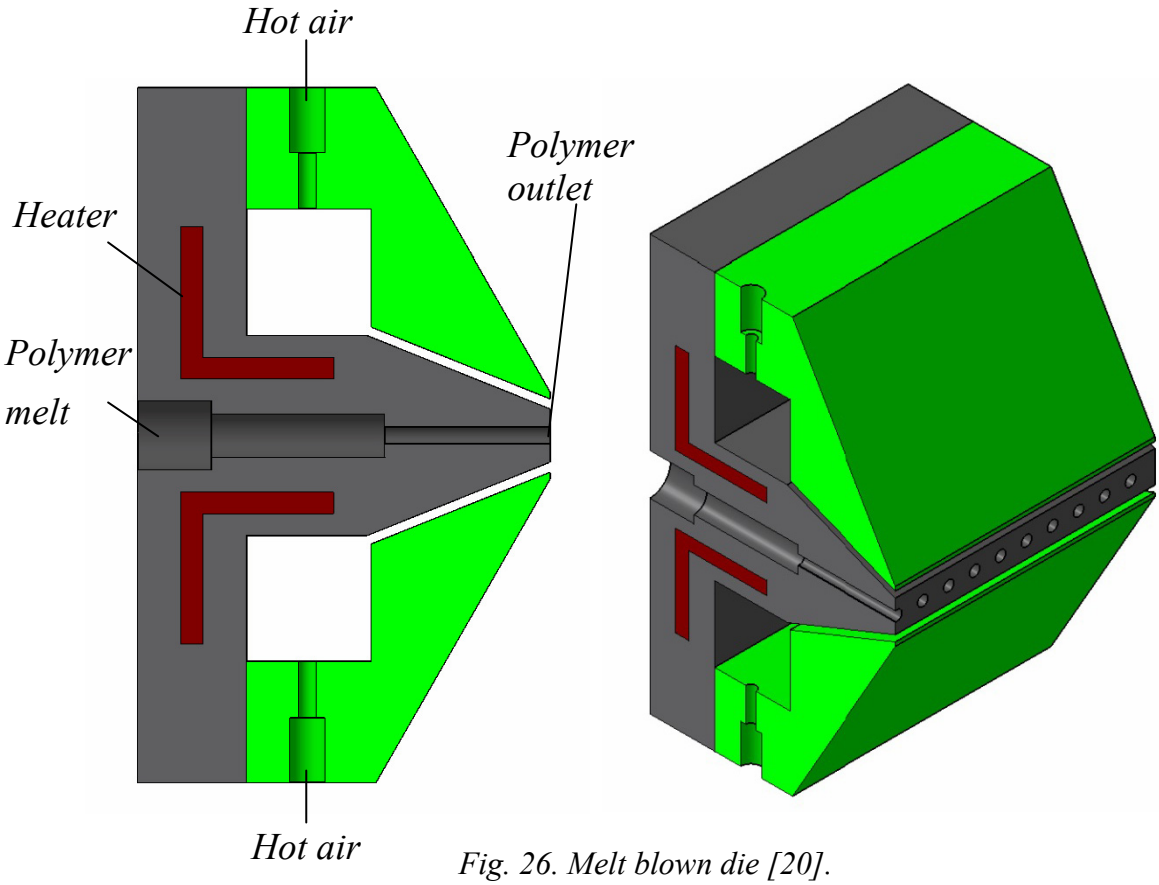

Fig. 26. Melt blown die [20].

In the late 1960s and early 1970s, Exxon Research, in looking for uses for its newly commercial polyolefin – polypropylene – try to use a polypropylene reactor slurry to produce synthetic paper. Dr Robert Buntin became aware of the Naval Research Laboratories publications and these served as a starting point for a multi-year, multi-million dollar project.

Exxon opted to license the resulting meltblowing technology, rather than commercialise it. Early successful licensees include 3M, Kimberly-Clark, Johnson & Johnson, James River, Web Dynamics and Ergon Nonwovens, followed by many others [2].

The melt-blown (MB) process is used not only for PP but also for many forms of thermoplastics. In the process, polyolefin is extruded through a large number of small holes located closely on a spinneret. A stream of molten polymer exiting from the spinneret holes is fed into a current of hot air moving at high speed. The molten stream of polymer is then broken up into an integrated network of very fine (microfiber range 0,01-0,02 dtex) entangled fibers of varying lengths, which are immediately deposited onto a rotating perforated cylinder surface to form a web. In general, the melt-blown nonwoven fabrics are lighter than spun-bonded fabrics and have lower strength. Their texture, however, renders them excellent for use in filtration and absorption applications, such as for industrial wipes, surgeons´ masks and gowns, and oil clean-up products [3].

Meltblowing is widely used to form nonwovens in the textile industry. In meltblowing, polymer melt is supplied through a die nosepiece (see Fig. 26). After, that polymer jets are pulled vigorously by the surrounding hot gas jets with velocities compared to the speed of sound. Under the action of the aerodynamic forces polymer jets rapidly thin to the final diameter of the order of 3-10 μm and solidify [21].

4 NANOFIBERS

Polymer nanofibers (polymer fibers with diameter $\approx 1\,\mu m$ or less) are increasingly being used in nonwoven materials, which take the form of sheets or mats of fibers connected together by physical entanglement rather than any knitting or stitching. Polymer nanofibers are attractive because of their large surface-area-to-volume ratio, which allows the role of surface functionalization to be greatly accentuated [22]. Possible applications for polymer nonafibers are summarized in Table 11.

Tab. 11. Applications of nanofibers [3].

Sector	***Application***
Electronics	Super capacitors
Biological and healthcare	Biosensors
	Tissue engineering
	Medical devices
	Wound dressing
	Cables for implantable devices
	Neural prostheses
	Drug-coated stents
	Artificial heart valves
Energy	Photovoltaics
	Fuel cells
	Battery separators
	Printable electronics
	Hydrogen storage
Biotechnology and environment	Separation membranes
	Affinity membranes
	Water filters
	Air filters
	Gas turbine filters
Others	Engine filters
	Personal protective masks and clothing

4.1 Polyolefin fibers

Polyolefin fibers are, in effect, aliphatic polymeric hydrocarbons. The chemical elements of which they are composed are carbon and hydrogen. Thus, polyolefin fibers possess very low densities (lower than water). The density of polyethylene (PE) fibers is 0,95-0,96 gcm^{-3}, that of polypropylene (PP) fibers is generally around 0,90-0,91 gcm^{-3}. The densities of other types of polyolefin fiber are also of this magnitude, or even less, depending on the size of the side groups and the predominant crystal structure in the fiber. In addition, in common with hydrocarbons of lower molar mass, polyolefin fibers also possess a high degree of resistance to many chemical agents. They are extremely hydrophobic: their moisture regain, for example, is almost negligible. The structures of some polyolefins are given in Table 12 [3].

Tab. 12. The structure of some polyolefins [3].

Polymer	***Repeat unit***
Polyethylene	$-(CH_2-CH_2)-$
Polyprophylene	$-(CH_2-CH(CH_3))-$
Poly(4-methyl-1-pentene)	$-(CH_2-CH(CH_2CH(CH_3)_2))-$
Poly(1-butene)	$-(CH_2-CH(CH_2CH_3))-$
Poly(3-methyl-1-butene)	$-(CH_2-CH(CH(CH_3)_2))-$

In the past decade, the use of polyolefins, especially polypropylene, has dominated the production of meltblown and spounded nonwovens. One of the main reasons for the growing use of polyolefins in nonwovens is that the raw materials are relatively inexpensive and available worldwide.

Polyolefin resins are widely used in nonwovens mainly because they offer a relatively attractive cost combined with good value and ease of use when compared to conventional resins, such as polyesters and polyamides. Moreover, continuing advances in polyolefin fiber grade resins are strengthening the olefin price/properties ratio, which make them more suitable for nonwoven applications.

Commercial polyolefin technologies over the last six decades have gone through significant changes. Figure 27 shows the stages of development in polyolefin technology. The figure indicates that the polyolefin technologies have gone through an introduction, growth, and stabilization or maturity phase [3].

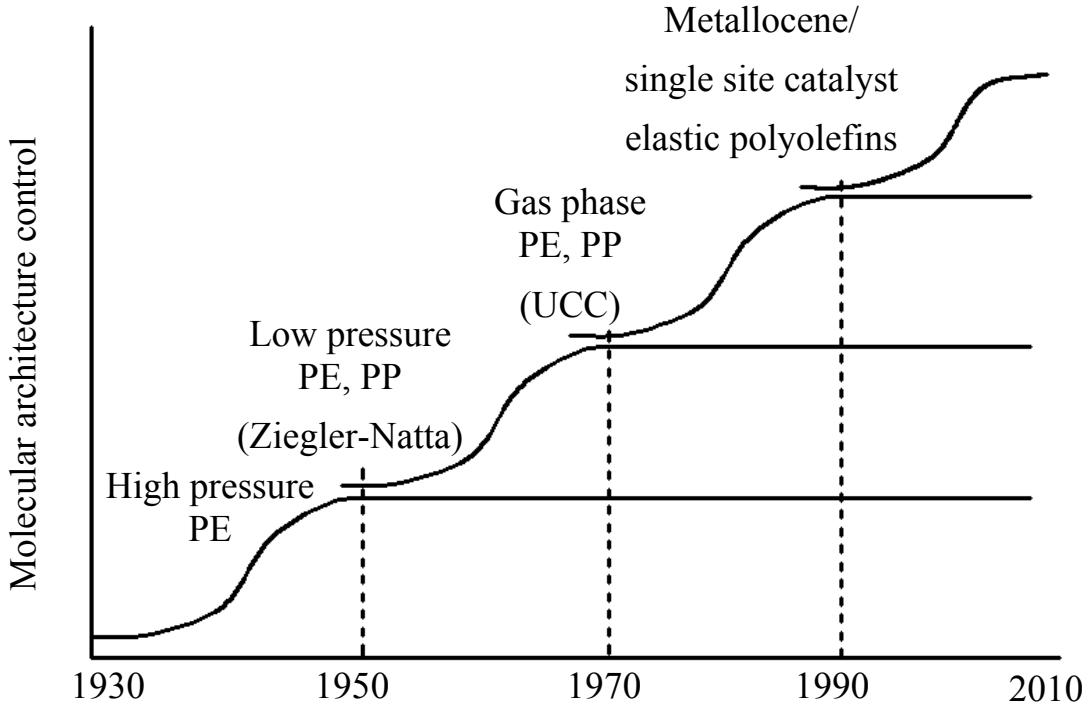

Fig. 27. Stages in development of polyolefin technology [3].

4.2 Nonwovens

Polyolefin nonwoven can be produced by dry lay-up from the staple fibers. The fiber bales are opened and carded or airlaid to form webs in parallel/cross laid, or random laid. The dry laid webs are consolidated with mechanical, thermal or chemical bonding techniques, but thermal bonding is the preferred one.

Alternatively, spun-bonded (SB), meltblown (MB) or film-fiber nonwovens are produced by a single-stage process, in which extrusion of fiber or film and web formation are integrated sequentially. Production lines combining both SB and MB processes are now being increasingly used for the formation of nonwoven composite multilayer fabrics. These fab-

rics combine the desirable properties of spun-bonded and melt-blown materials. The possible composite layer structures from these two processes are: SM, SMS, and SMMS. The external spun-bounded layers of either SMS or SMMS provide good mechanical properties, while the internal melt-blown web provides good filtration and absorption properties. The layers are bonded either thermally or mechanically, depending on the weight and desired application of the SMS product. Thinner webs are bonded by means of heated calender rollers, whereas thicker webs are mechanically needled [3].

4.2.1 Nonwoven definition

Nonwoven fabric technology is the most modern branch of the textile industry, and embodies both quite old and the very new processing techniques and materials. From a fairly modest beginning with only a limited variety of raw materials, processes, and end uses, the nonwoven industry has reached a status of enormous diversity. Today, nonwoven fabrics play key roles in hundreds of everyday products, from luxury automobiles to the familiar teabag.

The term “nonwoven fabrics” has been defined in many ways. In fact, the definition of nonwoven fabrics has been an area of considerable debate and discussion.

Nonwoven fabric is essentially an assemblage of fiber held together by mechanical or chemical means, resulting in a mechanically stable, self-supporting, and generally flexible, web-like structure.

However, the definition of nonwoven given by INDA (Association of Nonwoven Fabric Industry) is as follows: “A sheet, web, or batt of natural and/or man-made fibers or filaments, excluding paper, that may not have been converted into yarns, and that are bonded to each other by any of several means [3].

4.2.2 Nonwovens manufacturing system

The manufacture of nonwoven fabric is very different from that of woven and knitted fabrics (see Fig. 28). Each nonwoven manufacturing system involves the following generic steps [3]:

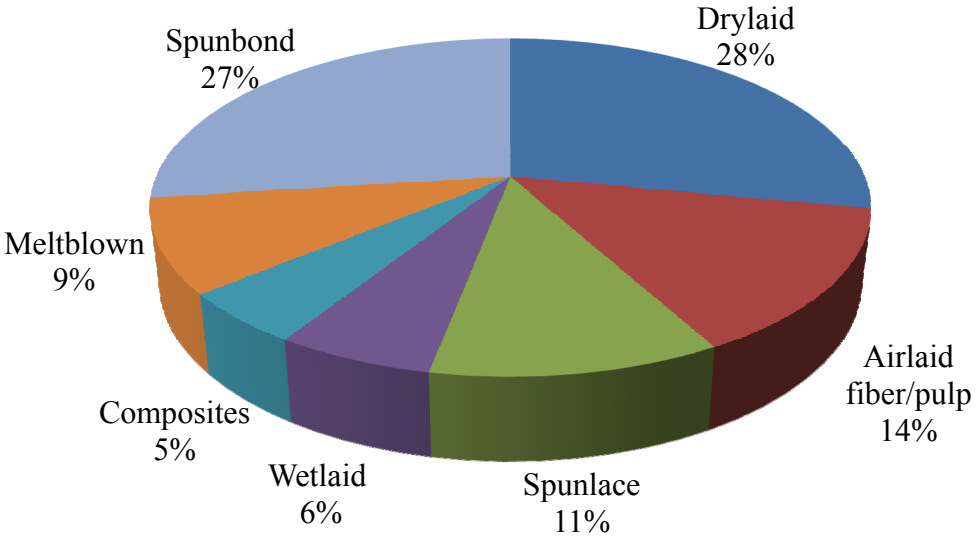

Fig. 28. Nonwoven market share by fabric type [2].

- fiber/raw material selection
- web formation
- web consolidation
- web finishing and converting

Pores size: Pore size is an important factor in liquid filtration because sieving is an important liquid filtration mechanism. Sieving is the same as blocking, i.e. a particle is blocked by a pore if the pore size is smaller than the particle size [2].

Pore size distribution: A soil´s porosity and pore size distribution characterize its pore space, that portion of the soil´s volume that is not occupied by or isolated by solid material. The basic character of the pore space affects and is affected by critical aspects of almost everything that occurs in the soil: the movement of water, air, and other fluids, the transport and the reaction of chemicals, and the residence of roots and other biota [23].

Fiber diameter: The fiber diameter is an independent variable and the probability of observing a particular fiber size [24].

Tab. 13. Summarization of the techniques for determination of pore size/fiber diameter distribution [3].

Techniques for analyze	
Pore size distribution	***Fiber diameter distribution***
Image analysis	Image analysis
3-D image	Manual measurements on SEM image
Magnetic resonance imaging	Distance transform algorithm
X-ray microtomography	Artifical vision systém
X-ray synchrotron radiation micro-tomography	
Artifical vision systém	

4.2.3 Nonwoven applications

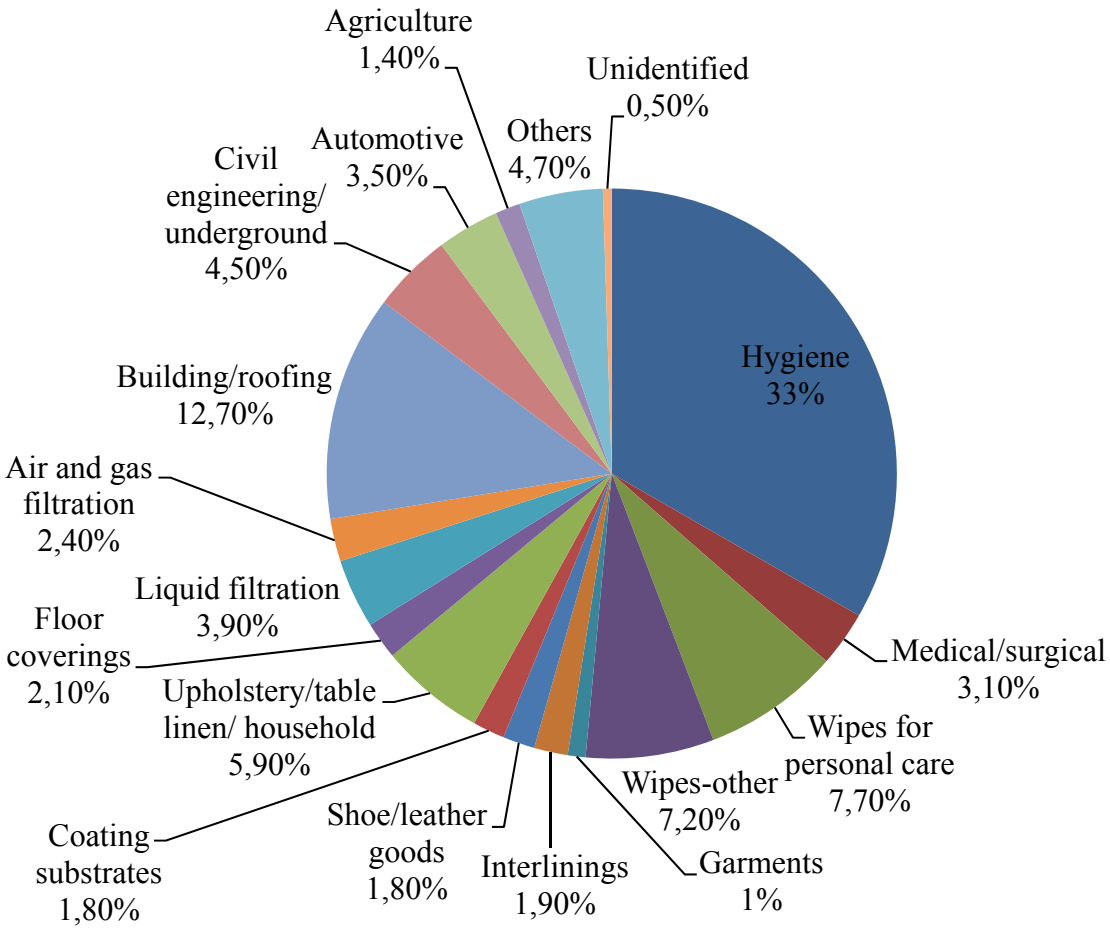

Fig. 29. Nonwoven applications [2].

a. Flame retardant nonwovens

Protective garments: The field of protective garments is relatively large with differing requirements since it incorporates the protection of men at work and military applications, as well as clothing for firefighters. Usually, protective fabrics are multilayer clothing containing up to five or six layers. Fire protective clothing for firefighters consists of at least four layers: outer and inner shell, moisture barrier, and thermal liner (Fig. 30). These layers are expected to provide adequate heat, flame, liquid, chemical and mechanical protection.

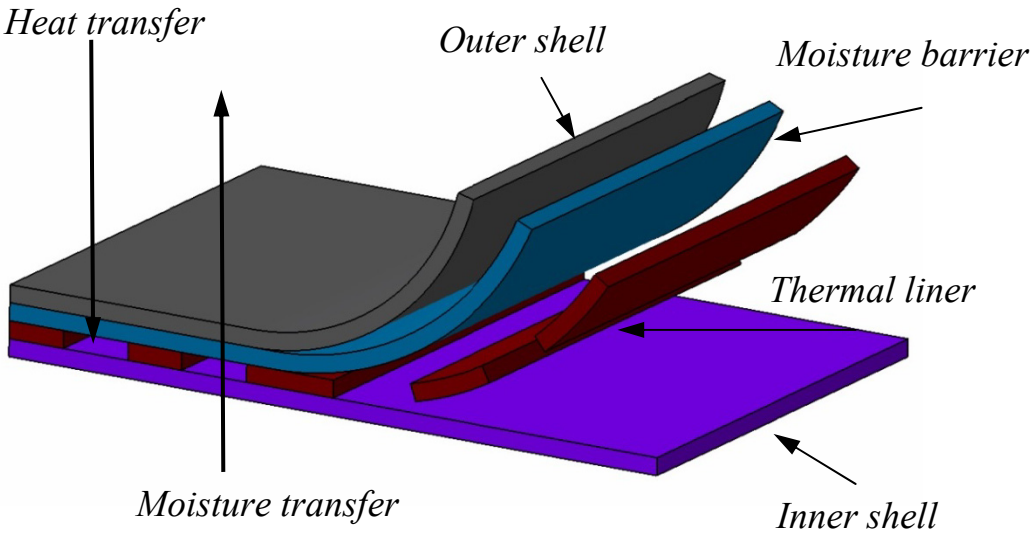

Fig. 30. Typical structure of protective garments for firefighters [2].

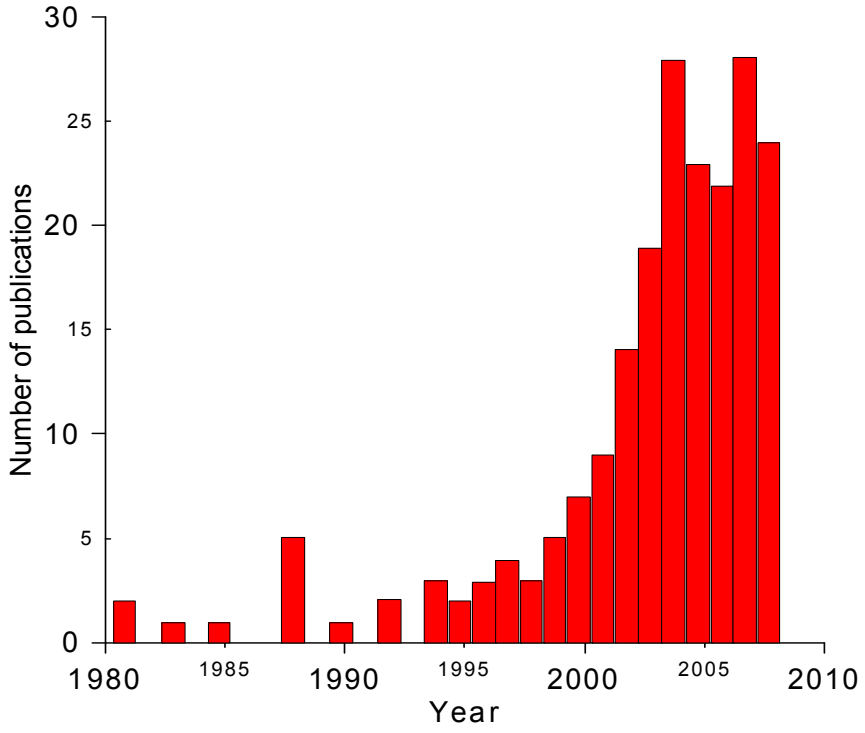

Fig. 31. Publications regarding flame retardant nonwovens since 1980 [2].

Fire-blockers for seat and upholstery: Fire-blockers are usually highly fire resistant materials that are placed beneath the exterior cover fabric of furnishing and the first layer of cushioning materials in seats, mattresses and upholsteries. The bulky cushioning materials represent the major fuel source and therefore the greatest hazard potential. The fire-blocker acts as a barrier between the heat source (flame, cigarette. etc.) and the cushioning materials limiting fire growth and development.

Another application of flame retardant nonwovens is flexible insulation panels for building construction. Although traditional thermal insulation materials such as mineral wool or polystyrene are widely used, the return to ecology and nature noticed in several application fields is also observed in the building industry [2].

b. Nonwoven personal hygiene materials

Modern disposable, absorbent nonwoven hygiene materials (NHMs) have made an important contribution to the quality of life and skin health of millions of people. Market segments and products falling under the heading of NHMs are as given in (Tab. 14). The advantages of using NHMs instead of traditional textiles are: excellent absorption, softness, smoothness, stretchability, comfort and fit, strength, double fluid barrier effect allowing moisture to be absorbed and retained, good uniformity, high strength and elasticity, good strike-through, low wet-back and run-off, cost-effectiveness, stability and tear resistance, opacity/strain hiding power, and high breathability [2].

Tab. 14. Application of nonwovens for personal hygiene [2].

Hygiene applications		
Diapers	***Feminine hygiene***	***Product for adult incontinence***
Diaper coversheet	Sanitary napkins	Protective underwear
Secondary facing	Panty shields	Adult brief with waistband
Acquisition/distribution layer	Tampons	Underpads
The absorbent core		
The back sheet		

c. Nonwovens for consumer and industrial wipes

The main technologies used to produce nonwoven wipes are spunlace, airlaid and their combination (airlace). Other technologies include drylaid, wetlaid, spunbond, meltblown,

CoForm and their combinations. The raw materials used include, but are not limited to, synthetic fibers such as poly ethylene terephthalate (PET), polypropylene (PP), and rayon, natural cellulose fibers such as wood pulp and cotton, and speciality materials such as bi-component fibers and nanofibers (see Tab. 15) [2].

Tab. 15. Application of nonwovens for wipes [2].

Applications of nonwoven wipes		
User	***Household cleaning***	***Industrial***
Baby wipes	Wet floor products	Wipes for food service
Personal care wipes:	Cleaning wipes	Industrial general wipes
Adult care wipes	Furniture polishing wipes	Industrial speciality wipes
Facial cleaning/makeup wipes		Medical wipes
Feminine care wipes		

d. Nonwovens in specialist and consumer apparel

Personal protective equipment: Personal protective equipment is used, or required, for a wide range of industrial or personal activities. Equipment can range from hard hats to fire extinguishers. Apparel for such activities is of great importance because it covers so much of the body and can provide the degree of protection suitable for a specific pursuit or workplace environment.

Medical apparel and accessories: It is estimated that 3,3 billion square yards of nonwovens go into medical applications in North America. Medical nonwoven garments are intended to protect health care workers from the "transfer of blood, body fluids, other potentially infectious materials, and associated microorganisms". Decontamination garments protect health care workers from infection or transfer of other agents during procedures to decontaminate medical instruments and devices.

Wearing apparel: Attempts by apparel designers to use nonwovens have been more successful when the nonwoven fabrics have some elastic properties to allow for fabric manipulation, stretching and compression that are desirable in constructing garments. When regular spunbonded nonwovens were used, designers opted for various techniques to simulate some shearing or three-dimensional bending properties.

When working with stretchable melt blown fabrics, garments with more pleasing drape and greater freedom in fitting and forming were possible [2].

e. Nonwovens textiles for residential and commercial interiors

Interior textiles are produced for either the "domestic" (also referred to as private or residential) or "contract" (also referred to as commercial) markets. Interiors textiles are usually discussed in relation to two key categories: furnishing fabrics and household textiles.

Furnishing fabrics include: upholstery fabrics, soft floor coverings, wall coverings, window furnishing (curtains, drapes, blinds) and accessories such as cushions and throws.

Household textiles include all textiles used in domestic interiors apart from furnishing fabrics. For example: bedding, towels, blankets, tablecloths and napkins (see Tab. 16.) [2].

Tab. 16. Application of nonwovens in textiles [2].

Applications of nonwoven textiles			
In bedding	***In upholstery and furnishing***	***In wallcoverings***	***For floor coverings***
Mattresses:	Support and cover materials	Backings	Needle-punched carpets
Support, covering and insulation	Foam replacements	Temporary wall partitioning	Backings
Mattress pads and external covers	Synthetic leathers		
Anti-microbial properties	Curtains		
Foam replacements	Durable fabric		
Fibrefill			
Pillows			
Quilts and duvets			
Blankets			

f. The use of nonwovens as filtration materials

There is a huge variety of filter media available. Textile fabrics, porous foams, films and sands can be used as filter media. In Figure 32, different objects sizes and basic filtration mechanisms are provided.

When nonwovens are used as filters, they offer a range of advantages above other filter media. For example, nonwovens offer large and adjustable surface properties and can be adapted to different filtration requirements (see Tab. 17).

Tab. 17. Applications of nonwovens in filtration [2].

Filtration	
Filter designs	***Filter applications***
Tube filters	Filters in automobiles
Cartridge filters	Filters for the manufacture of electronic components
Bag filters	Hot melt filtration
Filter candles	

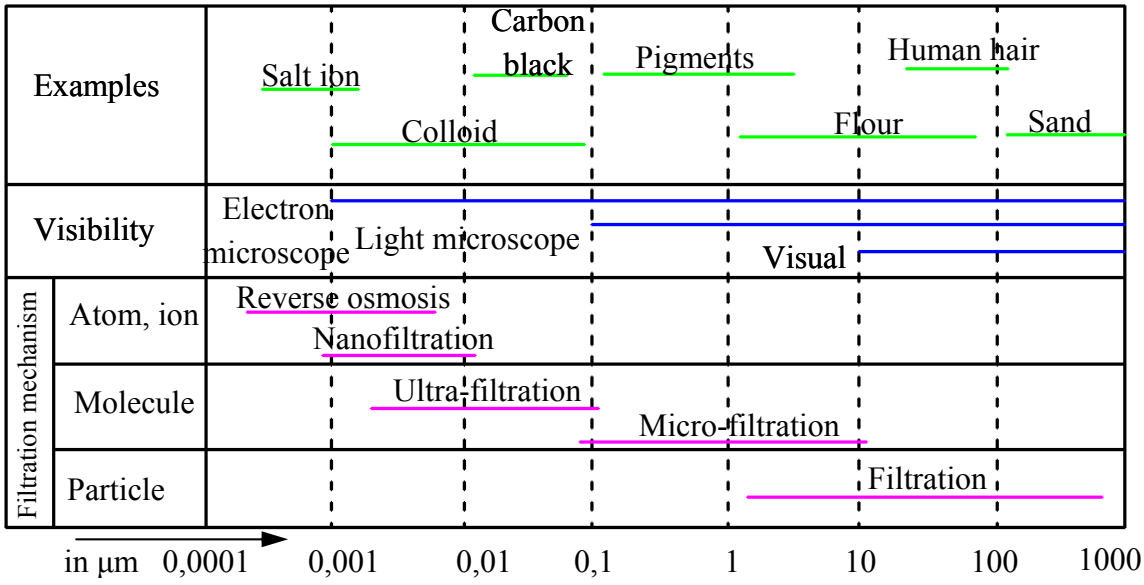

Fig. 32. Summarization of the different object sizes [2].

g. Nonwoven textiles in automotive interiors

The expansion of the industrial textile market is good for the textile industry and automotive textiles in particular are frequently in the media. An important factor in this is that the annual capacity of global vehicle production was expected to reach about 60 million units by 2008. When added to the 885 million units of existing motor vehicles, the worldwide automobile consumption forms a substantial market for automotive textiles Table 18 [2].

Tab. 18. Application of nonwovens in automotive [2].

Automotive applications	
Passenger compartment	***Trunk comparment***
Carpet	Trunk liners
Floor structure	Trunk load floor
Headliner	Package tray
Door trims	
Seat	

5 PARAMETERS INFLUENCING MELT BLOWING PROCESS

5.1 Processing conditions

Fabrication of nanofiber meltblown membranes and their filtration properties has been evaluated in [1]. The influence of different die configurations and operating conditions on fiber and web characteristics was investigated. Their performance was compared to a control meltblown sample produced by using a typical die design. It was found that production of nano-meltblown membranes with an average fiber size in range of 300-500 nm using this new die design is possible and report on process operating conditions that result in such structures. The lower basis weight also resulted in a lower pressure drop and overall, the new samples exhibited a higher quality factor, twice that of the control.

Development and filtration performance of polylactic acid meltblowns has been analyzed in [25]. It was found that biodegradable polylactic acid (PLA) can be used to make meltblowns (MBs). The key parameters regarding the filtration performance of PLA MBs was revealed to be the PLA chip drying process, the melt temperature, the hot air temperature, and the width of the air gap. The diameter of PLA MB fibers became larger with the increase of hot air temperature. With the increase of air gap width, the diameter of PLA MB fibers went up, whereas the crimp level went down.

Influence of Laval nozzles on the air flow field in melt blowing apparatus has been investigated in [26]. The baseline case without a nozzle was simulated and examined based on the y-component of the air velocity profile, $v_y(y)$, at the centerline as a function of P_{inlet}. As P_{inlet} increase: the air flow goes from subsonic to supersonic and the maximum value of $v_y(y)$ increases with increasing P_{inlet}, then starts to oscillate with the formation of compression waves in the supersonic region, $P_{inlet} \geq 15\ psig$. Simulation also showed that a Laval nozzle influences the air flow field by increasing the maximum value of $v_y(y)$ and eliminating the compression wave at a predictable value of P_{inlet}. Actual density oscillations in the supersonic flow field exiting a melt blowing die, with and without Laval nozzle.

Melt blowing thermoplastic polyurethane and polyether-block-amine elastomers: effect of processing conditions and crystallization on web properties has been revealed in [27]. Melt-blown webs of thermoplastic polyurethane (TPU) and poly(ether-block-amide) (PEBA) elastomers were produced at various die-to-collector distance, DCDs. The web tensile properties were measured and explained in terms of the crystallization kinetics along with the temperature profile of the process air. It was found that the air velocity drops rapidly as the distance from the melt-blowing die increases until approximately 5-6 cm below the die. After that, the velocity approaches a constant value. The process air temperature follows a similar profile where the temperature drops rapidly for the first 5-6 cm below the die and then varies only slowly thereafter. On increasing DCD, the fibers have traveled longer distances and crystallized more before reaching the forming belt. The fiber thus have lower temperatures before they contact with others already on the collector, thereby reducing interfiber adhesion and the web strength.

Three–dimensional model of the meltblowing process has been investigated in [28]. It was found that the effect of air temperature on the fiber diameter is not substantial. On the other hand, it was found that a higher air temperature results in higher amplitude of fiber vibration. Study also shown that the increase in the melt temperature may cause a substantial increase in the rate of fiber attenuation.

5.2 Equipment design

Air-flow field of the melt-blowing slot die via numerical simulation and multiobjective genetic algorithms has been discussed in [29]. A multiobjective optimization using genetic algorithms was proposed to obtain optimum air-flow field with the lowest velocity decay and temperature decay of the air-flow field of a melt-blowing slot die. Four main geometry parameters, including slot width, head width, slot angle and setback, were studied. The results also show that a smaller slot angle and large slot width resulted in a lower air velocity decay and temperature decay.

Fluid flow on coat-hanger die of meltblowing process has been analyzed in [30]. The fluid flow in the coat-hanger die was simulated by the finite element method and measured by particle image velocimetry. Both qualitative and quantitative comparisons showed good agreements in the flow patterns and calculated velocities at the die outlet. The deviation of velocity CV% value at the die outlet between the simulation results and experimental results was 2,92% only, which was considered to be reasonable in view of the complex geometric model and flow nature in the coat-hanger die. It was suggested that the proposed numerical methodology can be useable in the future design of the coat-hanger dies.

Numerical simulation and analysis of fluid flow in double meltblown die has been discussed in [31]. The fluid flow inside the meltblown die was analyzed, particularly the flow near the joint point of the double meltblown die and the entrance of the orifice. Velocity distribution at the outlet of the die was also analyzed through a comparison with the fluid flow in the double meltblown coat-hanger feed distributor. The results showed that the convergence flow around the entrance of the orifice can improve the velocity distribution at the die´s outlet to a certain extent. The improved uniformity of the velocity distribution at the outlet of the double meltblown die proved the feasibility of using side-by-side meltblown die to fabricate wider uniform meltblown webs.

Modified dual rectangular jets for fiber production has been investigated in [32]. Velocity field was measured below two parallel, rectangular air nozzles. The following five die (nozzle) types were tested see (Fig. 33-37):

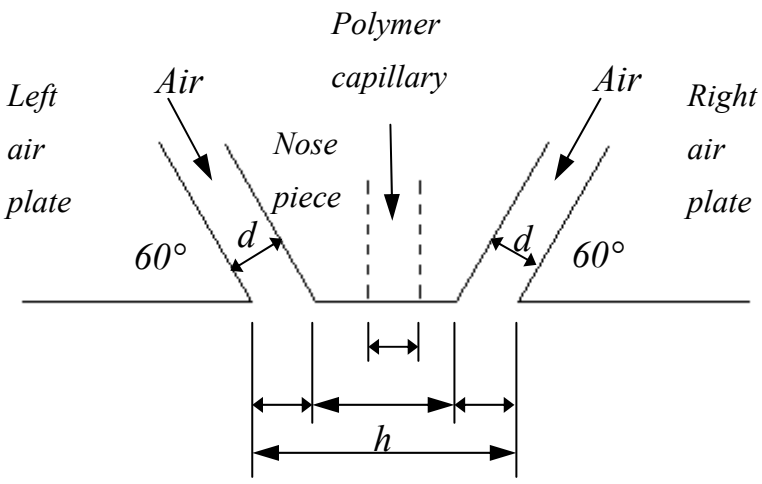

Fig. 33. A cross-sectional view of the 60° blunt air die [32].

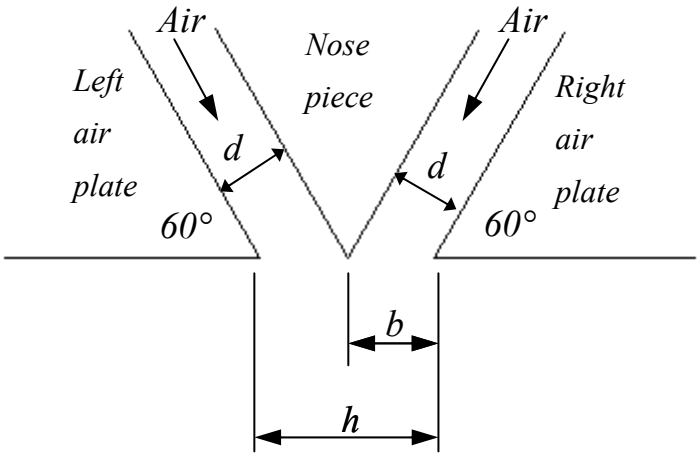

Fig. 34. A cross-sectional view of 60° sharp die [32].

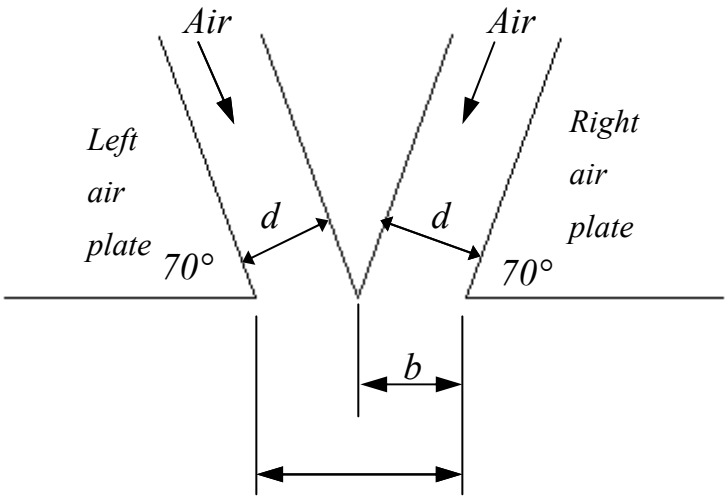

Fig. 35. The 70° sharp die [32].

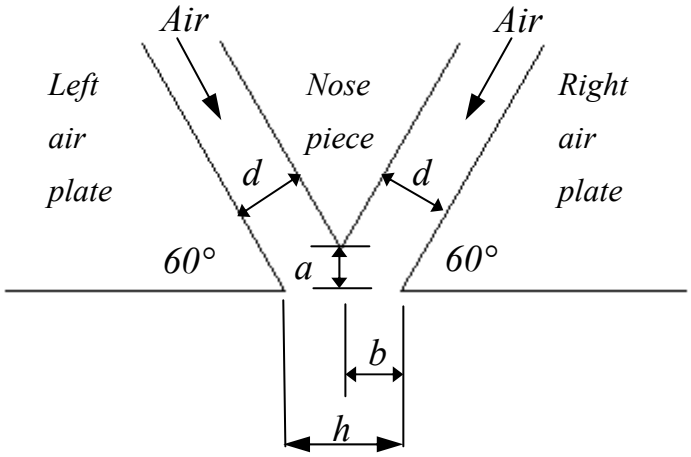

Fig. 36. The inset die [32].

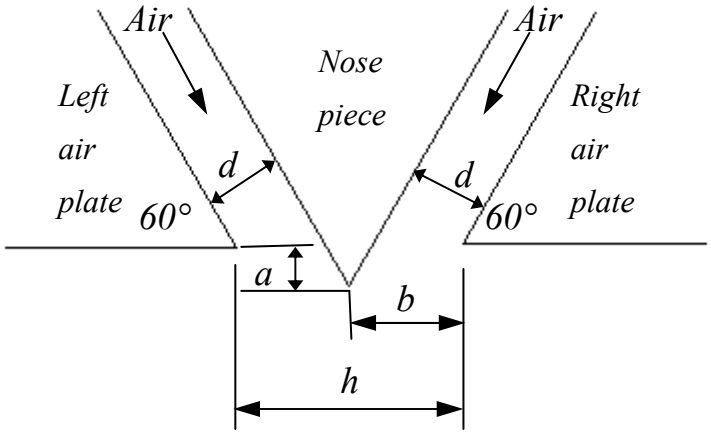

Fig. 37. The outset die [32].

It has been founded than the flow field of a sharp 60° die has a higher maximum velocity and the peaks merge sooner than velocity peaks of a blunt 60° die. Thus, a sharp 60°die is aerodynamically superior to a blunt 60° die. The maximum velocity of the sharp 70° die is higher than the velocity of the blunt 60° die. However, the maximum velocity of the sharp 70° die is less than the velocity of the sharp 60° die. Hence, of the three die types tested, the sharp 60° die is aerodynamically superior. Inset dies have higher velocities than flush dies. A slightly dulled 60° die is a good die configuration to start with when melt blowing a new fiber. The inset of the die can be varied unit the optimum inset is determined from actual melt-blowing experiments.

5.3 Nanofiber structure morphology

Fabrication and characterization of polypropylene nanofibers by meltblowing process using different fluids have been investigated in [19]. Polypropylene has been successfully used for the fabrication of nanowebs by meltblowing process with the injection of different fluids (such as air and water) at the vent port of commercial meltblowing equipment. The lowest average fiber diameters achieved were 755 and 438 nm by the use of air and water. The results obtained from thermo gravimetric analysis and intrinsic viscosity studies showed thermal degradation of the nanofibers during meltblowing. X-ray diffraction studies showed that all the meltblown polypropylene fibers produced with the injection of the fluids contained low degrees of crystallinity and monoclinic α-form.

Modeling the melt blowing of viscoelastic materials has been analyzed in [22]. Fiber diameter generally decreases with air flow rate (or shear stress on the fiber surface). For the experimental conditions considered by Tan et al. (2010), our slender-jet model combined with computational fluid dynamics calculations suggested that non-uniform shear stress and thermal effects do not play important roles. For sufficiently large elasticity, disturbances decay faster relative to the Newtonian case and the oscillation frequencies were found to be smaller.

Production of polypropylene melt blown nonwoven fabrics: Numerical simulation and prediction of fiber diameter has been discussed in [33]. The fiber diameter was directly related to the polymer throughput rate, polymer melt initial temperature, die-to-collector distance, air initial temperature, and air initial speed, i.e. the finer the geometric mean of fiber diameter, the more uniform is the fiber web. A lower polymer throughput rate, higher initial polymer melt temperature, higher air initial temperature, large die-to-collector distance, and higher air initial velocity can yield finer fibers.

Production of polypropylene melt blown nonwoven fabrics: Effect of process parameters has been investigated in [34]. The results showed that the web weight unevenness increased with the increased polymer throughput rate and accessory air pressure, the web weight unevenness decreased initially and then increased with the increased air initial pressure and die-to-collector distance. The fiber diameter decreased with the increased air initial pressure and accessory air pressure and reductions in air initial pressure, the fiber diameter decreased initially and then increased with the increased die-to-collector distance. It was concluded that the polymer throughput rate, accessory air pressure, air initial pressure and die-to-collector distance are the key factors in controlling the web weight unevenness of melt blowing nonwoven, and the lower polymer throughput rate, large air initial pressure, large accessory air pressure and die-to-collector distance will be of benefit to produce finer fiber diameter.

Prediction of angular and mass distribution in meltblown polymer lay-down has been analyzed in [21]. It was found that as screen speed increases, fibers are more uniformly oriented and deposited mass is more uniformly distributed. It was also found that screen speed

has no effect on polymer mass flow rate for a smoothly running operation. The results also showed that the lay-down non-uniformity can be attributed to the wide distribution of relaxation time rather than to the distribution of the activation energy of solidification.

Influence of viscosity and elasticity on diameter distribution has been investigated in [4]. Both melt viscosity (η_0) and elasticity (correlated here with the longest melt relaxation time λ_1) were found the control the diameter distribution of meltblown fibers. These rheological parameters influenced the average diameter (d_{av}) and the distribution of diameters (coefficient of variation, CV) of melt blown fibers in different ways. The main conclusion from this work were following. Increasing η_0 leads to an increase in d_{av} but has little impact on CV. On the other hand, increasing λ_1 beyond a threshold value reduces CV while simultaneously increasing d_{av}

Fiber diameter distributions and onset of fiber breakup has been studied in [24] for poly(butylene terephthalate), polypropylene and polystyrene. It has been found that it is possible to decrease the average fiber diameter below 500 nm by modulating several different processing parameters. It was concluded that the obtained results closed the gap between melt blowing technology and electrospinning in terms of the ability to produce nano-scale fibers.

6 CONSTITUTIVE EQUATIONS FOR POLYMER MELTS

Constitutive equations are mathematical relationship that allow computing of the stresses in a liquid for a given flow history. They are often derived from constitutive models, which imply a set of assumptions and idealization about the molecular or structural forces and motions producing stress. Polymers, characterized by relatively long macromolecules, do not obey simple physical laws because their behavior lies between Newtonian liquids and Hookean solids [35]. The Figure 38 shows different constitutive equations in the limits of low strain rates, low amplitude deformations, and high strain rates. Detail description of each model is provided in the next chapter.

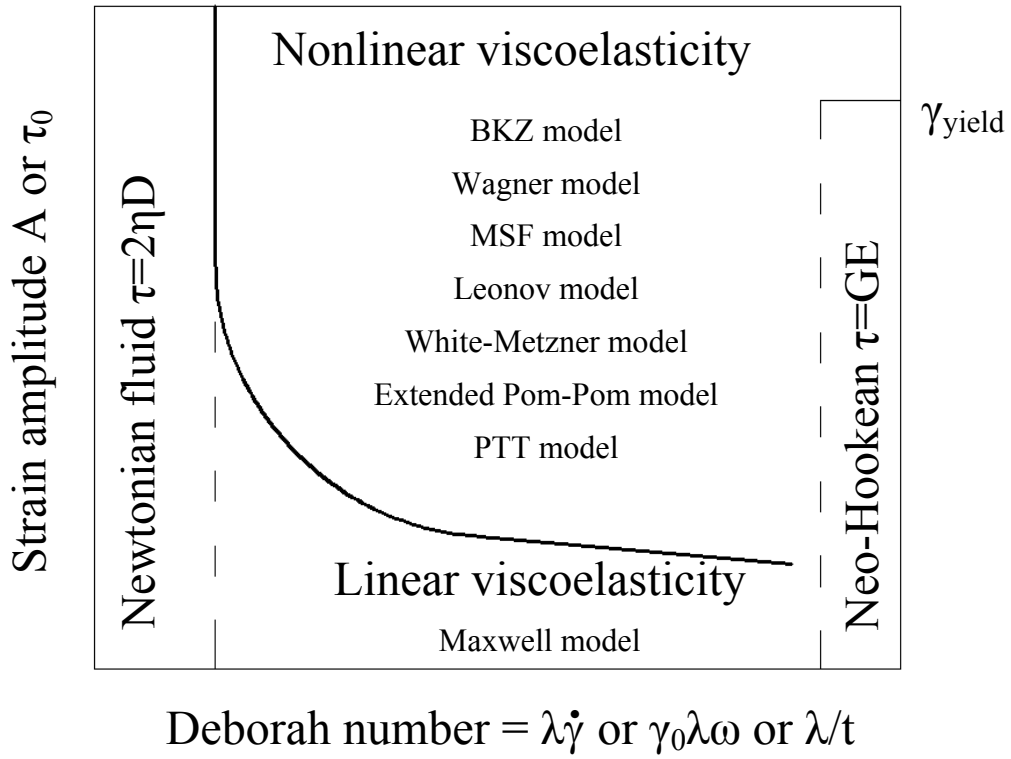

Fig. 38. Schematic diagram showing the behavior of viscoelastic fluids in the limits of low strain rates, low amplitude deformations, and high strain rates [9].

6.1 Viscous liquid

6.1.1 Generalized Newtonian fluid-model

The generalized Newtonian fluid model represents generalization of the well known Newtonian for incompressible fluids, which is given by the following expression:

$$\underline{\underline{\tau}} = 2\eta_0 \underline{\underline{D}} \tag{36}$$

where $\underline{\underline{\tau}}$ represent the extra stress tensor, η_0 is the Newtonian viscosity, and $\underline{\underline{D}}$ stand for the deformation rate tensor.

In the Generalized Newtonian fluid model, the constant Newtonian viscosity is replaced by the viscosity function depending on the deformation rate tensor invariants [5].

6.1.1.1 Power-Law model

The power-law model describes viscosity with a function that is proportional to some power of the shear rate second invariant of deformation rate tensor [5]:

$$\eta = m\left(II_D\right)^{\frac{n-1}{2}} \tag{37}$$

It is important to remember that this version is valid only for simple shear. In processing range of many polymeric liquids and dispersion the power-law is a good approximation to the data from viscosity versus shear rate. At high shear rate $\dot{\gamma} > 1$, the power –law fits the data well, with m representing a function of temperature. One of the obvious disadvantages of the power-law is that it fails to describe the low shear region. Since n is usually less than one, at low shear rate η goes to infinity rather than to a constant η_0 [9].

6.1.1.2 Carreau-Yasuda model

A viscosity model that capture more details of the shape of experimentally measured $\eta(\dot{\gamma})$ curves is the Carreau-Yasuda model. The Carreau-Yasuda model uses five parameters:

$$\frac{\eta\left(\sqrt{II_D}\right) - \eta_\infty}{\eta_0 - \eta_\infty} = \left[1 + \left(\sqrt{II_D}\lambda\right)^a\right]^{\frac{n-1}{a}} \tag{38}$$

or

$$\eta(\mathrm{II}_D) = \frac{\eta_0 a_t}{\left[1 + \left(\lambda a_t \sqrt{\mathrm{II}_D}\right)^a\right]^{(1-n)/a}} \tag{39}$$

where η_∞ is the viscosity function approaches the constant value η_∞ as $\dot{\gamma}$ gets large, η_0 is the viscosity function approaches the constant value η_0 as $\dot{\gamma}$ becomes small, a is the exponent affects the shape of the transition region between the zero-shear-rate plateau and rapidly decreasing (power-law-like) portion of the viscosity versus shear-rate curve, i.e. increasing a sharpens the transition, λ is the relaxation time of the liquid determining the shear rate at which the transition from Newtonian power-law model range takes the place, n is the power-law-index that is related to the slope of the rapidly decreasing portion of the η curve, a_t is temperature shift factor, II_D is the second invariant of the deformation rate tensor.

The role of each Carreau-Yasuda model parameter on the shear rate dependent viscosity is provided in [5, 36]

6.1.1.3 Macosko model

Macosko suggested the following viscosity function for the generalized Newtonian law:

$$\eta = \eta_0 \frac{\left(1 + m|\mathrm{II}_D|\right)^{(n-1)/2}}{\left[1 + 3m\left(3\mathrm{III}_D / \mathrm{II}_D\right)^2\right]^{(n-1)/2}} \tag{40}$$

where *m, n* and η_0 are adjustable model parameters, $\mathrm{II_D}$ and $\mathrm{III_D}$ represent second and third invariant of deformation rate tensor [9].

6.1.1.4 Zatloukal model

Zatloukal has proposed the following specific viscosity function in generalized Newtonian law, which allows properly represent flow behavior of the polymer melts in shear as well as extensional flows:

$$\eta\left(\mathrm{I}_{|D|}, \mathrm{II}_D, \mathrm{III}_D, |\mathrm{III}_D|\right) = A^{1-f\left(\mathrm{I}_{|D|}, \mathrm{II}_D, \mathrm{III}_D, |\mathrm{III}_D|\right)} \eta(\mathrm{II}_D)^{f\left(\mathrm{I}_{|D|}, \mathrm{II}_D, \mathrm{III}_D, |\mathrm{III}_D|\right)} \tag{41}$$

where $\eta\ (\mathrm{II_D})$ is given by the well known Carreau-Yasuda model, and exponent $f\left(\mathrm{I}_{|D|},\mathrm{II}_D,\mathrm{III}_D,|\mathrm{III}_D|\right)$ is given by Eq. (42).). The first, second and third invariant of the deformation rate tensor are defined as $\mathrm{I_D} = \mathrm{tr}(\mathrm{D}), \mathrm{II_D} = 2\mathrm{tr}(\mathrm{D}^2)$ and $\mathrm{III_D} = \det(\mathrm{D})$.

$$f\left(\mathrm{I}_{|D|},\mathrm{II}_D,\mathrm{III}_D,|\mathrm{III}_D|\right)=\left\{\tanh\left[\alpha\, a_t\left(1+\frac{1}{4\left(\sqrt{3}\right)^3}\right)^{-\psi}\left(\left|1+\frac{\mathrm{III}_D}{\mathrm{II}_D^{3/2}}\right|\right)^{\psi}\frac{\sqrt[3]{4|\mathrm{III}_D|+\mathrm{I}_{|D|}}}{3}+\beta\right]\frac{1}{\tanh(\beta)}\right\}^{\zeta} \tag{42}$$

where $\eta_0, \lambda, a, n, \alpha, \psi, \beta, \zeta$ are adjustable parameters and a_t is the temperature shift factor [35].

6.2 Linear viscoelasticity

6.2.1 Maxwell model

The Maxwell model can be represented by a purely viscous damper and a purely elastic spring connected in series and mathematically it relates the stress tensor and the deformation rate tensor through the following equation:

$$\underline{\underline{\tau}} + \lambda \overset{\nabla}{\underline{\underline{\tau}}} = 2\eta_0 \underline{\underline{D}} \tag{43}$$

The Maxwell model can also be expressed in the integral form [5]

$$\underline{\underline{\tau}}(t) = -\int_{-\infty}^{t}\left[\frac{\eta_0}{\lambda}e^{\frac{-(t-t')}{\lambda}}\right]\underline{\underline{\dot{\gamma}}}(t')\,dt' \tag{44}$$

where t' represents the dummy variable of integration, t is the current time at which the stress is calculated.

6.3 Nonlinear viscoelasticity

6.3.1 The BKZ model

Lodge´s rubberlike liquid model is the simplest theory of nonlinear viscoelasticity that is capable of predicting most features of the first appearance of nonlinear behavior, when both the size and the rate of the deformation exceed the ranges in which linear behavior is observed. The BKZ equation proposed by Bernstein, Kearsley and Zapas. Making use of

concepts originally used in the development of the theory of rubber viscoelasticity, they proposed the following form for the constitutive equation of a viscoelastic material.

$$\tau_{ij}(t) = \int_{-\infty}^{t} \left[2\frac{\partial u}{\partial I_1} Cij(t,t') - 2\frac{\partial u}{\partial I_1} B_{ij}(t,t') \right] dt' \tag{45}$$

where u is a time-dependent elastic energy potential function:

$$u = u(I_1, I_2, t - t') \tag{46}$$

This function must be determined experimentally, by the study of large, rapid deformations [37]. In these two above described equations, the symbol meaning is the following: Cij is the Cauchy tensor, B_{ij} is the Finger tensor, I_1, I_2 - first and second scalar invariant of a Finger tensor, τ_{ij} is the extra stress tensor.

6.3.2 The Wagner model

The direct analogy between elasticity of rubbers and flow of polymeric systems is the ground for several versions of the Wagner-models. In its initial form of W-I model, it was suggested that large deformations influence a relaxation spectrum and a constitutive equation of state has the following general form:

$$\sigma_{ij} = \int_{-\infty}^{t} M(t - t'; I_1, I_2) C_{ij}^{-1} dt' \tag{47}$$

where M is non-linear memory function dependent on variants of the deformation tensor.

The simplification of dividing of the memory function into the product of a linear member and the "function of influence":

$$M(t - t'; I_1, I_2) = m(t - t') h(I_1, I_2) \tag{48}$$

where the memory function $m(t - t')$ is determined in the range of linear viscoelasticity, and the function $h(I_1, I_2)$ is called the damping function, and the latter can be treated as the consequence of influence of deformations on viscoelastic behavior of material [10].

The final equation of W-I model takes the following form:

$$\sigma_{ij} = \int_{-\infty}^{t} m(t-t')h(I_1, I_2)C_{ij}^{-1}dt' \tag{49}$$

6.3.3 Molecular stress function (MSF) model

The MSF model is a single tube segment integral constitutive equation, with the main feature of including the stretch as a relative quantity inside the history integral. Considering the interchain tube pressure effect in the evolution equation for the stretch, elongation rheology of monodisperse linear polymer melts could be modeled successfully.

$$S_m(t,t') = f^2 S_{DE}^{IA}(t,t') \tag{50}$$

$S_m(t,t')$ is a general strain measure and might be considered as the deformation measure of the material. The square of the relative tension in the chain segments, f^2, is related to the strain energy stored in the polymeric system and is therefore strongly dependent on the molecular structure of the polymer. $S_{DE}^{IA}(t,t')$ is the strain measure representing the affine rotation of tube segments and corresponds to the so-called "independent alignment (IA)" assumption in the Doi-Edwards model [38].

6.3.4 The Leonov model

The Leonov model is based on hypothesis that the rubbery state (where equilibrium elastic deformations have been stored) is the internal thermodynamic equilibrium state in flow of viscoelastic fluids. Any deviation from this state cause non-equilibrium. In contrast to the KBZ and Wagner models, this model is of differential type. Its original derivation was based on irreversible thermodynamics and the classical potential function of the network theory of elasticity. Irreversible thermodynamics supplies the necessary relationship between the dissipative part of the strain rate and the dissipative part of stress. This constitutive model is derived from the thermodynamic idea that the stress in flowing polymer is related to the store elastic energy [10].

$$\sigma = 2\eta_0 sD + 2\sum_{k=1}^{N}\left(W_{k,1}C_k + C_k^{-1}W_{k,2}\right) \tag{51}$$

W_k is taken according to the classical potential function of the network theory of elasticity.

$$W_k = G_k\left(I_{k,1} - 3\right) \tag{52}$$

where C_k is the elastic strain tensor, $I_{k,1}$ is the first invariant of C_k, G_k is the modulus, D is the strain rate tensor, η_0 is the Newtonian viscosity of the fluid, s is rheological parameter lying between 0 and 1.

Although the Leonov model has been found to give an excellent agreement to transient and steady shear flow experiments for a number of polymer melts and solutions, it is incapable of representing elongational flows realistically, the steady elongational viscosity is virtually independent of strain rate. Thus, it is not surprising that considerable progress has been made to improve such behavior through generalization of the elastic potential, W [35]:

$$W = \frac{3G}{2(n+1)}\left\{(1-\beta)\left[\left(\frac{I_1}{3}\right)^{n+1} - 1\right] + \beta\left[\left(\frac{I_2}{3}\right)^{n+1} - 1\right]\right\} \tag{53}$$

where G is the Hooken elastic modulus, β and n are non-linear model parameters, I_1 and I_2 are invariants of the recoverable Finger tensor.

6.3.5 Modified White-Metzner model

The White-Metzner constitutive equation is a simple Maxwell model for which the viscosity and relaxation time are allowed to vary with the second invariant of the strain rate deformation tensor. It takes the following form [35]:

$$\underline{\underline{\tau}} + \bar{\lambda}(\mathrm{II}_D, T)\overset{\nabla}{\underline{\underline{\tau}}} = 2\eta(\mathrm{II}_D, T)\underline{\underline{D}} \tag{54}$$

where the $\underline{\underline{\tau}}$ is the stress tensor, $\bar{\lambda}(\mathrm{II}_D, T)$ stands for the deformation rate-dependent relaxation time, $\overset{\nabla}{\underline{\underline{\tau}}}$ is the upper convected stress tensor derivate, $\eta(\mathrm{II}_D, T)$ is the deformation rate-dependent viscosity and $\underline{\underline{\mathrm{D}}}$ is the deformation rate tensor.

6.3.6 Pom-Pom model

The recently introduced Pom-Pom model by McLeish and Larson (1998), improved with local branch-point displacement before maximum stretching and adopted in a multimode approach, seems to be a breakthrough in the field of viscoelastic constitutive equations due to separation of relaxation times for stretch and orientation allowing to overcome three drawbacks: solutions in steady state elongation show discontinuities, the equation for orientation in unbounded for high strain rates, the model does not have a second normal stress difference in shear. The extended Pom-Pom model does not show the three problems and is easy for implementation in finite element packages, because it is written in the following a single equation [35, 39]:

$$\overset{\nabla}{\underline{\underline{\tau}}} + \underline{\underline{\underline{\underline{\lambda(\tau)}}}}^{-1} \underline{\underline{\tau}} = 2G\underline{\underline{D}} \tag{55}$$

where $\overset{\nabla}{\underline{\underline{\tau}}}$ is the upper convected stress tensor derivate, $\underline{\underline{\underline{\underline{\lambda(\tau)}}}}^{-1}$ is the relaxation time tensor, $\underline{\underline{\tau}}$ is the stress tensor, G is the Maxwell modulus, $\underline{\underline{D}}$ is the deformation rate tensor.

6.3.7 PTT model

Based on network theory of rubber-like fluids, Phan Thien and Tanner developed in 1977 the PTT model which is one of the most widespread non-linear model in use [40](cf. critical appraisal by Quinzani et al.) and, when the lower convected term in the generalized Jaumann derivate is not considered, by setting the parameter $\xi = 0$ to avoid non-affine deformations, the constitutive equation is usually written as (PTT model):

$$f\tau + \lambda\left(\overset{\nabla}{\tau}\right) = 2\eta_P D \tag{56}$$

where D is the deformation rate tensor, $\overset{\nabla}{\tau}$ is the upper convected stress tensor derivate, τ is the stress tensor, and λ and η_P as a constant model parameters with the usual meaning [41].

The PTT model can be considered to be one of the most realistic models for polymer melts and concentrated solutions [42].

II. ANALYSIS

7 MATERIALS

In this work, the following polymer have been used:

- PP, Daploy WB180HMS: Melt Flow Rate (230˚C/ 2,16 kg) = 6 g/10min, Melting temperature = 163˚C, Properties – High melt strength and increased melt extensibility. Branched polymer.
- PP, Borflow HL504 FB B2-70006: Melt Flow Rate (230˚C/ 2,16 kg) = 450 g/10min, Melting temperature (DSC) = 161˚C, Molecular weight distribution - very narrow. Linear polymer.
- PP, Borflow HL508 FB : Melt Flow Rate (230˚C/ 2,16 kg) = 800 g/10min, Melting temperature (DSC) = 158˚C, Molecular weight distribution - very narrow. Linear polymer
- PP, Borflow HL512 FB B2-90367: Melt Flow Rate (230˚C/ 2,16 kg) = 1200 g/10min, Melting temperature (DSC) = 158˚C, Molecular weight distribution - very narrow. Linear polymer
- PP, Blend 1 (TPPP 122146-1): 90wt-% HL512FB + 10wt-% WB180HMS, Melt Flow Rate (230˚C/ 2,16 kg) = 800 g/10min
- PP, Blend 2 (TPPP 122146-2): 80wt-% HL512FB + 20wt-% WB180HMS, Melt Flow Rate (230˚C/ 2,16 kg) = 615 g/10min
- PP, Blend 3 (TPPP 122146-3): 70wt-% HL512FB + 30wt-% WB180HMS, Melt Flow Rate (230˚C/ 2,16 kg) = 440 g/10min

8 EQUIPMENT AND METHODS

In this work, the twin bore capillary rheometer RH7-2 (Rosand Precision, Ltd., Great Britain) has been used to determine basic rheological characteristics of given melt blown polymer samples. Description of the experimental set-up is provided in the next chapter.

8.1 Capillary rheometer Rosand RH7-2

The twin bore capillary rheometer Rosand RH7-2 (Rosand Precision, Ltd., Great Britain), allows to push the polymer melt in the controlled way through a defined capillary dies with simultaneous recording of corresponding pressure drops. Two measurements are usually performed simultaneously at the same time on two capillary dies having the same diameter but different length (long die and the orifice die with zero length). The capillary rheometer is depicted in (Fig. 39-41).

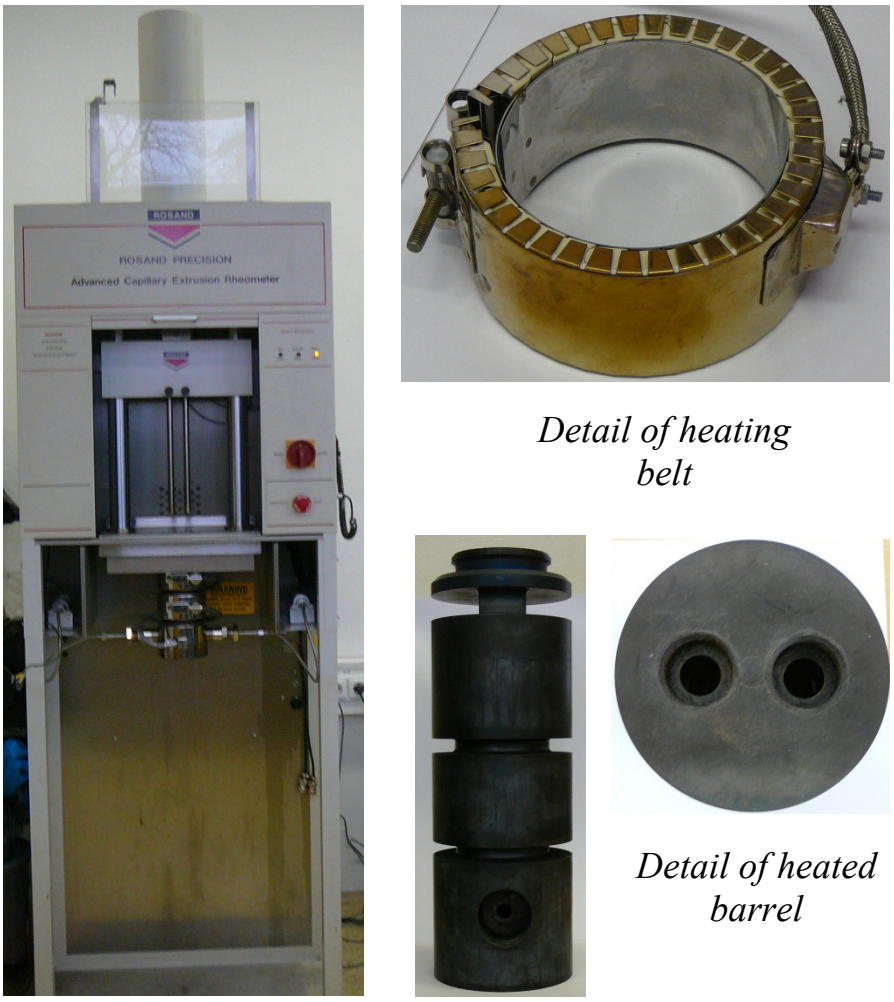

Fig. 39. Photo of Rosand RH7-2 twin-bore capillary rheometer.

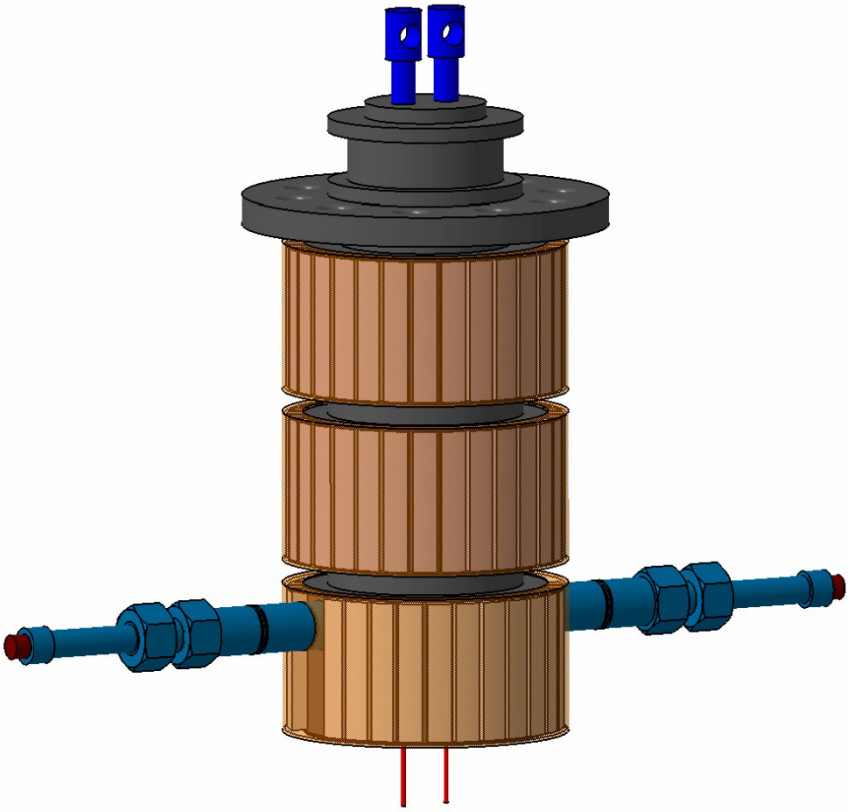

Fig. 40. Scheme of Rosand RH7-2 twin-bore capillary rheometer.

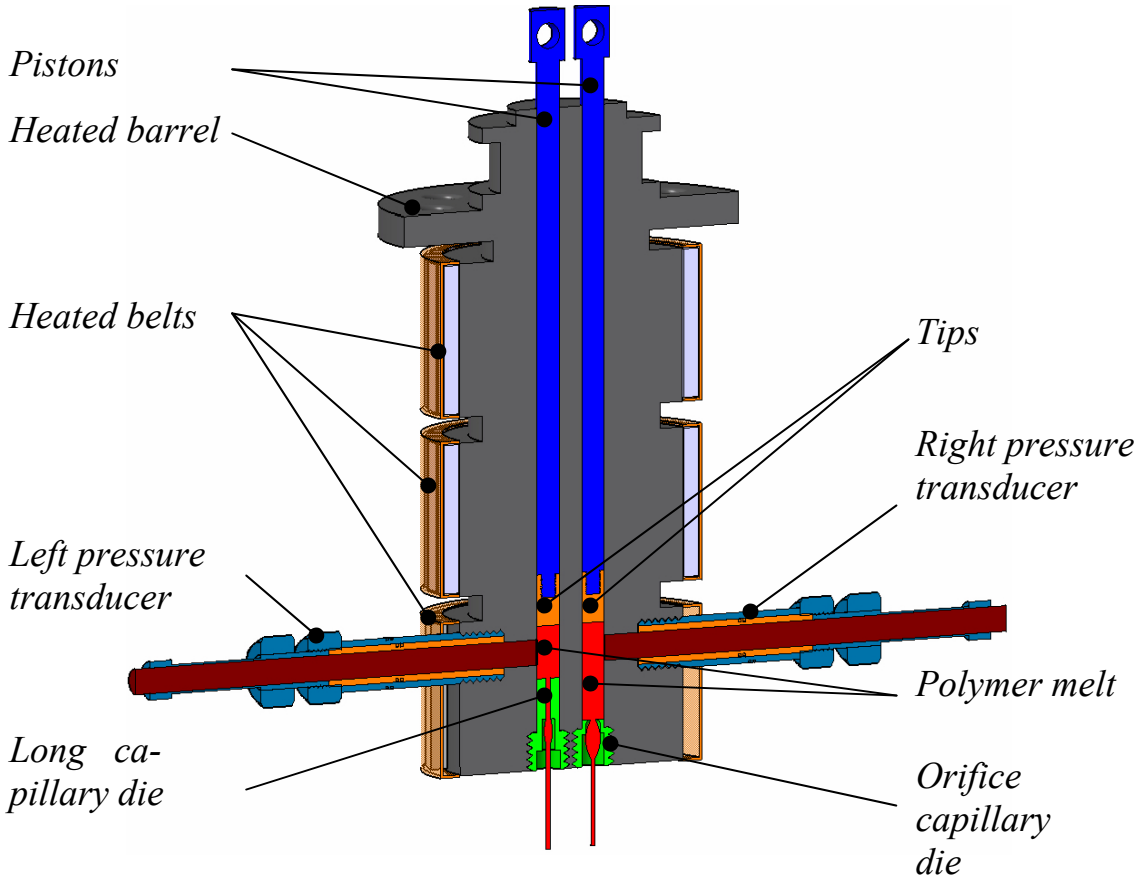

Fig. 41. Section of Rosand RH7-2 twin-bore capillary rheometer.

In order to evaluate the flow behavior in shear as well as the uniaxial and planar elongational flows, circular as well as rectangle dies with varied length and diameter/gap size depicted in (Fig. 42) were used. More detail information about the utilized dies are provided in (Tab. 19). Detail view of the utilized circular and rectangle dies is provided in (Fig. 43-44) and (Fig. 45-46) respectively. It has to be mentioned that the circle as well as rectangle orifice dies utilized in this work have open downstream region, which does not allows any polymer melt sticking at the die exit wall as visible in (Fig. 55, 57). Due to this reason, the measured entrance pressure drop can be considered to be very precise.

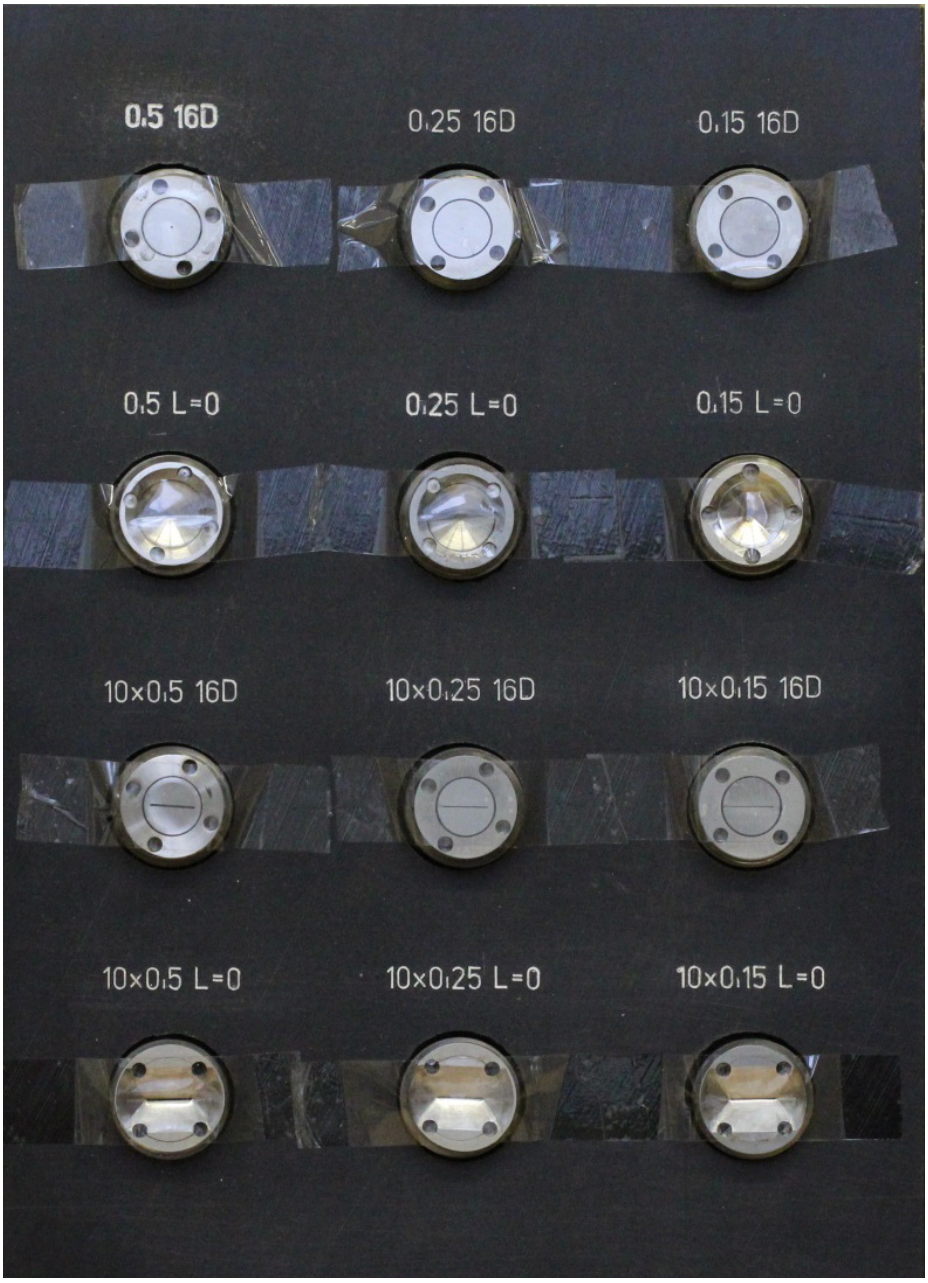

Fig. 42. Circular and rectangle dies utilized in this work.

Tab. 19. Detail description of circular and rectangle dies utilized in this work. Here D represents the capillary diameter, W is the width and H is the gap size, all in mm.

Type of flow	*Type of capillary die*	*Length of capillary [mm]*	*Diameter or dimensions of slot [mm]*
Uniaxial	Orifice (short)	0	D = 3
		0	D = 1
		0	D = 0,5
	Long	42	D = 3
		16	D = 1
		8	D = 0,5
Planar	Orifice (short)	0	W = 10, H = 1
		0	W = 10, H = 0,5
		0	W = 10, H = 0,15
	Long	16	W = 10, H = 1
		8	W = 10, H = 0,5
		2,4	W = 10, H = 0,15

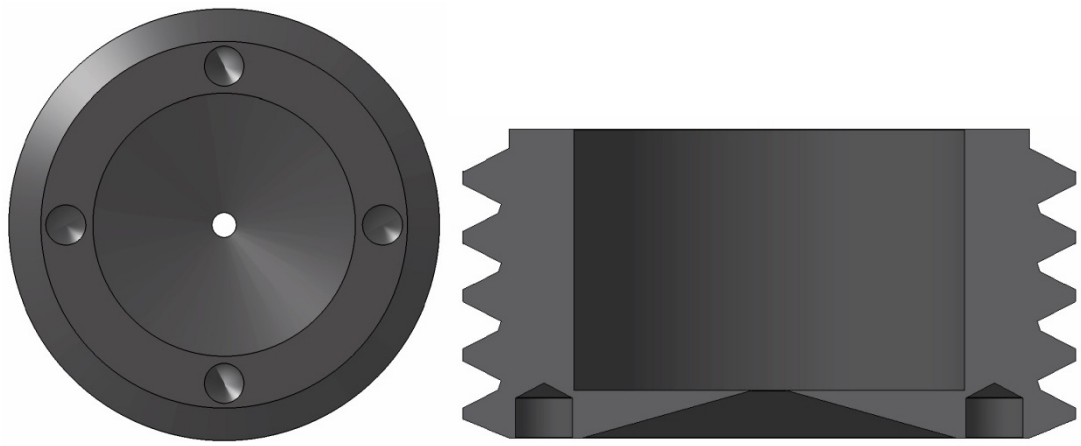

Fig. 43. Bottom (left) and section (right) view of the circle orifice die.

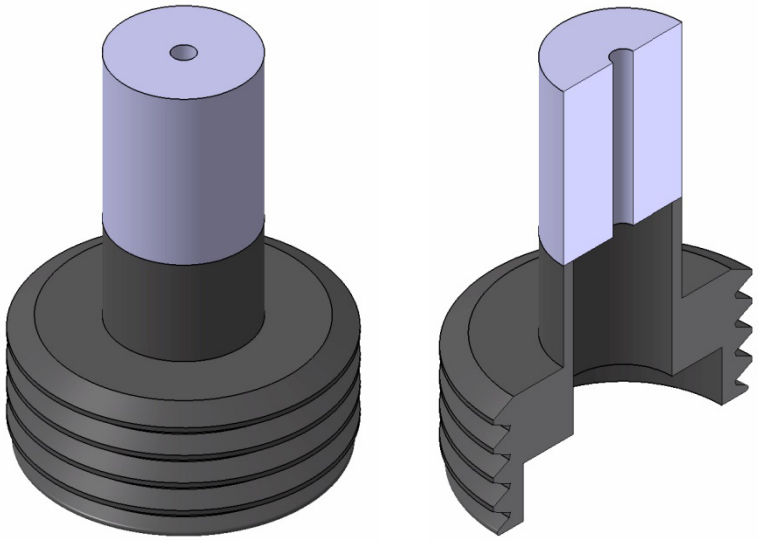

Fig. 44. Bottom (left) and section (right) view of the circle long die.

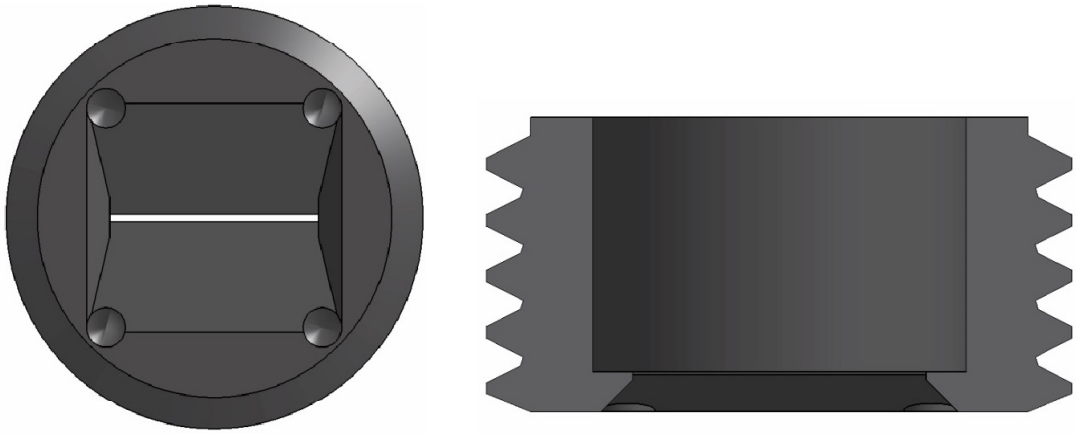

Fig. 45. Bottom (left) and section (right) view of the rectangle orifice die.

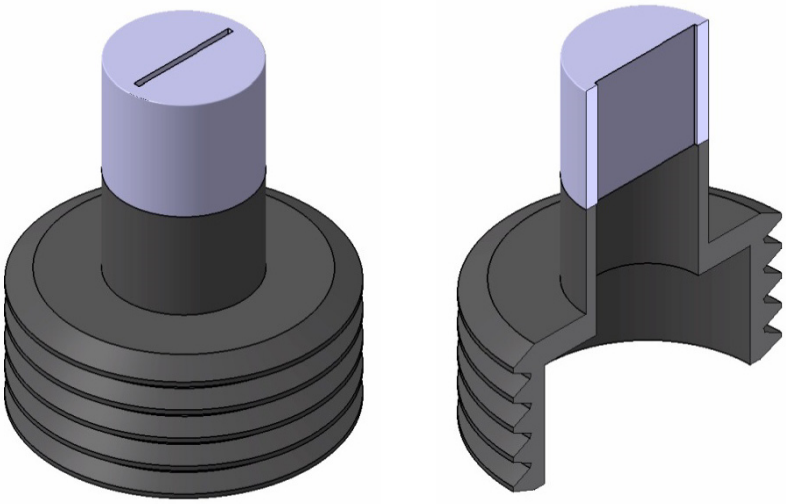

Fig. 46. Bottom (left) and section (right) view of the rectangle long die.

In order determine the pressure drop through the circle as well rectangle dies at wide range of deformation rates for all tested polymer samples, different pressure transducers (Dynisco, USA) were used (see Tab. 20).

Tab. 20. Pressure transducer types utilized in this work.

Range [PSI]	***Range [MPa]***
10000	68,9476
1500	10,3421
500	3,4473
250	1,7237

8.1.1 Shear viscosity determination

The shear flow behavior for all tested samples was evaluated by determination of the apparent wall shear stress and apparent wall shear rate from the measured long die pressure drop and piston speed. Bagley and Rabinowitsch corrections were consequently applied for the apparent wall shear stress and apparent wall shear rate, respectively (see Tab. 5 and chapter 2.1.1.2 for more details) in order to calculate correct value of the shear viscosity as the ratio of the corrected wall shear stress and corrected wall shear rate i.e. according to Eq. 3.

8.1.2 Uniaxial and planar entrance viscosities determination and evaluation

In order to evaluate flow behavior of tested polymer melts in uniaxial and planar elongational flows, entrance pressure drop was measured on the annular and rectangle orifice dies as the function of the apparent shear rate. Both measured variables were consequently used to calculate uniaxial entrance viscosity as well as planar entrance viscosity, which are defined according to [43] in the following way:

$$\eta_{ENTR,U} = \frac{P_{entr,\,circle}}{\dot{\gamma}_{APP}} \tag{57}$$

$$\eta_{ENTR,P} = \frac{P_{entr,\,rectangle}}{\dot{\gamma}_{APP}} \tag{58}$$

where $\eta_{ENTR,U}$ and $\eta_{ENTR,P}$ represents uniaxial and planar entrance viscosity, respectively, $P_{entr,\ circle}$ and $P_{entr,\ rectangle}$ represents entrance pressure drop through the circular and rectangle orifice die, respectively, and $\dot{\gamma}_{APP}$ represents apparent shear rate. In this work, the following function proposed in [43] was used to fit the measured entrance viscosity data.

$$\log(\eta_{ENT}) = \log\left(\frac{\eta_{ENT,0}}{\left[1+(\lambda'\dot{\gamma}_{APP})^{a'}\right]^{(1-n')/a'}}\right)\left[\frac{\tanh(\alpha\dot{\gamma}_{APP}+\beta)}{\tanh(\beta)}\right]^{\xi} \tag{59}$$

where the parameters α, β and ξ control the shape of the entrance viscosity maximum.

It is not difficult to show that based on [43-44], both entrance viscosities are linked together at the zero shear rate range through the following simple relationship:

$$\frac{\eta_{ENTR,U,0}}{\eta_{ENTR,P,0}} = \sqrt{2} \tag{60}$$

where $\eta_{ENTR,U,0}$ and $\eta_{ENTR,P,0}$ represents uniaxial and planar entrance viscosity plateau, respectively. Moreover, there is direct relations between the $\eta_{ENTR,\ U,\ 0}$ and zero shear viscosity as shown in [43], which is only orifice die design dependent, (i.e. it does not depends on the polymer type used).

$$\frac{\eta_{ENTR,U,0}}{2\eta_0} = const. \tag{61}$$

8.2 Meltblown line

Production of the nanofiber based nonwovens for chosen polymer was realized on the pilot plant meltblown line, which is depicted in (Fig. 47). The meltblown line consist of extruder (Fig. 48), melt blown die (Fig. 49) equipped by die nosepiece (Fig. 50), collector (Fig. 51), exhaust and reservoir (Fig. 52). It should be mentioned that the die nosepiece visualized in (Fig. 50) has the following parameters: length 350 mm, active part 250 mm, 0,4 mm diameter orifice spaced 470 per active part. During the meltblown nonwoven production, the following processing conditions were varied: melt temperature, die-collector distance and collector belt speed.

Fig. 47. Melt blown pilot plant line.

48a, *48b,*

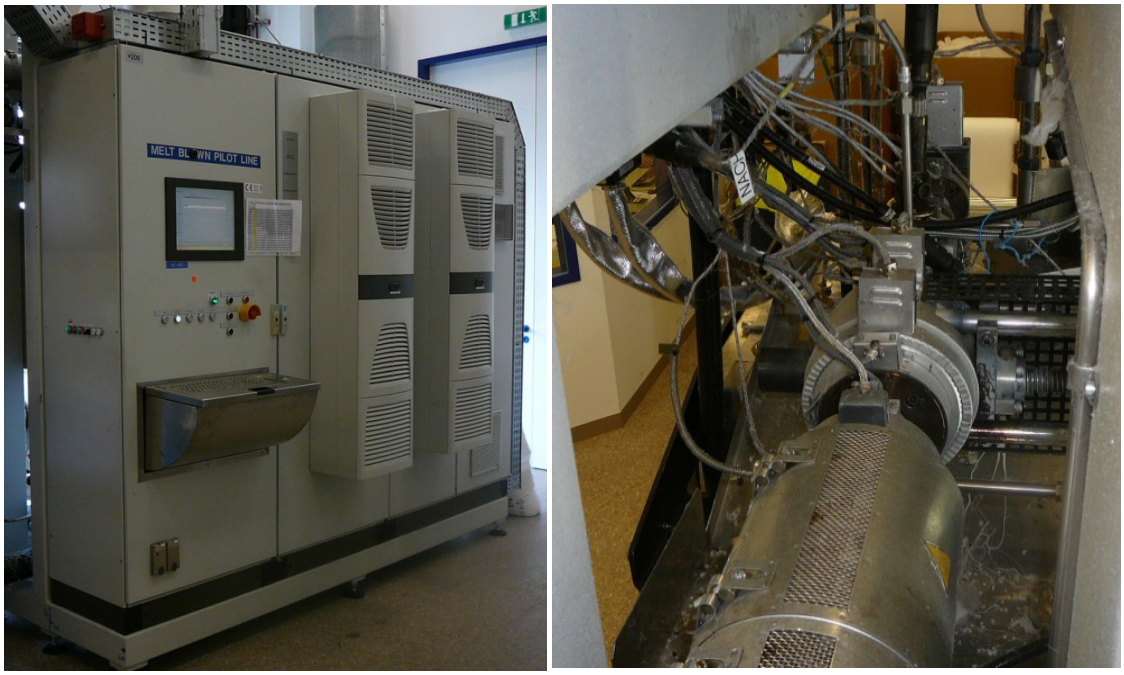

48c,

Fig. 48. Melt blown extruder. 48a, Control unit. 48b) detail view of the feeding part inclunding the hopper. 48c) Detail view of the extruder heating belts.

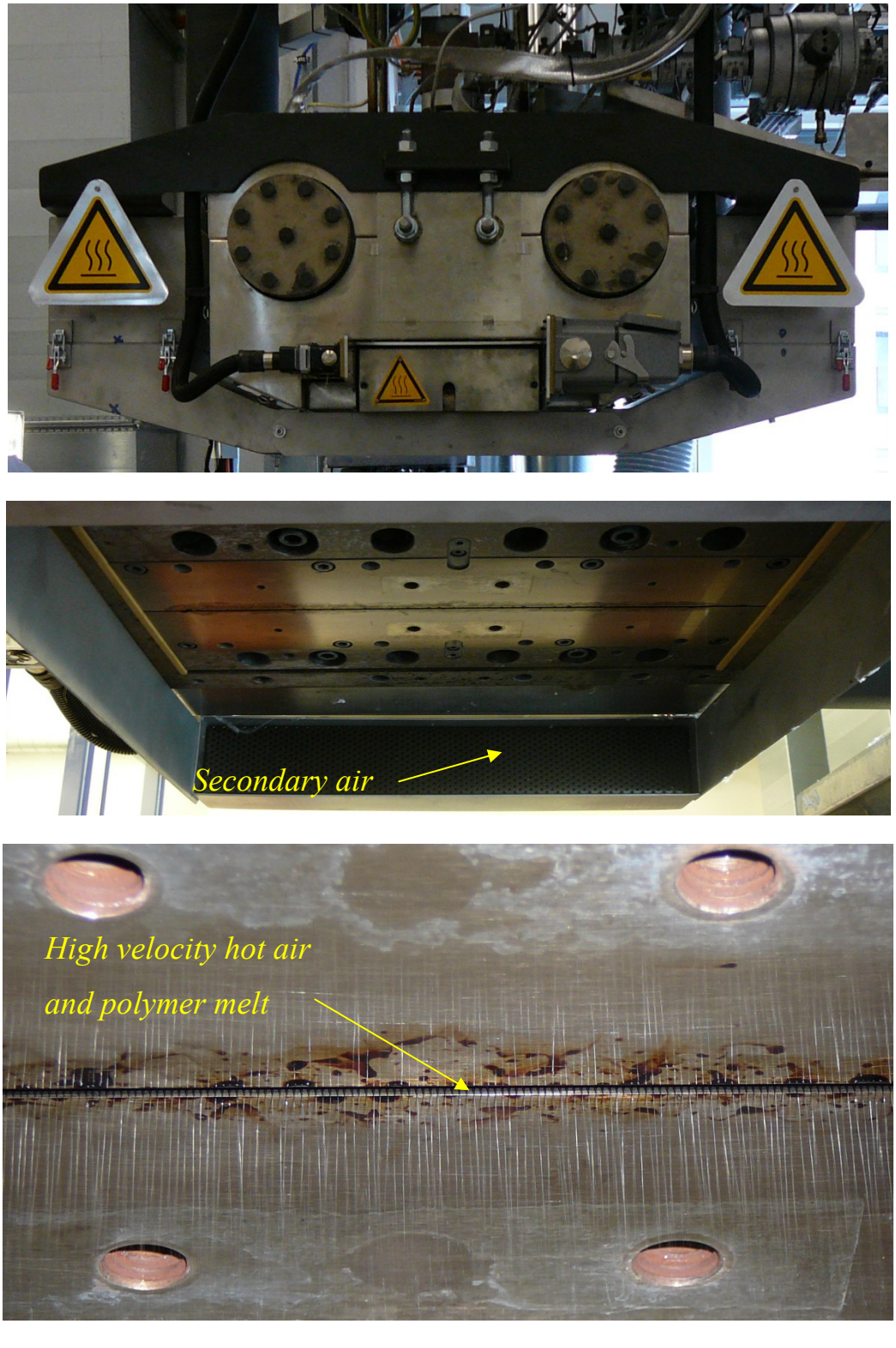

Fig. 49. Meltblown die visualization (top-side view, middle-angle view, bottom-detail view allowing to seeing the fiber formation).

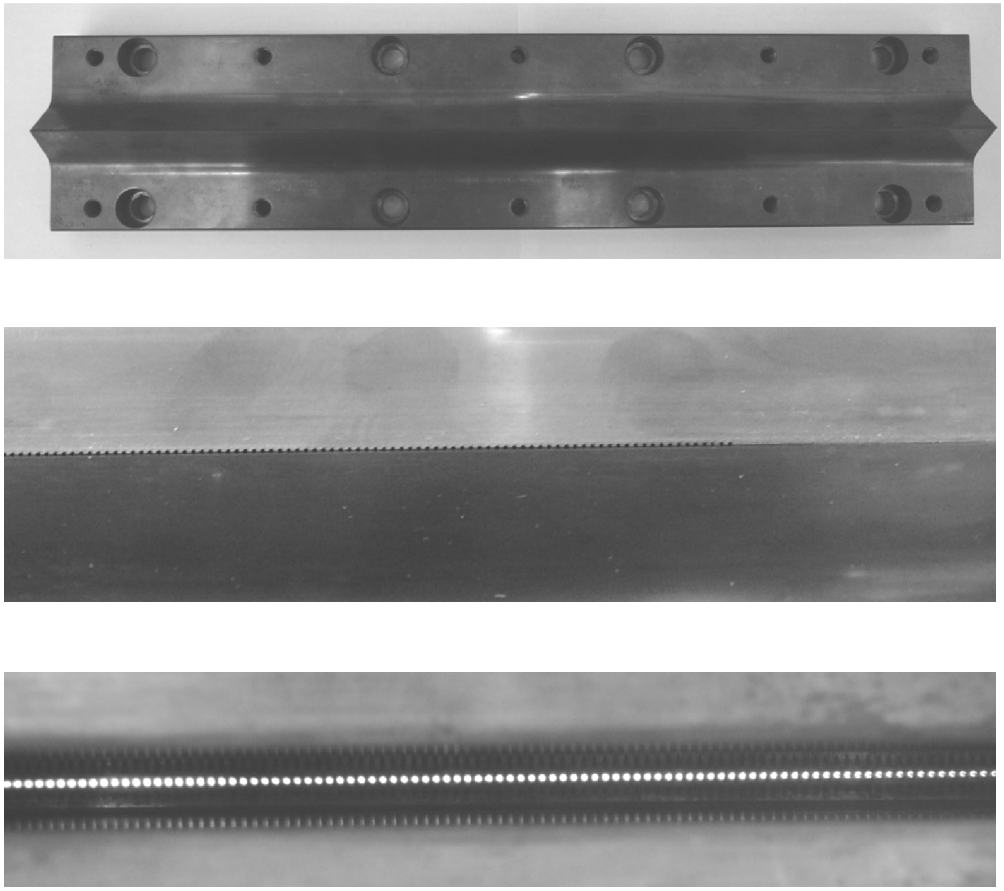

Fig. 50. Visualization of the die nosepiece (top-full view, middle-right side view, bottom- detail view of the 0,4 mm diameter orifice).

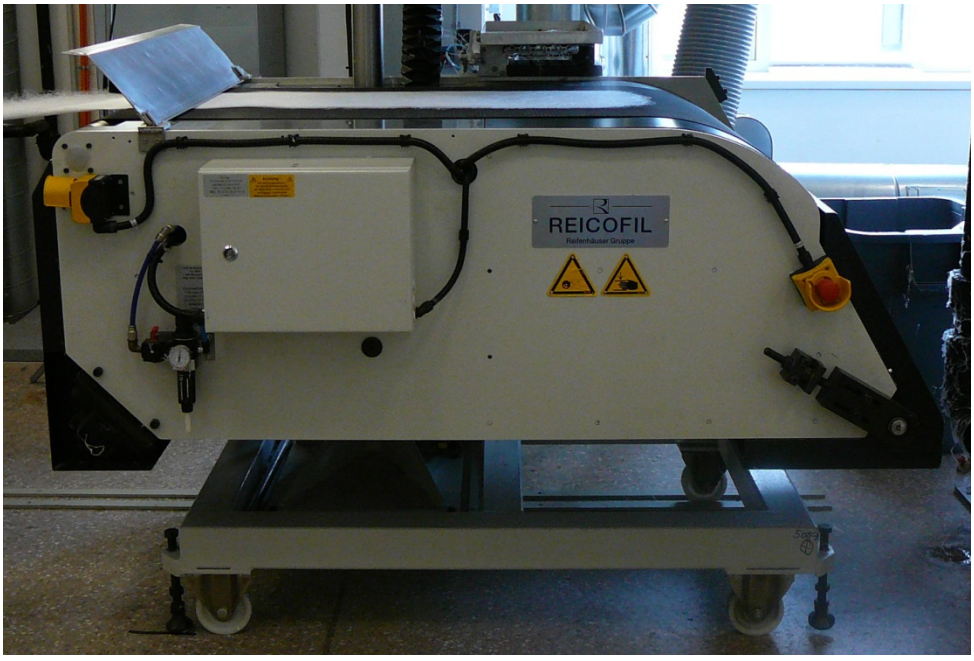

Fig. 51. Collector

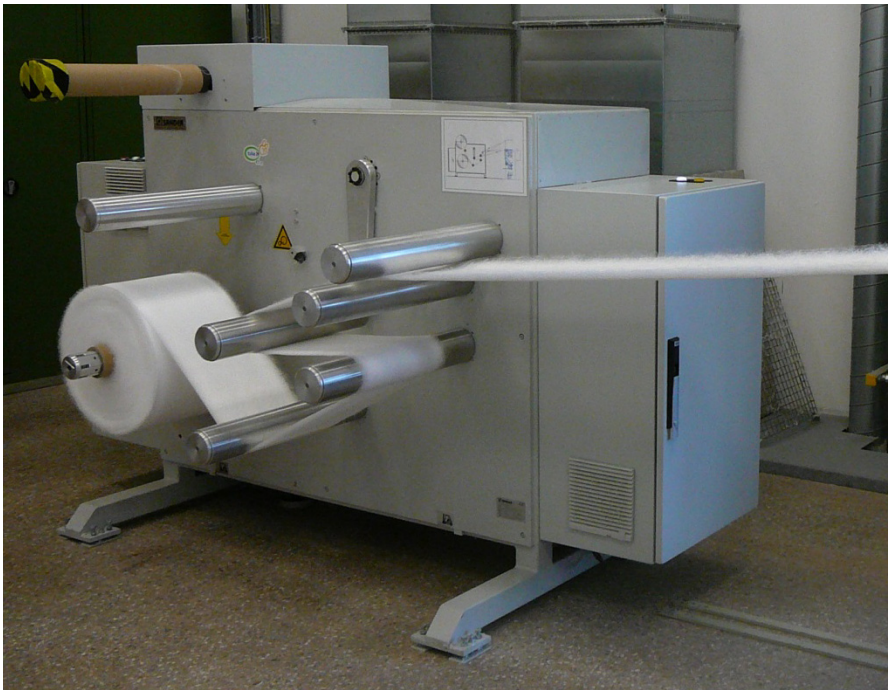

Fig. 52. Exhaust and reservoir.

8.3 Tabletop TM-1000 SEM microscope

In order to determine basic morphological characteristics of the produced meltblown nonwovens such as fiber diameter distribution, the simple to use HITACHI Tabletop TM-1000 SEM microscope was used (see Figs. 53-54).

Fig. 53. HITACHI Tabletop TM-1000 SEM microscope visualization, working place.

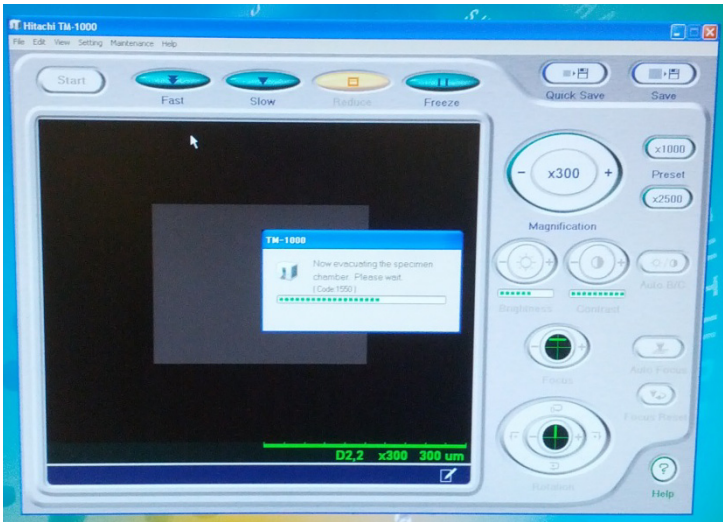

Fig. 54. HITACHI Tabletop TM-1000 SEM microscope visualization typical screenshot of the microscope software.

8.4 AKUSTRON air permeability tester

With the aim to evaluate the sample porosity for all produced meltblown samples, air permeability was determined by the AKUSTRON air permeability tester, which is visualized in (Fig. 54). In this work, the air permeability is represented by the speed of the air in mm/s passing the nonwoven at constant value of the pressure drop, equal to 200 Pa.

Fig. 55. Visualization of the AKUSTRON air permeability tester.

RESULTS AND DISCUSSION

Rheological evaluation of tested melt blown polymer samples in shear, uniaxial and planar extensional flows

In order to determine basic rheological characteristics in shear as well as elongational flows, circular as well as rectangle dies were utilized. Due to the extremely low viscosity of all tested samples and very high temperature, unwanted polymer melt leakage was detected between the die and barrel as visible in Figure 56.

Fig. 56. Unwanted polymer melt leakage flow at the long die (left) and orifice die (right).

In such case, the pressure drop through the utilized capillaries was artificially low and thus, its consequent usage in the shear and elongational viscosities was not possible. In order to eliminate the polymer melt leakage flow, polytetrafluoroethylene tape was used to seal the clearance between the die and the barrel as visible in Figures 57-58. This allowed to prevent unwanted polymer melt leakage and measurements of the pressure drops was reliable within the wide range of deformation rates.

In the first step, strain rate dependent shear viscosity as well as uniaxial and planar entrance viscosities have been determined at 230^{o}C for the polymers having the highest (branched PP Daploy) and smallest (linear PP HL512FB) melt index and the obtained data were consequently fitted by the Eq.39 and Eq. 59 for shear and entrance viscosity, respectively, as visible in Figures 59-61. It can be clearly seen that both chosen models can describe the measured data very well. The occurrence of the overshoot in the entrance viscos-

ity for PP Daploy polymer sample, which is visible in Figure. 60, confirms the presence of the branches, which is in good correspondence with the experimental data reported in [43].

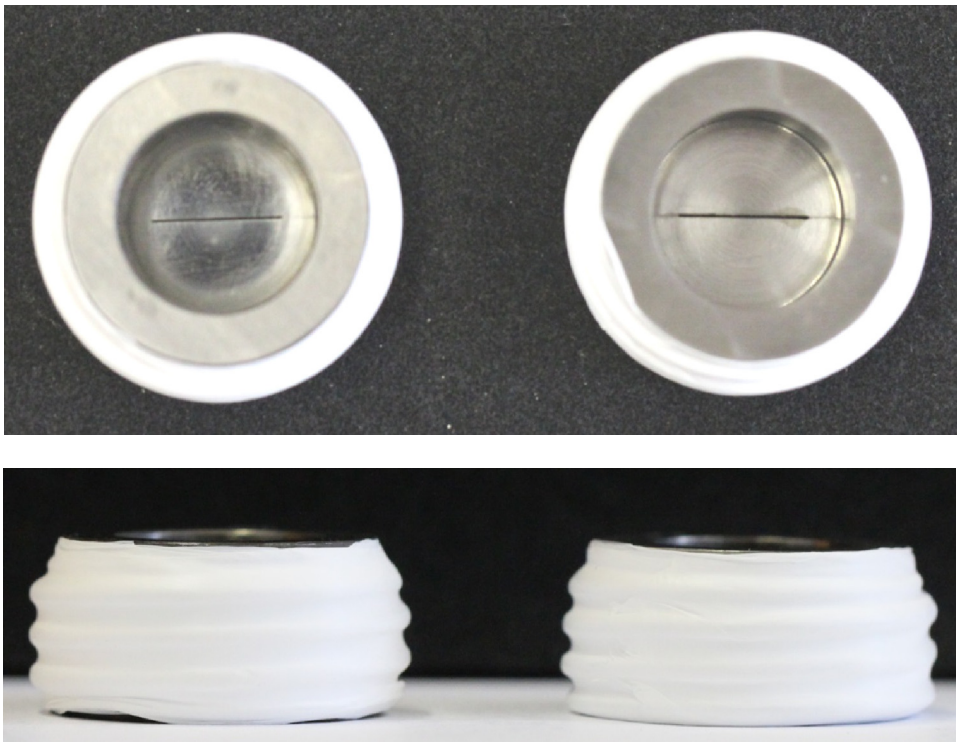

Fig. 57. Utilized polytetrafluoroethylene tape on the long die (left) and orifice die (right).

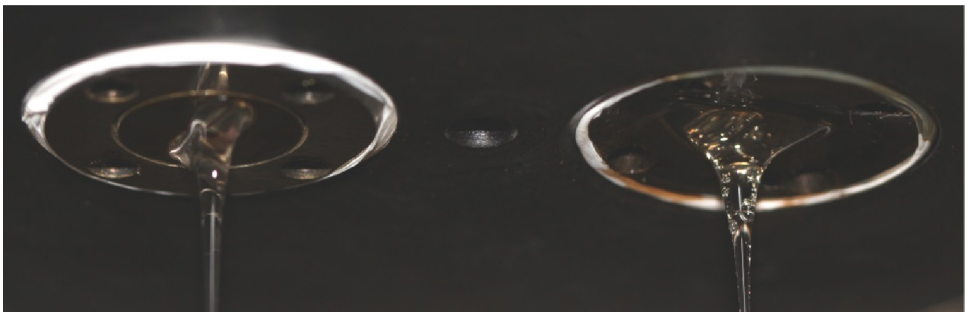

Fig. 58. Visualization of the flow through long die (left) and orifice die (right) without unwanted polymer melt leakage flow.

Interestingly, within the range of investigated deformation rates, only small (if any) overshoot in planar entrance viscosity was found, as visible in Figure 60. These experimental data suggests that flow behavior of this polymer in uniaxial and planar elongational flows will be different. On the other hand, for the linear PP HL512FB, no overshoot in uniaxial and planar entrance viscosities was found which is also consistent with the experimental data reported in [43] for linear polymer melts.

In the second step, shear, uniaxial and planar entrance viscosities were determined for remaining samples, i.e. for HL508FB, HL504FB and Blend 1 (90wt-% HL512FB + 10wt-% Daploy), Blend 2 (80wt-% HL512FB + 20wt-% Daploy) and Blend 3 (70wt-% HL512FB + 30wt-% Daploy), and the obtained shear and entrance viscosity data were fitted by the Eq.39 and Eq. 59, respectively (see Figs. 62-64). To do this, it was necessary to utilize physical constrain for zero deformation rate uniaxial and planar entrance viscosities defined by Eq.61 as well as to determine $\eta_{ENTR,U,0}/(2\eta_0)$ ratio for the utilized annular orifice die design from the measured data where both plateau values were measurable (here the $\eta_{ENTR,U,0}/(2\eta_0)$ ratio was found to be 1,76826 based on the HL512FB data depicted in Figures 62-64). Model parameters for all polymer samples are summarized in Tables 21-23. As it can be seen, also in this case, the chosen mathematical models can represent the measured rheological data very well. With respect to the experimental data for the Blends 1-3 depicted in Figures 62-64, clearly, continues increase of highly viscous PP Daploy amount in the HL512FB+Daploy PP blends leads to the increase in shear, uniaxial and planar entrance viscosities as expected. The most interesting polymers to be compared rheologicaly in more detail with respect to the nanofiber formation during meltblown process is linear PP HL508FB and slightly branched PP Blend 1 (90wt-% HL512FB + 10wt-% Daploy) having practically identical shear viscosity curves but different uniaxial and planar entrance viscosities (see Figs. 65-66).

Tab. 21. Parameters of Carreau-Yasuda model T=230°C

Function	***Carreau-Yasuda model***				
Material	***η_0 (Pa.s)***	***λ (s)***	***a (-)***	***n (-)***	***b (-)***
Daploy	3000	1,119000	0,56548	0,46433	0,02433
HL504FB	19,47125	0,001178	1,207615	0,491130	0,02318
HL508FB	9,742137	0,000752	1,402342	0,580867	0,02497
HL512FB	6,867669	0,000765	1,505550	0,665461	0,02421
Blend 1	9,458639	0,001049	1,623742	0,644978	-
Blend 2	12,05149	0,001005	1,614599	0,563726	-
Blend 3	16,52453	0,001885	1,723808	0,630532	-

Tab. 22. Parameters of uniaxial entrance viscosity model, Eq. 59, at T=230°C for all tested polymer samples

Function	***Carreau-Yasuda model***						
Material	***η_0' (Pa.s)***	***λ' (s)***	***a' (-)***	***n' (-)***	***α' (-)***	***β' (-)***	***ξ' (-)***
Daploy	2000	0,827634	65,46019	0,78561	0,449985	1,026186	0,65695
HL504FB	68,8604	0,004003	3,2546	0,76237	0	1	0
HL508FB	40,41943	0,004308	2,9531	0,74448	0	1	0
HL512FB	24,28768	0,001029	7,2719	0,79237	0	1	0
Blend 1	33,45066	0,012248	105,4818	0,73314	0,008119	1,034119	0,718832
Blend 2	42,62033	0,391069	1,182179	0,80508	0,018004	0,585378	0,51275
Blend 3	58,4393	0,263587	0,770437	0,80004	0,048319	1,465538	2,44485

Tab. 23. Parameters of planar entrance viscosity model, Eq. 59, at T=230°C for all tested polymer samples

Function	***Carreau-Yasuda model***						
Material	***η_0' (Pa.s)***	***λ' (s)***	***a' (-)***	***n' (-)***	***α' (-)***	***β' (-)***	***ξ' (-)***
Daploy	4670,640	2,05756	64,8807	0,73517	1,52195	1,73565	0,75834
HL504FB	69,20728	0,00624	1,225148	0,715898	0	1	0
HL508FB	35,0096	0,00221	8,537095	0,617276	0	1	0
HL512FB	29,55281	0,004015	1,975729	0,71357	0	1	0
Blend 1	34,73300	0,003202	1,853524	0,612267	0,21249	0,82337	0,06519
Blend 2	56,36680	0,001811	0,375301	0,545432	0,14263	0,03494	0,02596
Blend 3	65,87369	0,028021	2,117257	0,739728	0,36146	0,42148	0,070379

In more detail, even if shear viscosity curves for both polymers are virtually the same, uniaxial entrance viscosity for PP Blend 1 (90wt-% HL512FB + 10wt-% Daploy) is higher in comparison with PP HL508FB whereas planar entrance viscosity for PP Blend 1 (90wt-% HL512FB + 10wt-% Daploy) is smaller in comparison with PP HL508FB. This suggests that PP Blend 1 could flow much easily through the flat converging channels inside the meltblown dies in comparison with PP HL508FB, i.e. the material distribution inside the die could be consider to be more homogenous along the die width for Blend 1 in comparison with PP HL508FB. On the other hand, higher uniaxial entrance viscosity for Blend 1 could influence more positively the fiber formation for this polymer between the die and the collector in comparison with PP HL 508FB polymer. Due to above described interesting rheological features of Blend 1 and PP HL508FB polymer, only these two polymers are considered for the consequent experimental study on the melt blown line.

Finally, temperature sensitivity parameters for all tested polymer samples were evaluated from deformation rate dependent shear viscosities determined at 190^{o}C, 210^{o}C and 230^{o}C. For such purpose, the Carreau-Yasuda model defined by Eq.39 using the following type of temperature shift factor was utilized:

$$a_T = \exp\left[-b\left(T - T_r\right)\right] \tag{62}$$

where b represents temperature sensitivity parameter, T_r is the reference temperature and T stands for the arbitrary value of the temperature. The comparison between the experimental data and model fits are provided in Figures 67-68 for Daploy and HL 508FB (note that for HL 504FB and HL 512FB samples, the rheological data provided in [36] were used). Temperature sensitivity parameters for all investigated polymer samples are summarized in Tables 21. Due to the fact that the temperature sensitivity parameter b is comparable for all investigated samples, it can be reasonable to consider that all prepared blends will behaves in the similar way as the basic blend components i.e. PP HL512FB and Daploy as well as the PP HL508FB.

Determination of basic morphological characteristics of nanofiber based nonwovens produced by the melt blown technology

As it has been explained in the previous chapter, only the PP polymers having virtually the same behavior in shear flow but different behavior in elongational flows (i.e. HL508FB and blend of 90wt-% HL512FB + 10wt-% Daploy) were considered for the production of polymeric nanofibers on the melt blown line. In more detail, for each polymer, melt temperature (T_1=250^{o}C, T_2=270^{o}C), Die-Colector Distance (DCD_1=200mm, DCD_2=500mm) and collector belt speed was varied during production of nanofiber based nonwovens on the melt blown line in order to evaluate the following basic characteristics: the air permeability, the average fiber diameter and the coefficient of variation for average fiber diameter. In order to evaluate the average fiber diameter as well as the coefficient of variation for average fiber diameter in statistically correct way, four samples taken from different places were used for each produced nonwoven. Moreover, in order to evaluate as much as possible number of small and high fibers, three different magnifications (1000x, 2500x, 4000x) were used for each sample by using SEM microscopy. In total, there were 4x3=12 samples to be analyzed for one nonwoven, which was produced from given polymer at given processing conditions. In order to determine average fiber diameter as well as coefficient of variation for the average fiber diameter from SEM images and digital image analysis technique, the recently developed UTBsoft Filtration v1.0.1 simulation software (Morphology module) by Wannes Sambaer and Martin Zatloukal was used. In more detail, the SEM image of the melt blown sample (see example in Fig. 69a) was firstly converted to black and white image. Then, the centerline as well as fiber boundary for each fiber was detected. Finally, the circle was fitted in each centerline point to determine its diameter. In this way, all countable fiber centerline points were analyzed and recorded in the file (see Fig. 69b for example). Log-normal fiber diameter distribution was found for all investigated melt blown samples having the following basic properties [45]: Traditionally, the mean μ and the standard deviation σ of log(measured fiber diameter in nm) are utilized, however, there are clear advantages using "back-transformed" values (the values are in terms of measured fiber diameter in nm instead of its logarithmic value):

$$\mu^* := e^{\mu}, \sigma^* := e^{\sigma} \tag{63}$$

which simply means that fiber diameter measured in nm is distributed according to the log-normal law with median μ^* and multiplicative standard deviation σ^*. The coefficient of

variation (or relative standard deviation expressed as a percentage) is defined for the Log-normal distribution as follows:

$$CV = \sqrt{exp\left(\sigma^2\right) - 1}\ \text{x}\ 100\% \tag{64}$$

Fig. 70 shows typical Log-normal distribution of fiber diameters obtained by the above described methodology for a PP meltblown sample produced in this work. All basic characteristics of produced meltblown nonwovens are summarized in Tables 24-25.

Evaluation the relationship between flow behaviour of tested polymer samples, processing conditions and final nanofiber based nonwoven product properties

The effect of processing conditions on the produced meltblown nonwoven characteristics

The effect of melt temperature, collector belt speed and die-collector distance on the air permeability, the area weight, the average fiber diameter and the coefficient of variation for fiber diameter is provided in Figures. 71-95. As it can be seen in Figures 71-73, melt temperature increase leads to air permeability decrease whereas increase in collector belt speed or in the die-colector distance leads to the air permeability increase, which can be explained by the sample porosity change and the obtained trends are comparable for both tested polymers.

The effect of melt temperature, collector belt speed and die-collector distance on the area weight is provided in Figures 74-76. The experimental results shows that the area weight does not seems to be virtually influenced by the melt temperature and die-collector-distance (within the applied range for both variables) whereas the increase in the collector belt speed causes reduction in the area weight. Also in this case, the obtained trends are comparable for both tested polymers even if the variation of the area weight for branched Blend 1 polymer tends to by lower in comparison with linear HL508FB sample, which can be explained by more homogeneous polymer distribution of Blend 1 in the flat die in comparison with HL508FB sample due to its lower planar entrance viscosity as visible in Figure 66.

The effect of melt temperature, collector belt speed and die-collector distance on the average fiber diameter is provided in Figures 77-79. As visible, the effect of all investigated processing parameters on the average fiber diameter has no unique trend for both samples.

The effect of melt temperature, collector belt speed and die-collector distance, DCD, on the coefficient of variation for average fiber diameter, CV is provided in Figures. 80-91. Here, for the increased melt temperature of both tested polymers, firstly the CV increases (for low DCD and low collector belt speed), then CV remains constant (for high DCD and high belt speed), and finally, CV decreases (for high DCD and low belt speed). Importantly, almost in all cases, the branched Blend 1 polymer shows lower CV than linear HL508FB sample. From the basic research as well as practical point of view, the case at which the CV increases with the increased temperature at the low DCD and low collector belt speed (the most dangerous case) is of high interest. Thus, in the next chapter, only this type of the processing conditions with respect to polymer sample rheology is discussed in more detail.

The effect of uniaxial elongational rheology on the produced meltblown nonwoven characteristics

In this chapter, the effect of elongational rheology on the produced meltblown nonwoven characteristics is discussed for one set of meltblown processing conditions at which the lowest values for the melt temperature (250^{o}C), DCD (200m) and collector belt speed (4,25 m/min), i.e. at conditions, at which the differences in the uniaxial entrance viscosities of both chosen polymer melts are the highest, but the shear viscosities are practically the same (see Fig. 65). The level of the uniaxial entrance viscosity difference between branched Blend 1 sample and linear HL508FB sample is quantified here through the following Strain Hardening Ratio (SHR):

$$SHR = \frac{\eta_{ENTR,U,MAX}}{\eta_{ENTR,U,0}} \tag{65}$$

where $\eta_{ENTR,U,MAX}$ represents the maximum value of the uniaxial entrance viscosity and $\eta_{ENTR,U,0}$ is the zero deformation rate uniaxial entrance viscosity. It is clearly visible in Figure. 92, that branched Blend 1 shows uniaxial strain hardening (SHR>1) whereas HL508FB do not (SHR=1), thus both samples can be clearly differentiated by using SHR with respect to uniaxial entrance viscosity.

The effect of SHR on the air permeability, average fiber diameter and coefficient of variation for average fiber diameter at given processing conditions is provided in Figures. 93-

95. Clearly, slight increase in SHR leads to air permeability increase (6,6% change), average fiber diameter decrease (13,2% change) and coefficient of variation for average fiber diameter decrease (7,9% change).

Tab. 24. Processing conditions of meltblown line.

Sample No.	***Temperature*** **[°C]**	***Die to collector distance*** **[mm]**	***Speed belt*** **[m/min]**	***Air permeability*** **[mm/s]**
Sample 1	250	500	4,7	465
Sample 2	250	500	19	1748
Sample 3	250	200	16,6	1043
Sample 4	250	200	4,2	283
Sample 5	270	500	4,7	300
Sample 6	270	500	19,1	1332
Sample 7	270	200	18,5	910
Sample 8	270	200	4,3	241
Sample 9	270	500	4,8	325
Sample 10	270	500	18,7	1330
Sample 11	270	200	18,7	871
Sample 12	270	200	4,1	260
Sample 13	250	500	4,8	458
Sample 14	250	500	19	1669
Sample 15	250	200	18,6	1160
Sample 16	250	200	4,2	303

Note: Samples 1-8 are HL508FB, Samples 9-16 are Blend 1

Tab. 25. Basic morphological characteristics of produced meltblown samples.

Sample No.	***Temperature*** **[°C]**	***Die to collector distance*** **[mm]**	***Speed belt*** **[m/min]**	***Average fiber diameter*** **[nm]**	***Coeficient of variation*** **[%]**
1	250	500	4,7	1524,755	93,656
2	250	500	19	1568,556	92,086
3	250	200	16,6	1441,451	81,191
4	250	200	4,2	1588,547	90,028
5	270	500	4,7	1239,367	89,008
6	270	500	19,1	1228,57	92,132
7	270	200	18,5	1137,889	89,333
8	270	200	4,3	1722,265	91,693
9	270	500	4,8	1276,439	84,612
10	270	500	18,7	1486,62	91,670
11	270	200	18,7	1226,027	88,150
12	270	200	4,1	1791,095	89,866
13	250	500	4,8	1764,006	93,702
14	250	500	19	1498,994	91,323
15	250	200	18,6	1436,481	86,081
16	250	200	4,2	1462,177	83,443

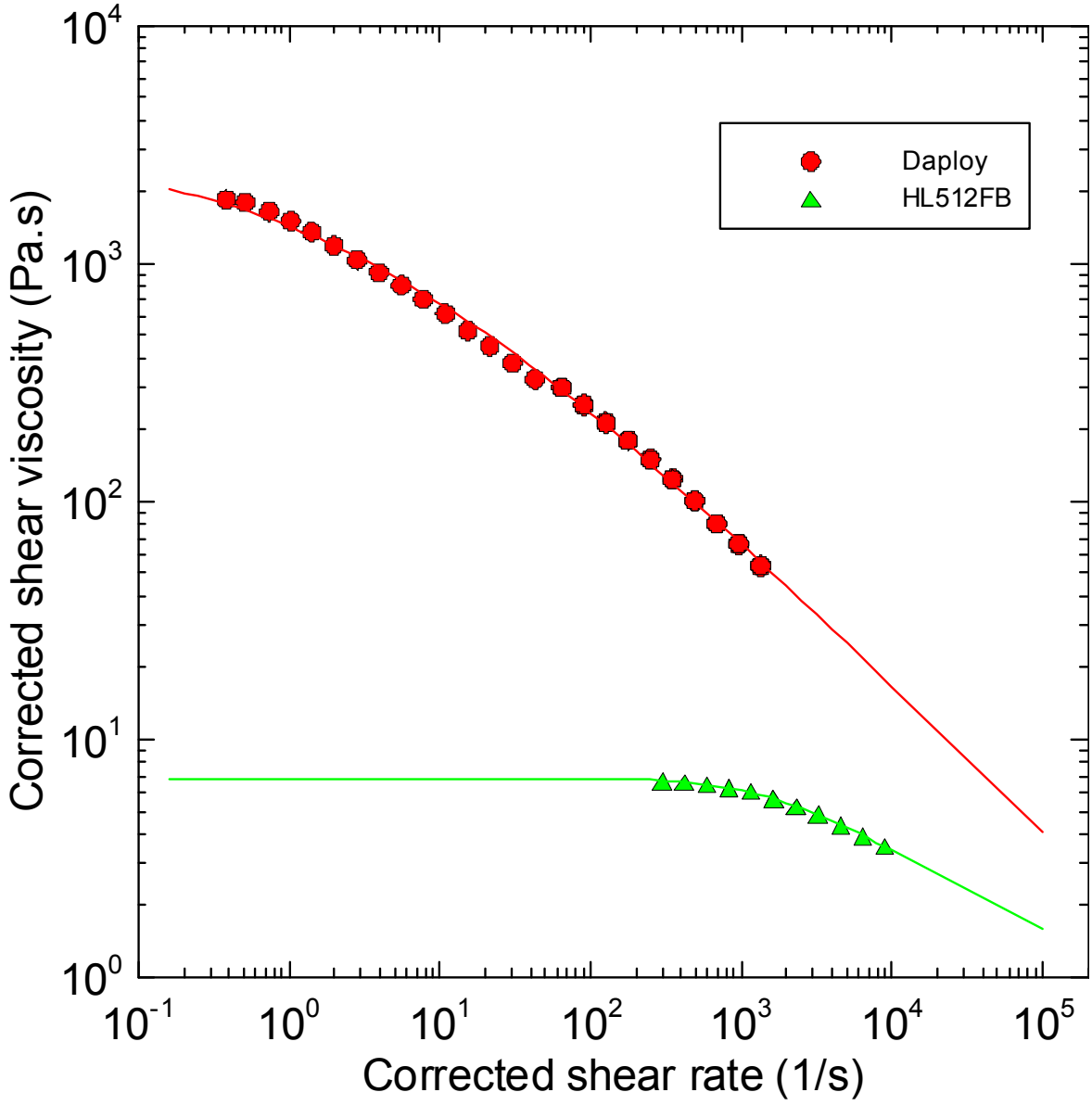

Fig. 59. Comparison between deformation rate dependent shear viscosity for two different polymers (Daploy and HL512FB) and Carreau-Yasuda model fits at T=230°C.

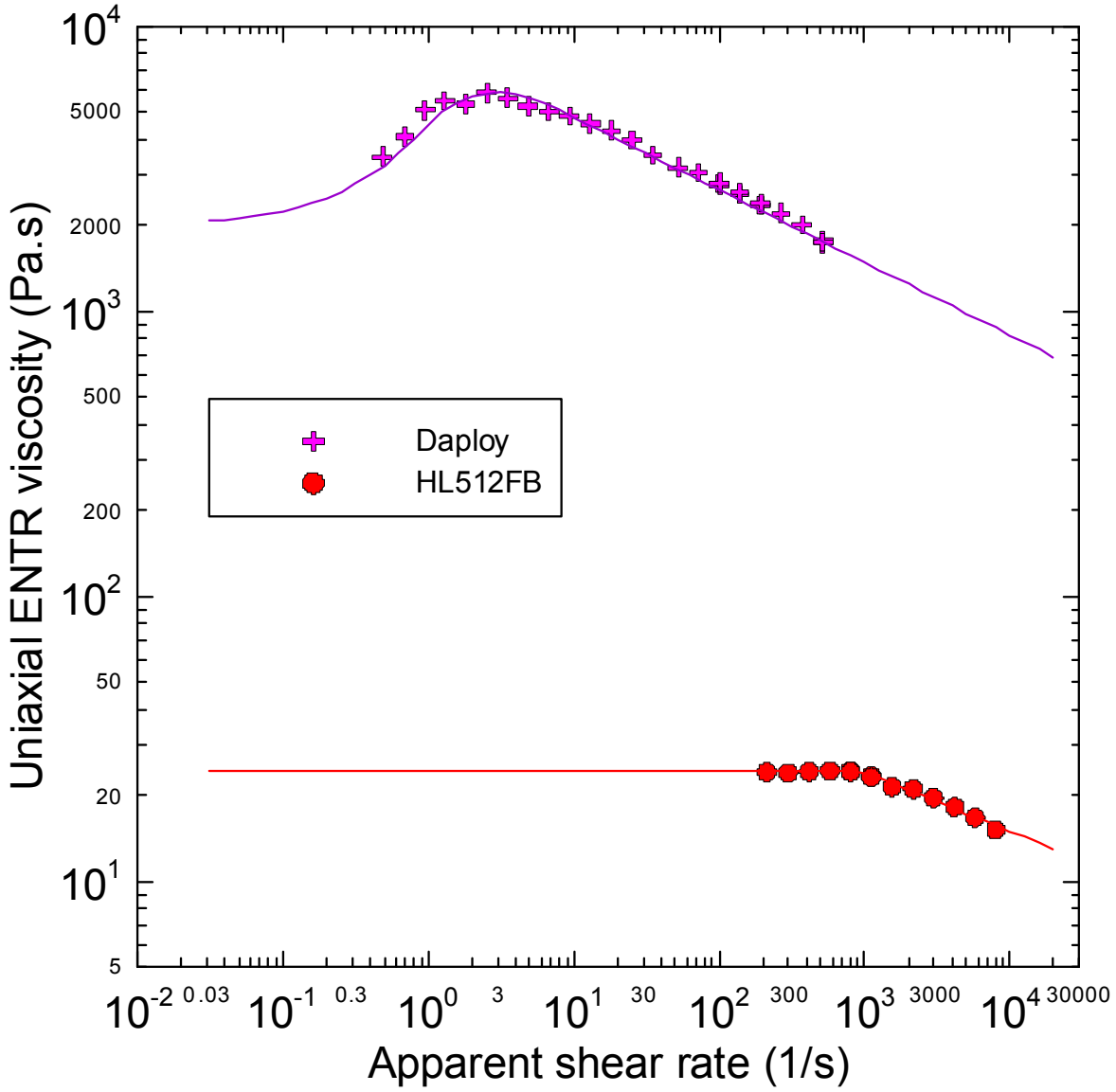

Fig. 60. Comparison between deformation rate dependent uniaxial entrance viscosity for two different polymers (Daploy and HL512FB) and Eq.(59) model fits at T=230°C.

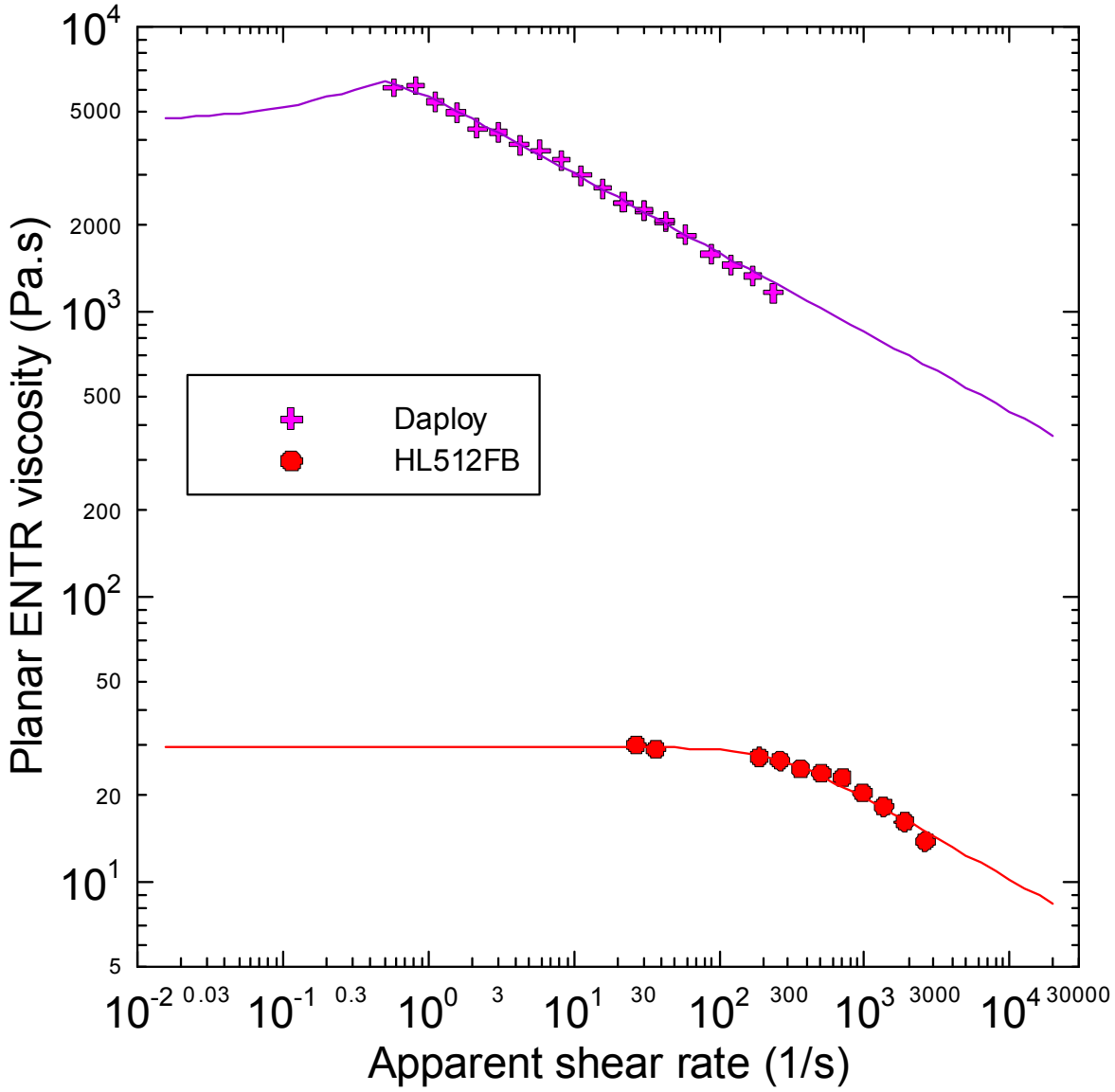

Fig. 61. Comparison between deformation rate dependent planar entrance viscosity for two different polymers (Daploy and HL512FB) and Eq.(59) model fits at T=230°C.

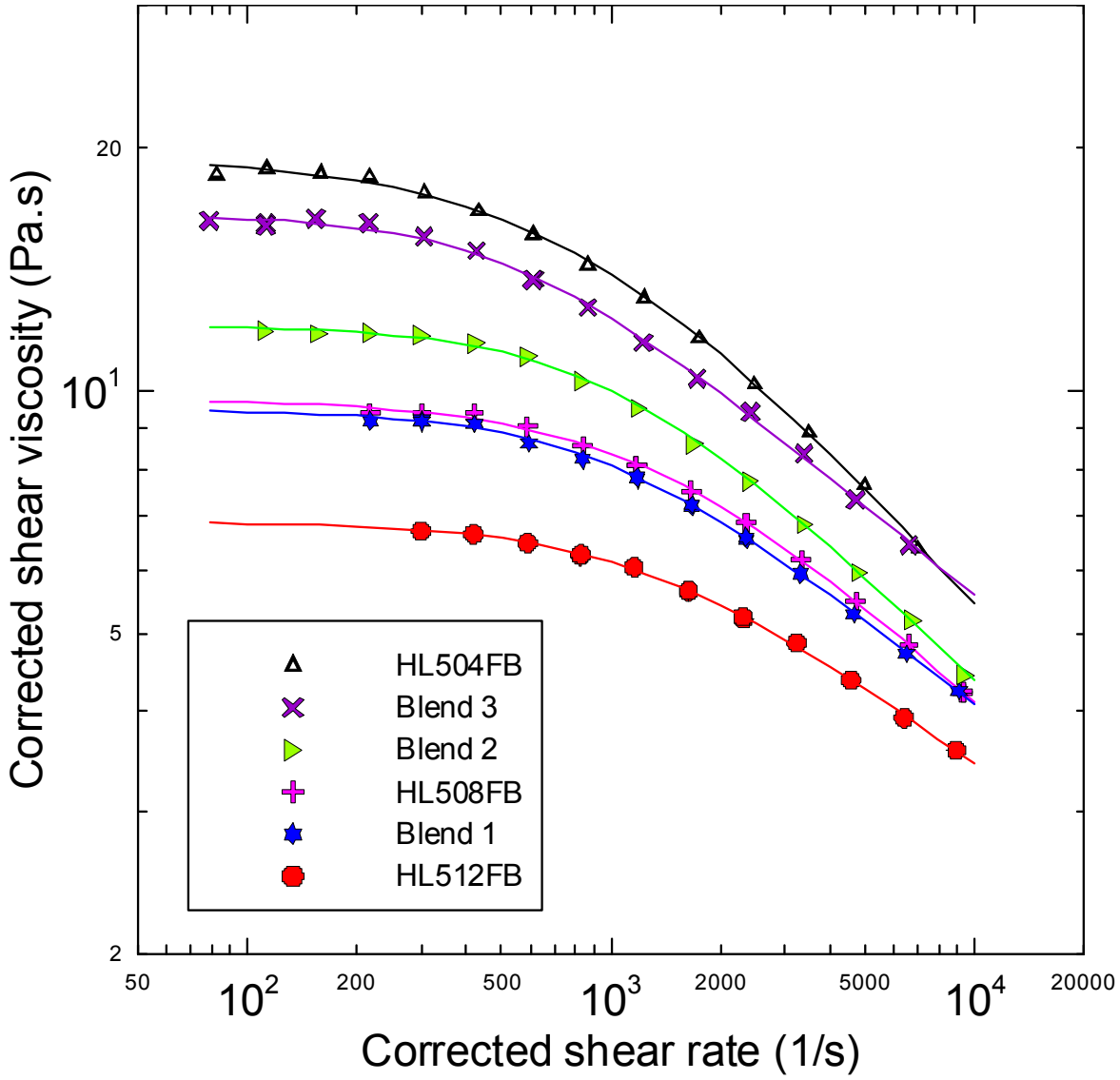

Fig. 62. Comparison between deformation rate dependent shear viscosity for three different PP homopolymers (HL504FB, HL508FB, HL512FB), three different blends (Blend 1, Blend 2, Blend 3) and Carreau-Yasuda model fits at T=230°C.

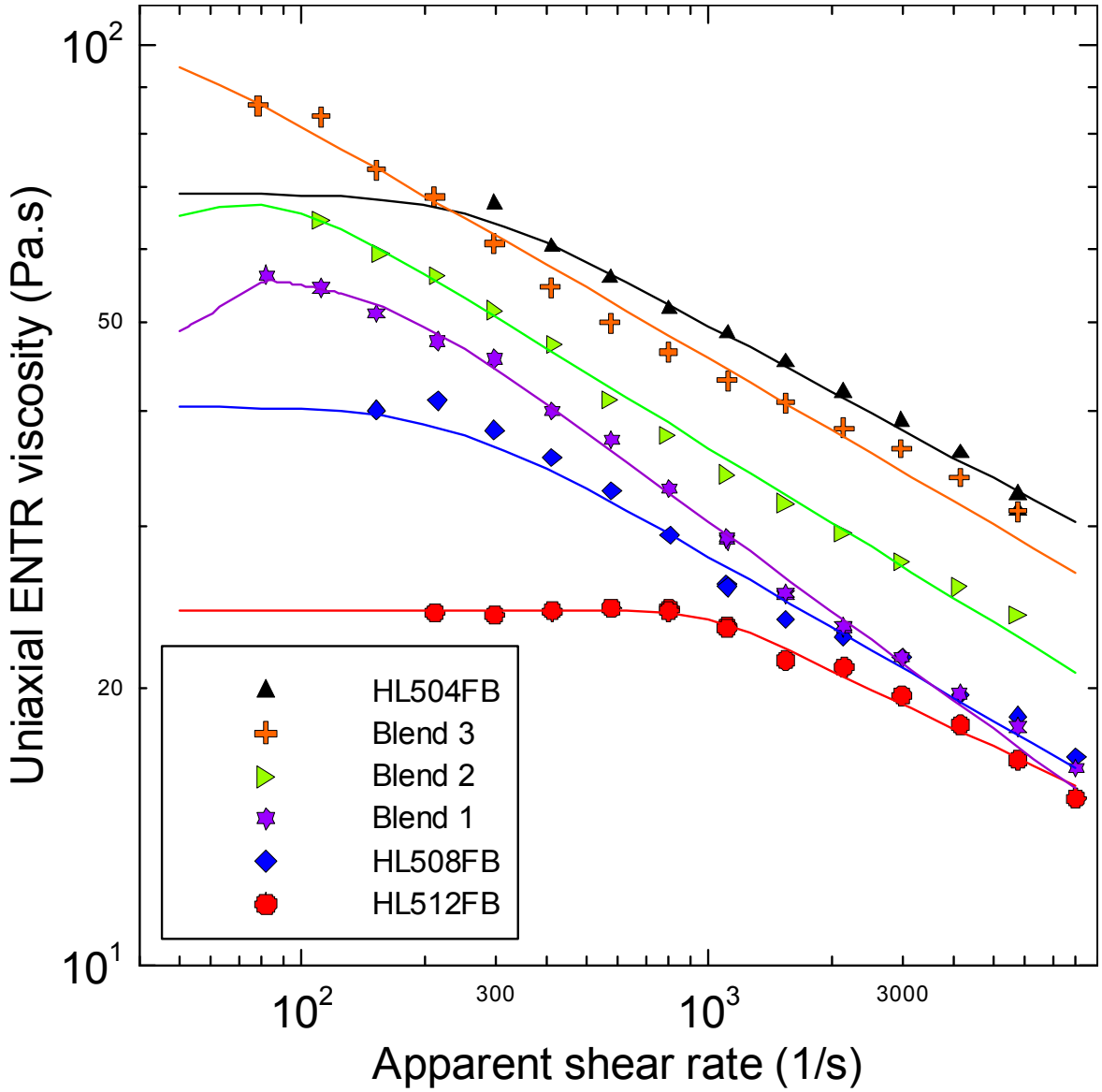

Fig. 63. Comparison between deformation rate dependent uniaxial entrance viscosity for three different PP homopolymers (HL504FB, HL508FB, HL512FB), three different blends (Blend 1, Blend 2, Blend 3) and Eq. (59) model fits at T=230°C.

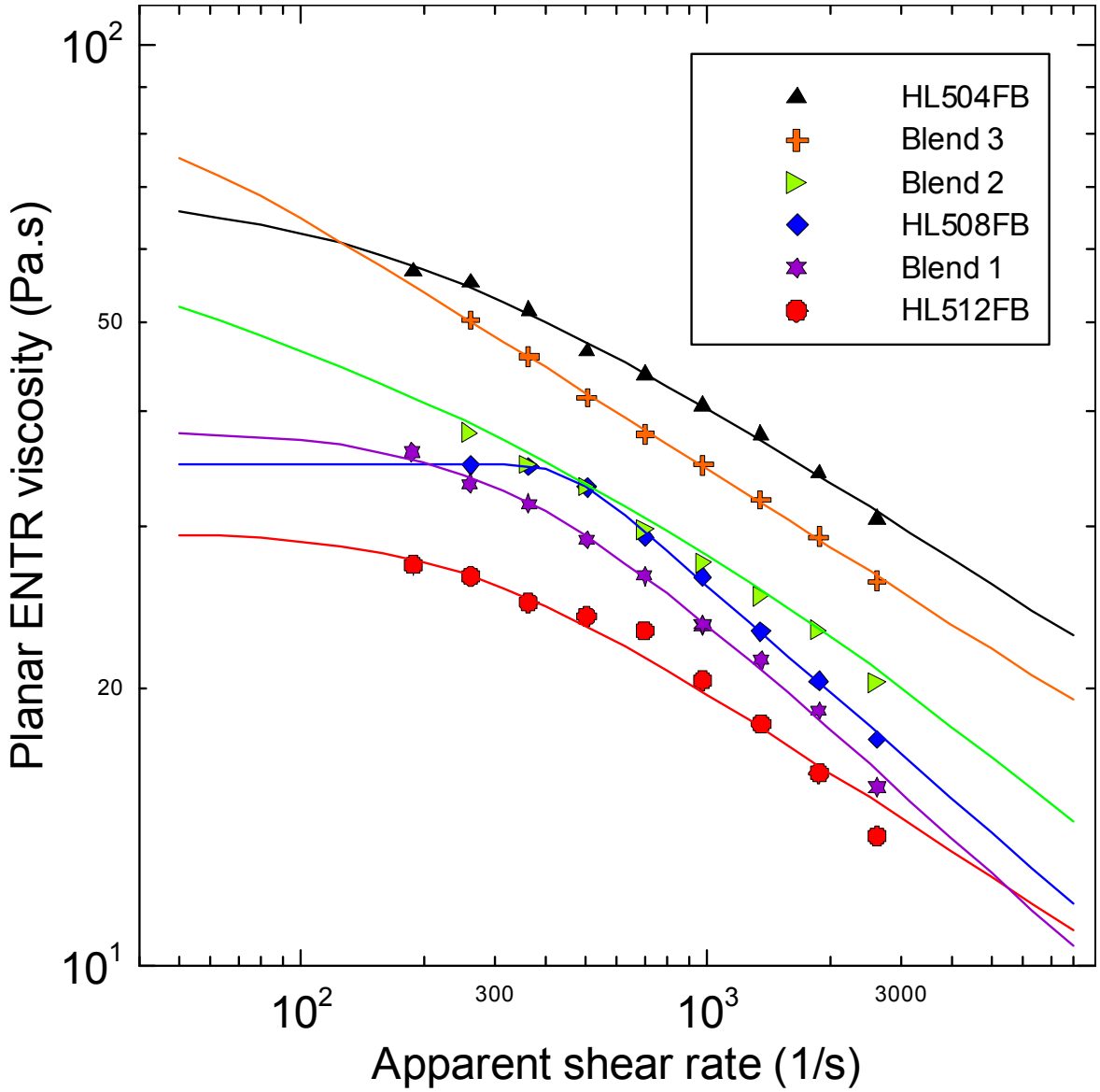

Fig. 64. Comparison between deformation rate dependent planar entrance viscosity for three different PP homopolymers (HL504FB, HL508FB, HL512FB), three different blends (Blend 1, Blend 2, Blend 3) and Eq. (59) model fits at T=230°C.

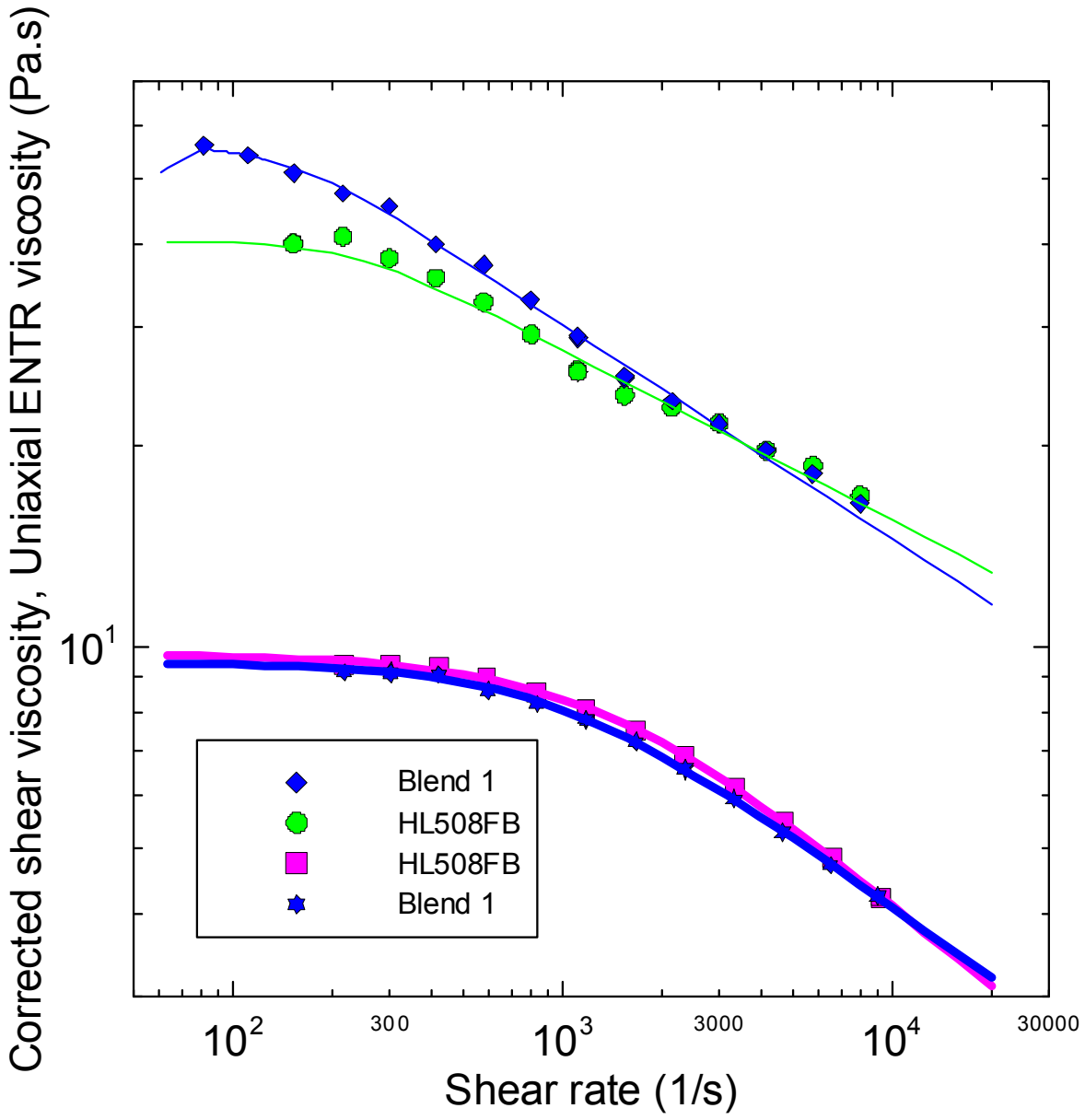

Fig. 65. Comparison between deformation rate dependent shear and planar entrance viscosities for HL512FB, Blend 1 and model fits (Carreau Yasuda model and Eq.59) at T=230°C.

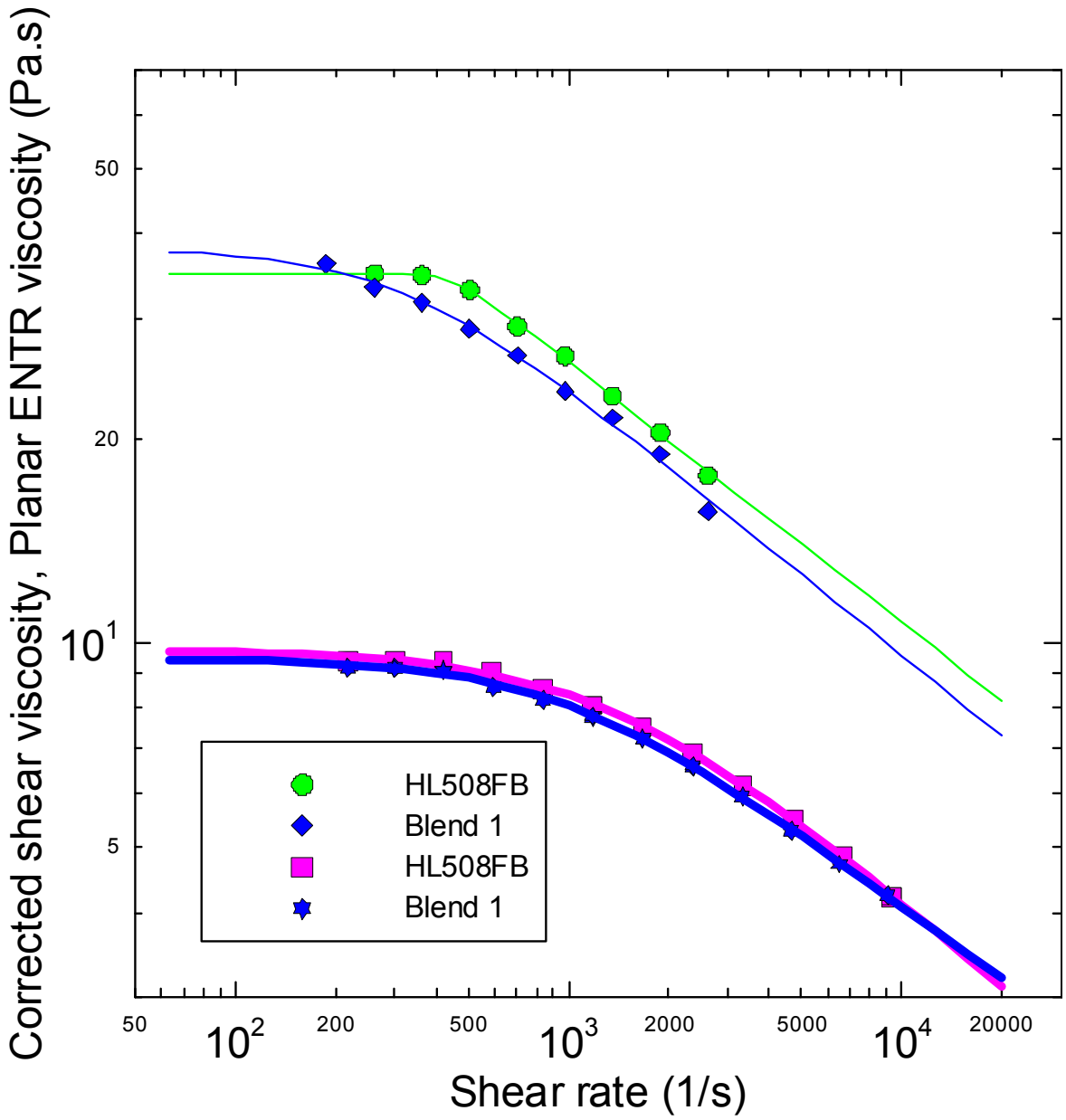

Fig. 66. Comparison between deformation rate dependent shear and uniaxial entrance viscosities for HL512FB, Blend 1 and model fits (Carreau Yasuda model and Eq.59) at T=230°C.

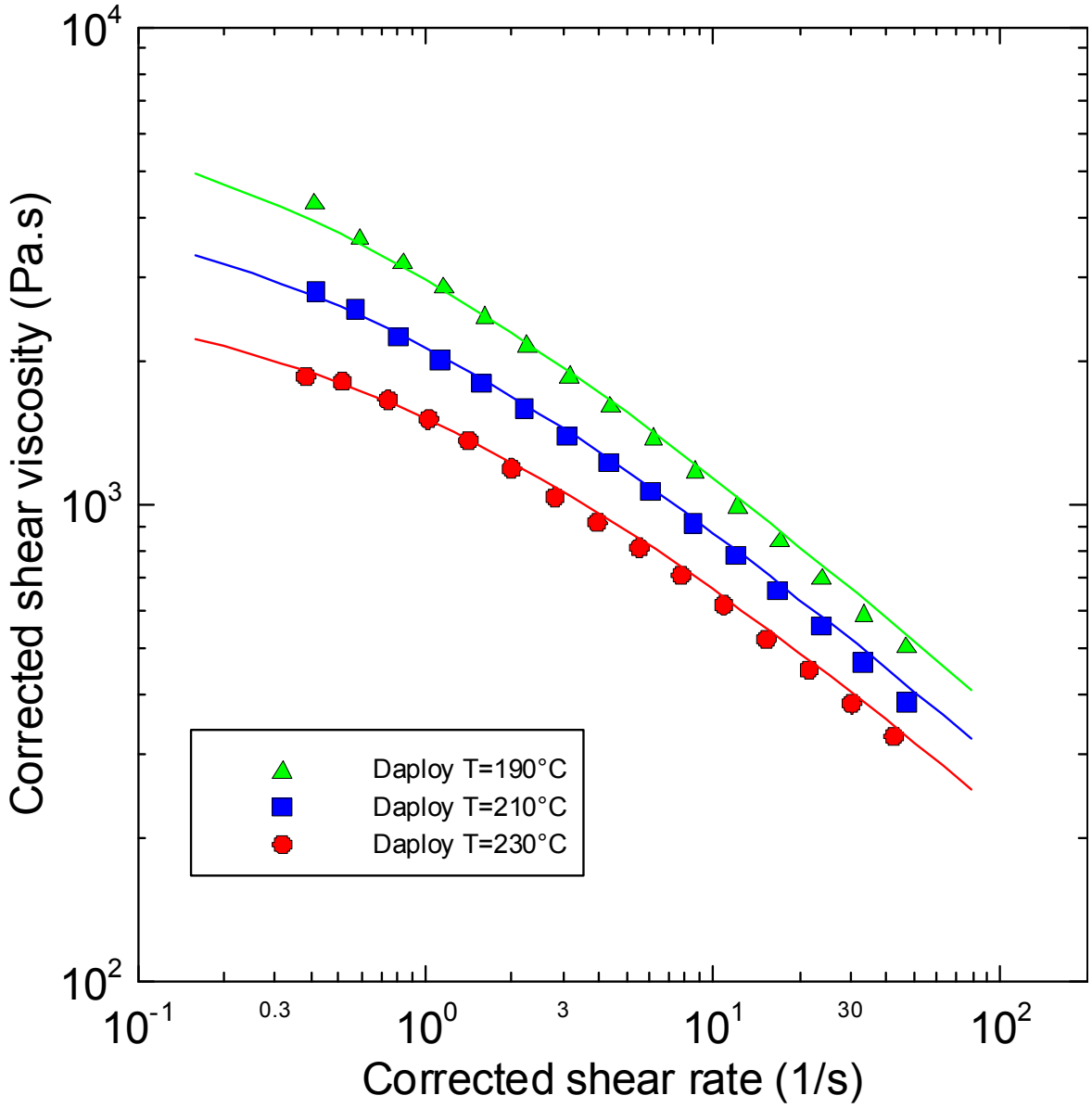

Fig. 67. Comparison between deformation rate dependent shear viscosities measured at three different temperatures for Daploy sample and model fits (Carreau Yasuda model and Eq.62).

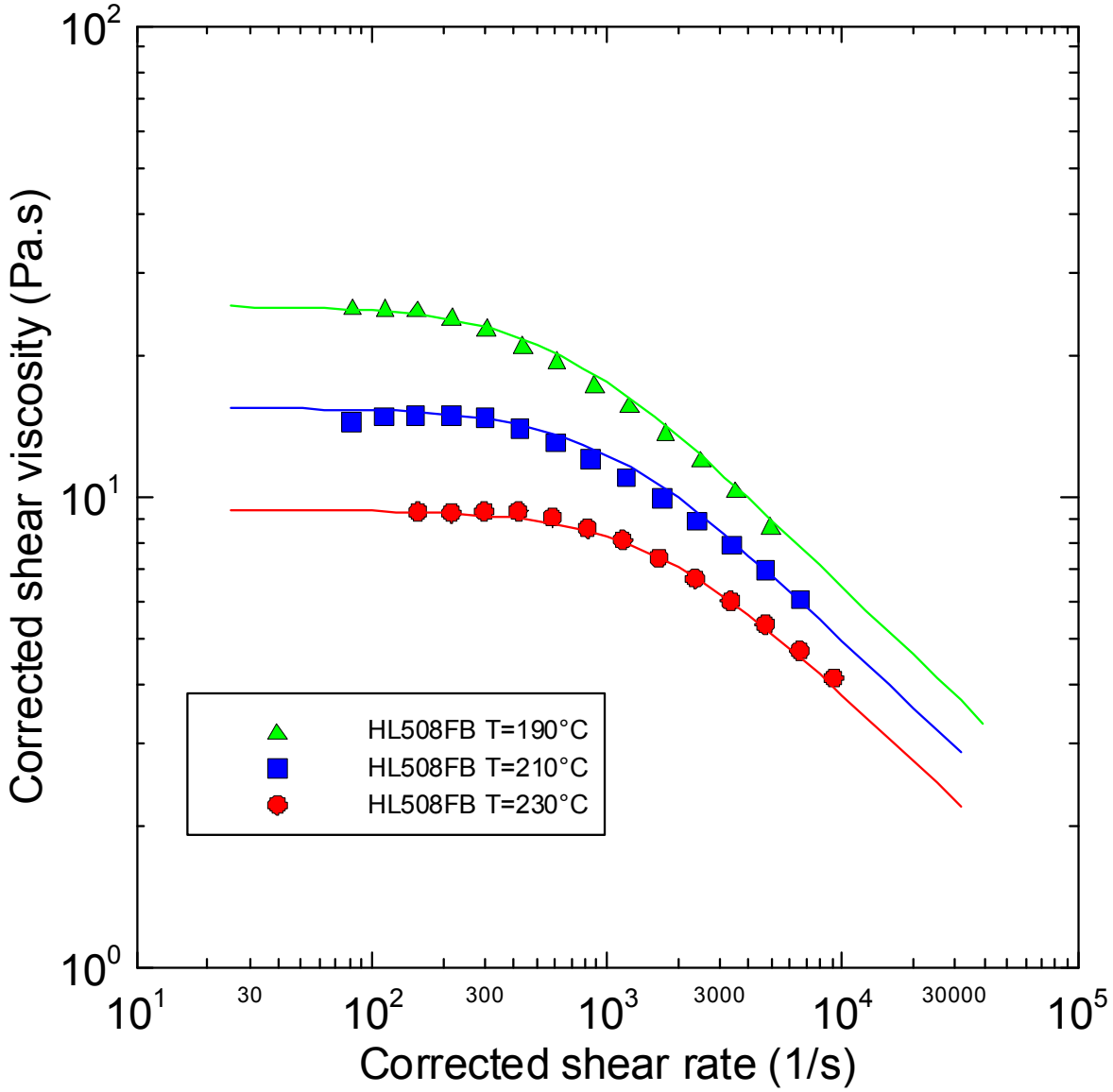

Fig. 68. Comparison between deformation rate dependent shear viscosities measured at three different temperatures for HL508FB sample and model fits (Carreau Yasuda model and Eq.62).

69a)

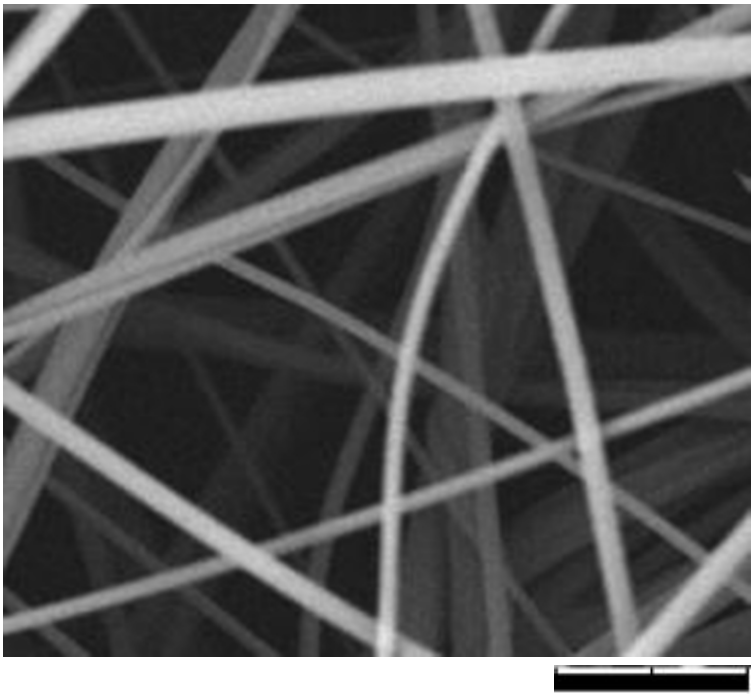

69b)

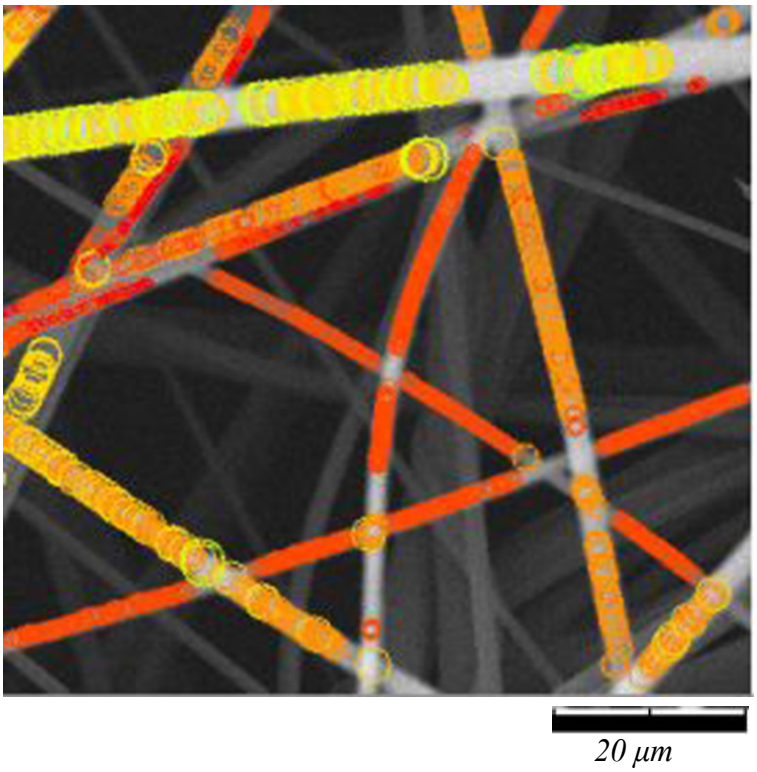

Fig. 69. Determination of fiber diameter distribution from SEM image for produced meltblown nonwoven sample. 68a) Original SEM image, 68b) Fitted circles along the fiber centerlines.

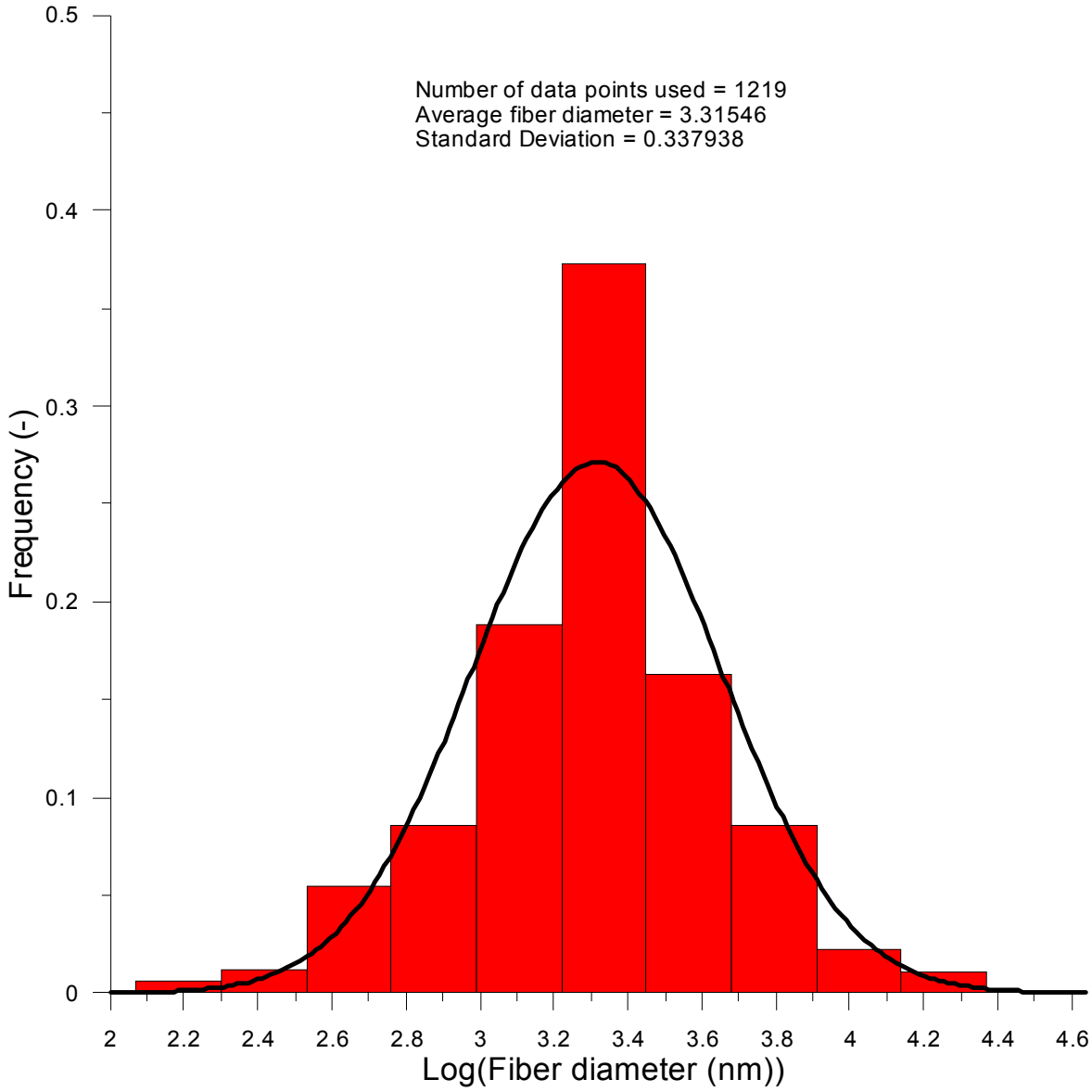

Fig. 70. Typical log-normal fiber diameter distribution for produced typical meltblown sample obtained by using digital image analysis.

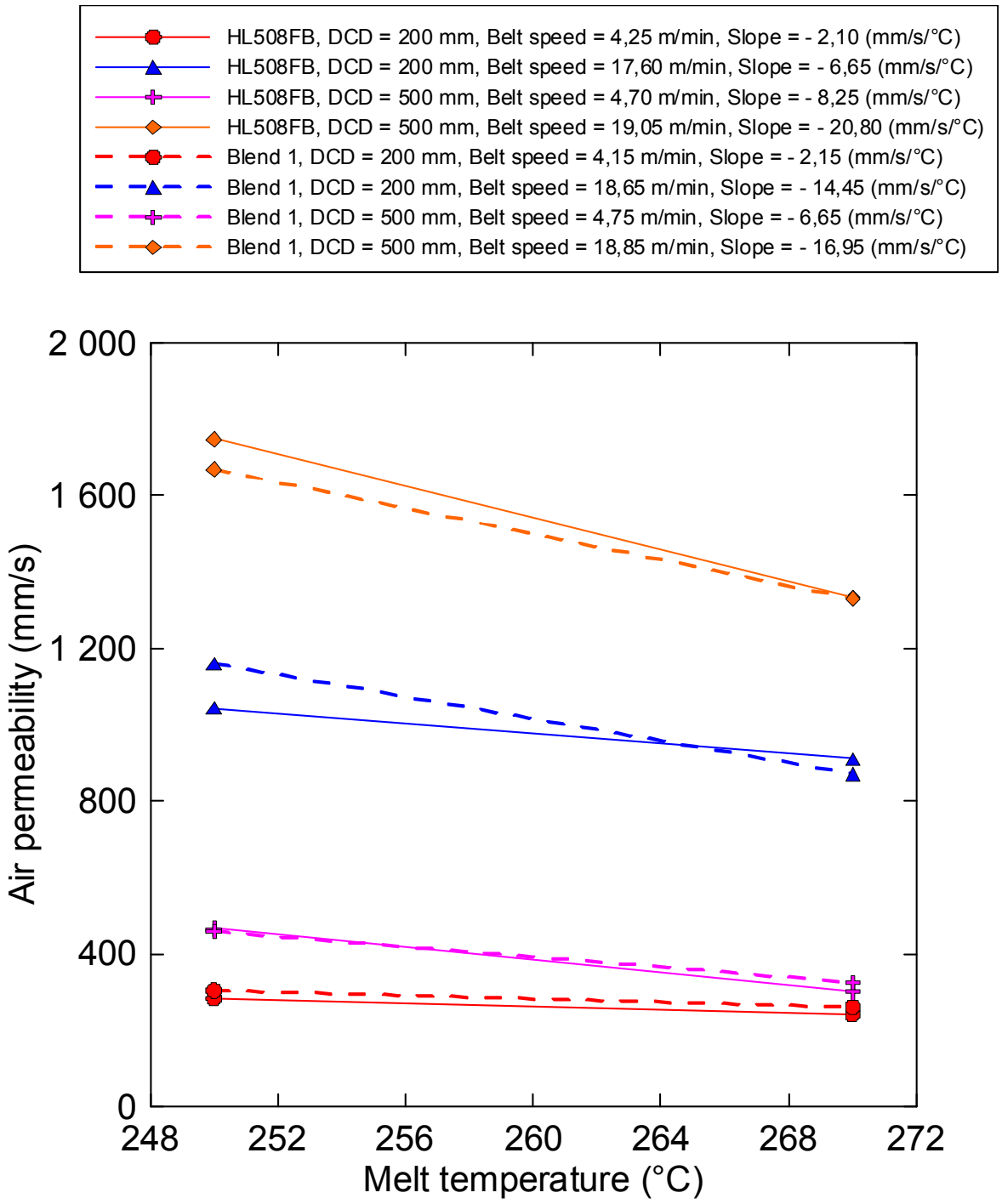

Fig. 71. The effect of the melt temperature on the air permeability for nonwovens prepared from HL508FB and Blend 1 at different processing conditions.

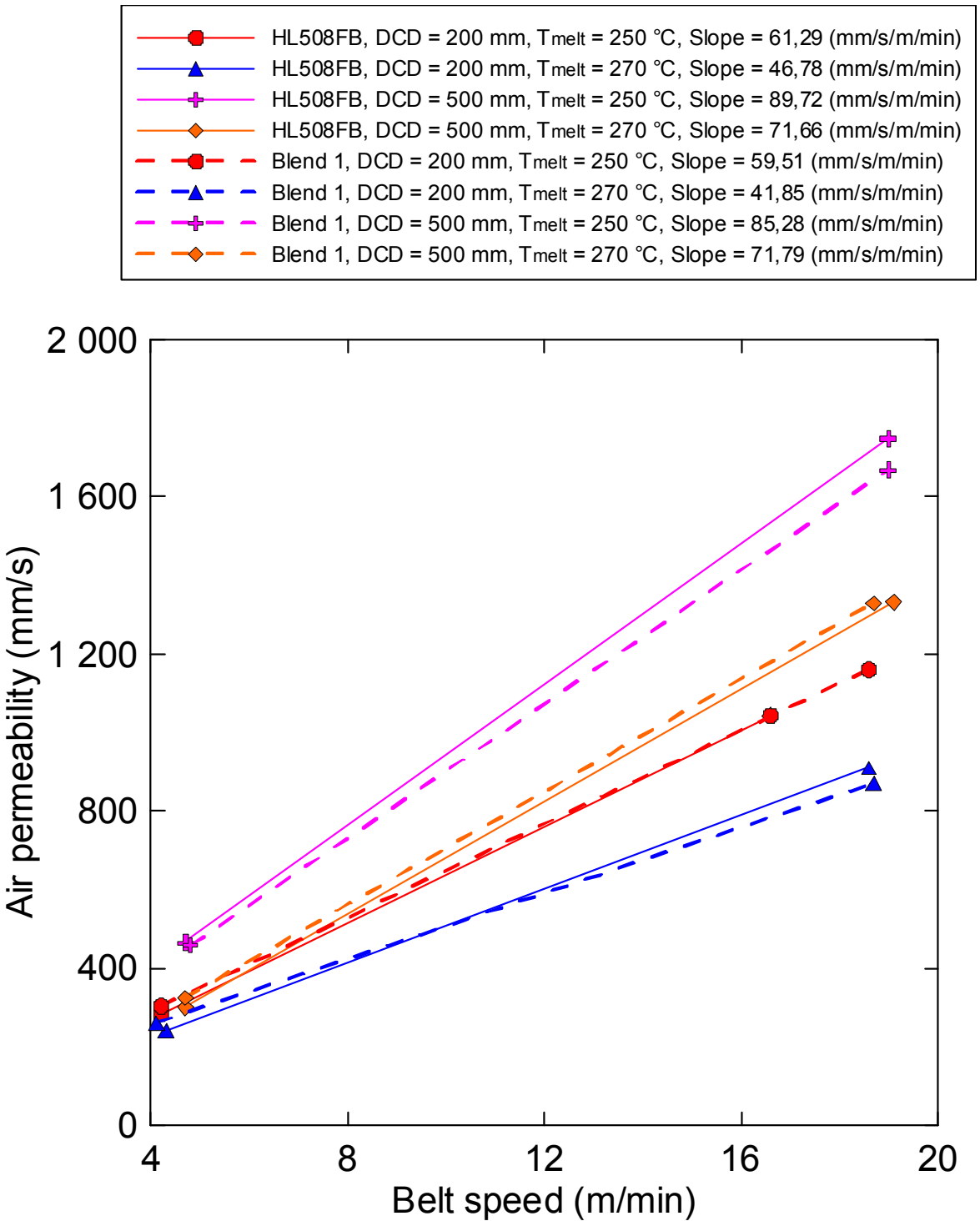

Fig. 72. The effect of the belt speed on the air permeability for nonwovens prepared from HL508FB and Blend 1 at different processing conditions.

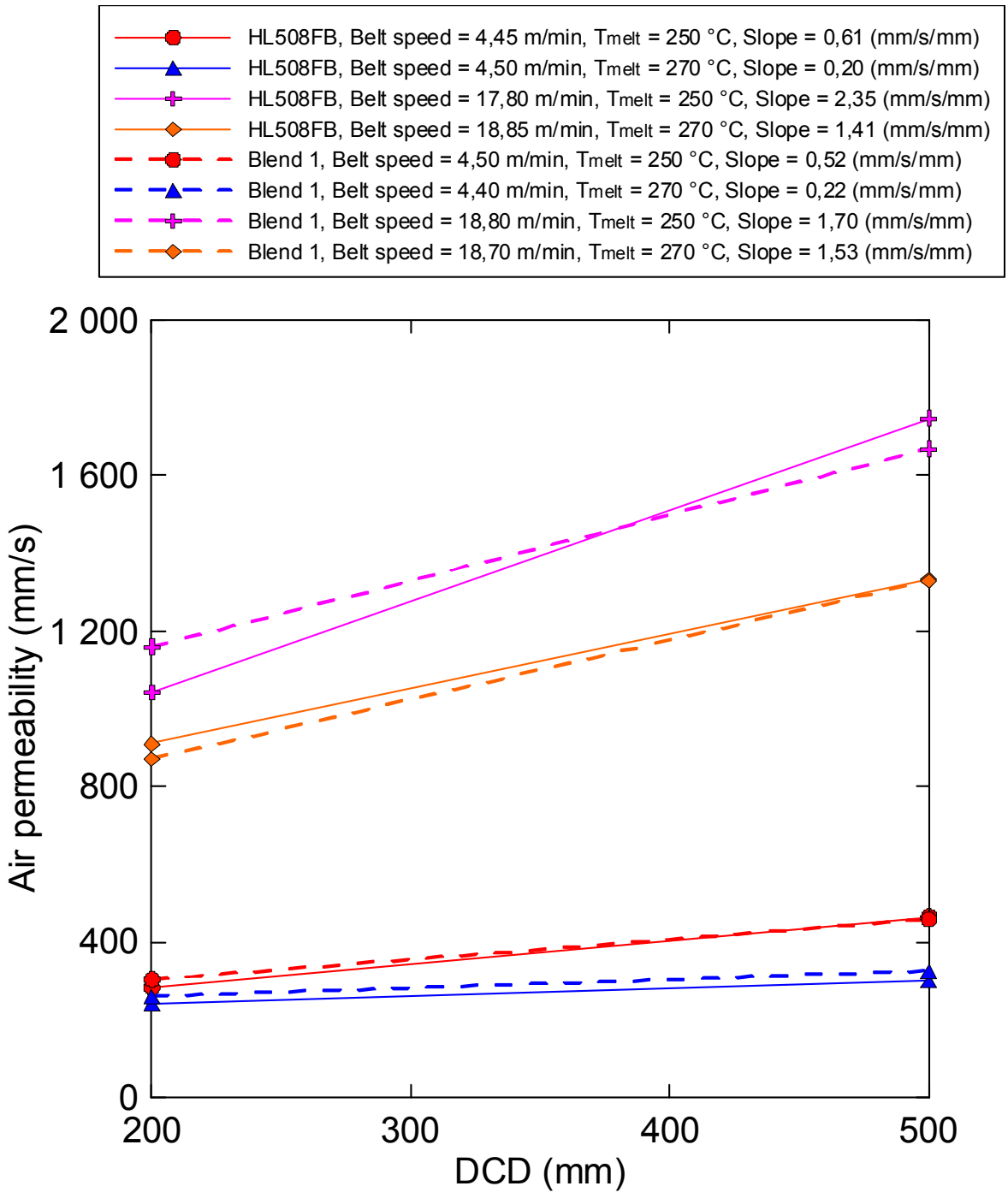

Fig. 73. The effect of the die-collector distance on the air permeability for nonwovens prepared from HL508FB and Blend 1 at different processing conditions.

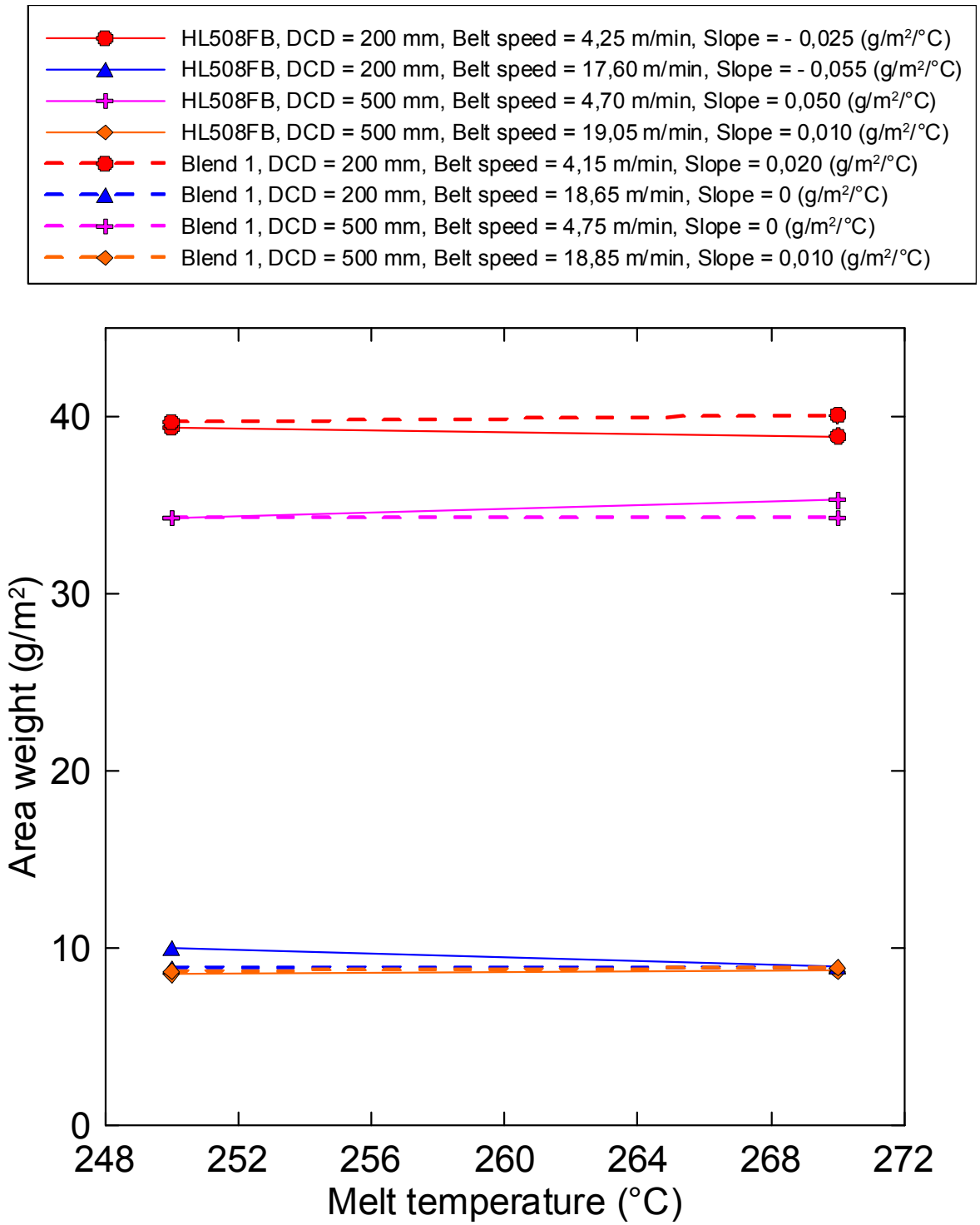

Fig. 74. The effect of the melt temperature on the area weight for nonwovens prepared from HL508FB and Blend 1 at different processing conditions.

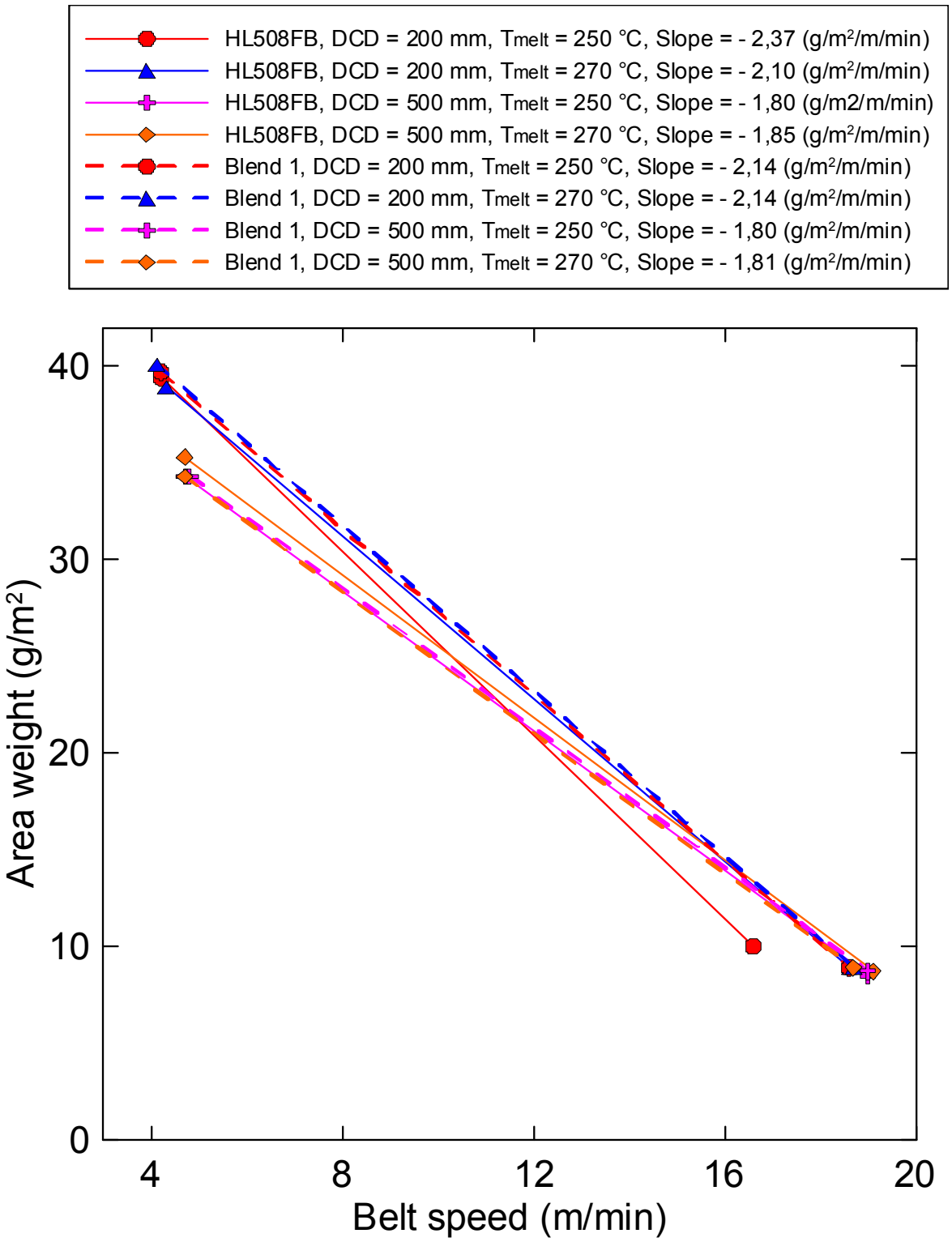

Fig. 75. The effect of the belt speed on the area weight for nonwovens prepared from HL508FB and Blend 1 at different processing conditions.

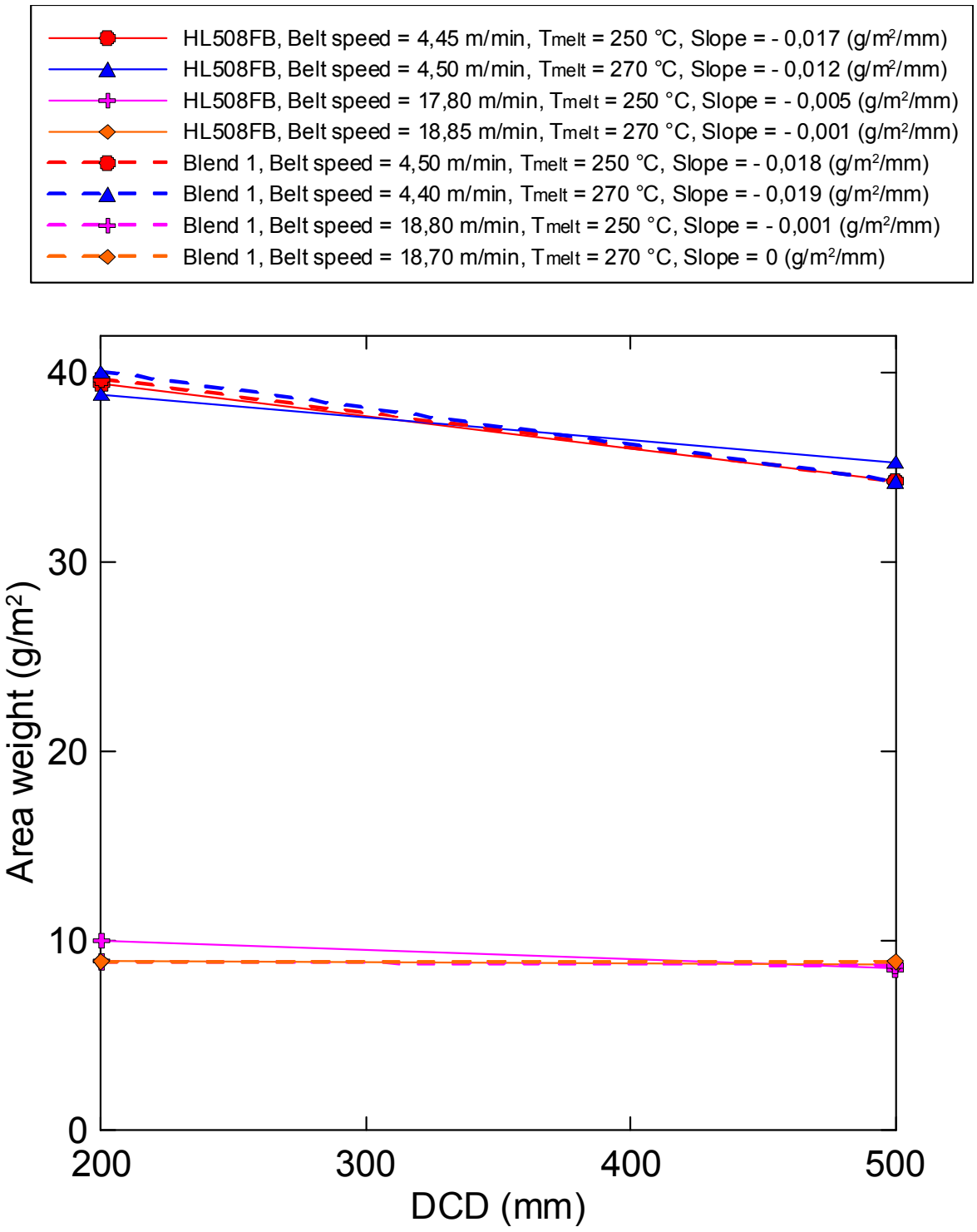

Fig. 76. The effect of the die-collector distance on the area weight for nonwovens prepared from HL508FB and Blend 1 at different processing conditions.

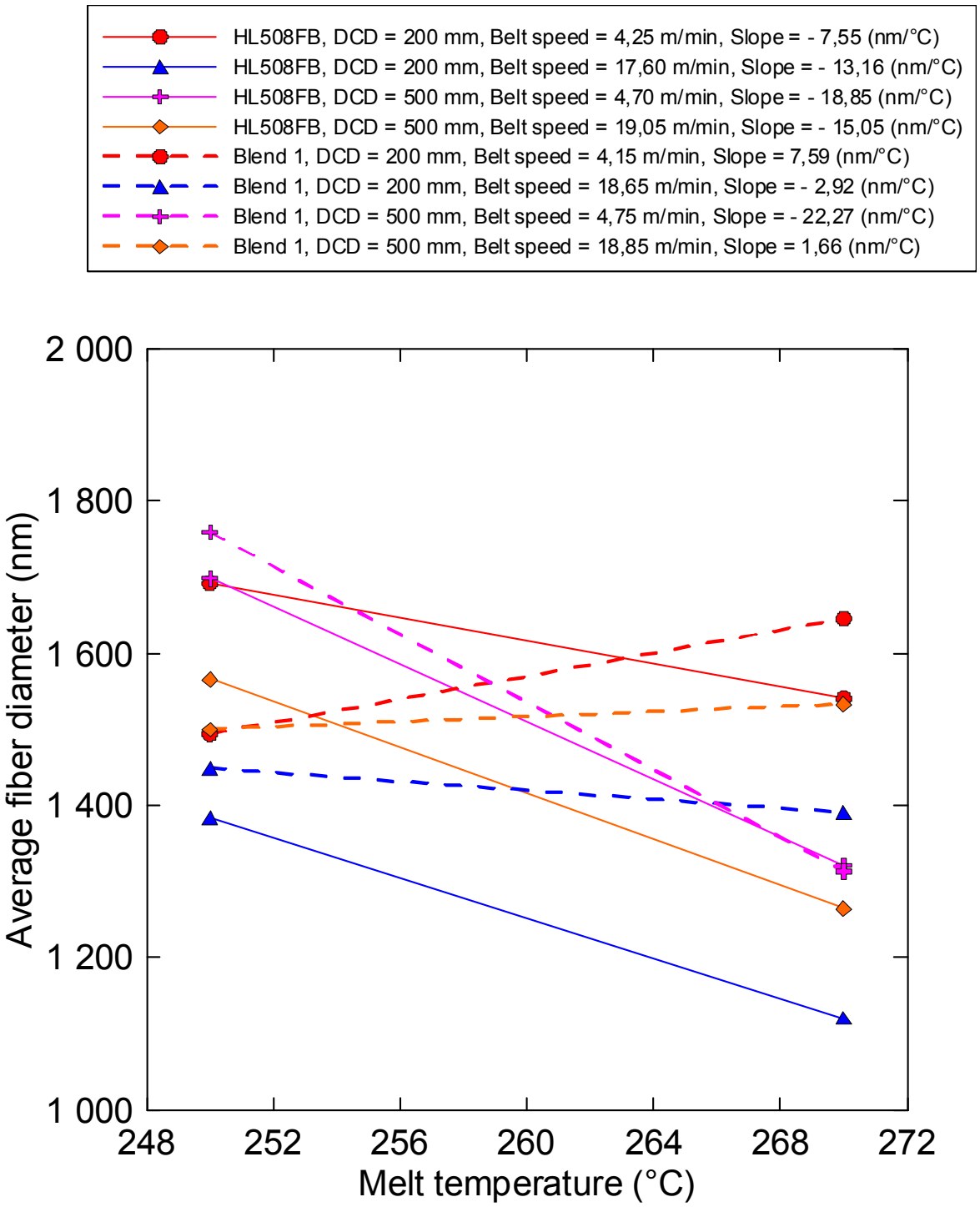

Fig. 77. The effect of the melt temperature on the average fiber diameter for nonwovens prepared from HL508FB and Blend 1 at different processing conditions.

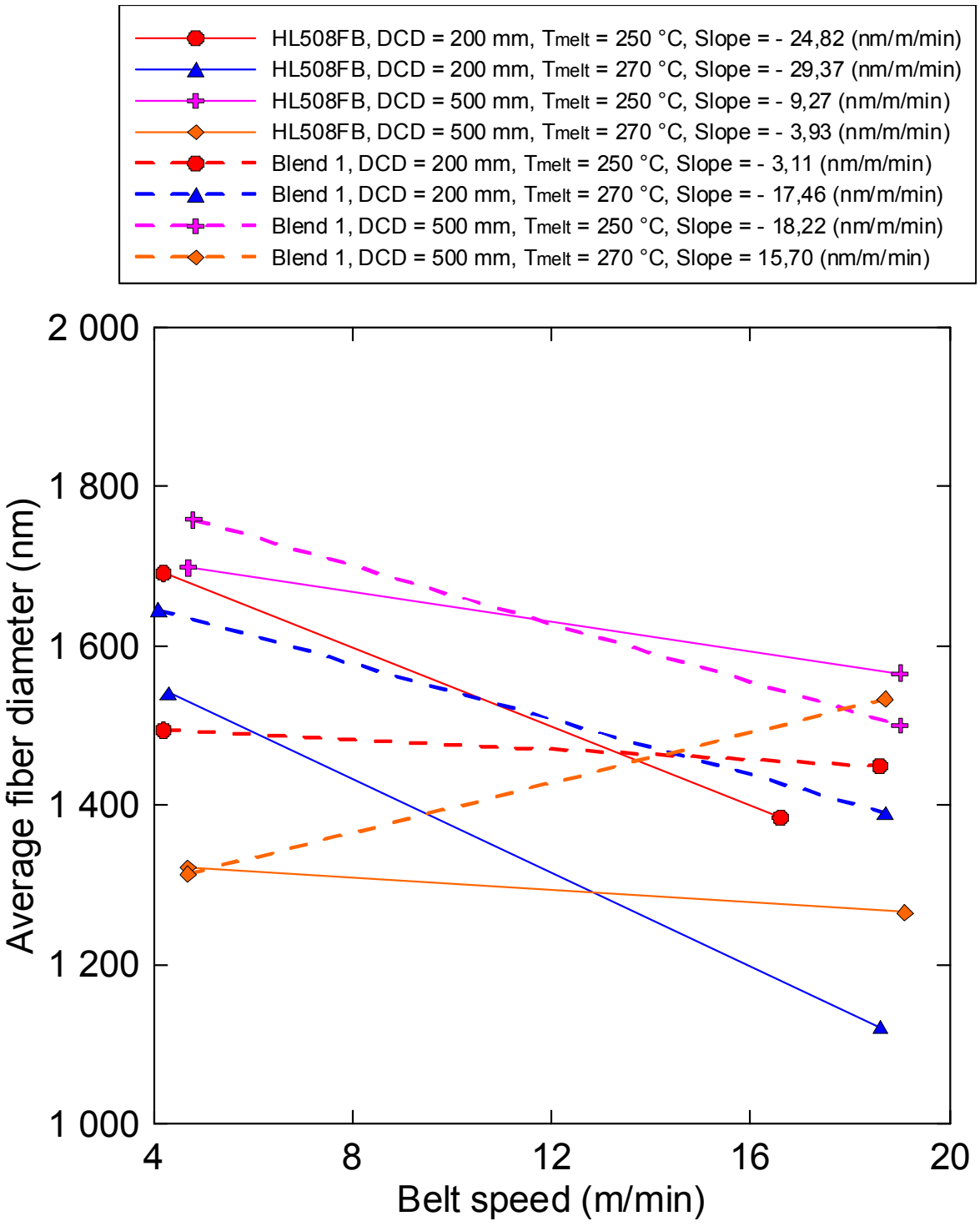

Fig. 78. The effect of the belt speed on the average fiber diameter for nonwovens prepared from HL508FB and Blend 1 at different processing conditions.

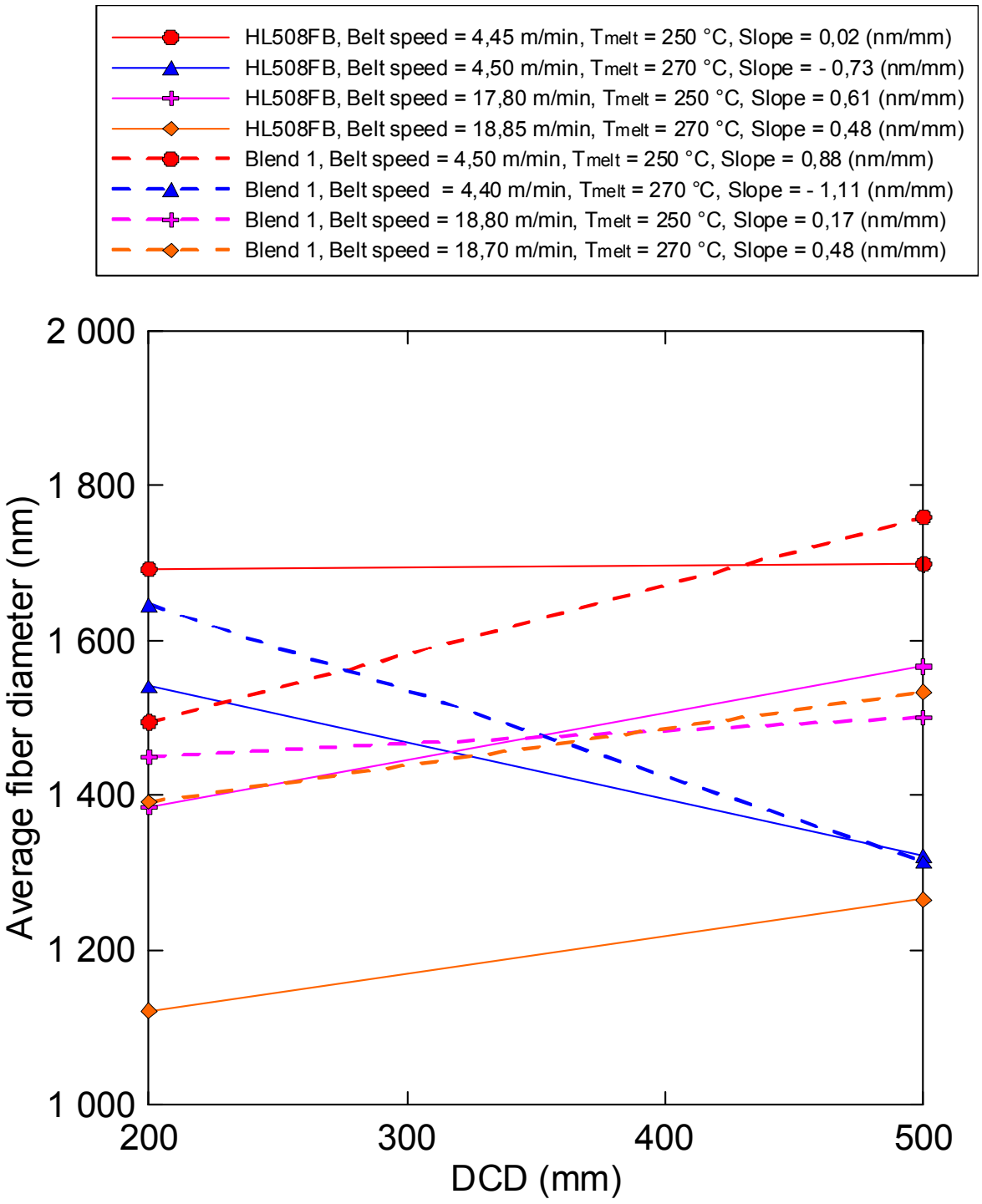

Fig. 79. The effect of the die-collector distance on the average fiber diameter for nonwovens prepared from HL508FB and Blend 1 at different processing conditions.

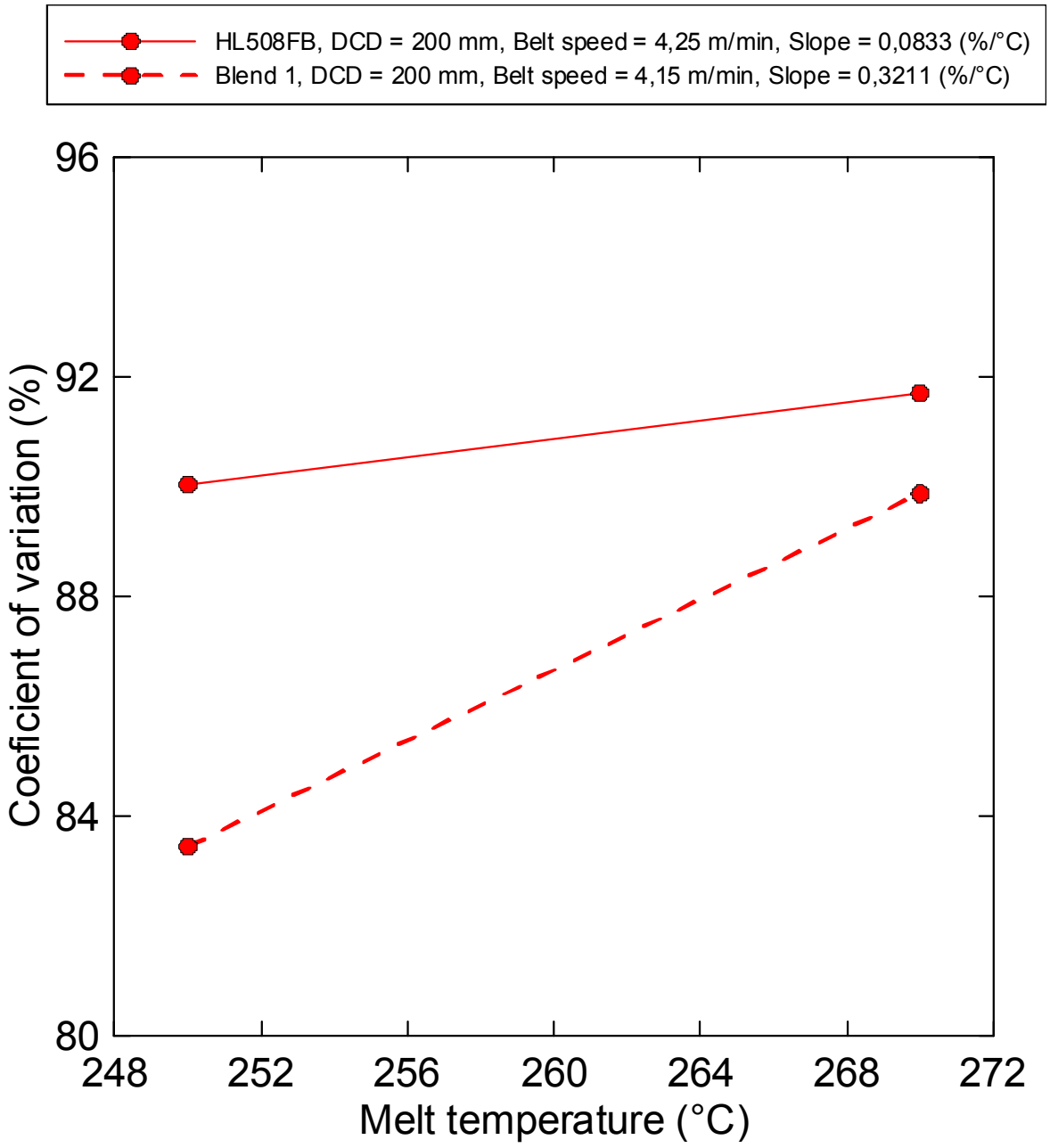

Fig. 80. The effect of the melt temperature on fiber diameter coefficient of variation for nonwovens prepared from HL508FB and Blend 1 at DCD=200mm and belt speed=4,25m/min.

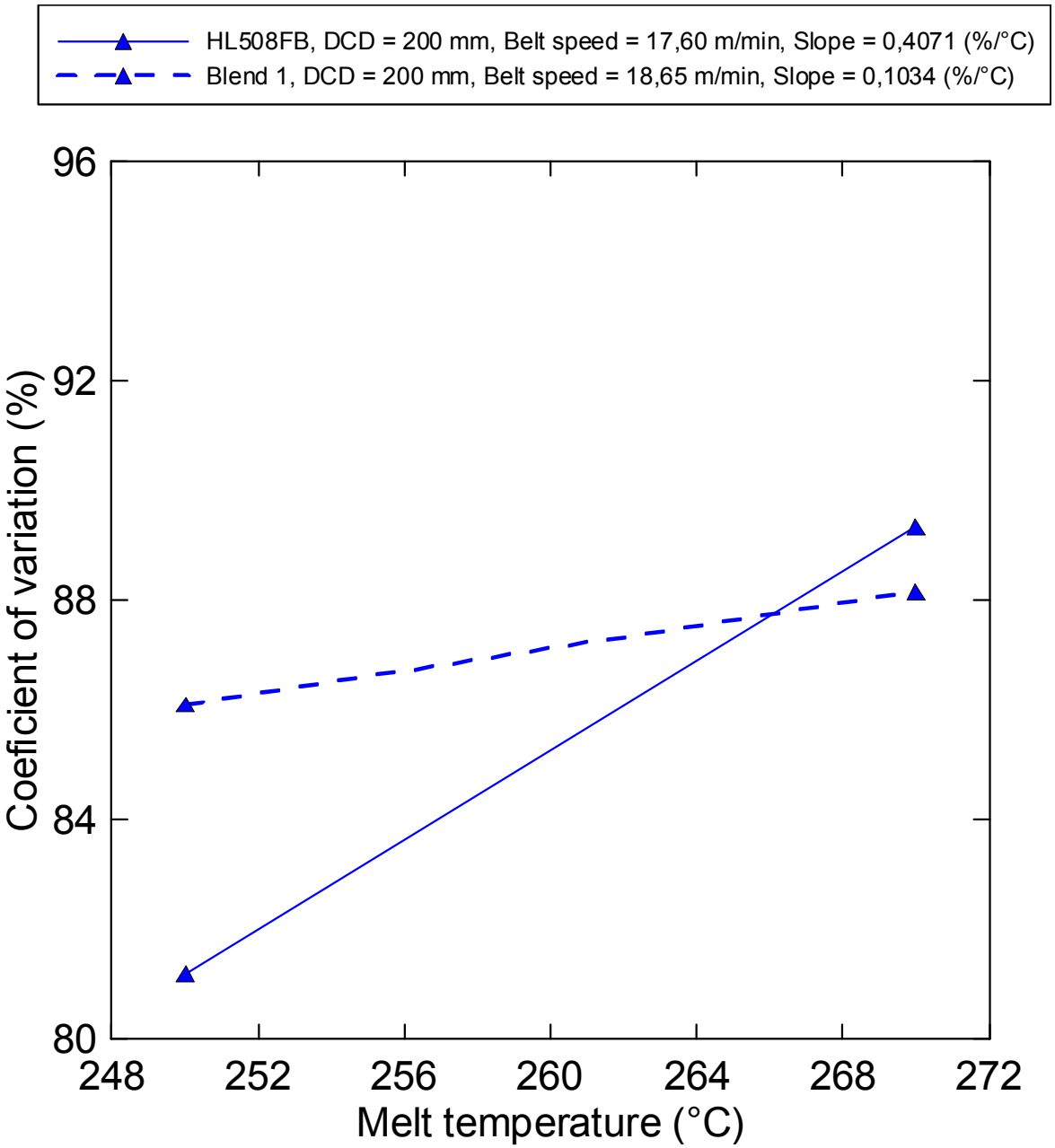

Fig. 81. The effect of the melt temperature on fiber diameter coefficient of variation for nonwovens prepared from HL508FB and Blend 1 at DCD=200mm and belt speed=17,60m/min.

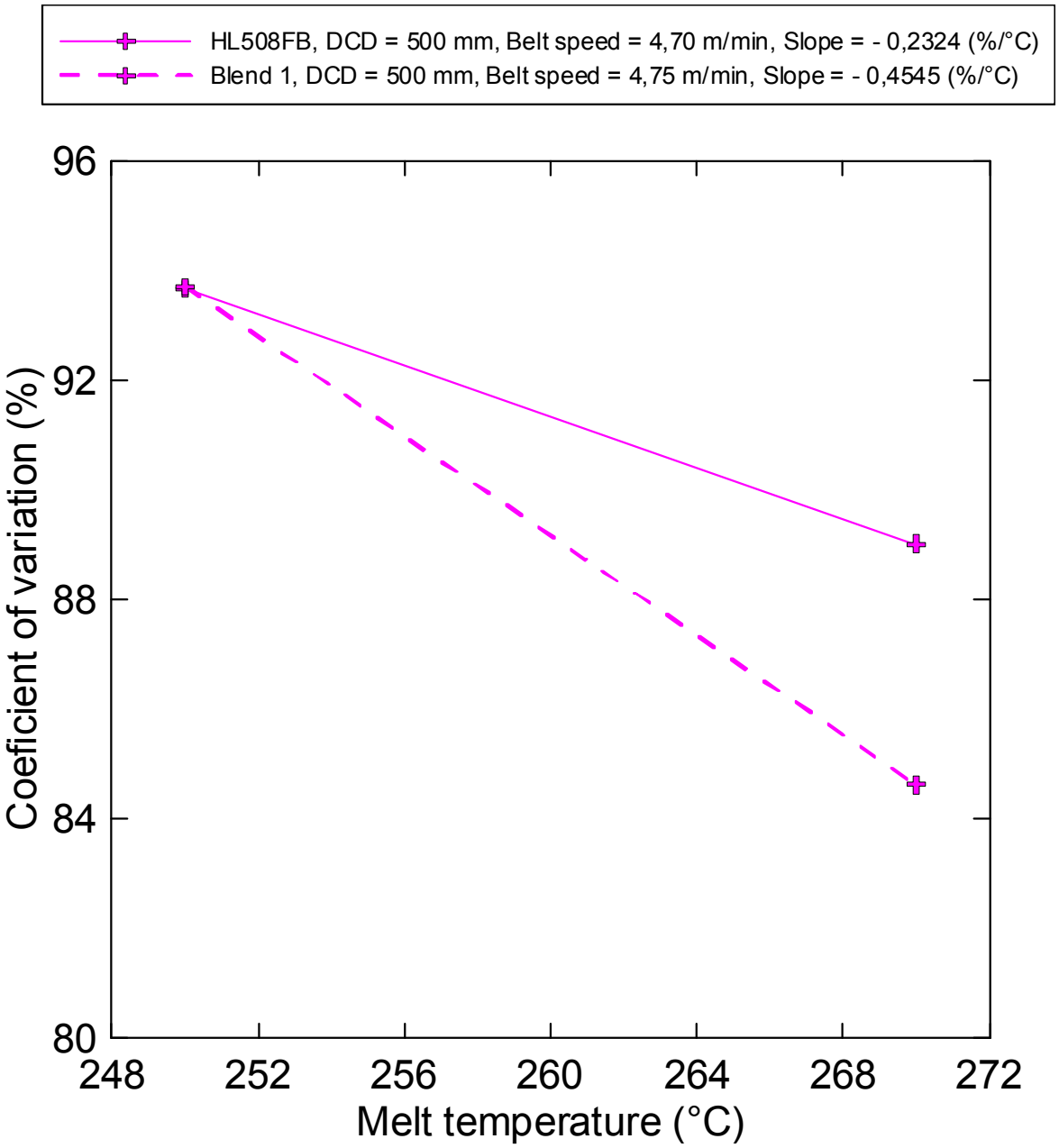

Fig. 82. The effect of the melt temperature on fiber diameter coefficient of variation for nonwovens prepared from HL508FB and Blend 1 at DCD=500mm and belt speed=4,70m/min.

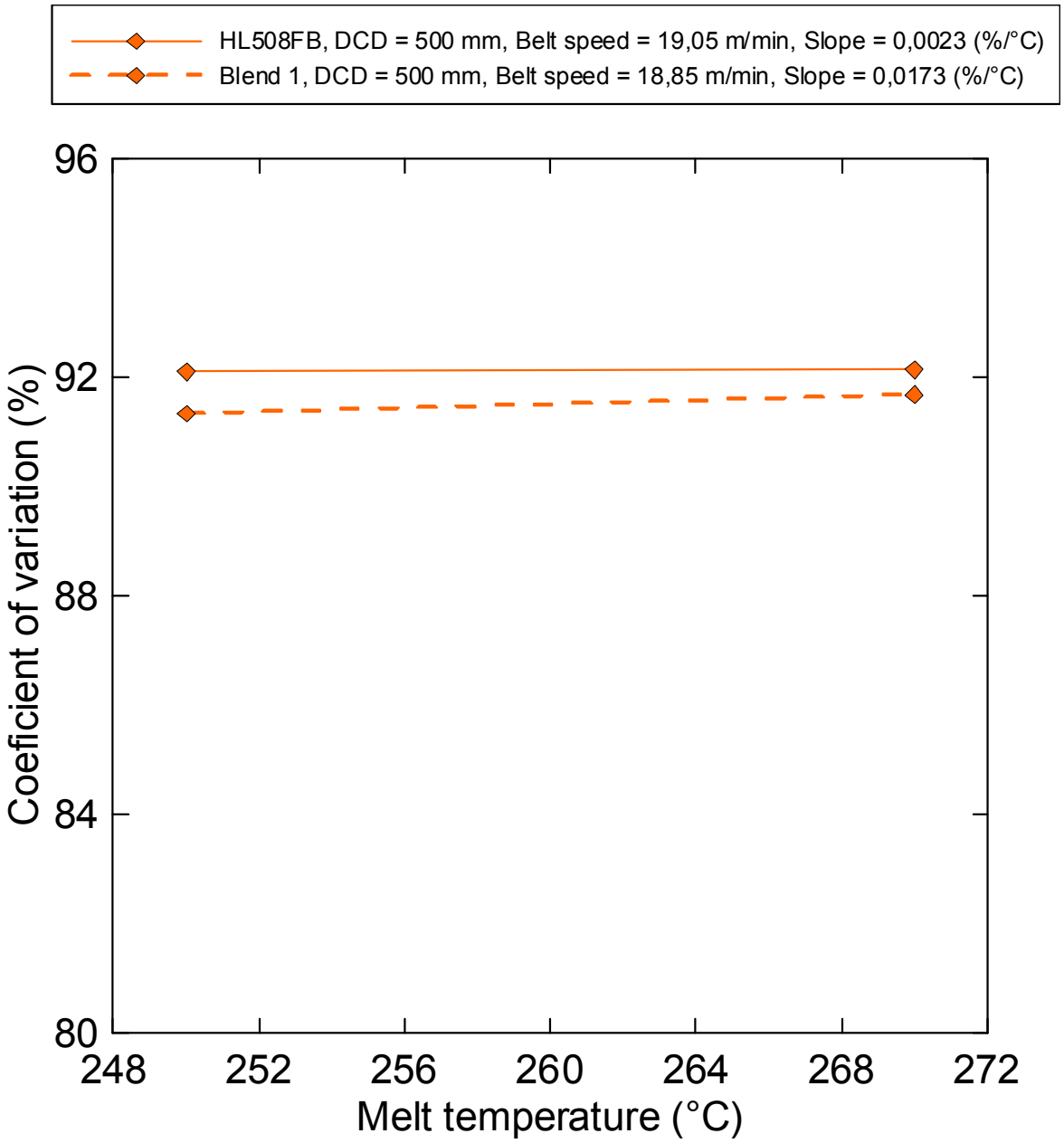

Fig. 83. The effect of the melt temperature on fiber diameter coefficient of variation for nonwovens prepared from HL508FB and Blend 1 at DCD=500mm and belt speed=19,05m/min.

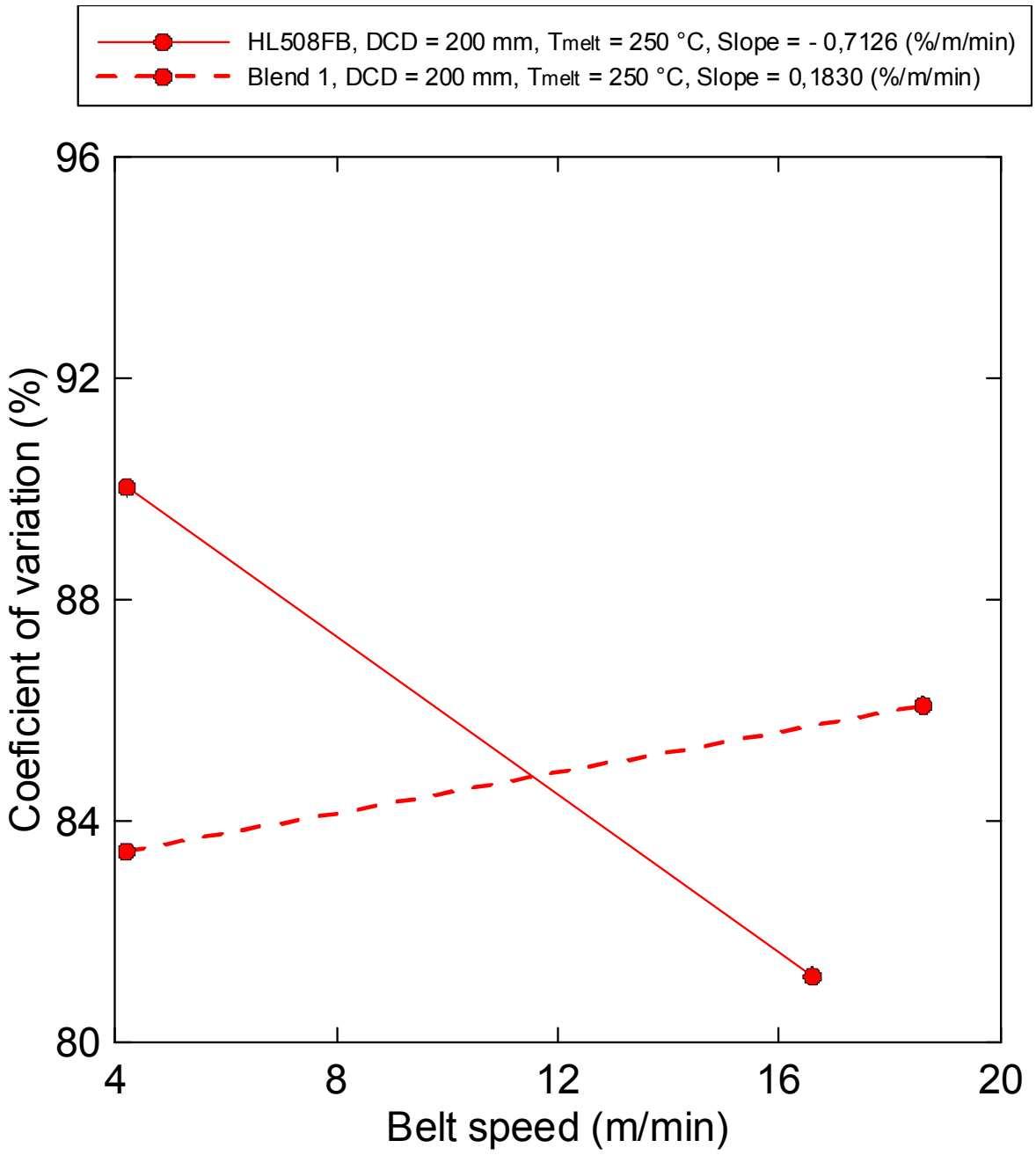

Fig. 84. The effect of the belt speed on fiber diameter coefficient of variation for nonwovens prepared from HL508FB and Blend 1 at DCD=200mm and melt temperature=250°C.

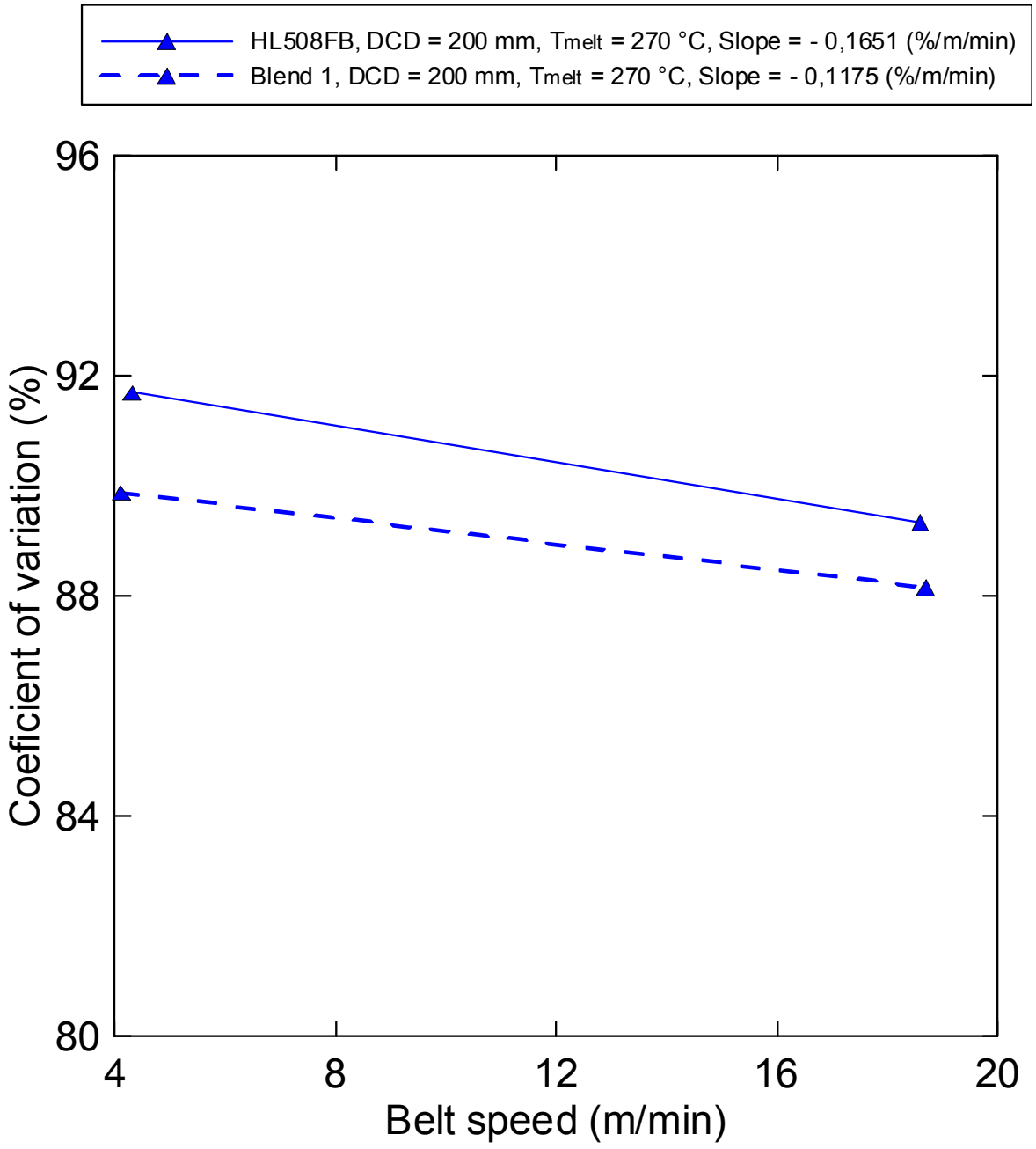

Fig. 85. The effect of the belt speed on fiber diameter coefficient of variation for nonwovens prepared from HL508FB and Blend 1 at DCD=200mm and melt temperature=270°C.

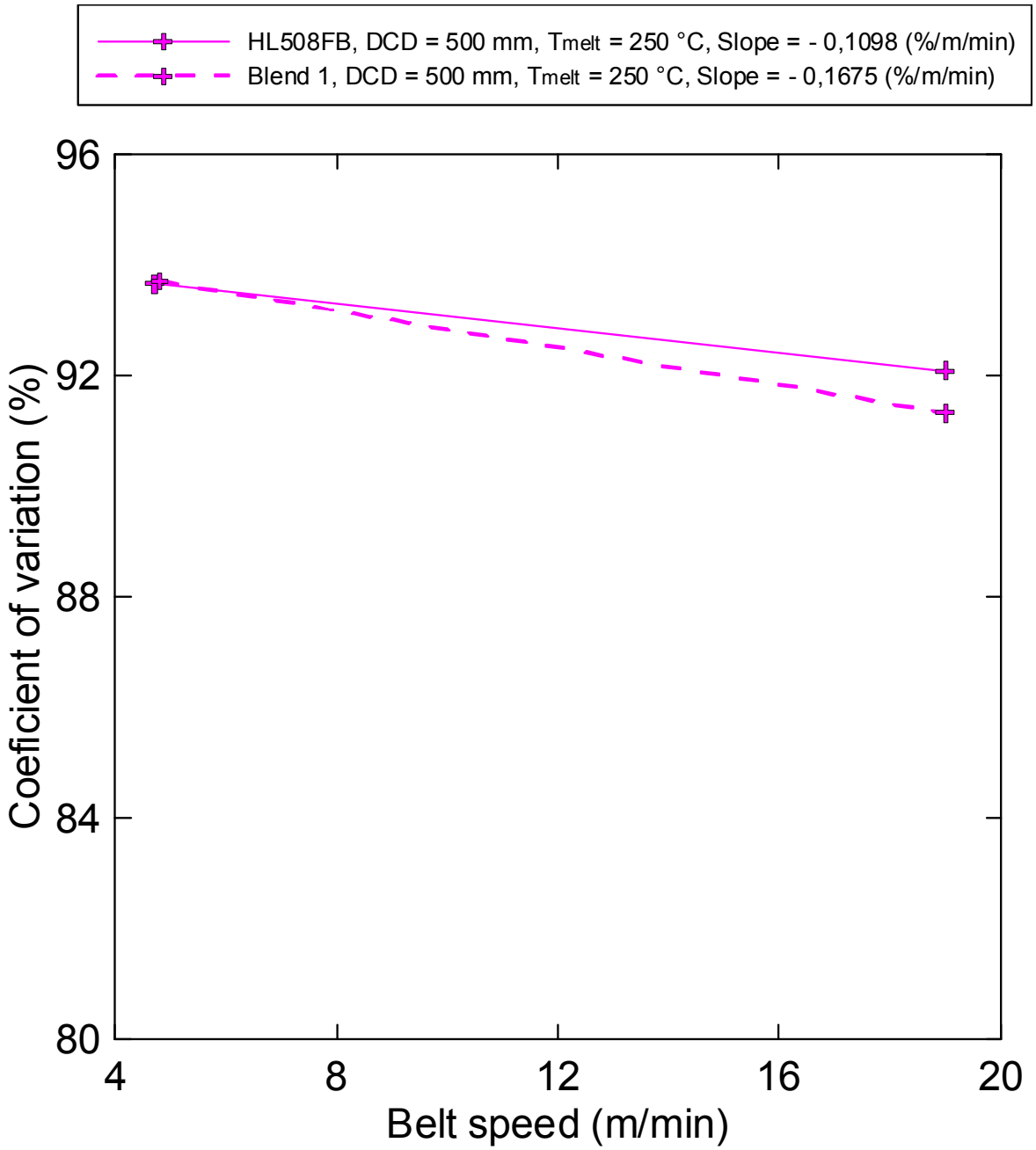

Fig. 86. The effect of the belt speed on fiber diameter coefficient of variation for nonwovens prepared from HL508FB and Blend 1 at DCD=500mm and melt temperature=250°C.

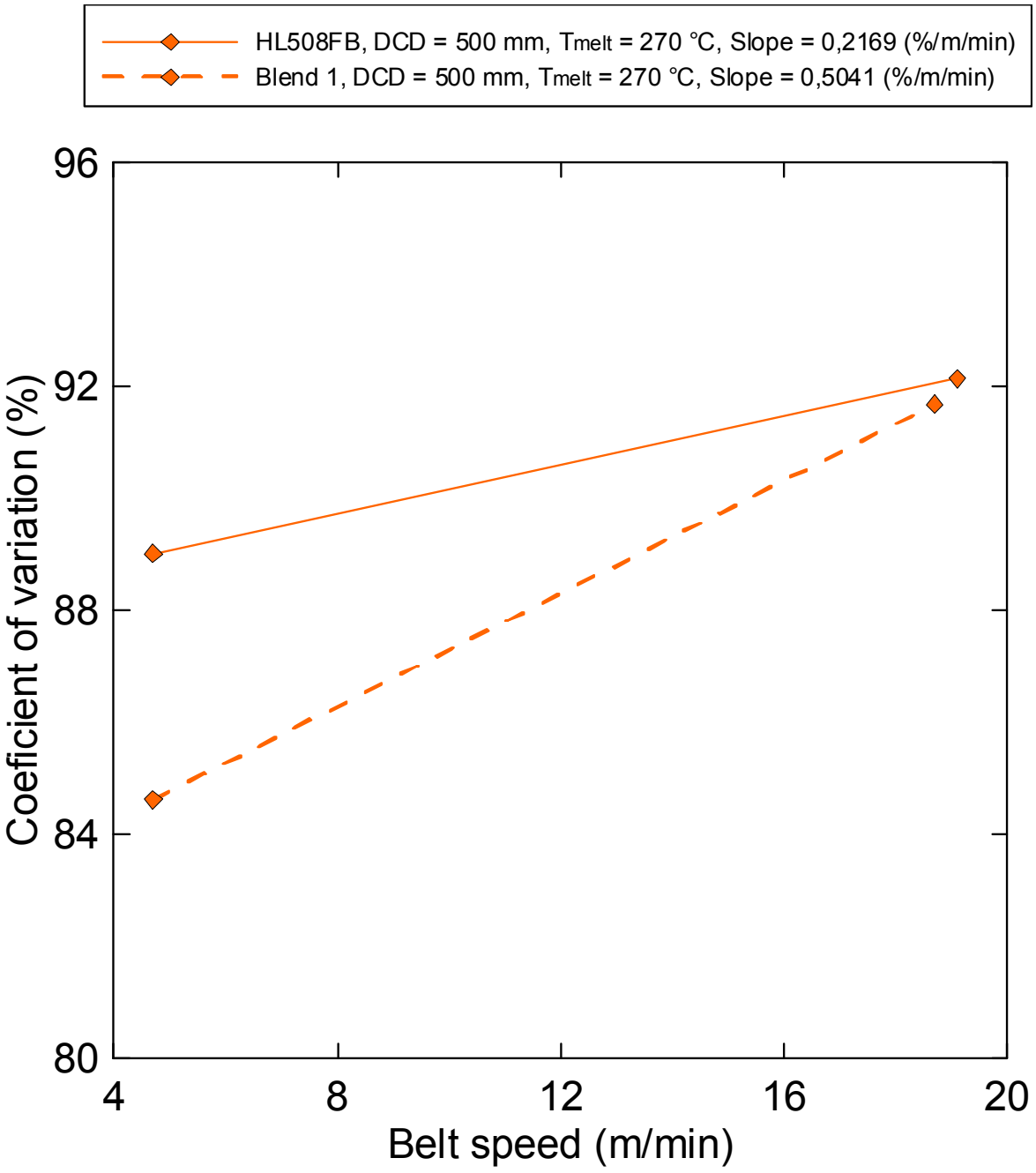

Fig. 87. The effect of the belt speed on fiber diameter coefficient of variation for nonwovens prepared from HL508FB and Blend 1 at DCD=500mm and melt temperature=270°C.

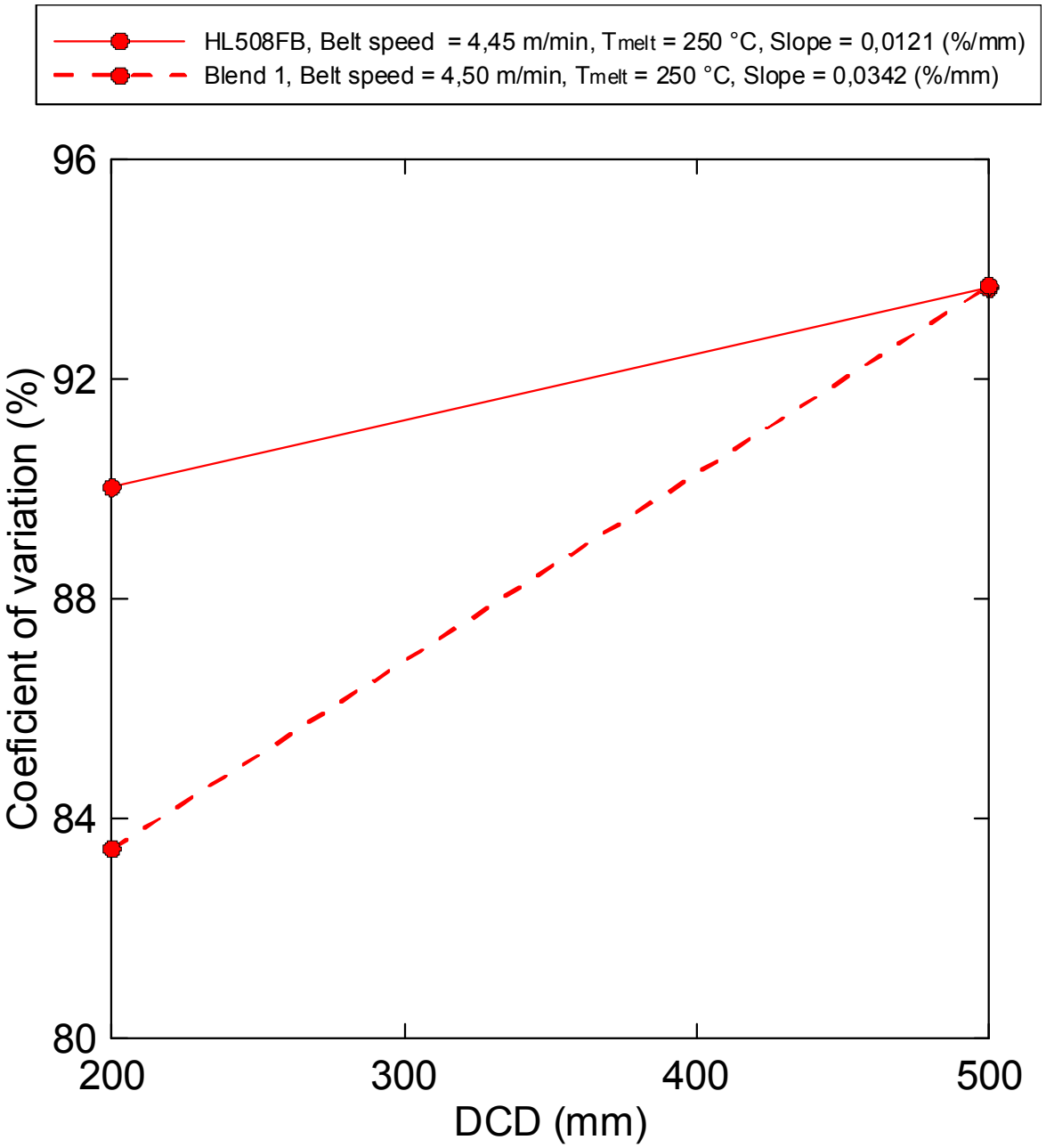

Fig. 88. The effect of the die-collector distance on fiber diameter coefficient of variation for nonwovens prepared from HL508FB and Blend 1 at belt speed=4,45m/min and melt temperature=250°C.

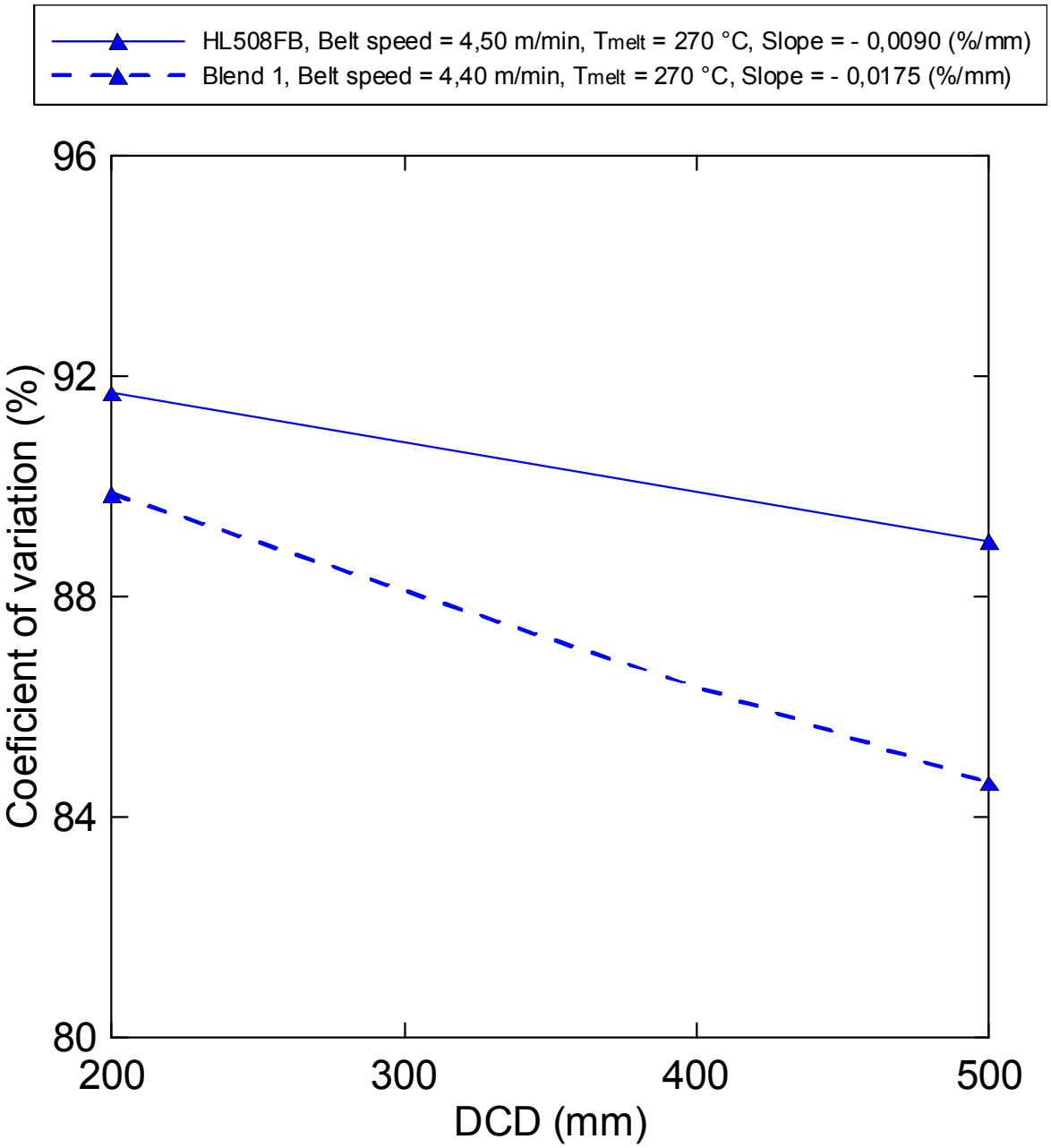

Fig. 89. The effect of the die-collector distance on fiber diameter coefficient of variation for nonwovens prepared from HL508FB and Blend 1 at belt speed=4,5m/min and melt temperature=270°C.

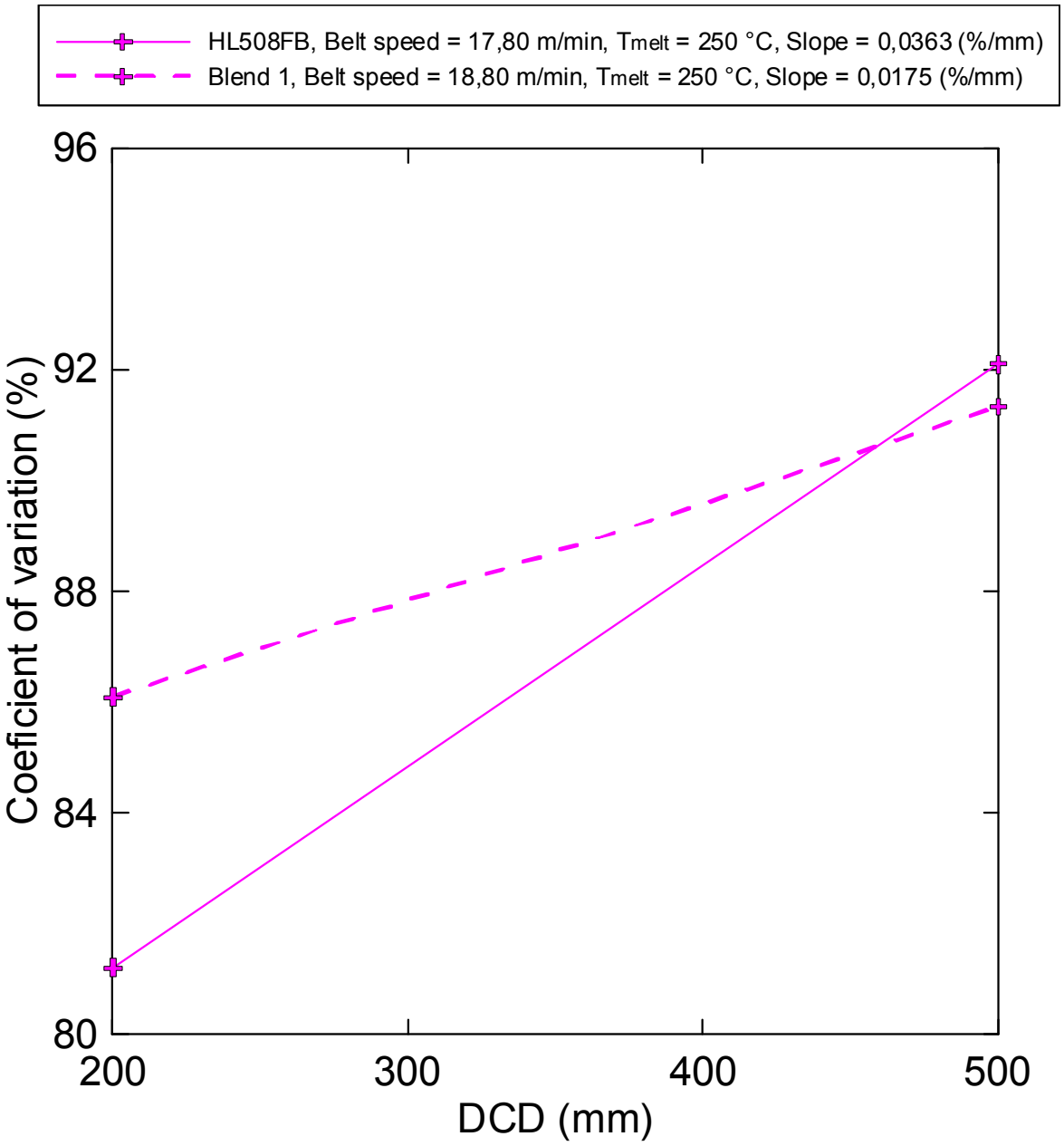

Fig. 90. The effect of the die-collector distance on fiber diameter coefficient of variation for nonwovens prepared from HL508FB and Blend 1 at belt speed=17,8m/min and melt temperature=250°C.

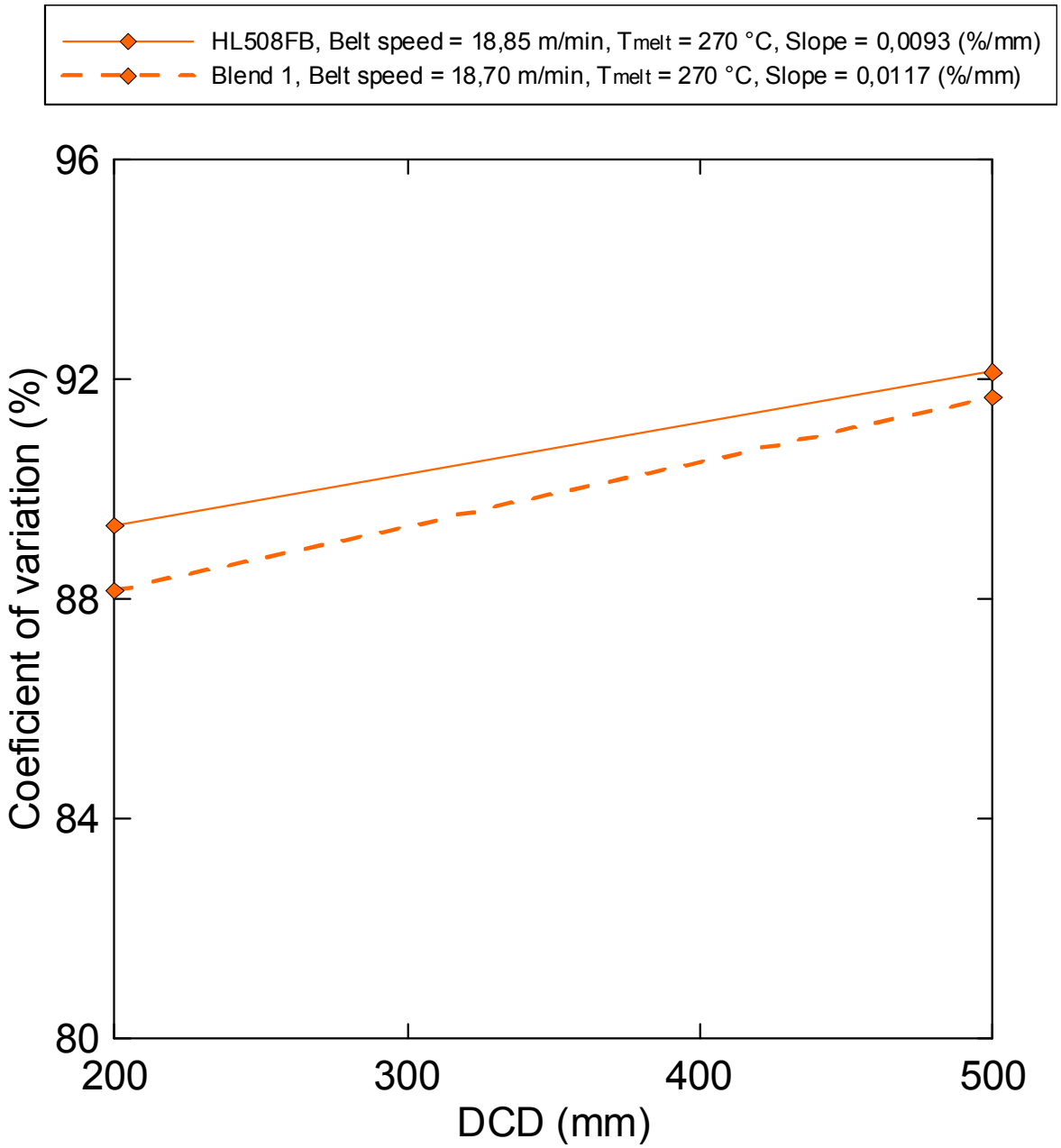

Fig. 91. The effect of the die-collector distance on fiber diameter coefficient of variation for nonwovens prepared from HL508FB and Blend 1 at belt speed=18,85m/min and melt temperature = 270°C.

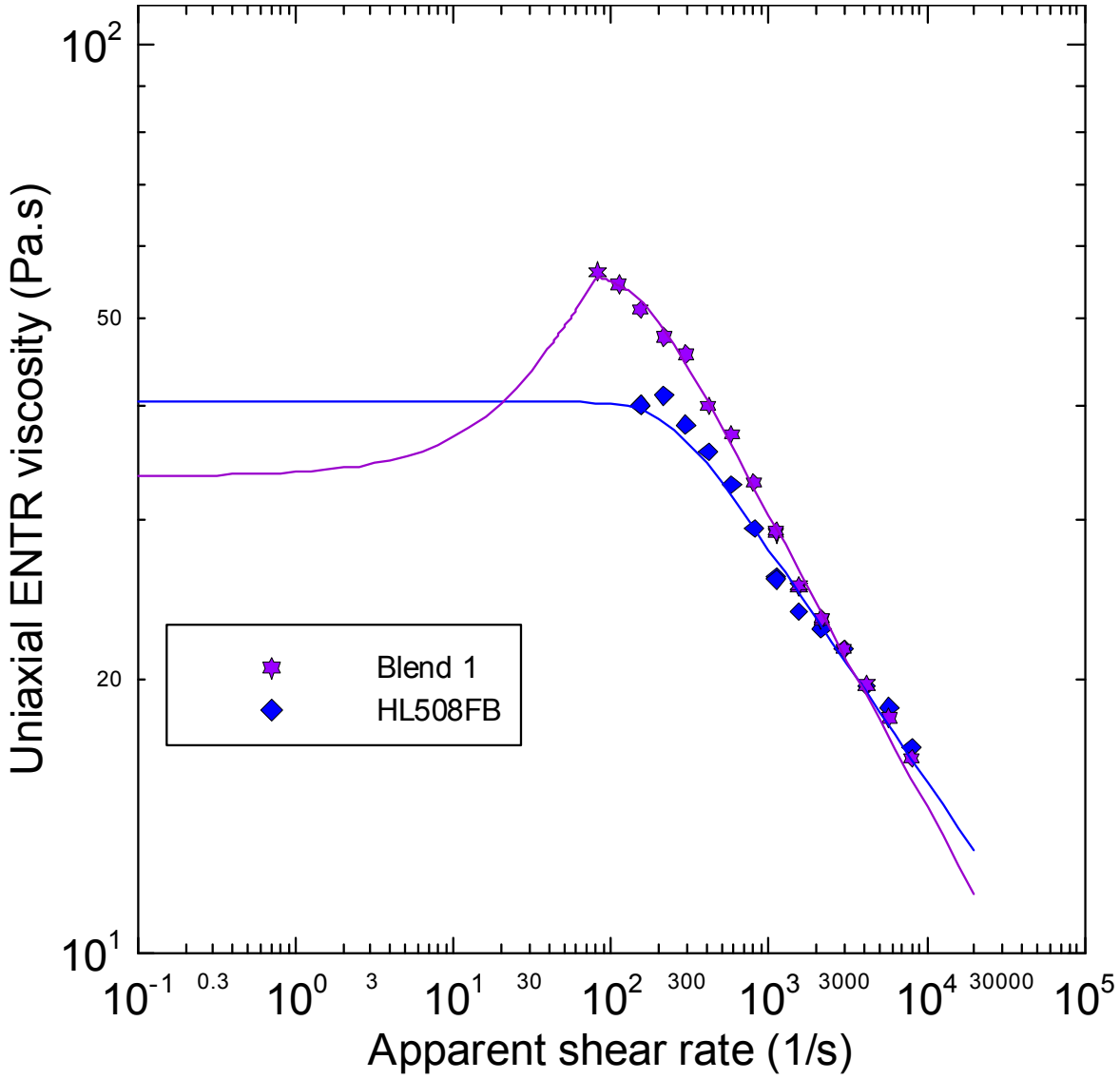

Fig. 92. Comparison between deformation rate dependent uniaxial entrance viscosities for HL508FB and Blend 1 at T=230°C. Here the line represents the entrance viscosity model fitting line given by Eq.59, which satisfies physical constrains for zero deformation rate range according to Eq.60-61.

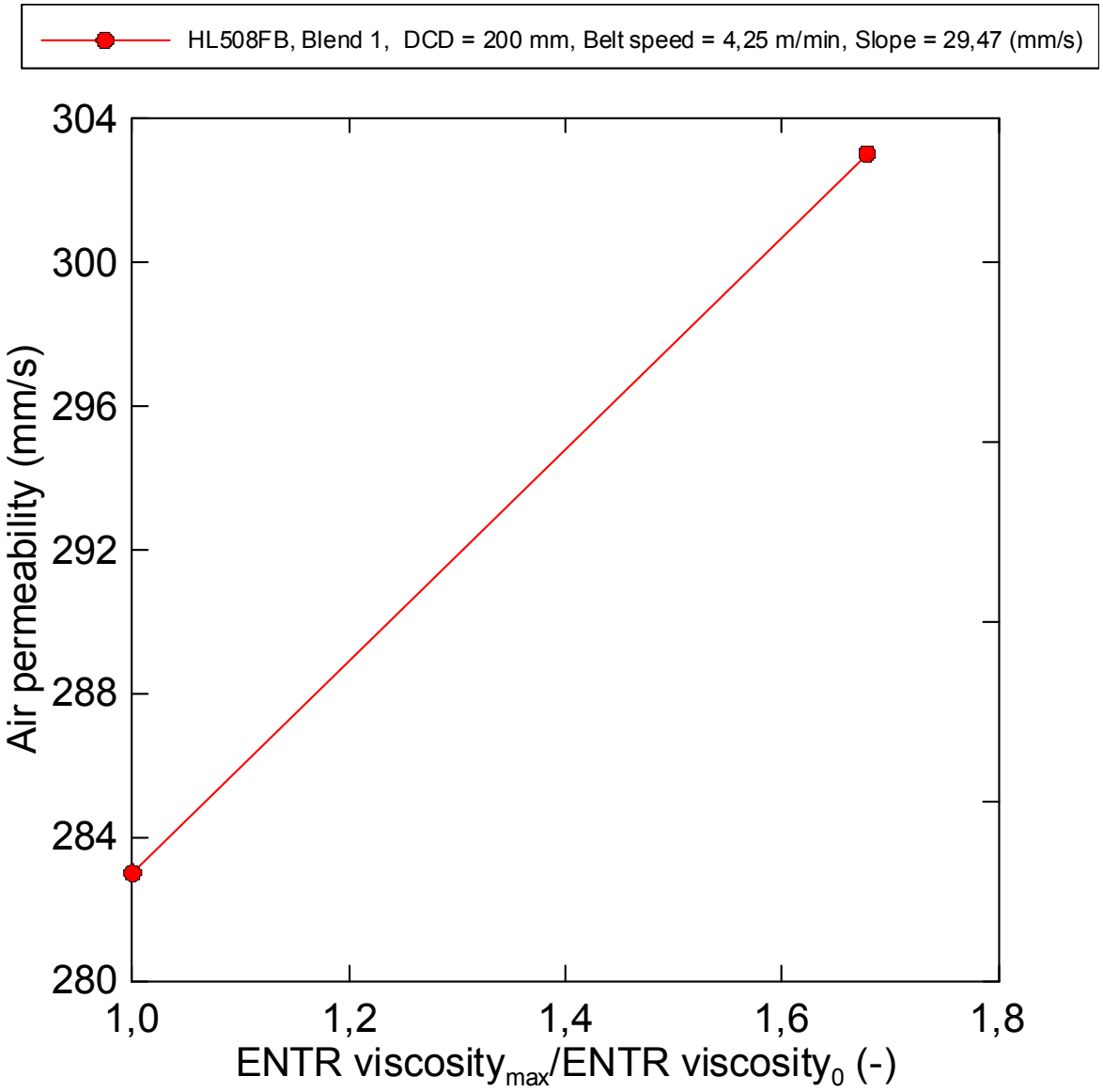

Fig. 93. The effect of strain hardening ratio in uniaxial entrance viscosity on the air permeability of the produced meltblown nonwoven at given processing conditions.

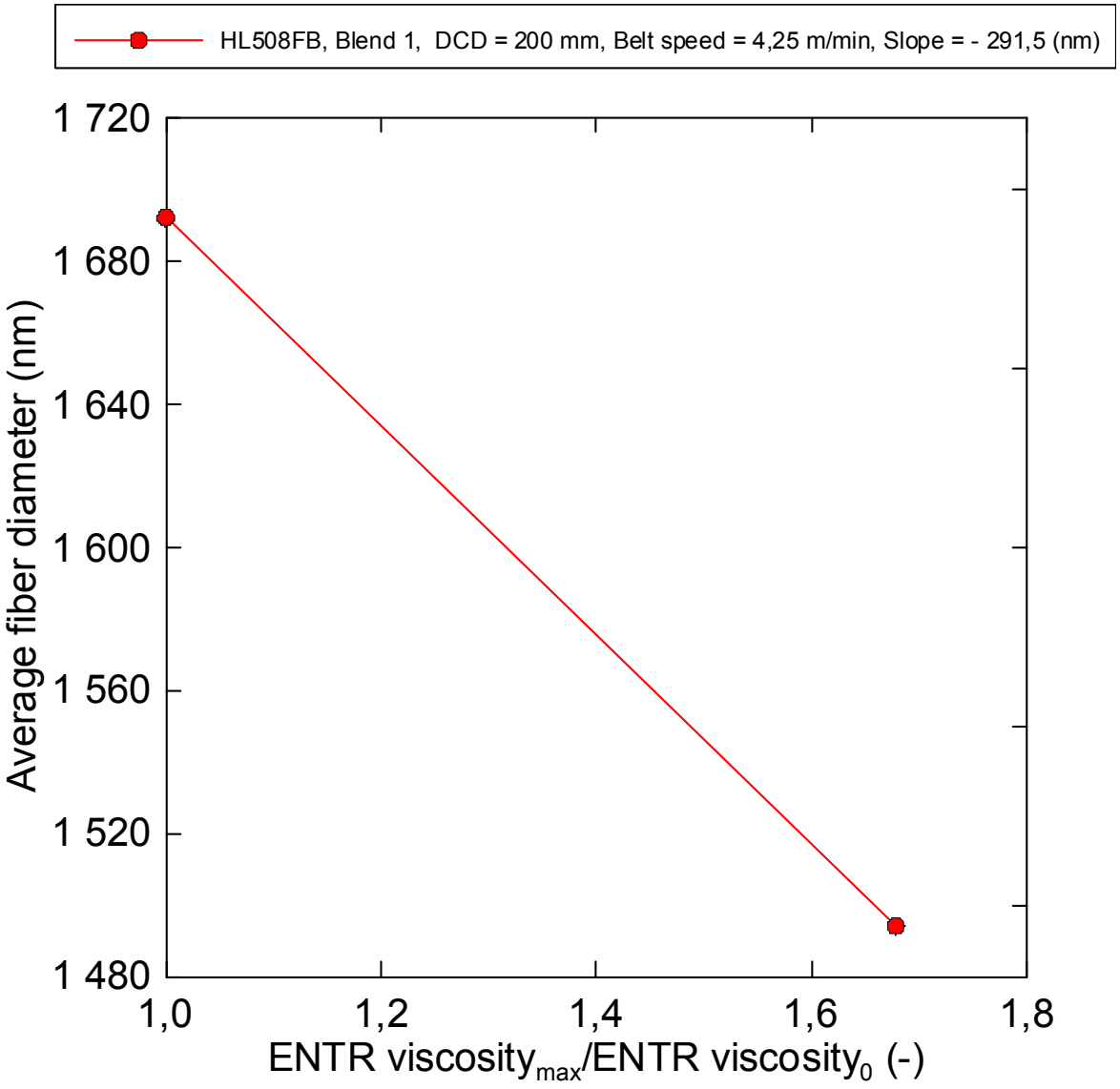

Fig. 94. The effect of strain hardening ratio in uniaxial entrance viscosity on the average fiber diameter of the produced meltblown nonwoven at given processing conditions.

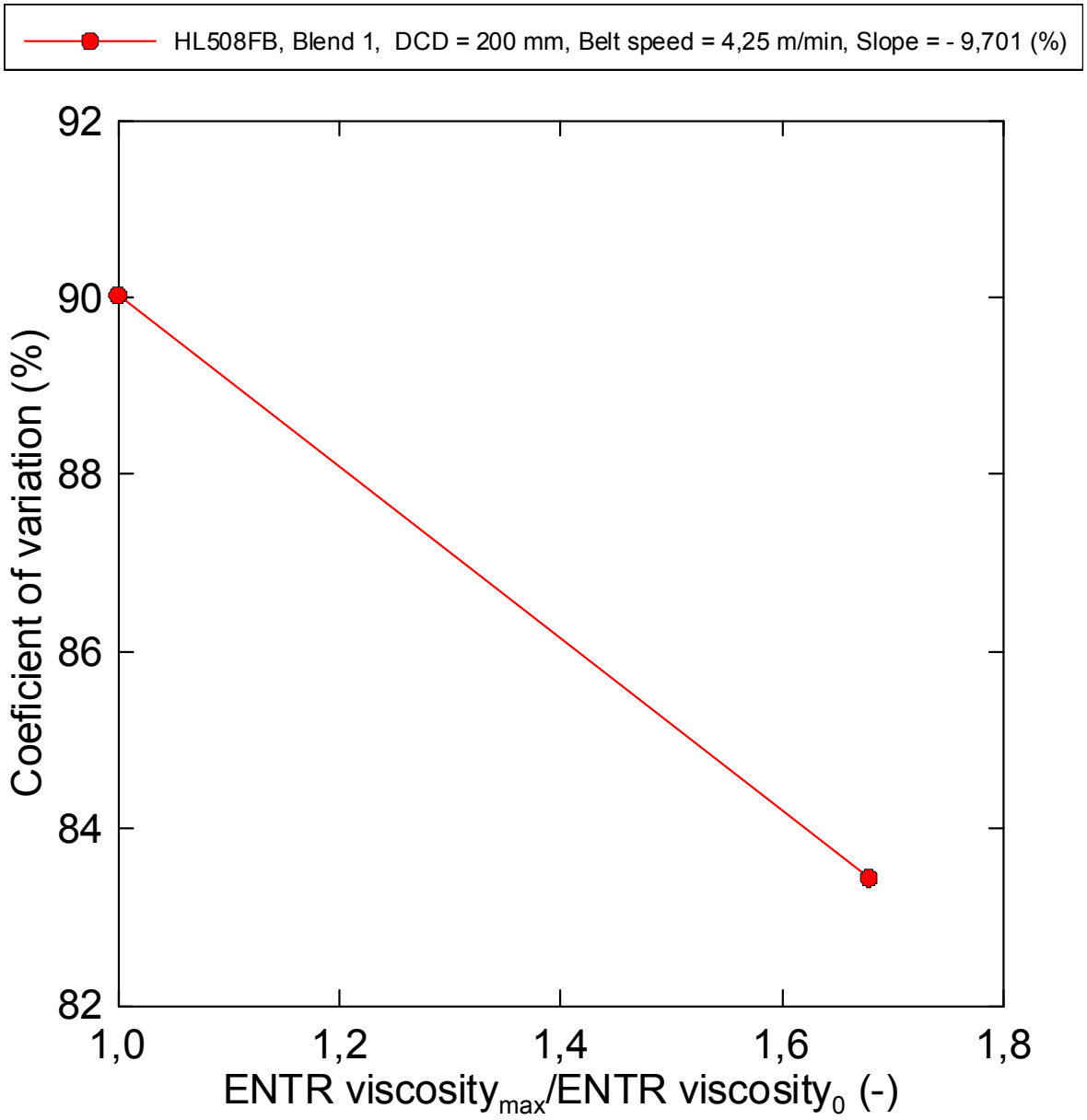

Fig. 95. The effect of strain hardening ratio in uniaxial entrance viscosity on the coefficient of variation for average fiber diameter of the produced meltblown nonwoven at given processing conditions.

CONCLUSION REMARKS

1. Rheological characterization of linear and branched melt blown polypropylene samples was performed in shear as well as elongational flows by using twin bore capillary rheometer and novel circular and rectangle dies. It was revealed that an overshoot in uniaxial and planar entrance viscosities occurs for branched polypropylene samples but not for the linear ones. In more detail, the overshoot intensity was found to be higher for uniaxial entrance viscosity in comparison with the planar entrance viscosity.

2. It was found that the combination of 10wt-% branched PP Daploy WB180HMS together with 90wt-% linear PP Borflow HL512 FB B2-90367 leads to the branched polypropylene blend having the same shear viscosity as the linear PP Borflow HL512 FB B2-90367 sample, however, their uniaxial and planar entrance viscosities were found to be different. In more detail, the uniaxial entrance viscosity for branched PP blend was found to be higher in comparison with the corresponding linear PP sample whereas planar entrance viscosity for branched PP blend was smaller in comparison with linear PP sample.

3. The effect of elongational rheology of polypropylene samples and melt blown processing conditions (melt temperature, die-collector distance, collector belt speed) on the basic characteristics of the produced nanofiber based nonwovens (area weight, air permeability, average fiber diameter, coefficient of variation for the average fiber diameter) was investigated on the melt blown pilot plant line. It was found that even if the effect of melt blown processing conditions on the nonwoven production for branched PP blend and the corresponding linear PP is comparable, the branched PP blend showed the tendency to create fibers with smaller average fiber diameter (13,2% difference), smaller coefficient of variation for the average fiber diameter (7,9% difference) and higher air permeability (6,6% difference) in comparison with the corresponding linear PP. This suggests that utilization of the branched polypropylenes with controlled shear, uniaxial and planar entrance viscosities could significantly enhance the production of nanofiber based nonwovens through the melt blown technology.

BIBLIOGRAPHY

[1] HASSAN, M. A., B. Y. YEOM, A. WILKIE, B. POURDEYHIMI, S. A. KHAN. Fabrication of nanofiber meltblown membranes and their filtration properties. *Journal of Membrane Science*, 2013, vol. 427, p. 336-344.

[2] CHAPMAN, R. *Applications of nonwovens in technical textiles*. 1st pub. Boca Raton, Fla: CRC Press, 2010, 212 p. ISN 978-1-4398-3057-4.

[3] UGBOLUE, S. *Polyolefin fibres: industrial and medical applications*. 1st pub. Cambridge: Woodhead, 2009, 407 p. ISBN 978-1-84569-207-0.

[4] TAN, D. H., C. ZHOU, C. J. ELLISON, S. KUMAR, C. W. MACOSKO, F. S. BATES. Meltblown fibers: Influence of viscosity and elasticity on diameter distribution. *Journal of Non-Newtonian Fluid Mechanics*, 2010, vol. 165, no. 15-16, p. 892-900.

[5] MORRISON, F. A. *Understanding rheology*. New York: Oxford University Press, 2001, 545 p. ISBN 0195141660.

[6] COLLYE, A. A. and D. W. CLEGG. *Rheological measurement*. 2nd ed. London: Chapman & Hall, 1998, 779 p. ISBN 0-412-72030-2.

[7] MUSIL, J. *Development of improved entrance pressure drop technique for extensional viscosity determination*. Zlín: Tomas Bata University in Zlín. Faculty of Technology. Department of Production Engineering, 2008. 156 p., 42 p. appendices. Supervisor Prof. Ing. Martin Zatloukal, PhD.

[8] COGSWELL, F. N. *Polymer melt rheology: a guide for industrial practice*. London: Godwin in association with the Plastics and Rubber Institute, 1981, 178 p. ISBN 0470271027.

[9] MACOSKO, CH. W. *Rheology: principles, measurements, and applications*. New York: Wiley, 1994, 550 p. ISBN 0-471-18575-2.

[10] MALKIN, A. J. and A. I. ISAYEV. *Rheology: concepts, methods, and applications*. Toronto: ChemTec Publishing, 2006, 474 p. ISBN 1-895198-33-x.

[11] BRYDSON, J. *Flow properties of polymer melts*. 2nd ed. London: George Godwin Limited in association with the Plastics and Rubber Institute, 1981, 226 p. ISBN 0-7114-5681-x.

[12] VAN WAZER, J. R. *Viscosity and flow measurement: a laboratory handbook of rheology*. New York: Interscience Publishers, 1963, 460 p.

[13] CHHABRA, R. and J. RICHARDS. Non-Newtonian flow and applied rheology: engineering applications. 2nd ed. Amsterdam: Butterworth-Heinemann, 2008, 518 p. ISBN 978-0-7506-8532-0.

[14] BIRD, R., R. C. ARMSTRONG and O. HASSAGER. *Dynamics of polymeric liquids*. New York: John Wiley & Sons, 1977, 470, [89] p. ISBN 0-471-07375-x.

[15] DEALY, J. M. and R. G. LARSON. *Structure and rheology of molten polymers: from structure to flow behavior and back again*. Munich: Hanser Publishers, 2006, 516 p. ISBN 1-56990-381-0.

[16] AUHL, D., D. M. HOYLE, D. HASSELL, T. D. LORD, O. G. HARLEN, M. R. MACKLEY, T. C. B. MCLEISH. Cross-slot extensional rheometry and the steady-state extensional response of long chain branched polymer melts. *Journal of Rheology*, 2011, vol. 55, no. 4, p. 875-900.

[17] COVENTRY, K. D., M. R. MACKLEY. Cross-slot extensional flow birefringence observations of polymer melts using a multi-pass rheometer. Journal of Rheology, 2008, vol. 52, no. 2, p. 401-415.

[18] WENTE, V. A. Superfine thermoplastic *fibers. Industrial and engineering chemistry*, 1956, vol. 48, no. 8, p. 1342-1346.

[19] NAYAK, R., I. L. KYRATZIS, Y. B. TRUONG, R. PADHYE, L. ARNOLD, G. PEETERS, M. O´SHEA, L. NICHOLS. Fabrication and characterization of polypropylene nanofibres by meltblowing process using different fluids. *Journal of Materials Science*, 2013, vol. 48, no. 1, p. 273-281.

[20] *Melt blown line – patent.*

URL: < http://www.google.cz/patents/US3849241> [cit. 2013- 4- 4]

[21] SINHA-RAY, S., A. L. YARIN and B. POURDEYHIMI. Prediction of angular and mass distribution in meltblown polymer lay-down. *Polymer*, 2013, vol. 54, no. 2, p. 860-872.

[22] ZHOU, C., D. H. TAN, A. P. JANAKIRAMAN, S. KUMAR. Modeling the melt blowing of viscoelastic materials. *Chemical Engineering Science*, 2011, vol. 66, no. 18, p. 4172-4183.

[23] NIMMO, J. R., Encyclopedia of soils in the environment. London: Elsevier, 2004, v. 3, p. 295-303.

[24] ELLISON, CH. J., A. PHATAK, D. W. GILES, C. W. MACOSKO, F. S. BATES. Melt blown nanofibers: Fiber diameter distributions and onset of fiber breakup. *Polymer*, 2007, vol. 48, no. 11, p. 3306-3316.

[25] LIU, Y., B. CHENG, G. CHENG. Development and filtration performance of polylactic acid meltblowns. *Textile Research Journal*, 2010, vol. 80, no. 9, p. 771-779.

[26] TAN, D. H., P. K. HERMAN, A. JANAKIRAMAN, F. S. BATES, S. KUMAR, C. W. MACOSKO. Influence of Laval nozzles on the air flow filed in melt blowing apparatus. *Chemical Engineering Science*, 2012, vol. 80, 342-348.

[27] BEGENIR, A., S. MICHIELSEN, B. POURDEYHIMI. Melt-Blowing Thermoplastic Polyurethane and Polyether-Block-Amine Elastomers: Effect of Processing Conditions and Crystallization on Web Properties. *Polymer Engineering and Science*, 2009, vol. 49, no. 7, p. 1340-1349

[28] MARLA, V. T. and R. L. SHAMBAUGH. Three-Dimensional Model of the Melt-Blowing Process. *Industrial and Engineering Chemistry Research*, 2003, vol. 42, no. 26, p. 6993-7005.

[29] SUN, Y. F., B. W. LIU, X. H. WANG, Y. C. ZENG. Air-Flow Field of the Melt-Blowing Slot Die via Numerical Simulation and Multiobjective Genetic Algorithms. *Journal of Applied Polymer Science*, 2011, vol. 122, no. 6, p. 3520-3527.

[30] MENG, K., X. WANG, Q. CHEN. Fluid flow in coat-hanger die of melt blowing process: comparison of numerical simulations and experimental measurements. *Textile Research Journal*, 2011, vol. 81, no. 6, p. 1686-1693.

[31] MENG, K. and X. WANG. Numerical simulation and analysis of fluid flow in double melt-blown die. *Textile Research Journal*, 2013, vol. 83, no. 3, p. 249-255

[32] TATE, B. D. and R. L. SHAMBAUGH. Modified Dual Rectangular Jets for Fiber Production. *Industrial and Engineering Chemistry Research.*, 1998, vol. 37, no. 9, p. 3772-3779.

[33] BO, Z. Production of polypropylene melt blown nonwoven fabrics: Numerical simulation and prediction of fibre diameter. *Indian Journal of Fibre & Textile Research*, 2012, vol. 37, no. 3, p. 280-286.

[34] BO, Z. Production of polypropylene melt blown nonwoven fabrics: Effect of process parameters. *Indian Journal of Fibre & Textile Research*, 2012, vol. 37, no. 4, p. 326-330.

[35] ZATLOUKAL, M. Differential viscoelastic constitutive equations for polymer melts in steady shear and elongational flows. *Journal of Non-Newtonian Fluid Mechanics*, 2003, vol. 113, no. 2-3, p. 209-227.

[36] DRABEK, J. *Applied rheology for melt blown technology*. Zlín: Tomas Bata University in Zlín. Faculty of Technology. Department of Production Engineering, 2011. 102 p. Supervisor Prof. Ing. Martin Zatloukal, PhD.

[37] DEALY, J. M. and K. F. WISSBRUN. *Melt rheology and its role in plastics processing: theory and applications*. Dordrecht: Kluwer Academic Publishers, 1999, 665 p. ISBN 0-4127-3910-0.

[38] HUGO ROLÓN-GARRIDO, V. H., M. ZATLOUKAL, M. H. WAGNER. Increase of long-chain branching by thermo-oxidative treatment of LDPE: Chromatographic, spectroscopic, and rheological evidence. *Journal of Rheology*, 2013, vol. 57, no. 1, p. 105-129.

[39] VERBEETEN, W. M. H., G. W. M. PETERS, F. P. T. BAAIJENS. Differential constitutive equations for polymer melts: The extended Pom-Pom model. *Journal of Rheology*, 2001, vol. 45, no. 4, p. 823-843.

[40] QUINYANI, L. M., R. C. ARMSTRONG, R. A. BROWN. Use of couple birefringence and LDV studies of flow through a contraction to test constitutive equations for concentrated polymer solutions. *Journal of Rheology,* 1995, vol. 39, 1201-1228.

[41] OLIVEIRA, P. J. Alternative derivation of differential constitutive equations of the Oldroyd-B type. *Journal of Non-Newtonian Fluid Mechanics*, 2009, vol. 160, no. 1, p. 40-46.

[42] DE PAULO, G. S., M. F. TOMÉ, S. MCKEE. A marker-and-cell approach to viscoelastic free surface flows using the PTT model. *Journal of Non-Newtonian Fluid Mechanics*, 2007, vol. 147, no. 3, p. 149-174.

[43] ZATLOUKAL, M., J. VLČEK, C. TZOGANAKIS, P. SÁHA. Improvement in techniques for the determination of extensional rheological data from entrance

flows: Computation and experimental analysis. *Journal of Non-Newtonian Fluid Mechanics,* 2002, vol. 107, no. 1-3, p. 13-37.

[44] ZATLOUKAL, M. Measurement and modeling of planar and uniaxial extensional viscosities for LDPE polymer melt. *Annual Technical Conference – ANTEC, Conference Proceedings*, 2012, vol. 1, p. 66-70.

[45] LIMPERT, E., W. A. STAHEL, M. ABBT. Log-normal distributions across the sciences: keys and clues. *BioScience*, 2001, vol. 51, no. 5, p. 341-352.

LIST OF ABBREVIATIONS

H	Distance between desks	m
v_1	Velocity in 1-direction	$m.s^{-1}$
v_2	Velocity in 2-direction	$m.s^{-1}$
v_3	Velocity in 3-direction	$m.s^{-1}$
$\dot{\gamma}_0$	Shear rate	s^{-1}
$\underline{v}$	Vector of velocity	$m.s^{-1}$
$\underline{\underline{\dot{\gamma}}}$	Shear rate tensor	s^{-1}
$\dot{\varsigma}(t)$	Function of $\partial v_1 / \partial x_2$	s^{-1}
η	Shear viscosity	Pa.s
τ_{21}	Shear stress	Pa
τ_{11}	Normal stress in 1-direction	Pa
τ_{22}	Normal stress in 2-direction	Pa
τ_{33}	Normal stress in 3-direction	Pa
Ψ_1	First normal-stress coefficient	$Pa.s^2$
Ψ_2	Second normal-stress coefficient	$Pa.s^2$
N_1	First normal stress difference	Pa
N_2	Second normal stress difference	Pa
ω	Frequency of the cosine function	Hz
$\dot{\gamma}_0$	Constant amplitude of the shear rate function	s^{-1}
G	Elastic modulus	Pa
G'	Storage modulus	Pa
G''	Loss modulus	Pa
G^*	Complex modulus	Pa

τ_0	Shear stress	Pa
γ_0	Shear strain	1
tan δ	Loss tangent	1
η'	Real part of complex dynamic viscosity	Pa.s
η''	Imaginary part of complex dynamic viscosity	Pa.s
η^*	Complex dynamic viscosity	Pa.s
J^*	Complex compliance	Pa^{-1}
J'	Storage compliance	Pa^{-1}
J''	Loss compliance	Pa^{-1}
$\dot{\varepsilon}$	Extensional rate	s^{-1}
$\dot{\varepsilon}_0$	Extensional rate	s^{-1}
b	Adjustable parameter from Eq. 11, 13, 16	1
F_x	Force in x-direction	N
F_y	Force in y-direction	N
F_z	Force in z-direction	N
$\dot{\varepsilon}_{xx}$	Extensional rate in x-direction	s^{-1}
$\dot{\varepsilon}_{yy}$	Extensional rate in y-direction	s^{-1}
$\dot{\varepsilon}_{zz}$	Extensional rate in z-direction	s^{-1}
η_0	Newtonian viscosity	Pa.s
$\eta_{E,U}$	Uniaxial elongation viscosity	Pa.s
$\eta_{E,B}$	Biaxial elongation viscosity	Pa.s
$\eta_{E,P}$	Planar elongation viscosity	Pa.s
P	Pressure	Pa

L_C	Length of the capillary	m
D_C	Diameter of capillary die	m
D_1	Diameter of barrel	m
ϕ	Capillary die entrance angle	°
ΔP	Total pressure drop	Pa
$\dot{\gamma}_{APP}$	Apparent shear rate	s^{-1}
Q	Volume flow rate	$m^3.s^{-1}$
π	Ludolf´s number	1
R_C	Capillary die radius	m
τ_{xy}	Shear stress	Pa
P_{LC}	Stands for pressure drop measured on long capillary	Pa
P_{OC}	Stands for pressure drop measured on orifice capillary	Pa
L_{LC}	Length of the long capillary	m
B_L	Ratio of extrudate to die diameter from long die	1
γ_R	Recoverable shear strain	1
σ_E	Extensional stress	Pa
n	Represent index of non-Newtonian behavior	1
η_E	Uniaxial extensional viscosity	Pa.s
ε_R	Recoverable elongation strain	1
B_0	Ratio of extrudate to die diameter from orifice die	1
E	Extension modulus	Pa
σ_R	Rupture stress	Pa
P_K	Pressure spent on an increase of kinetic energy of the stream	Pa

P_V	Pressure responsible for overcoming resistance of flow through a capillary	Pa
ρ	Density	kg/m^3
α	Coefficient reflecting	1
R	Radius	m
L	Length	m
Δp_{cap}	Capillary pressure drop	Pa
Δp_{end}	End pressure drop	Pa
M	Torgue	N.m
p-p	Plane-plane	-
c-p	Cone plane	-
$\dot{\gamma}_R$	Deformation rate at the channel wall (in a simple shear)	s^{-1}
F_{c-p}	Force cone-plane	N
F_{p-p}	Force plane-plane	N
R_{c-p}	Radius cone-plane	m
R_{p-p}	Radius plane-plane	m
σ^*	Stress amplitude	Pa
γ^*	Strain amplitude	1
δ	Phase lag	rad
ω	Angular velocity	rad.s^{-1}
Ω	Rotation rate	rad. s^{-1}
F_z	Normal force	N
γ_{yield}	Yield strain	1
$\underline{\underline{\tau}}$	Extra stress tensor	Pa

$\underline{\underline{D}}$	Stand for the deformation rate tensor	s^{-1}
m	Function of temperature	1
I_D	First invariant of deformation rate tensor	s^{-1}
II_D	Second invariant of deformation rate tensor	s^{-2}
III_D	Third invariant of deformation rate tensor	s^{-3}
η_0	Newtonian viscosity	Pa.s
η_∞	Limiting shear viscosity at infinite shear rate	Pa.s
λ	Relaxation time	s
a	Adjustable parameter Eq. 39	1
a_t	Arrhenius equation for temperature-depend shift factor	1
m, n	Adjustable parameters Eq. 40	1
$a, n, \alpha, \beta, \psi, \zeta$	Adjustable parameters Eq. 42	1
$\overset{\nabla}{\underline{\underline{\tau}}}$	Upper convected tress tensor derivate	Pa. s^{-1}
t'	Time dummy variable of integration	s
t	Current time	s
$\underline{\underline{\dot{\gamma}}}$	Tensor shear rate	s^{-1}
u	Time-dependent elastic energy potential function	J
C_{ij}	Cauchy tensor	1
B_{ij}	Finger tensor	1
I_1	First scalar invariant of a Cauchy tensor	1
I_2	Second scalar invariant of a Cauchy tensor	1
$S_m(t,t')$	General strain measure	1

f^2	The square of the relative tension	1
$S_{DE}^{IA}(t,t')$	The strain measure	1
W	Elastic potential	Pa
s	Rheological parameter lying between 0 and 1	1
C_k	Elastic strain tensor	1
$I_{k,1}$	The first invariant of C_k	1
$\overset{\nabla}{\tau}$	Upper convected tress derivate	$Pa.s^{-1}$
$\overline{\lambda}(\mathrm{II}_D,T)$	Stands for the deformation rate dependent relaxation time and second invariant	s
$\eta(\mathrm{II}_D,T)$	Second invariant of deformation rate tensor and temperature dependent shear viscosity	Pa.s
$\underline{\underline{\lambda(\tau)}}^{-1}$	Relaxation time tensor	s
t	Time	s

LIST OF FIGURES

LIST OF TABLES

APPENDICES

Appendix P I: SEM pictures

Appendix P II: CD-ROM

APPENDIX P I: SEM PICTURES

96 A)

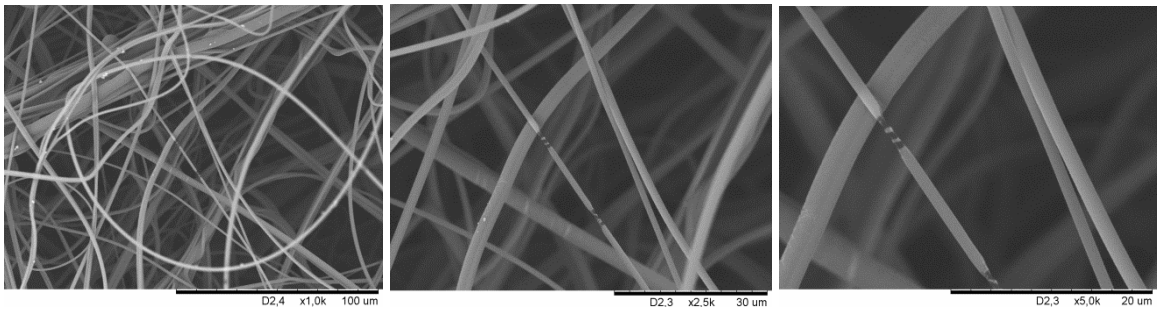

96 B)

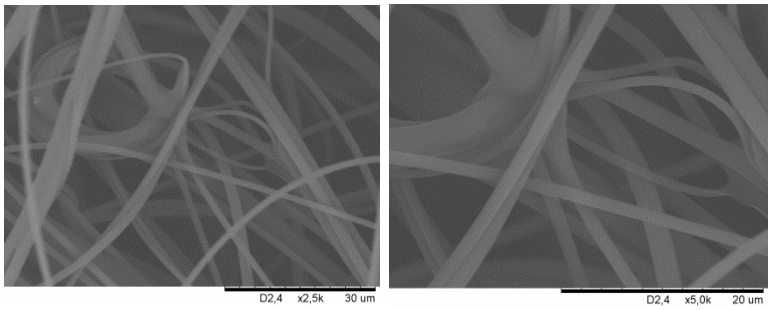

96 C)

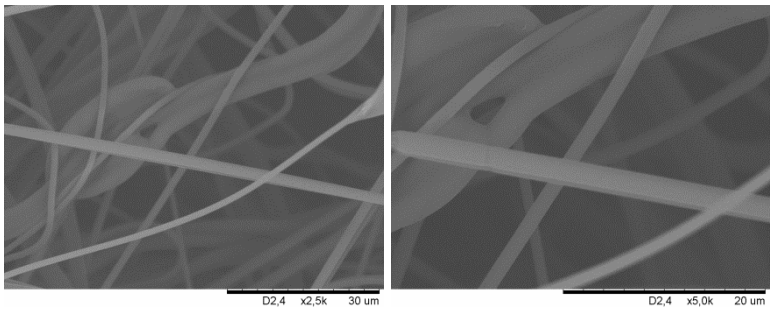

96 D)

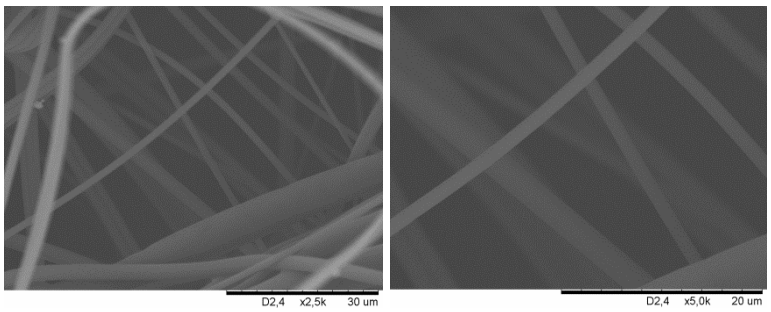

Fig. 96. SEM images for sample 1 at four different areas and different magnifications. 96 A) area 1 (left – 1000x, middle – 2500x, right – 5000x), 96 B) area 2 (left – 2500x, right – 5000x), 96 C) area 3 (left – 2500x, right – 5000x), 96 D) area 4 (left – 2500x, right – 5000x).

97 A)

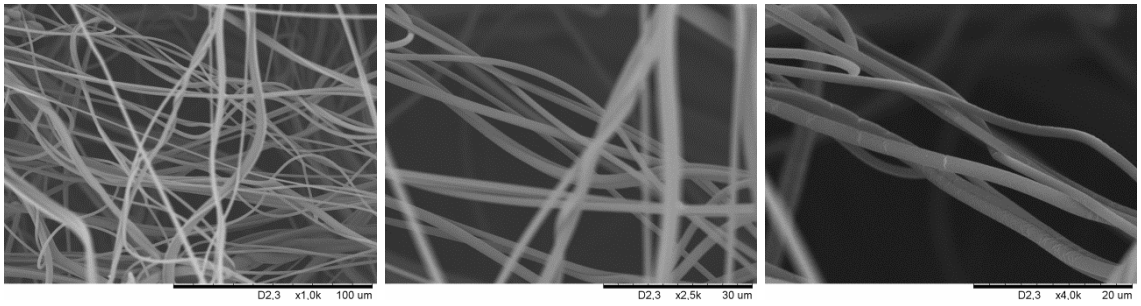

97 B)

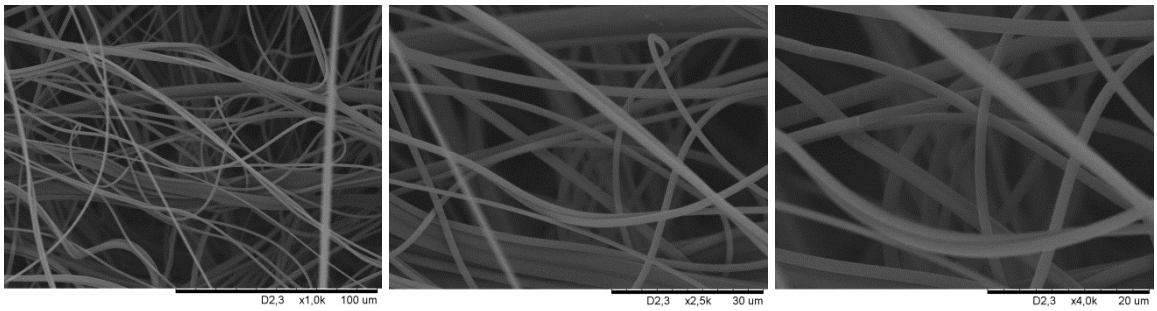

97 C)

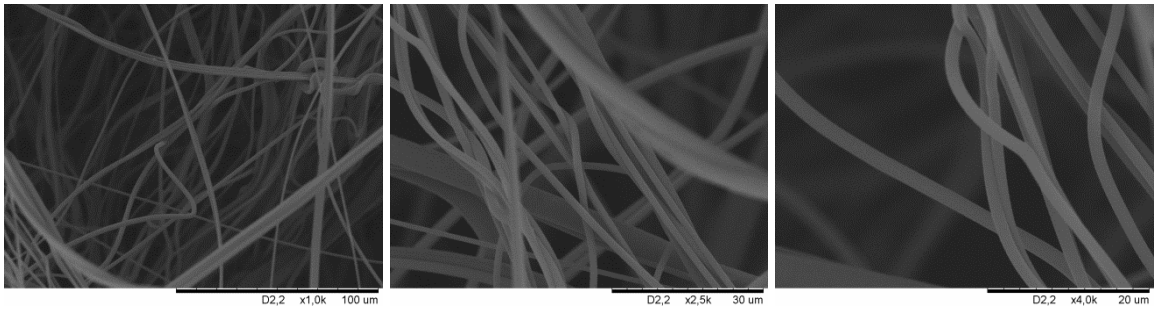

97 D)

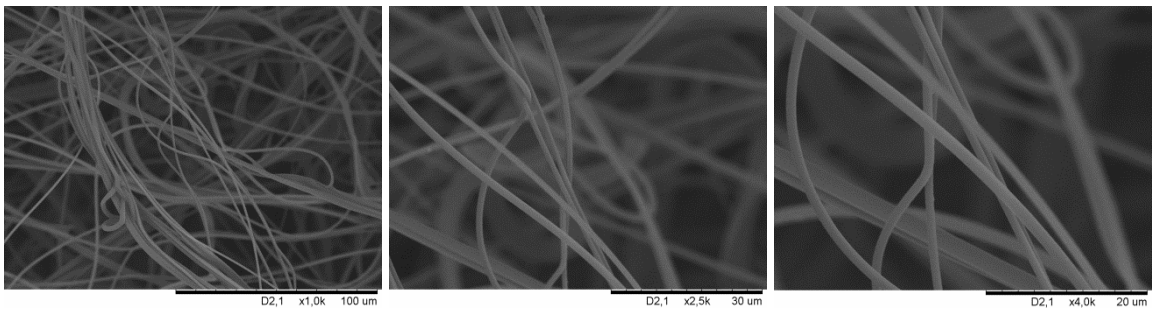

Fig. 97. SEM images for sample 2 at four different areas and three different magnifications (left – 1000x, middle – 2500x, right – 4000x). 97 A) area 1, 97 B) area 2, 97 C) area 3, 97 D) area 4.

98 A)

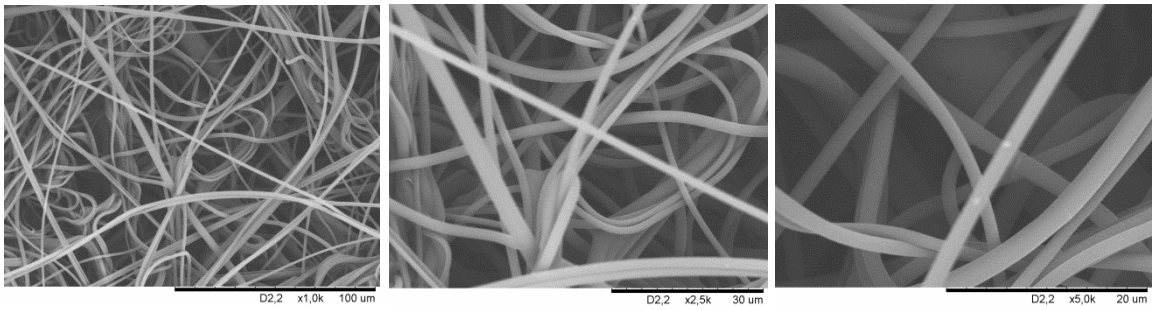

98 B)

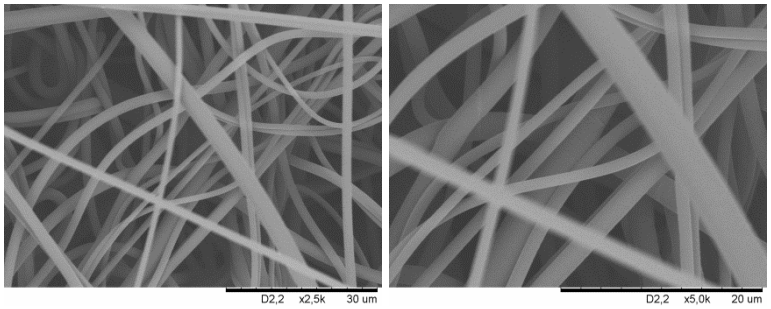

98 C)

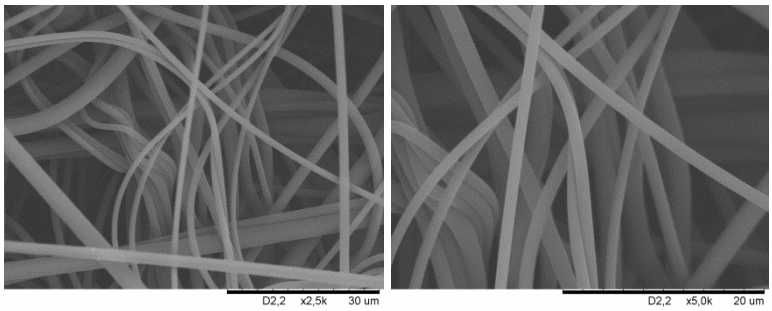

98 D)

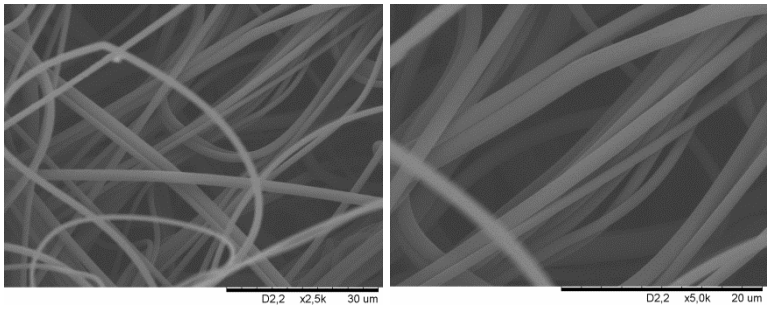

Fig. 98. SEM images for sample 3 at four different areas and different magnifications. 98 A) area 1 (left – 1000x, middle – 2500x, right – 5000x), 98 B) area 2 (left – 2500x, right – 5000x), 98 C) area 3 (left – 2500x, right – 5000x), 98 D) area 4 (left – 2500x, right – 5000x).

99 A)

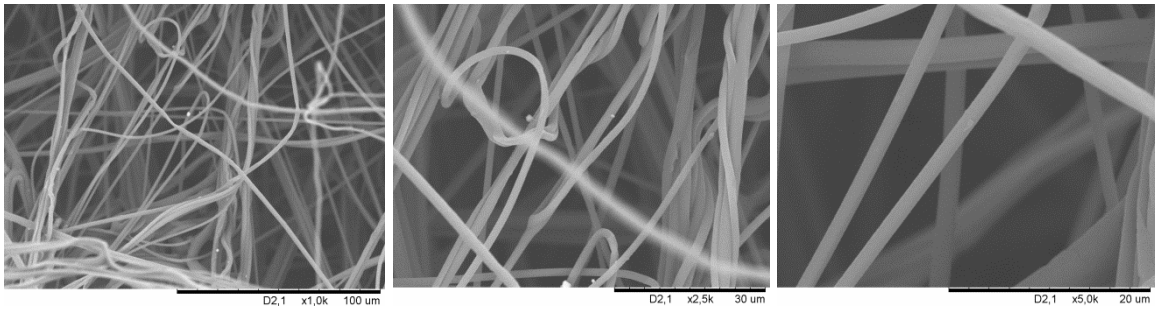

99 B)

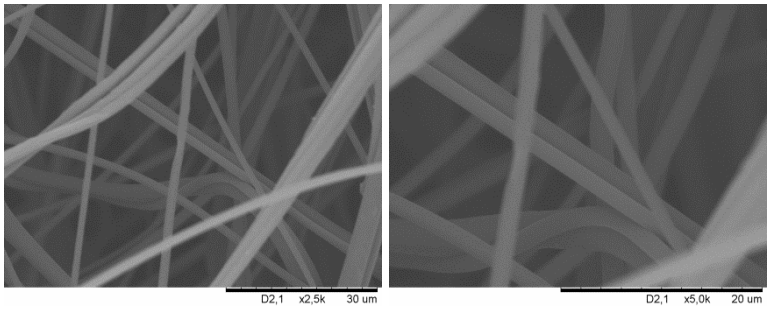

99 C)

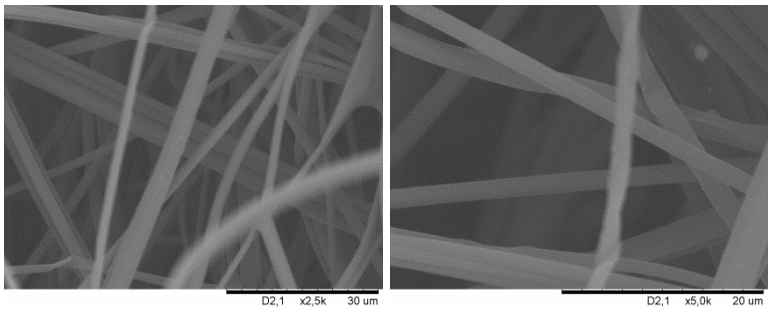

99 D)

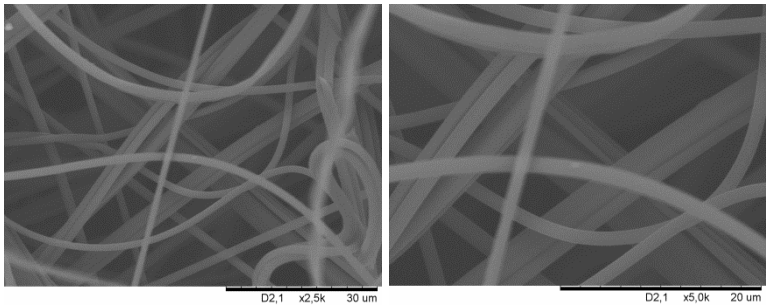

Fig. 99. SEM images for sample 4 at four different areas and different magnifications. 99 A) area 1 (left – 1000x, middle – 2500x, right – 5000x), 99 B) area 2 (left – 2500x, right – 5000x), 99 C) area 3 (left – 2500x, right – 5000x), 99 D) area 4 (left – 2500x, right – 5000x).

100 A)

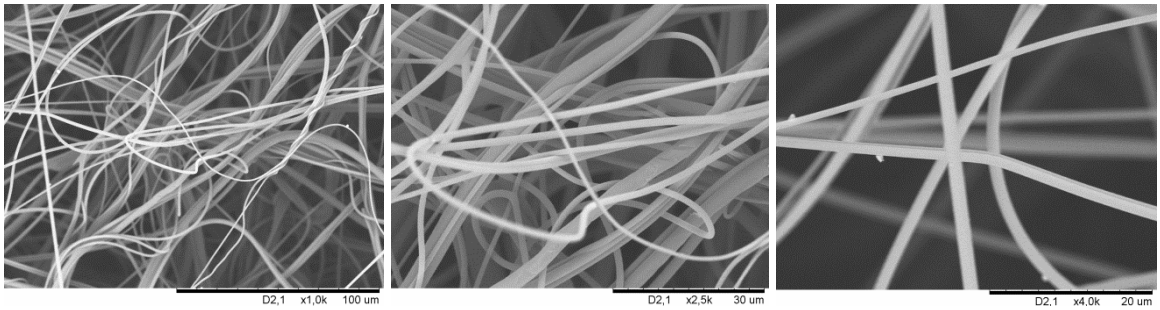

100 B)

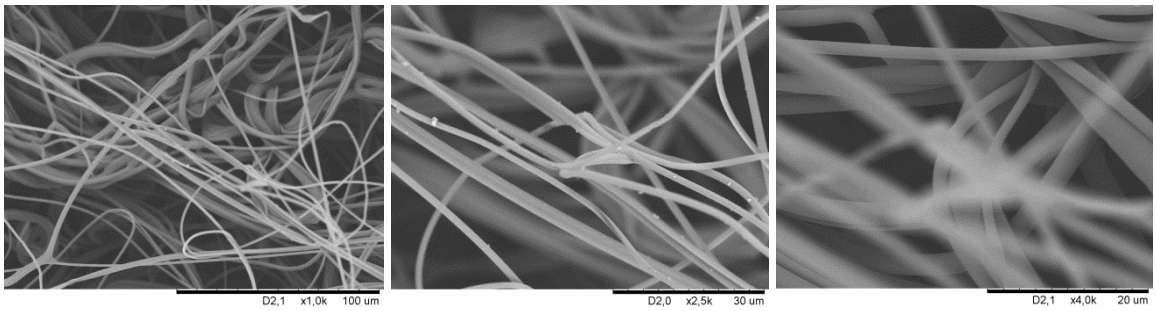

100 C)

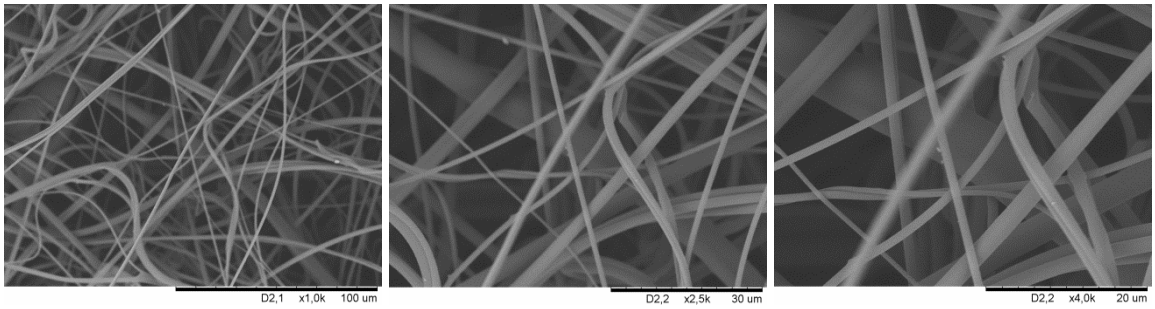

100 D)

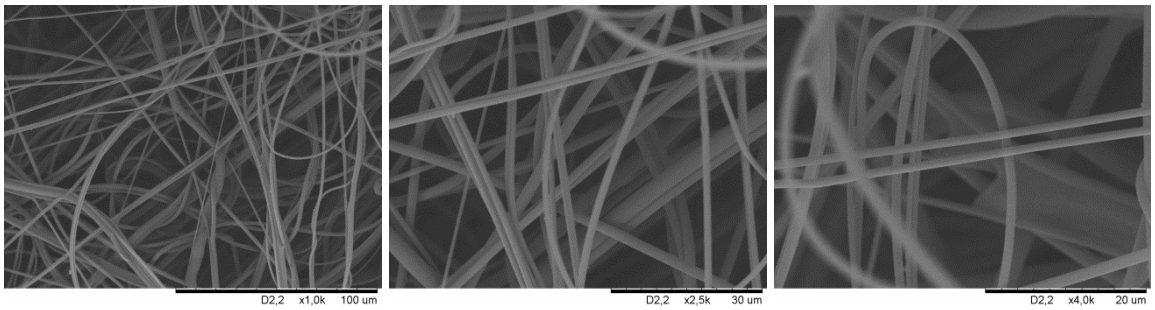

Fig. 100. SEM images for sample 5 at four different areas and three different magnifications (left – 1000x, middle – 2500x, right – 4000x). 100 A) area 1, 100 B) area 2, 100 C) area 3, 100 D) area 4.

101 A)

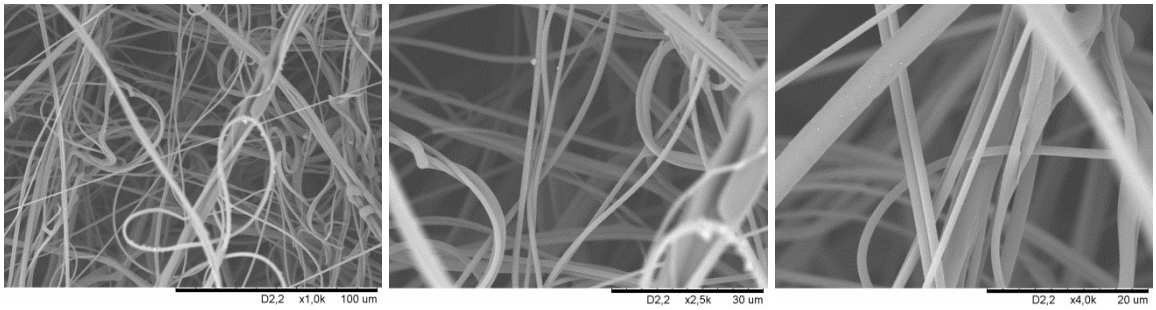

101 B)

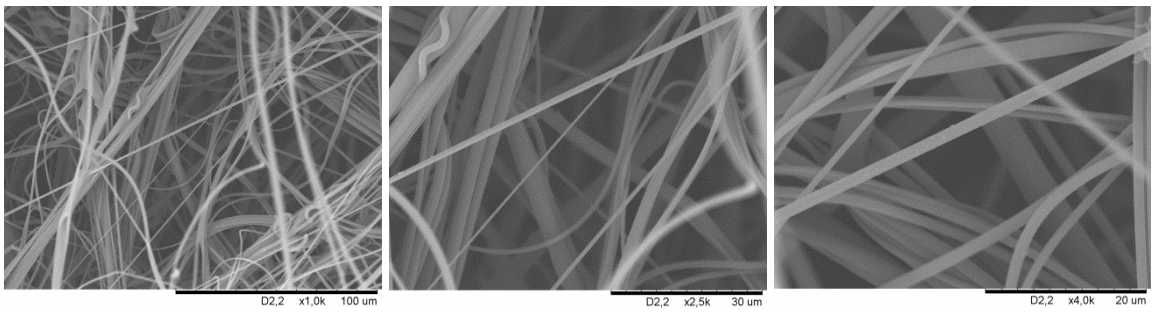

101 C)

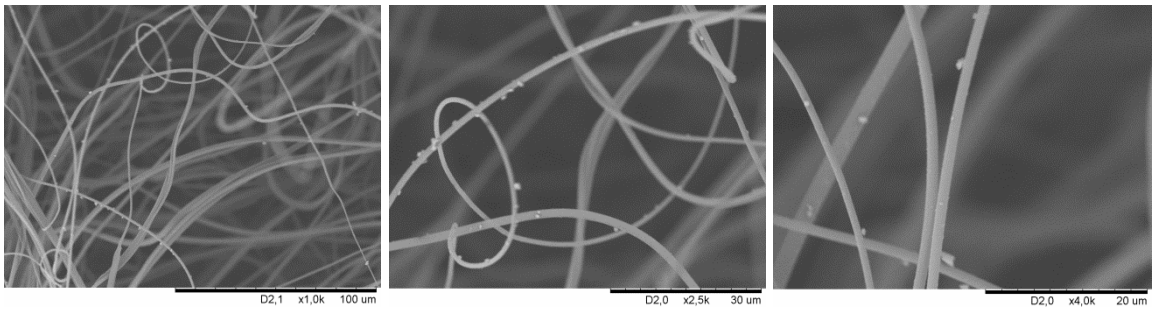

101 D)

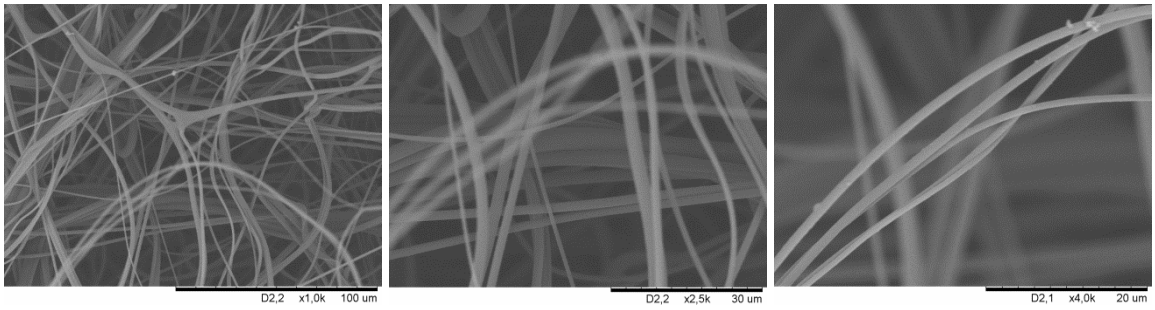

Fig. 101. SEM images for sample 6 at four different areas and three different magnifications (left – 1000x, middle – 2500x, right – 4000x). 101 A) area 1, 101 B) area 2, 101 C) area 3, 101 D) area 4.

102 A)

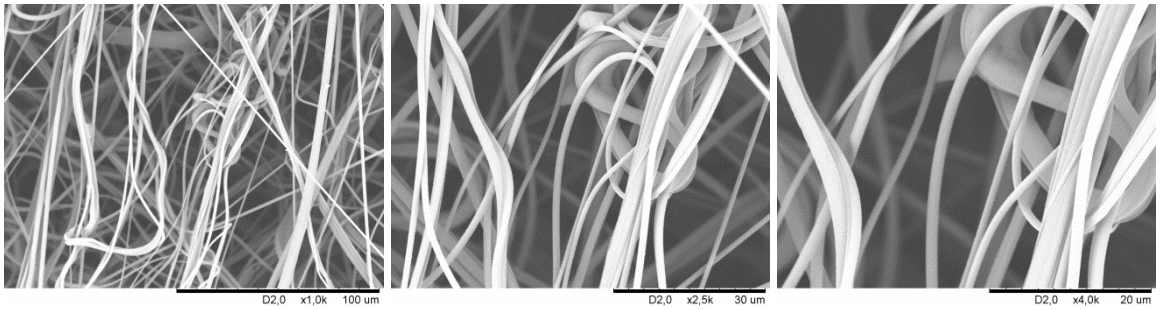

102 B)

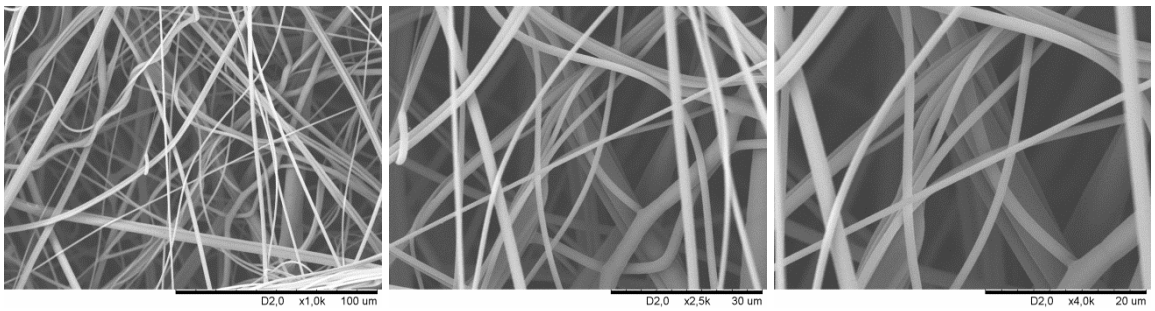

102 C)

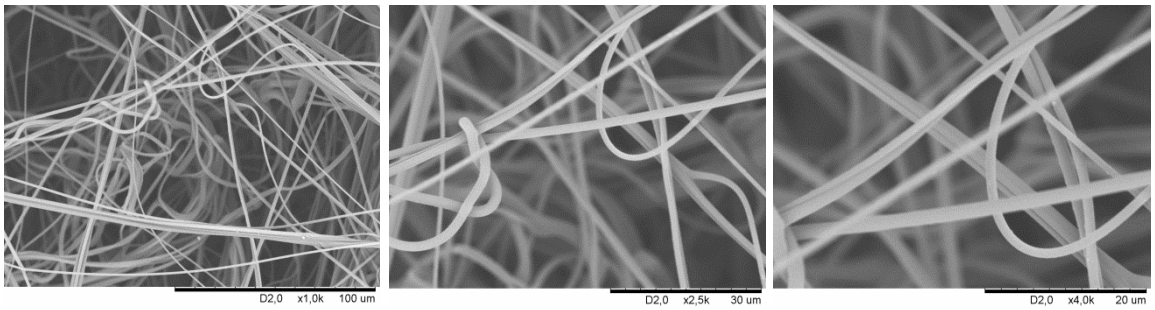

102 D)

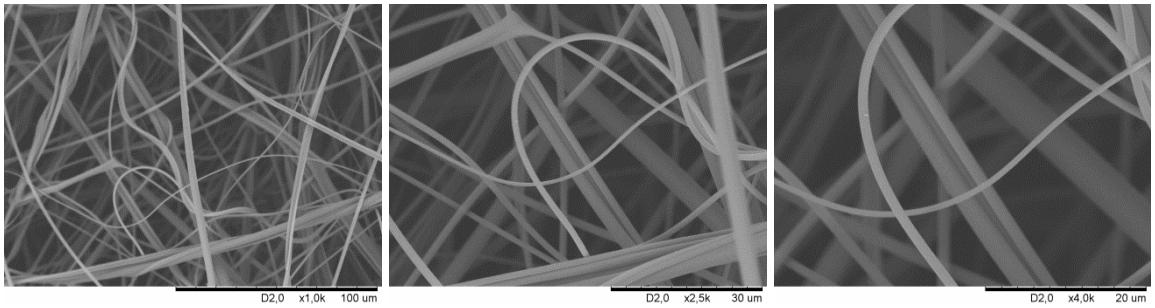

Fig. 102. SEM images for sample 7 at four different areas and three different magnifications (left – 1000x, middle – 2500x, right – 4000x). 102 A) area 1, 102 B) area 2, 102 C) area 3, 102 D) area 4.

103 A)

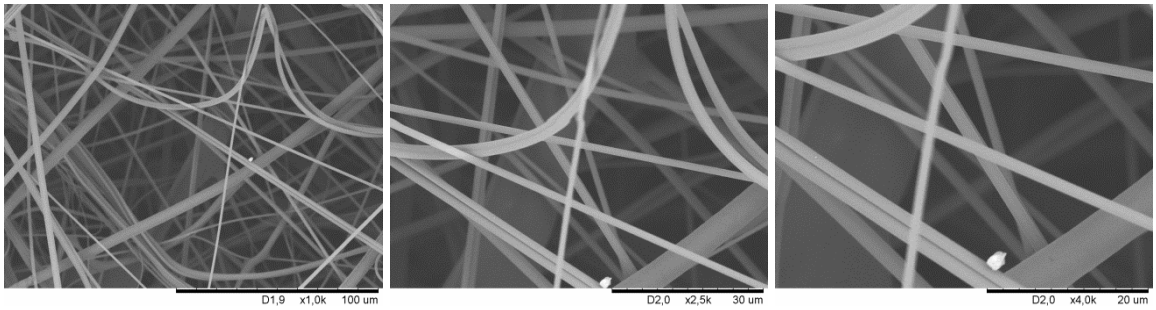

103 B)

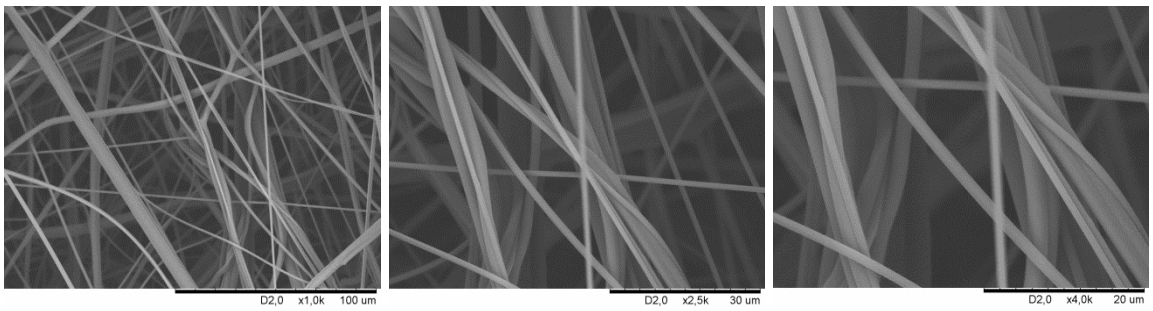

103 C)

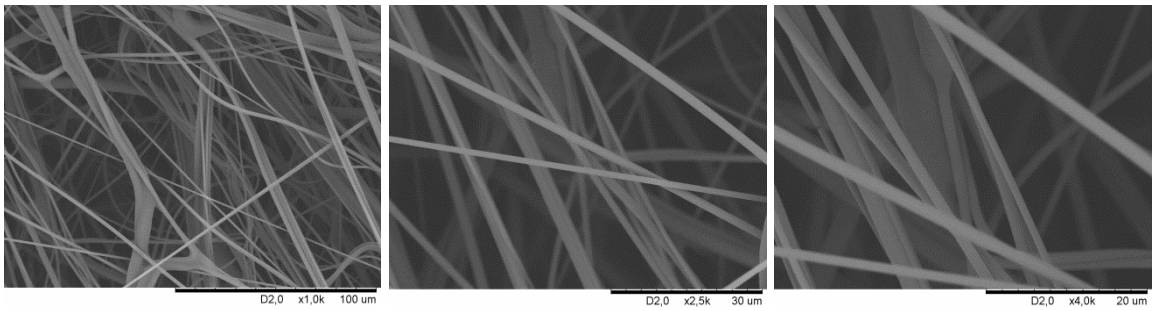

103 D)

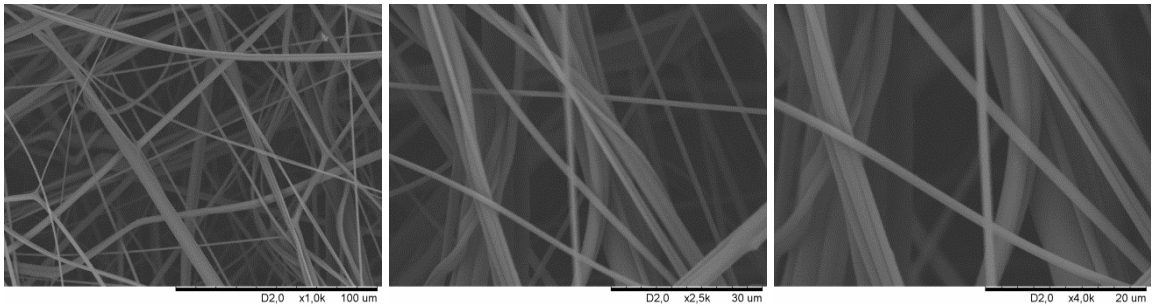

Fig. 103. SEM images for sample 8 at four different areas and three different magnifications (left – 1000x, middle – 2500x, right – 4000x). 103 A) area 1, 103 B) area 2, 103 C) area 3, 103 D) area 4.

104 A)

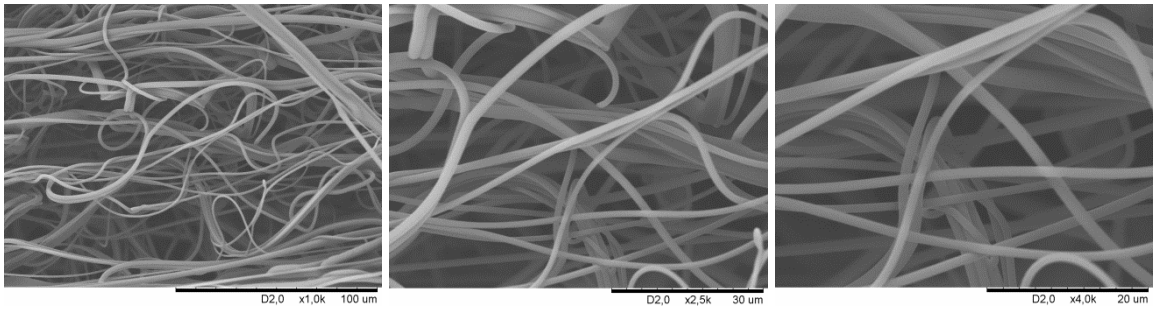

104 B)

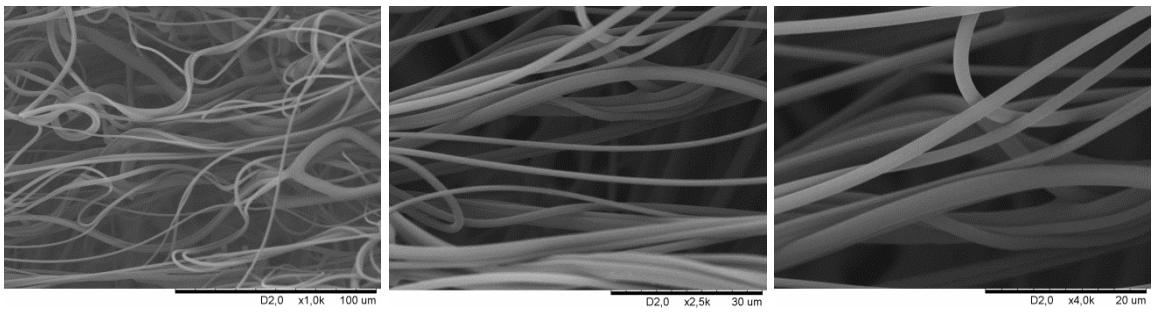

104 C)

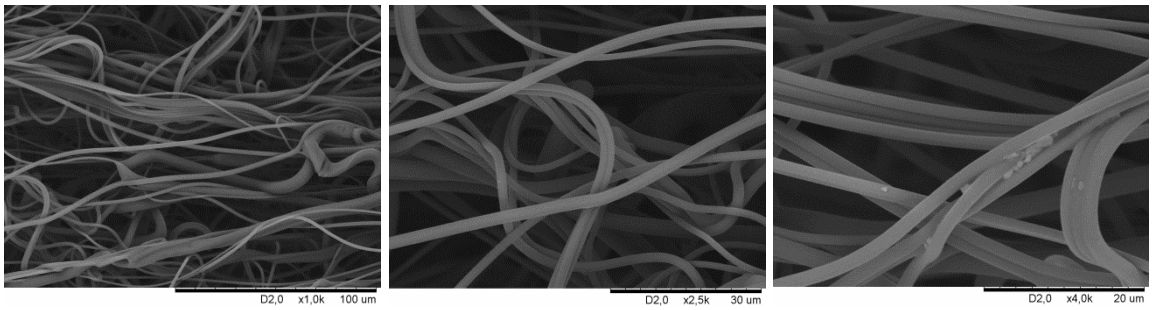

104 D)

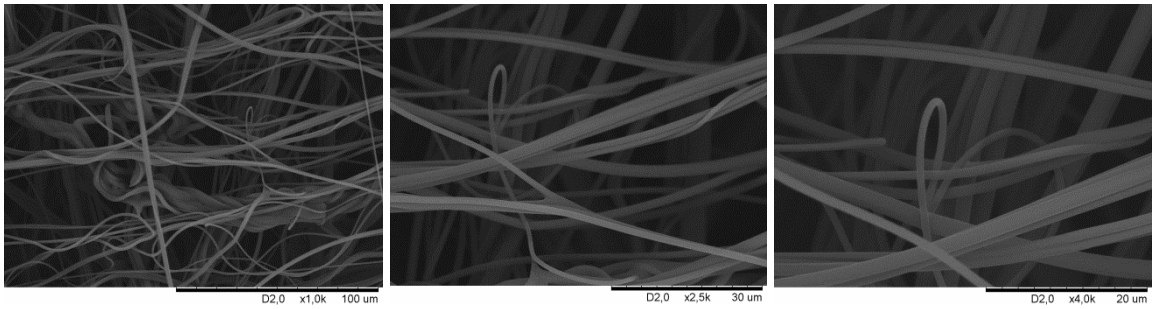

Fig. 104. SEM images for sample 9 at four different areas and three different magnifications (left – 1000x, middle – 2500x, right – 4000x). 104 A) area 1, 104 B) area 2, 104 C) area 3, 104 D) area 4.

105 A)

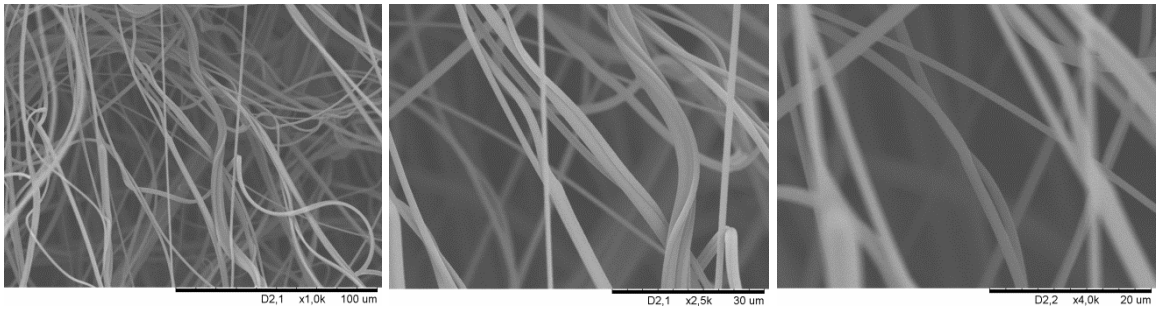

105 B)

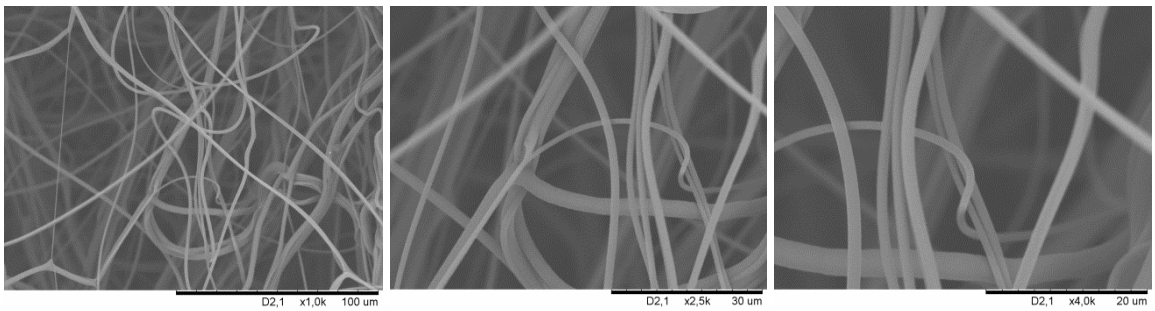

105 C)

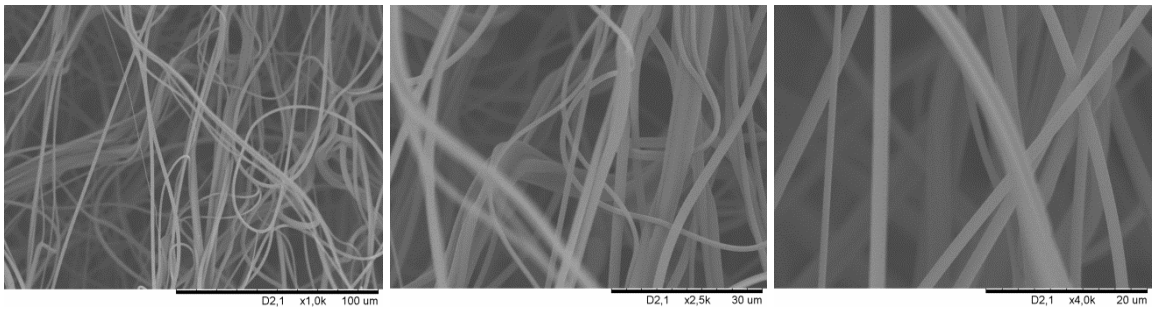

105 D)

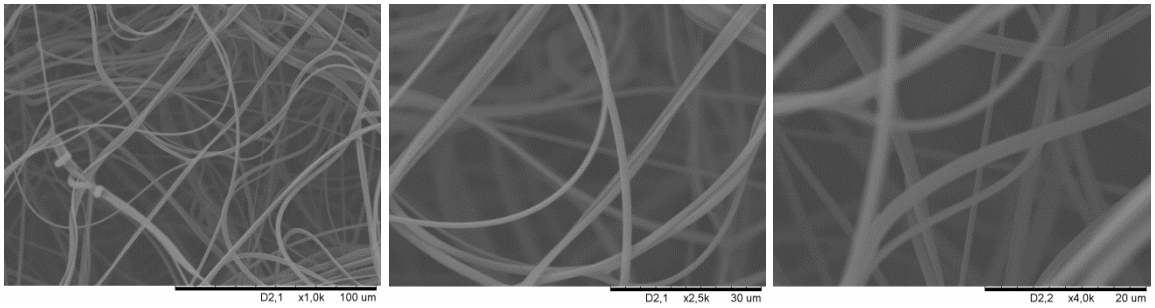

Fig. 105. SEM images for sample 10 at four different areas and three different magnifications (left – 1000x, middle – 2500x, right – 4000x). 105 A) area 1, 105 B) area 2, 105 C) area 3, 105 D) area 4.

106 A)

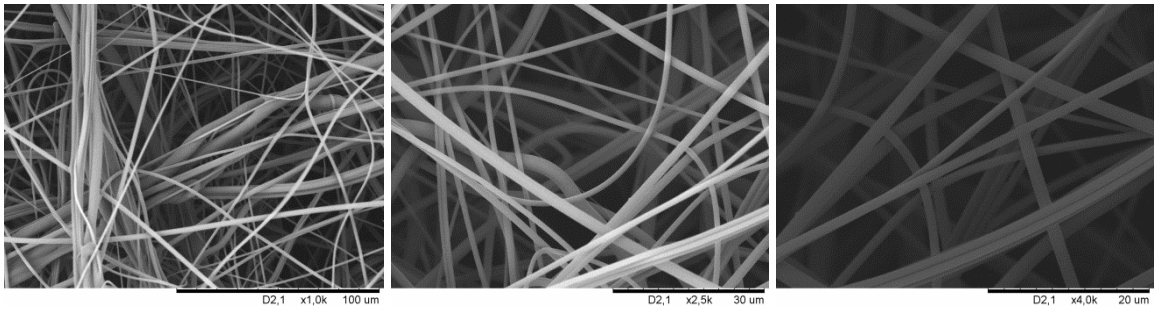

106 B)

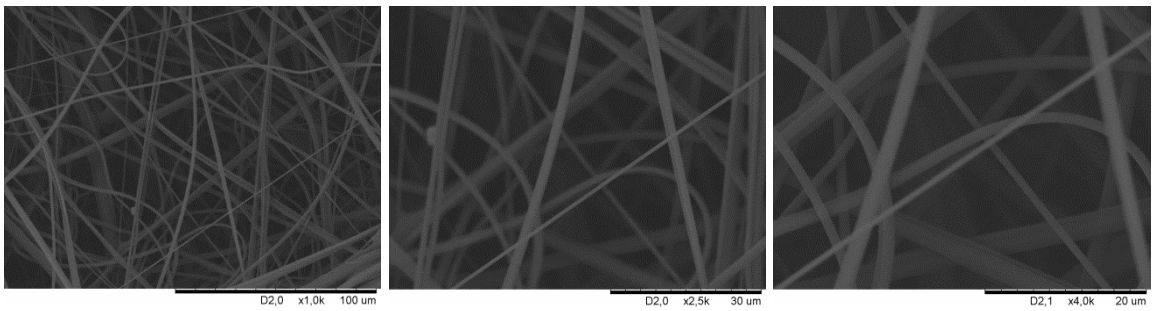

106 C)

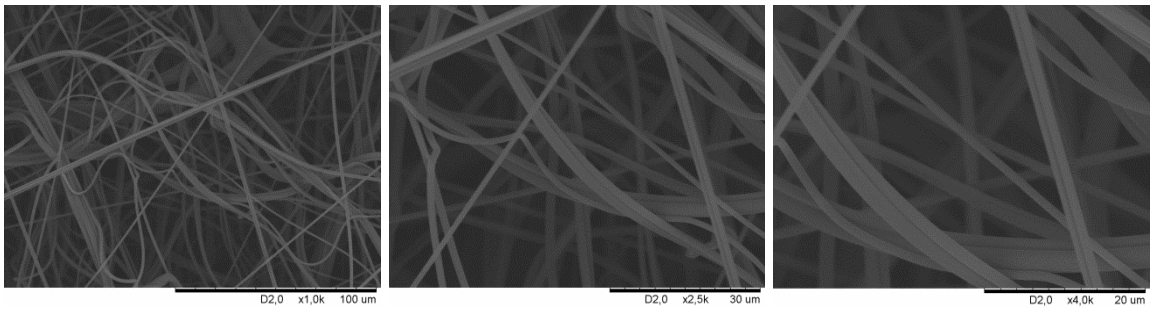

106 D)

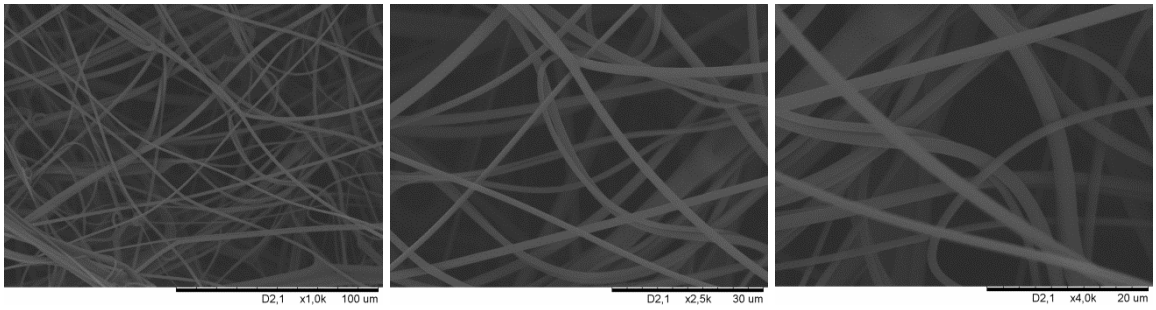

Fig. 106. SEM images for sample 11 at four different areas and three different magnifications (left – 1000x, middle – 2500x, right – 4000x). 106 A) area 1, 106 B) area 2, 106 C) area 3, 106 D) area 4.

107 A)

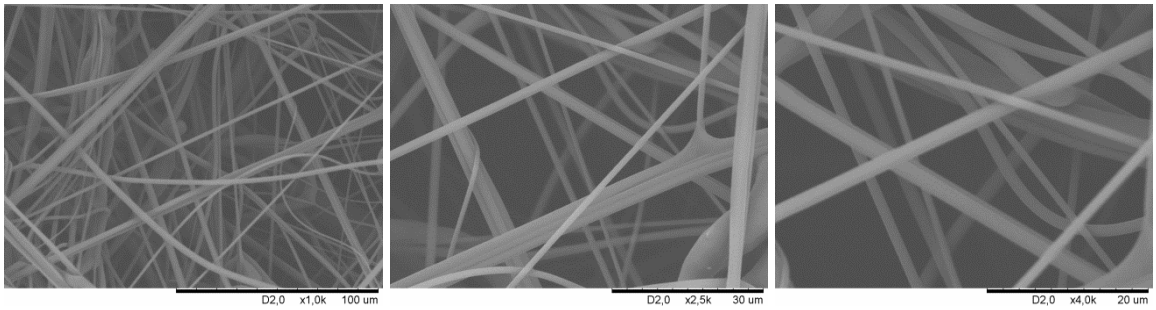

107 B)

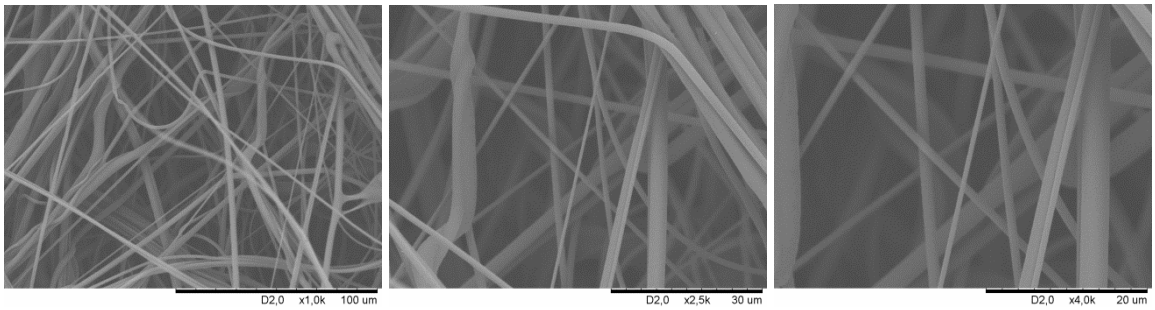

107 C)

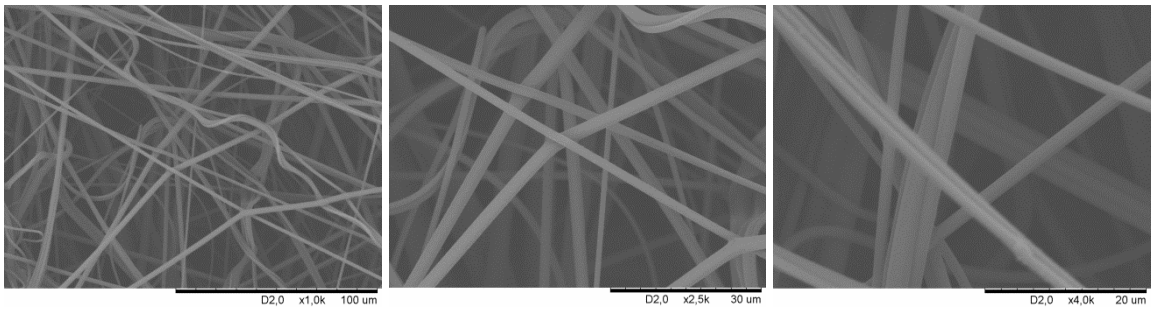

107 D)

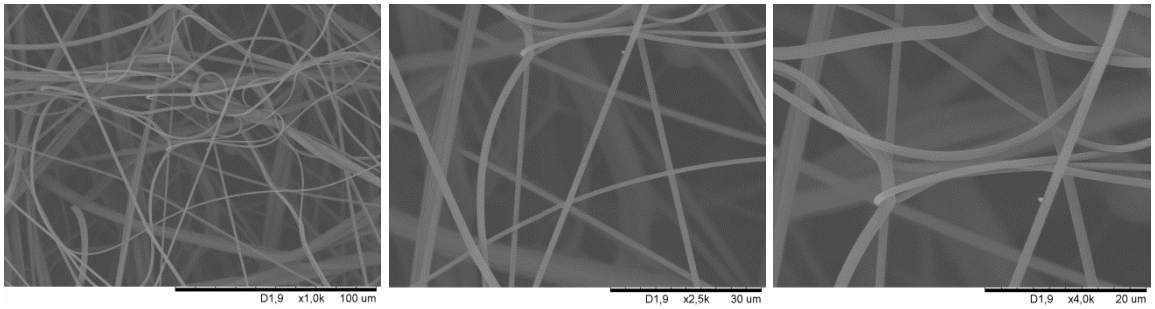

Fig. 107. SEM images for sample 12 at four different areas and three different magnifications (left – 1000x, middle – 2500x, right – 4000x). 107 A) area 1, 107 B) area 2, 107 C) area 3, 107 D) area 4.

108 A)

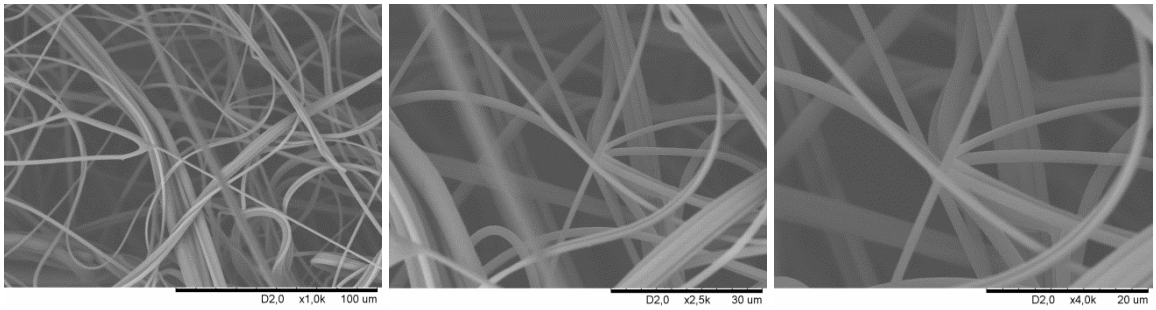

108 B)

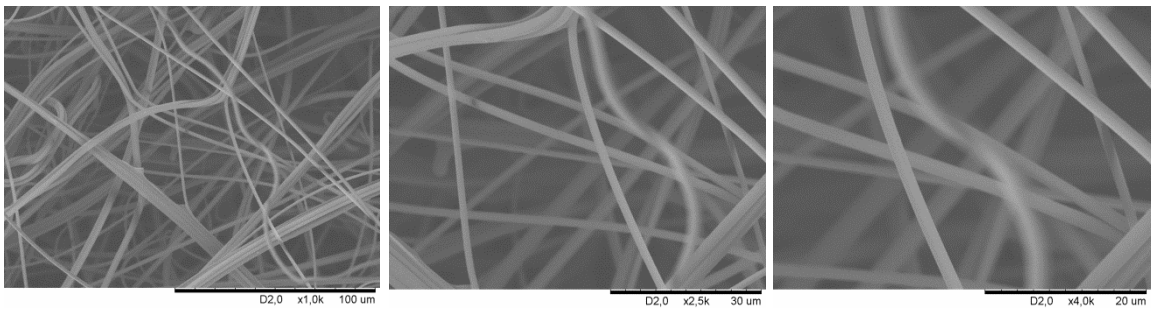

108 C)

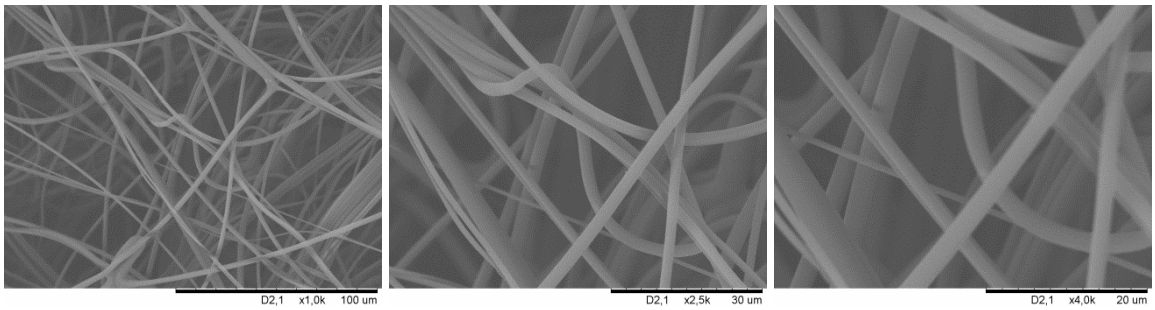

108 D)

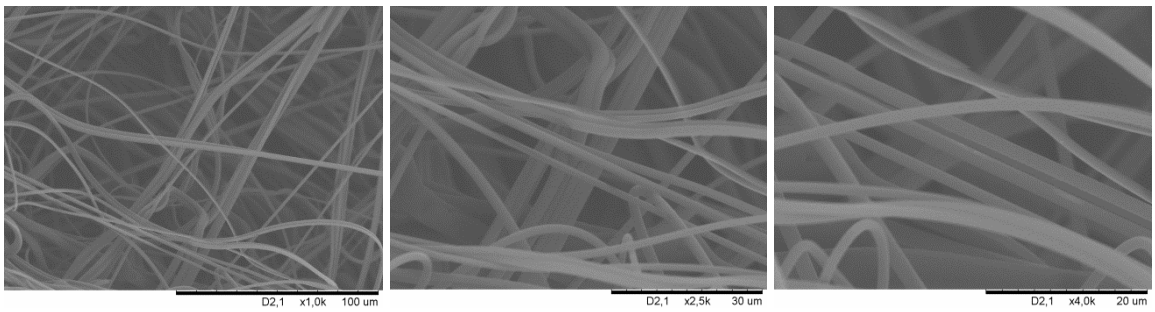

Fig. 108. SEM images for sample 13 at four different areas and three different magnifications (left – 1000x, middle – 2500x, right – 4000x). 108 A) area 1, 108 B) area 2, 108 C) area 3, 108 D) area 4.

109 A)

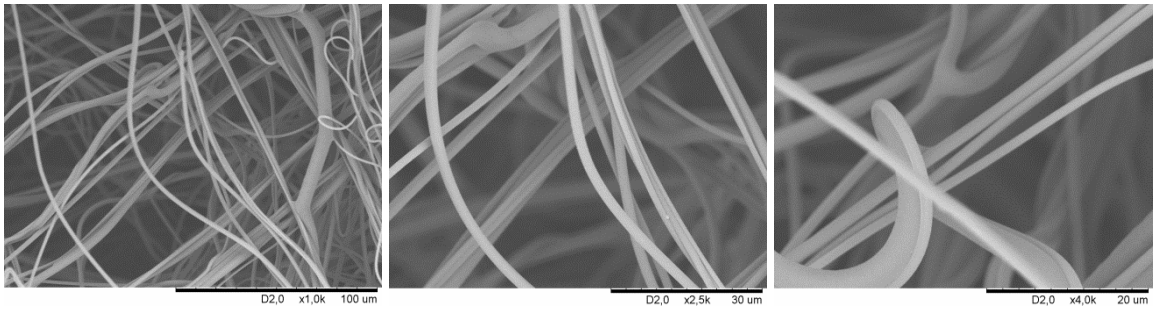

109 B)

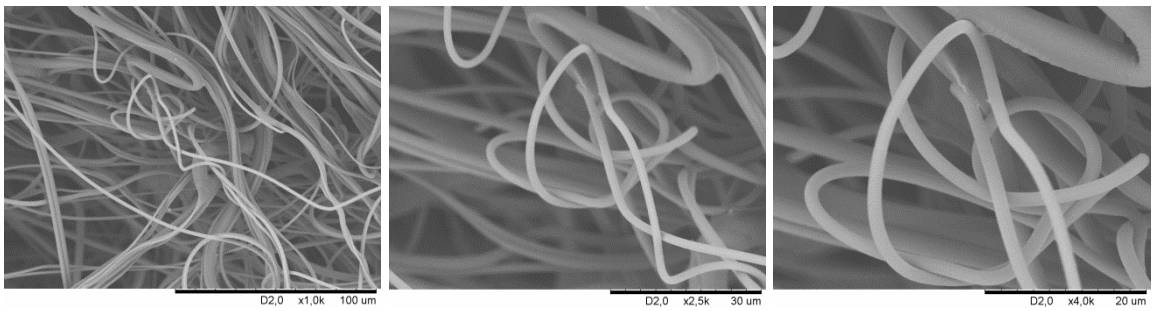

109 C)

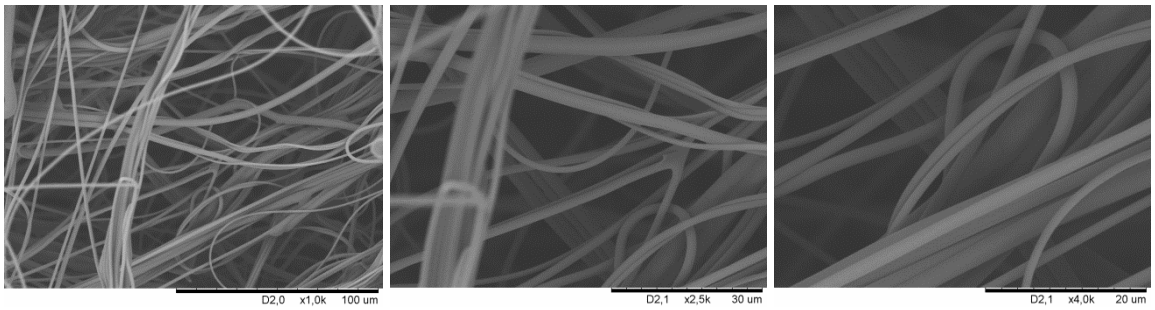

109 D)

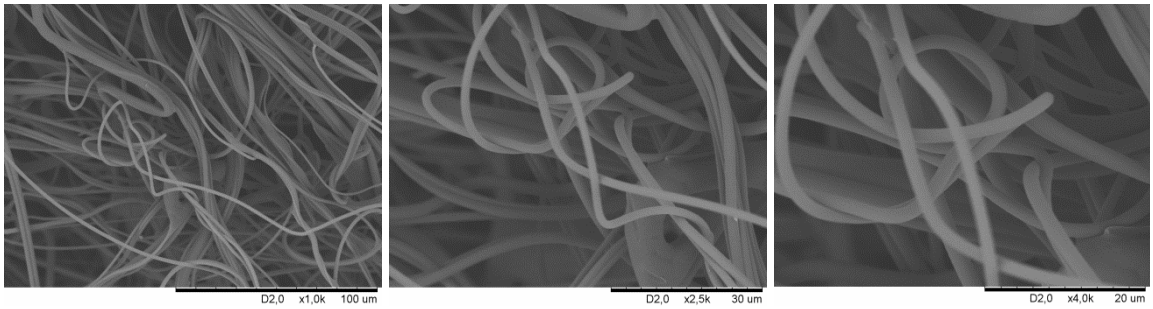

Fig. 109. SEM images for sample 14 at four different areas and three different magnifications (left – 1000x, middle – 2500x, right – 4000x). 109 A) area 1, 109 B) area 2, 109 C) area 3, 109 D) area 4.

110 A)

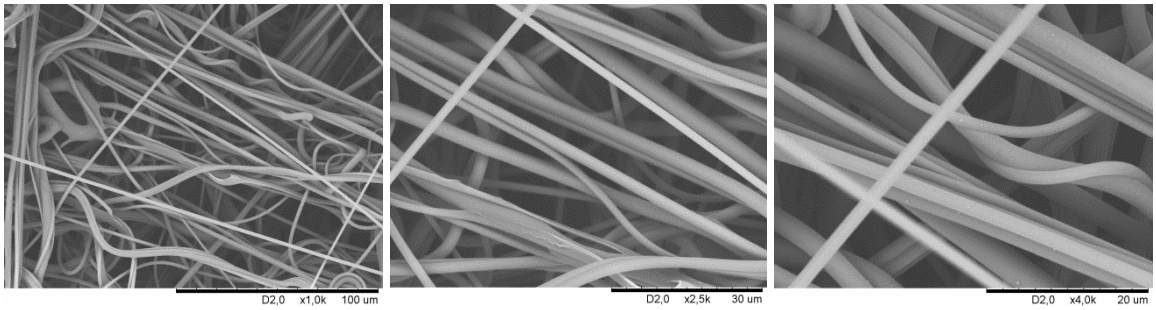

110 B)

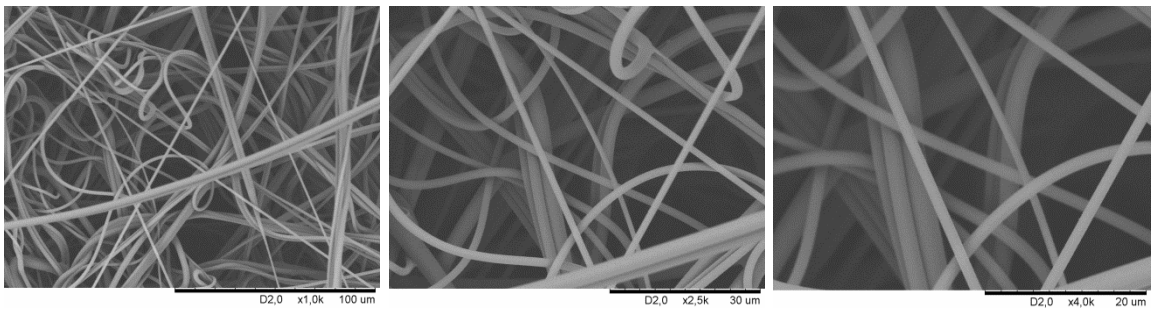

110 C)

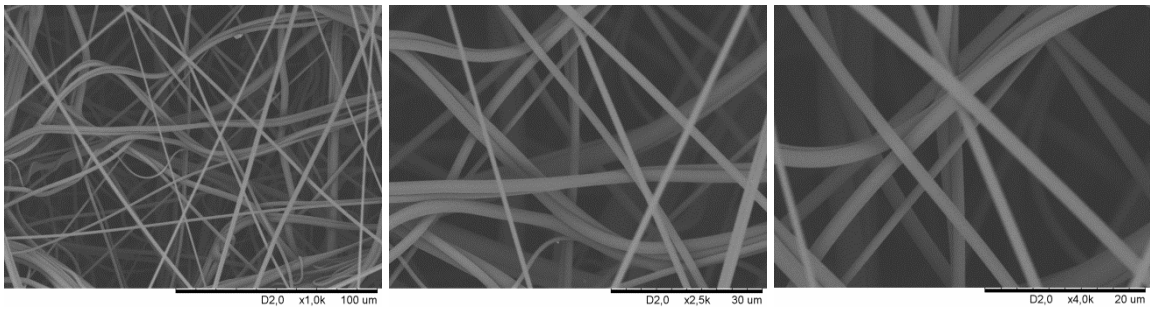

110 D)

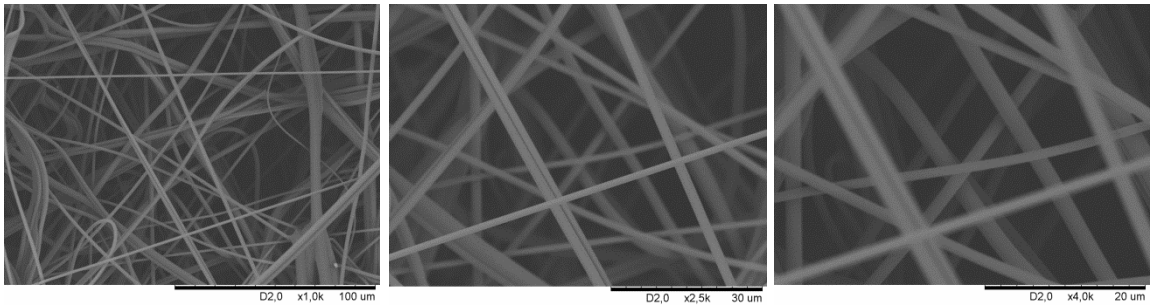

Fig. 110. SEM images for sample 15 at four different areas and three different magnifications (left – 1000x, middle – 2500x, right – 4000x). 110 A) area 1, 110 B) area 2, 110 C) area 3, 110 D) area 4.

111 A)

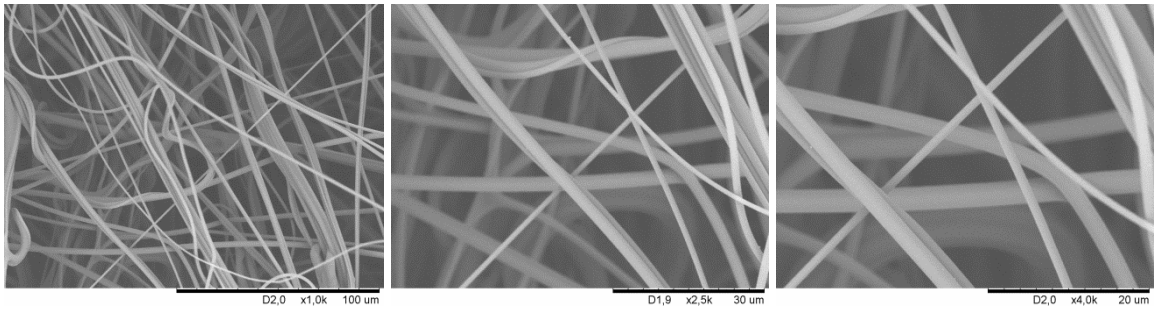

111 B)

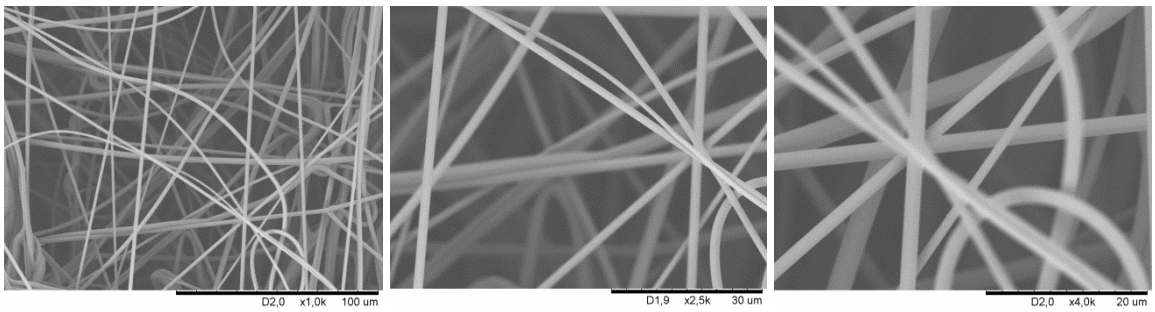

111 C)

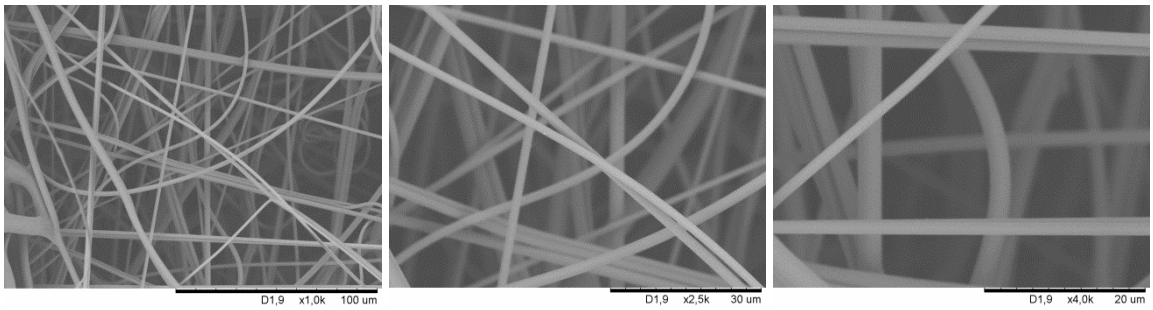

111 D)

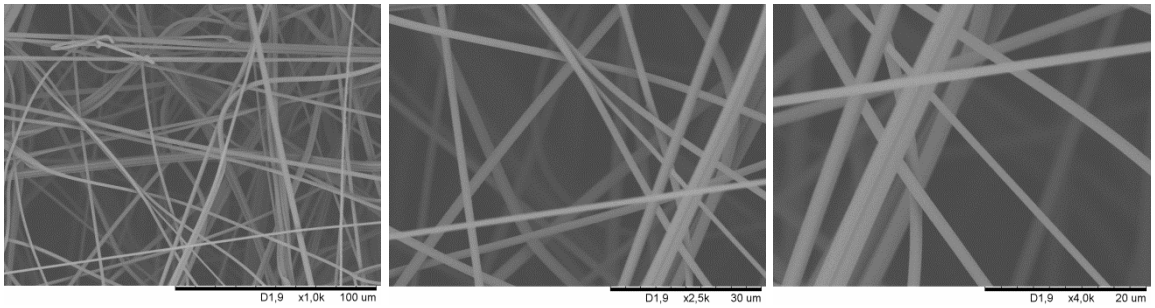

Fig. 111. SEM images for sample 16 at four different areas and three different magnifications (left – 1000x, middle – 2500x, right – 4000x). 111 A) area 1, 111 B) area 2, 111 C) area 3, 111 D) area 4.